Theoretical analysis and design
of high-performance frequency converters
for LIDAR systems

**Dissertation zur Erlangung des Doktorgrades
der Naturwissenschaften (Dr. rer. nat.)**

**Fakultät Naturwissenschaften
Universität Hohenheim**

Institut für Physik und Meteorologie

vorgelegt von
Gerd Achim Wagner

aus Kirchheim unter Teck
2009

This thesis was accepted as a doctoral dissertation in fulfillment of the requirements for the degree "Doktor der Naturwissenschaften" by the Faculty of Natural Sciences at the University of Hohenheim, Stuttgart, Germany on 2 July 2009.

Date of oral examination: 24 July 2009

Examination committee:

Supervisor and reviewer: Prof. Dr. V. Wulfmeyer
                          Institute of Physics and Meteorology,
                          University of Hohenheim

Co-reviewer   PD Dr. A. Giesen
                          German Aerospace Center (DLR) - Institute of Technical Physics,
                          Stuttgart

Additional examiner: Prof. Dr. K. Jetter
                          Institute of Applied Mathematics and Statistics,
                          University of Hohenheim

Dean: Prof. Dr. H. Breer
                          Faculty of Natural Sciences
                          University of Hohenheim

Summary

Frequency converters based on parametric and nonparametric frequency conversion are analyzed with respect to the specifications for high-average power water-vapor DIAL transmitters (DIAL: Differential Absorption LIDAR; LIDAR: Light Detection and Ranging). A Ti:Sapphire laser was selected as a suitable frequency converter to fulfill simultaneously all the requirements in the wavelength range of 935 nm and 820 nm. As thermal effects have a decisive influence on the overall performance and laser resonator design, they were simulated on Ti:Sapphire laser crystals in detail for different crystals, pump, and cooling configurations using finite element analysis (FEA). The performance and spectral properties of the Ti:Sapphire laser transmitter were modeled with a rate-equation approach for stable and unstable resonators. First theoretical results of an end-pumped Ti:Sapphire laser based on an optimized, asymmetric confocal unstable ring resonator design are presented. The obtained results can especially be used for the further development of a Ti:Sapphire laser to serve as a demonstrator for a future space-borne DIAL system transmitter according to the WALES (Water Vapor Lidar Experiment in Space) specifications. Furthermore, the adaptation of the developed theory modules to other lasing materials and configurations is straightforward.

Zusammenfassung

Frequenzkonverter basierend auf parametrischer und nichtparametrischer Frequenzkonversion wurden hinsichtlich der Spezifikationen für Wasserdampf-DIAL-Transmitter mit hoher mittlerer Leistung untersucht (DIAL: Differentielles Absorptions LIDAR; LIDAR: Light Detection and Ranging). Ein Titan-Saphir Laser wurde als geeigneter Frequenzkonverter ausgewählt, um gleichzeitig alle Anforderungen im Wellenlängenbereich von 935 nm und 820 nm zu erfüllen. Da thermische Effekte einen entscheidenden Einfluss auf die gesamte Leistung und das Laserresonatordesign haben, wurden sie detailiert an Titan-Saphir Laserkristallen für verschiedene Kristalle, Pump- und Kühlanordnungen mit Hilfe Finiter Elemente Analyse (FEA) simuliert. Die Leistung und spektralen Eigenschaften des Titan-Saphir Laser Transmitters wurden durch einen Bilanzgleichungsansatz für stabile und instabile Resonatoren modelliert. Erste theoretische Ergebnisse eines endgepumpten Titan-Saphir Lasers basierend auf einem optimierten, asymmetrischen konfokalen instabilen Ringresonatordesign werden gezeigt. Die erlangten Ergebnisse können insbesondere für die Weiterentwicklung eines Titan-Saphir Lasers verwendet werden, der als Demonstrator für einen zukünftigen weltraumgestützten DIAL Transmitter nach den WALES (Water Vapor Lidar Experiment in Space) Spezifikationen dienen soll. Ausserdem ist eine Anpassung der entwickelten Theoriemodule an andere Lasermaterialien und Konfigurationen unkompliziert.

Contents

List of Figures

List of Tables

Nomenclature and List of Symbols

Nomenclature

2d	2 dimensions
3d	3 dimensions
ACURR	Asymmetric confocal unstable ring resonator
AMR	Adaptive mesh refinement
APD	Avalanche photo diode
BR	Brewster-cut (crystal)
BRC	Brewster-cut crystal with cooler
BRUEC	Brewster-cut crystal with undoped end-caps
CAD	Computer aided design
CCD	Charge-coupled device
DIAL	Differential absorption lidar
DSP	Dual-side pumped (crystal)
EOM	Electro-optical modulator
ESA	European Space Agency
ESA	Excited state absorption
FC	Frequency converter
FEA	Finite element analysis
FOM	Figure of merit
FT	Fourier transformation
FWHM	Full-width at half maximum
FWM	Four-wave mixing
HEM	Heat exchanger method
HTC	Heat transfer coefficient
LASER	Light amplification by stimulated emission of radiation
LIDAR	Light detection and ranging
MOPA	Master oscillator power amplifier
NASA	National Aeronautics and Space Administration
OC	Output coupler
OPD	Optical path difference
OPO	Optical parametric oscillator
PCM	Phase conjugate mirror
PP	Plane-parallel
PZT	Piezoelectric mirror translator
RAMAN	Raman frequency converter
SBS	Stimulated Brillouin scattering

SHG	Second harmonic generation
SNR	Signal to noise ratio
SP	Spectral purity
SR	Stable resonator
SRS	Stimulated Raman scattering
SSP	Single-side pumped (crystal)
THG	Third harmonic generation
TISA	Titanium-doped Sapphire (Ti^{3+}:Al_2O_3)
UR	Unstable resonator
VRM	Variable reflectivity mirror
WALES	Water vapor lidar experiment in space

List of Latin Symbols

$\text{cond}(A)$	Spectral condition number of matrix
$\tilde{E}$	Phasor amplitude of electric field
$\tilde{E}_L$	Phasor amplitude of electric field (laser)
$\tilde{E}_{inj}$	Phasor amplitude of electric field (injection seeder)
$\vec{b}$	Vector with observations
$\vec{D}$	Electric displacement vector
$\vec{E}$	Electric field vector
$\vec{e}_L$	Unit vector for laser polarization
$\vec{e}_S$	Unit vector for Stokes polarization
$\vec{K}_p$	Wave vector of pump radiation
$\vec{K}_S$	Wave vector of Stokes radiation
$\vec{K}_{As}$	Wave vector of anti-Stokes radiation
$\vec{n}$	Normal vector
$\vec{P}$	Dielectic polarization vector
$\vec{r}$	Residual (vector)
$\vec{x}$	Solution vector
$\vec{x}_1$	Solution vector 1
A	Beam propagation matrix element
A	Coefficient matrix
A	Pumped area of crystal
A_a	Field amplitude of anti-Stokes radiation
A_a^*	Complex conjugate field amplitude of anti-Stokes radiation
A_p	Field amplitude of pump radiation
A_p^*	Complex conjugate field amplitude of pump radiation
A_s	Field amplitude of Stokes radiation

A_s^*	Complex conjugate field amplitude of Stokes radiation
B	Beam propagation matrix element
C	Beam propagation matrix element
c	Speed of light
C_p	Specific heat at constant pressure
C_{const}	Radiation constant
D	Beam propagation matrix element
D	Discrimination between lowest order modes
d	Resistive layer thickness
dE_{out}/dE_{pump}	Change of output energy with pump energy (slope efficiency)
dn/dT	Change of refractive index of sapphire with temperature
E	Scalar (real-valued) electric field
$E(x_1)$	Output electric field
$E_0(x_0)$	Input electric field
E_1	Complex field amplitude of idler wave
E_1^*	Complex conjugate field amplitude of idler wave
E_2	Complex field amplitude of signal wave
E_2^*	Complex conjugate field amplitude of signal wave
E_3	Complex field amplitude of pump wave
E_3^*	Complex conjugate field amplitude of pump wave
E_L	Laser photon energy
E_n	Electric field of transverse mode n
E_{LON}	Total energy of natural unseeded (multimode) contribution
E_{LOS}	Energy of seeded mode
E_{out}	Output pulse energy
E_{pump}	Pump-pulse energy
E_{sat}	Saturation fluence
E_{ST}	Stored pump laser energy
f	Focal length of thermal lens
f_a	Boltzmann occupation factor
f_x	Focal length in tangential plane
f_y	Focal length in sagittal plane
$f_{L,\{s,t\}}$	Focal length of cylindrical lens for sag. (s), tang. (t) plane
$f_{T,th,\{s,t\}}$	Focal length in sag. (s) and tang. (t) plane after principal plane transf.
$f_{th,\{s,t\}}$	Focal length of thermal lens in sagittal (s), tangential plane (t)
g	Raman gain coefficient at ω_s
g	Raman gain coefficient
$G(r)$	Correction term due to transmission changes of backscattered light

$g(z,t)$	Laser gain function
$G_{on}(r)$	On-line correction term
h	Heat transfer coefficient
h	Planck's constant
I	Intensity
I_L	Pump laser intensity
K	Petermann excess noise factor
k	Thermal conductivity
k_1	Thermal conductivity of subdomain 1
k_2	Thermal conductivity of subdomain 2
k_B	Boltzmann constant
K_C	Thermal conductivity of laser material
K_i	Coupling constant of mode i
k_S	Number of all Stokes modes
K_{00}	Lowest mode order Petermann excess noise factor for unstable resonator
L	Crystal length
L	Dissipative cavity loss
l	Laser crystal length
l'	Resonator length
$l_{i(,\{s,t\})}$	Free-space propagation distance i in sagittal (s), tangential plane (t)
l_{tot}	Total cavity loss
LW	Linewidth
M	Beam propagation matrix
M	Magnification (unstable resonator)
m	Reduced mass of site (molecule)
m	Super-Gaussian exponent in y-direction
M^2	Beam quality factor
M_g	Geometric magnification
M_s	Brewster-cut crystal beam propagation matrix sagittal plane
M_T	Transformation matrix between principal planes
M_t	Brewster-cut crystal beam propagation matrix tangential plane
M_x	Magnification in sagittal plane
M_y	Magnification in tangential plane
M_{CCW}	Beam propagation matrix - counter-clockwise direction
M_{CW}	Beam propagation matrix - clockwise direction
M_{eff}	Effective magnification (unstable resonator)
M_{FS}	Free-space beam propagation matrix
M_{GA}	Beam propagation matrix of Gaussian (gain) aperture

M_L	Beam propagation matrix of thin lens
M_M	Beam propagation matrix of curved (spherical) mirror
$M_{T,s}$	Brewster-cut crys. prop. matrix for sag. plane after principal plane transf.
$M_{T,t}$	Brewster-cut crys. prop. matrix for tang. plane after principal plane transf.
M_{TH}	Beam propagation matrix of Brewster-cut crystal under thermal load
M_{VRM}	Beam propagation matrix of variable (Gaussian) reflectivity mirror
N	Number density of Raman active sites (molecules)
n	Inversion density
n	Refractive index of Ti:Sapphire
n	Super-Gaussian exponent in x-direction
$n(0)$	Initial inversion density
$n(t)$	Inversion density
n_0	Number density of Ti^{3+}-ions
n_0	Refractive index of sapphire
N_1	Population of lower lasing level
n_1	Refractive index at idler wave
N_2	Population of upper lasing level
n_2	Refractive index at signal wave
n_3	Refractive index at pump wave
n_i	Photon number of mode i
n_s	Number (population) of Stokes generated photons
n_v	Number (population) of Stokes generated photons
N_{GA}	Fresnel number for the Gaussian aperture
N_{WV}	Water-vapor number density
OPD	Optical path difference
OPD_{mirror}	Optical path difference of equivalent (concave) mirror
P	Received power
P	Spectral purity
p	Polarization
$P(t)$	Temporal shape of pump pulse
$p(x,y,z)$	Normalized pump-beam profile
P_0	Single-side pump power (end-pumped geometry)
$p_G(x,y,z)$	Normalized Gaussian pump-beam profile
P_s	Injection seeder power
$P_{on}(r)$	Received power of off-line wavelength
$P_{on}(r)$	Received power of on-line wavelength
P_{calc}	Calculated spectral purity
$p_{G,\theta}(x,y,z)$	Normalized Gaussian beam profile for Brewster-cut crystal

P_{int}	Power in resonator
P_{out}	Laser output power
P_{ph}	Fraction of pump power resulting in heating
$p_{SG}(x, y, z)$	Normalized super-Gaussian pump-beam profile
$PBUT$	Pulse built-up time
Q	Heat source
q_0	Heat flux to subdomain inward normal
$Q_{G,\theta}(x, y, z)$	Heat source for Brewster-cut crystal pumped with Gaussian beam profile
R	Focal length of equivalent (concave) mirror
R	Output-coupler reflectivity
R	Radius of curvature of mirror
r	Mirror radius
r	Range
$R(0)$	Center reflectivity of VRM
$R(x)$	Reflectivity profile of VRM
R_0	Center reflectivity of VRM
r_0	Rod radius of crystal
R_m	Radius of curvature of magnifying wave
R_p	Pumping rate
R_{opt}	Optimum output coupler reflectivity
$sgxp$	Super-Gaussian exponent (GLAD)
T	Temperature
T	Transmission through absorption cell
t	Time
T_0	Prescribed temperature
T_0	Transmission without absorption cell
T_1	Temperature of subdomain 1
T_2	Temperature of subdomain 2
T_p	Pump pulse length
T_R	Resonator round-trip time
t_r	Resonator round-trip time
T_{amb}	Temperature of surrounding environment
T_{inf}	Ambient bulk temperature
T_{OC}	Output coupler transmission
V	Loss factor per resonator round-trip (unstable resonator)
V	Pumped crystal volume
V'	Resonator (mode) volume
$V_0(0)$	Fundamental mode field at the origin

$V_0(x)$	Fundamental mode field
V_n	Mode field of transverse mode n
W_p	Pump rate
$W_p(t)$	Pumping rate
x	Interaction length (Raman crystal)
x	Spatial coordinate; x-direction
y	Spatial coordinate; y-direction
z	Interaction or absorption length coordinate
z	Spatial coordinate; z-direction

List of Greek Symbols

α	Small-signal absorption coefficient at pump wavelength
α	Thermal expansion coefficient of sapphire
α_m	Molecular extinction coefficient
α_p	Particle extinction coefficient
$\alpha_{532,\pi}$	Absorption coefficient at 532 nm for π-polarization
$\alpha_{800,\pi}$	Absorption coefficient at 800 nm for π-polarization
$\alpha_{\downarrow,on}$	Effective on-line downward propagation absorption coefficient
$\alpha_{\downarrow}$	Effective downward propagation absorption coefficient
α_{off}	Effective off-line propagation absorption coefficient
$\alpha_{\uparrow,on}$	Effective on-line upward propagation absorption coefficient
$\alpha_{\uparrow}$	Effective upward propagation absorption coefficient
β	Backscatter coefficient
β	Rate constant for the radiationless transitions
χ	Linear susceptibility
$\chi^{(2)}$	Second-order nonlinear dielectric susceptibility
$\chi^{(3)}$	Third-order nonlinear dielectric susceptibility
$\chi^{(i)}$	Nonlinear dielectric susceptibility tensor of order i
χ_t	Time dependent susceptibility
$\chi_{eff}^{(2)}$	Effective second-order nonlinear susceptibility
χ_{ijk}	Components of third-rank nonlinear dielectric susceptibility tensor
$\Delta\nu$	Fourier-transform-limited linewidth
$\Delta\tau$	Pulse duration (Full width at half maximum, FHWM)
ΔE	Energy barrier for quenching process
Δk	Phase-mismatch parameter
ΔV	Loss per resonator round-trip (unstable resonator)
Δ	Wave vector mismatch
δ	Delta function

$\Delta\nu$	Half-width of resonance at half-maximum intensity
$\Delta\nu_{osc,UR}$	Linewidth of unstable resonator laser
$\Delta\nu_{osc}$	Linewidth of laser
ϵ/t_r	Resonator loss rate per round-trip
ϵ	Dielectric permeability of media
ϵ	Permittivity of material
ϵ_0	Permittivity of free space
ϵ_z	Change of crystal length in z-direction
ϵ_{ij}	Stress-strain components
η_a	Absorption efficiency
η_c	Color efficiency
η_f	Fluorescence storage efficiency (pump efficiency)
η_h	Fraction of pump energy dumped as heat
η_o	Optical coupling efficiency
η_Q	Quantum efficiency
η_{a_1}	Efficiency of radiation coupled into the laser cavity mode
η_{a_2}	Overlap between pump and cavity modes
η_{a_3}	Radiation absorbed by the laser crystal
η_{excit}	Excitation efficiency
η_{extr}	Extraction efficiency
η_{off}	Off-line system efficiency
η_{on}	On-line system efficiency
η_{slope}	Slope efficiency
η_{sys}	System efficiency
η_{total}	Total laser efficiency
Γ	Linewidth of Raman transistion
γ	Inversion reduction factor
$\Gamma(x)$	Euler Gamma function
γ_0	Eigenvalue of fundamental mode
γ_1	Eigenvalue of 2nd lowest mode
γ_n	Eigenvalue of transverse mode n
γ_2	Decay rate of energy level 2 to level 1
γ_{ci}	Cavity decay rate of mode i
γ_c	Cavity decay rate of mode (single-mode operation)
λ	Wavelength
λ_L	Laser wavelength
λ_l	Lasing wavelength
λ_p	Pump wavelength

μ_0	Magnetic permeability of free space
μ_L	Refractive index at laser frequency
μ_S	Refractive index at Stokes frequency
∇	Nabla operator
ν	Laser (photon) frequency
ν_L	Laser photon frequency
ν_l	Lasing frequency
ν_p	Pump frequency
$\nu_{aS,i}$	Higher order (i) frequency of anti-Stokes photons
ν_{aS}	Frequency of anti-Stokes photons
ν_p	Frequency of pump photons; elastic scattered pump photons
ν_{Rs}	Raman shift
$\nu_{S,i}$	Higher order (i) frequency of Stokes photons
ν_S	Frequency of Stokes photons
ω_0	Difference of angular frequencies of pump and Stokes
ω_0	Resonator carrier frequency
ω_1	Frequency of idler wave
ω_2	Frequency of signal wave
ω_3	Frequency of pump wave
ω_a	Optical frequency of anti-Stokes beam
ω_i	$1/e^2$-radius of mode in front of VRM
ω_L	Angular frequency of laser radiation
ω_m	$1/e^2$-radius of intensity profile (VRM)
ω_p	$1/e^2$-pump-beam radius
ω_p	Optical frequency of pump beam
ω_S	Angular frequency of Stokes radiation
ω_s	Optical frequency of Stokes beam
ω_x	$1/e^2$-pump-beam radius in x-direction
ω_y	$1/e^2$-pump-beam radius in y-direction
ω_{cf}	Minimum mode radius
$\omega_{g,\{s,t\}}$	Gaussian (gain) aperture radius in sagittal (s), tangential plane (t)
ω_{ga}	$1/e$-amplitude radius of variable reflectivity mirror
$\omega_{VRM,\{s,t\}}$	Variable reflectivity mirror radius in sagittal (s), tangential plane (t)
$\partial n/\partial T$	Change of refractive index of sapphire with temperature
$\partial n/\partial \epsilon_{ij}$	Elasto-optical coefficients
$\partial \alpha/\partial q$	Normal mode derivative of the polarizability tensor
$\phi(0)$	Initial photon density
$\phi(t)$	Photon density

ϕ_{λ_1}	Laser mode photon density
$\phi_{\lambda_{1,s}}$	Seeder photon density
$\phi_{\lambda_{av}}$	Virtual noise mode photon density
ρ	Density of material
$\rho(x)$	Field reflectivity profile of VRM
$\rho_{i,\{s,t\}}$	Radius of curvature of mirror i in sagittal (s) and tangential plane (t)
σ	Absorption cross section
σ	Resonator losses
σ_{off}	Off-line absorption cross section
σ_{on}	On-line absorption cross section
σ_e	Stimulated emission cross section
$\sigma_\downarrow$	Effective downward absorption cross section
$\sigma_\uparrow$	Effective upward absorption cross section
σ_{abs}	Ground-state absorption cross-section at pump wavelength
σ_{e,λ_1}	Stimulated emission cross section of lasing wavelength
$\sigma_{e,\lambda_{av}}$	Stimulated emission cross section of virtual noise mode wavelength
$\sigma_{e,eff}$	Effective stimulated emission cross section
τ^{-1}	Total decay rate of radiative and nonradiative transitions
τ_f	Fluorescence lifetime
τ_p	Pulse length
τ_r^{-1}	Radiative decay rate
$\tau_{nr_0}^{-1}$	Nonradiative decay rate
τ_{therm}	Thermal relaxation time
θ	Shear angle
θ_B	Brewster angle (air-Sapphire)
θ_{B*}	Brewster angle (Sapphire-air)
θ_i	Angle of incidence at mirror i
$\tilde{\gamma}_{0,0}$	Eigenvalue of fundamental mode (spherical resonator)
$\tilde{\chi}$	Frequency dependent complex susceptibility
$d\Omega$	Solid angle of initial spontaneous emission

1 Introduction and scientific motivation

In 1988, the *Intergovernmental Panel on Climate Change (IPCC)* was established by the *World Metrological Organization (WMO)* and the *United Nations (UN)*. Since then, the IPCC reports showed, that a global anthropogenic climate change is very likely to happen with various regional extends. In addition, extreme weather will intensify in number and magnitude. The resulting social and economic consequences could be on an unprecedented scale.

However, satellites to globally monitor atmospheric key variables like water-vapor, wind [ADM], and temperature with high spatial resolution using differential absorption lidar (DIAL) technology are not in orbit up to now, or even not on an official roadmap of the major space agencies [ESA, NASA]. Moreover, the high-resolution data are not available to climate and weather modelers to set up the initial fields of their models, in spite of the fact that a significant impact of airborne water-vapor DIAL data on mesoscale weather forecasting [WWRP] has already been demonstrated [Wulfmeyer06].

The current situation of inacurrate spatial and temporal initialization of the water vapor field makes nowcasting very difficult. A water-vapor DIAL system with high resolution, high accuracy, and large range together with improved data assimilation techniques can be used for better initialization of the water vapor field. This leads to an improved and extended nowcasting [Wulfmeyer03]. Additionally, ground-based 3d-scanning DIAL systems as the "Lidar reference system" can significantly advance our knowledge about atmospheric turbulence. Moreover, ground-based scanning systems are demonstrators for the technological feasibility of high-average power DIAL systems.

Although the technology involving active remote sensing has been intensively developed for more than two decades and offers advantages over passive remote sensing [Wulfmeyer05], it is still a challenge to built a DIAL system based on a high-power transmitter. This is mainly due to the high requirements on the passive and active stability of the transmitters and the overall complexity of the systems. Additionally, single components of the transmitters, e.g. pump diodes, optics, and crystals, have to prove long-term stability under a rough environment.

In fact, the basic problems of the development of a high-power laser transmitter are known since almost shortly after the invention of the laser, and unfortunately, the same problem areas still remain until today. Efforts to overcome the obstacles mostly failed due to poor engineering and the provisional character of the solution. Furthermore, the developed DIAL systems still show a high degree of maintenance, making it hardly possible to be operated on an aircraft, and impossible to be operated on a spaceborne platform. Even a full autonomous operated ground-based demonstrator is not yet available.

Previous efforts concentrated mainly on solving problems with single system components

of the transmitter, receiver, and data acquisition. Detailed specifications of ground-based, airborne, and spaceborne platforms were not available due to the lack of simulators, and parts of the specifications are still under discussion within the DIAL community. A complete water-vapor DIAL system is commercially not yet available.

The work presented here is divided into the following parts. First, the basic DIAL operation principle is reviewed in short together with overall requirements set to the frequency converter transmitter. After that, three possible candidates for a high-power frequency converter are compared theoretically regarding their capabilities for a DIAL transmitter. Due to the long-term experience at IPM (Institute of Physics and Meteorology, University of Hohenheim, Stuttgart, Germany) with laser transmitter development, a frequency converter based on a Ti:Sapphire laser is theoretically investigated regarding its thermal load on the crystal, overall performance, and spectral behavior with emphasis on spectral purity. The theoretical analysis is carried out for a stable and unstable resonator design and is embedded in a complete design cycle.

As unstable resonator designs will become more important in future laser design due to their scientific potential regarding the mode structure and mode volume, the design procedure of an unstable resonator for a high-power end-pumped Ti:Sapphire laser is carried out, and its expected performance together with expected experimental results are presented. Additionally, active stabilization techniques for pulsed lasers are reviewed and analyzed, as this is a key technology for a DIAL transmitter. The modification and extension of the developed models and design procedures presented here to other frequency converters and resonator configurations is straightforward. The work closes with a summary, an outlook, and future recommendations.

The theoretical analysis and system concept designs for a high-power DIAL transmitter were carried out within the framework of the "Lidar reference project" funded by the German research foundation (DFG) and the "Frequency converter project" funded by the German aerospace agency (DLR). The work was performed at the Institute of Physics and Meteorology (IPM) at the University of Hohenheim, Stuttgart, Germany.

2 DIAL principle and transmitter requirements

Besides the technological challenges of building a high-power scanning DIAL system as indicated in the previous section, a DIAL system being capable of measuring at day and night is the key instrument to study the Earth's atmosphere and related processes therein. Due to the large variability of water vapor in the atmosphere together with a high temporal and spatial variation, the need for a scanning water-vapor DIAL is quite obvious. The topics to be studied cover the following atmospheric processes: convection initiation, formation and organization of clouds and precipitation, turbulent boundary layer processes. In addition, the 2d-, 3d-data fields provided can be used for sensor validation and calibration. Their assimilation in weather forecast systems can improve the initialization of the models and their overall verification [Wulfmeyer03, Grzeschik08]. Similar studies also apply for other constituents of the atmosphere, e.g. O_3, CH_4, CO_2, that can be tracked by tuning the transmitter on suitable absorption wavelengths and adjusting the receiver path and the data processing accordingly.

The DIAL principle (Differential absorption LIDAR; LIDAR: light detection and ranging) is based on the emission of two pulses with alternating frequencies. One pulse is emitted on an absorption maximum (online wavelength) in the electromagnetic spectrum of the species, and the other pulse is emitted on a low-absorption part in the spectrum of the species, close to the online wavelength (offline wavelength). Other contributions of aerosol, backscatter and absorption can usually be considered to be the same for on- and offline wavelength. It is assumed, that the constitution and spatial distribution of the atmosphere does not change during emission and reception of the two pulses, and that the same volume is being probed. Taking the ratio of the received power, a measure that is nearly proportional to the number density of the observed species (e.g. H_2O, O_3, CH_4, CO_2) is achieved. A scheme of a DIAL system is depicted in Fig. 2.1. A convenient differential expression of the LIDAR equation is given by [Bösenberg05, Bösenberg98]

$$\frac{d}{dr}\ln\left(P\,r^2\right) = \frac{d}{dr}\ln(\eta_{sys}) + \frac{d}{dr}\ln(\beta) - 2\alpha_p - 2\alpha_m \qquad (1)$$
$$-\alpha_\uparrow - \alpha_\downarrow + G(r),$$

where r is the range, P is the received power, η_{sys} is the system efficiency, β is the backscatter coefficient, and α_p, α_m are the particle and molecular extinction coefficients, respectively. $\alpha_\uparrow$ and $\alpha_\downarrow$ are effective absorption coefficients for up- and downward propagation due to Doppler-broadened light with various contributions of Rayleigh and backscatter coefficients, and the water-vapor distribution itself also modifies the spectral distribution of the backward propagated light. A correction term $G(r)$ is introduced to account for transmission changes of the backscattered light. Taking the ratio of the received power for on- and offline wavelengths
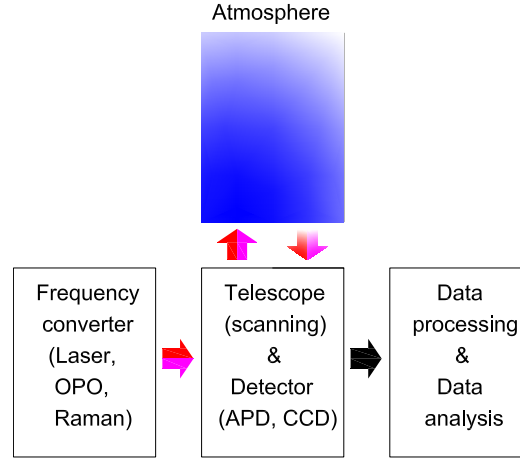
Figure 2.1: Scheme of DIAL system (APD: Avalanche photo diode, CCD: Charge-coupled device). A DIAL system mainly consists of three units: frequency converter (transmitter), receiver (telescope), and data acquistion (including data processing).

results in

$$\frac{d}{dr} \ln\left(\frac{P_{on}(r)}{P_{off}(r)}\right) = \frac{d}{dr} \ln\left(\frac{\eta_{on}}{\eta_{off}}\right) + \alpha_{\uparrow,on} + \alpha_{\downarrow,on} - 2\alpha_{off} + G_{on}(r) \tag{2}$$

The first term in Eq. 2 accounts for the system efficiency in on-and offline mode. $\alpha_{\uparrow,on}$ and α_{off} can be written as

$$\alpha_{\uparrow,on;off} = \sigma_{(on;off)} N_{WV}, \tag{3}$$

where $\sigma_{(on;off)}$ is the absorption cross section and N_{WV} is the water-vapor number density. $\alpha_{\downarrow,on}$ is more complex due to the spectral change of the backscattered light, and the correction term $G_{on}(r)$ is discussed in [Bösenberg98, Vogelmann08].
With the above considerations, the DIAL equation reads

$$N_{WV}(r) = \frac{1}{\sigma_{\uparrow} + \sigma_{\downarrow}} \left(G(r) - \frac{d}{dr} \ln\left(\frac{P_{on}(r)}{P_{off}(r)}\right) \right), \tag{4}$$

with the effective absorption cross sections $\sigma_{(\uparrow;\downarrow)}$. Without corrections, the DIAL equation is given by

$$N_{WV}(r) = \frac{1}{2\sigma} \frac{d}{dr} \ln\left(\frac{P_{on}(r)}{P_{off}(r)}\right). \tag{5}$$

The requirements for a DIAL transmitter are listed in Tab. 2.1 with emphasis in transmitter requirements for a spaceborne platform according to the WALES (WALES: Water Vapour

Lidar Experiment in Space[1]) specifications [WALES04] of ESA (European Space Agency), and ground-based scanning operation [Wulfmeyer01a, Wulfmeyer01b]. The wavelengths are given for a ground-based, and an air-, spaceborne system according to the different transmission and absorption characteristics due to upward and downlooking operation modes. To achieve a good signal-to-noise ratio (SNR), the pulse energy should generally be as high as possible. A higher repetition rate allows for signal averaging to obtain a higher SNR, or is necessary for a scanning capability. The pulse duration defines the range-resolution. The pulse linewidth, tunability, and spectral purity are the spectral characteristics of the transmitter. Their requirements are given according to the water-vapor spectroscopy data. The conversion efficiency should be as high as possible, and the beam quality can be important in long-term operation due to possible energy fluctuations leading to optical damage. The boresight stability and the beam divergence are critical parameters in order to eliminate systematic errors in regions with incomplete overlap between transmitter and receiver.

Table 2.2 gives an overview of current water-vapor DIAL systems. It can be seen that lasers are widely used as frequency converters. Especially Ti:Sapphire lasers are attractive due to their wide tuning range (670-1070 nm), which covers the 820 nm and the 935 nm absorption bands of water vapor. For the same reason, optical parametric oscillators (OPO) are also widely used as frequency converters. Up to date, the wavelengths within the specifications (Tab. 2.1) required for a water-vapor DIAL system cannot directly generated. A combination of a pump (laser) with a suitable frequency converter (OPO, Raman, laser) is needed. The analysis presented here is therefore of special interest. However, direct wavelength creation with lasers around 940 nm (935 nm, 942 nm, 944 nm) based on mixed Garnet crystals [Treichel04] are under investigation and development (943 nm: see [Kallmeyer07]).

---

[1]WALES reached phase A level status (Earth Explorer, Living Planet Programme, ESA).

Table 2.1: Transmitter requirements for a high-power water-vapor DIAL. Note: the requirements for a future DIAL system transmitter for ground-based, airborne or spaceborne operation are very similar.

Parameter, Unit	Value	Comment or WALES specifications
Wavelength region, nm	820	ground-based system
	935	air-,-spaceborne system
		WALES wavelengths:
		935.906 nm : weak line
		935.561 nm : medium strong line
		935.685 nm : strong line
		935.851 nm : offline
Pulse energy, mJ	75	for each wavelength (WALES)
Energy instability, % RMS	< 4	
Repetition rate, Hz	25	for each wavelength (WALES)
Pulse duration, ns	< 200	
Conversion efficiency, %	> 20	optical-optical
Pulse linewidth, MHz	< 160	(WALES)
Frequency instability, MHz	< 60	(WALES)
Tunability, GHz	± 10	
Spectral purity, %	> 99.7	> 99.9 (WALES)
Polarization, %	> 99	
Beam quality, M^2	< 3	
Boresight stability, μrad	< 15	

Table 2.2: Specifications of selected water-vapor DIAL systems (order arbitrary).

System, nationality, platform type	Frequency converter technology	Wavelength, nm	Pulse energy, mJ	Repetition rate, Hz	Linewidth, MHz	Pulse length, ns	Frequency stability, MHz	Spectral purity, %	Energy fluctuation, % rms	$\Delta\nu_{on,off}$, GHz	Beam stability, μrad	Reference
MPI I, GER, ↓	Alexandrite laser	720-780	(>) 50	(>) 15	(<) 40	< 200	± 15	(>) 99.99	< 8	50	0.4	[Wulfmeyer98a],a
NASA LARC, USA, ↑	Alexandrite lasers	725-780	30	10	0.7 pm	200	n.s.	> 99.85	n.s.	n.s.	< 0.2	[Browell98],b
NASA LASE, USA, ↑	Ti:Sapphire laser	813-818	10	10	< 0.25 pm	35	n.s.	> 99	n.s.	n.s.	< 0.4 mrad	[Browell98],c
CNRS, FRA, ↑	Alexandrite laser	727-770	50	10	1.3 pm	n.s.	n.s.	> 99.99	n.s.	442 pm	< 0.4	[Bruneau01a],d
DLR, GER, ↑	KTP OPO	935	12	100	140	7	n.s.	> 99	n.s.	n.s.	n.s.	[Poberaj02],e
DLR II, GER, ↑	KTP OPO	935	45 (60)	100	150	5.5	< 30	> 99.95	n.s.	WALES	n.s.	[Wirth08],f
MPI II, GER, ↓	Ti:Sapphire laser	820	18.6	50	22.5	11.2	n.s.,o.m.	99.97	n.s.	n.s.	n.s.	[Ertel05],g
IMK FZK, GER, ↓	Ti:Sapphire amplifier	700-950	250	20	130-250	2-4	± 5	> 99.9	n.s.	n.s.	n.s.	[Vogelmann08],h
UHOH, GER, ↓ ○	Ti:Sapphire laser	820	16 (27)	250	< 157	40	< 10	> 99.6	3.7	n.s.	< 5	[Schiller09],i

↓: groundbased platform, ↑: airborne platform, ○: scanning capability, n.s.: not specified, o.m.: other method (not comparable), t.b.c.: to be confirmed, $\Delta\nu_{on,off}$: on-,offline difference in GHz

a: Master laser: cw-Ti:Sapphire laser; slave laser: Alexandrite laser.
b: 2 Alexandrite lasers for on-,offline.
c: LASE: Lidar Atmospheric Sensing Experiment (developed at LaRC).
d: Complete airborne lidar system name: LEANDRE II (Lidar pour l'Etude des interactions Aérosols Nuages Dynamique Rayonnement et du cycle de l'Eau;
additional associated references: [Bruneau01b, Bruneau94, Bruneau91].
e: Additional associated references: [Fix98, Ehret98].
f: Multi-wavelength capability according to WALES specifications. 60 mJ pulse energy with reduced spectral purity of 99%.
g: Dual-wavelength capability.
h: System location: Schneefernerhaus, 2675 m asl (above sea level), Zugspitze, Germany.
i: System mounted on mobile platform. Transmitter description in [Schiller09].

MPI: Max-Planck-Institut für Meteorologie, Hamburg, Germany.
NASA LaRC: NASA Langley Research Center, USA.
CNRS: Service d Aéronomie du Centre National de la Recherche Scientifique, Université Pierre et Marie Curie, Paris, France.
DLR: Deutsche Forschungsanstalt für Luft und Raumfahrt, Oberpfaffenhofen, Germany.
IMK FZK: Institut für Meteorologie und Klimaforschung, Forschungszentrum Karlsruhe, Garmisch-Partenkirchen, Germany.
UHOH: Institut für Physik und Meteorologie, Universität Hohenheim, Stuttgart, Germany.

3 Suitable frequency converters and performance modeling

Various methods for creating the required radiation in the wavelength range found in Tab. 2.1 can be applied. The methods can be divided into parametric and nonparametric processes. In an ideal parametric process, the (nonlinear) medium (e.g. crystal) does not exchange energy with an applied field (pump radiation, photons), and initial and final quantum states are the same. Energy and momentum conservation is given by the (pump) photons only, and the energy levels are considered to be virtual energy levels with a lifetime given by the uncertainty principle. In a nonparametric process, the radiation interacts with the medium by absorption, spontaneous, and stimulated emission using real energy levels. However, at high pump radiation intensities, nonlinear effects can also occur in nonparametric processes, as it is the case, e.g., in saturable absorbers and in the saturation of laser amplifiers. Therefore, the abovementioned division can not be seen as a strict definition, rather is it a classification on a basic level.

Table 3.1 lists a selection of parametric, nonparametric, and nonparametric nonlinear interactions. The relation between the electric displacement $\vec{D}(t)$ and the electric field $\vec{E}(t)$ can be written as

$$\vec{D}(t) \;=\; \epsilon \, \vec{E}(t) \tag{6}$$

$$=\; \epsilon_0 \, \vec{E}(t) + \vec{P}(t) \,, \tag{7}$$

with t being the time, ϵ, ϵ_0 are the permittivity and the permittivity of free space, respectively, and $\vec{P}$ being the dielectric polarization given by

$$\vec{P}(t) \;=\; \epsilon_0 \, \chi \, \vec{E}(t) \,, \tag{8}$$

Table 3.1: Selection of parametric, nonparametric, and nonparametric nonlinear processes (see [Bloembergen96]).

Parametric	Nonparametric	Nonparametric nonlinear
Optical parametric oscillator (OPO)	Laser	Saturable absorber
Second-harmonic generation (SHG)		Saturation of laser amplifier
Third-harmonic generation (THG)		Stimulated Raman scattering
Four-wave mixing (FWM)		Stimulated Brillouin scattering
		Multiphoton absorption
		Raman laser

with χ being the linear susceptibility. At high radiation intensities, the linear relation is no longer valid and $\vec{P}$ must be developed in a power series with

$$\vec{P}(\vec{E}(t)) \;\; = \;\; \epsilon_0 \, (\chi \, \vec{E}(t) + (\chi^{(2)} \, \vec{E}(t)) \, \vec{E}(t) + ((\chi^{(3)} \, \vec{E}(t)) \, \vec{E}(t)) \, \vec{E}(t) + \dots) \,, \tag{9}$$

where $\chi^{(i)}$ are the nonlinear dielectric susceptibility tensors of the corresponding order. It should be noted that Eqs. 8,9 are only valid in the case of a lossless, nondispersive medium. A second order nonlinear effect can be written as

$$\vec{P}^{(2)}(\vec{E}(t)) \;\; = \;\; \epsilon_0 \, ((\chi^{(2)} \, \vec{E}(t)) \, \vec{E}(t)) \,, \tag{10}$$

or in components by

$$P_i^{(2)} \;\; = \;\; \epsilon_0 \, \sum_{jk} \chi_{ijk,t} \, E_j(t) \, E_k(t) \,, \tag{11}$$

with χ_{ijk} being a third-rank tensor with $\tilde{\chi}_{ijk} = \tilde{\chi}_{ikj}$ ($\tilde{\chi}$: frequency dependent complex susceptibility) for the lossy case, and $\chi_{ijk,t} = \chi_{jik,t}$ (χ_t: time dependent susceptibility), $\chi_{ijk} = \chi_{jik}$ with real $\chi^{(2)}$ tensors, respectively, for the lossless case [Weber93]. Therefore, the lossy and lossless case can be distinguished by the elements and structure of the corresponding tensor.

In the following, all three frequency converter concepts based on parametric (OPO, Ch. 3.1), nonparametric nonlinear processes (Raman laser, Ch. 3.2), and nonparametric processes (laser, Ch. 3.3) are discussed, and suitable performance modeling methods are outlined.

3.1 Optical parametric oscillator (OPO)

In an optical parametric oscillator, a nonlinear medium with susceptibility $\chi^{(2)}$ is placed inside a resonator (Fig. 3.1). The applied pump radiation with frequency ω_3 is depleted and converted in a second-order nonlinear process into a signal wave with frequency ω_2 and an idler wave with frequency ω_1 (three wave interaction):

$$\omega_3 \;\; = \;\; \omega_2 + \omega_1 \,. \tag{12}$$

If the resonator is resonant only at the signal wave, it is called a singly-resonant OPO (SRO), otherwise if the resonance is given at signal and idler waves, it is a doubly-resonant OPO (DRO). Tuning of an OPO is possible by the phase-matching condition. For spectral narrowing, an OPO can also be injection-seeded.
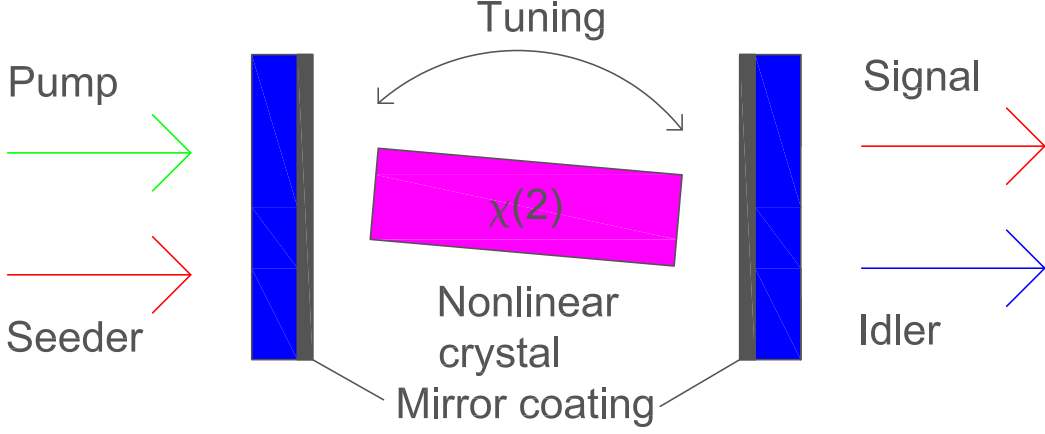
Figure 3.1: Scheme of OPO frequency converter set up.

The interaction of the three fields can be described by coupled-wave equations [Ebrahimzadeh07]:

$$\frac{dE_1(z)}{dz} = i\,\kappa_1\,E_3(z)\,E_2^*(z)\,\exp(i\,\Delta k\,z) \tag{13}$$

$$\frac{dE_2(z)}{dz} = i\,\kappa_1\,E_3(z)\,E_1^*(z)\,\exp(i\,\Delta k\,z) \tag{14}$$

$$\frac{dE_3(z)}{dz} = i\,\kappa_1\,E_1(z)\,E_2^*(z)\,\exp(i\,\Delta k\,z). \tag{15}$$

Here, z is the (interaction) length coordinate, E_1, E_2, and E_3 are the complex field amplitudes of idler, signal and pump, and the E_j^* ($j=\{1,2,3\}$) are the complex conjugate of them. κ_j is given by $\kappa_j=\omega_j\,\chi_{eff}^{(2)}/2\,n_j\,c$ with $j=\{1,2,3\}$, n_j is the refractive index, $\chi_{eff}^{(2)}$ is the (effective) second-order nonlinear susceptibility, and Δk is the phase-mismatch parameter with

$$\Delta k = k_3 - k_2 - k_1 \tag{16}$$

$$= \frac{n_3}{\lambda_3} - \frac{n_2}{\lambda_2} - \frac{n_1}{\lambda_1}, \tag{17}$$

where n_j and λ_j are the refractive index and the wavelength. For optimum conversion, $\Delta k=0$ has to be fulfilled. The phase and therefore ω_1 and ω_2 can be adjusted by changing the angle or the temperature of the crystal.

Theoretical modeling of OPOs has been performed by e.g. [Harris69, Brosnan79] and more recently by [Smith95, Breteau93, Granot00]. Spectral narrowing of a pulsed OPO by injection seeding has been demonstrated in 1969 [Bjorkholm69]. Concerning the nonlinear crystals [Dmitriev99], besides other materials, potassium titanyl phosphate (KTiOPO$_4$, KTP), and the isomorphic potassium titanyl arsenate (KTiOAsO$_4$, KTA) [Bierlein89, Emanueli03] are being frequently used in OPOs. High-average signal powers of 33 W at 1534.7 nm have been achieved by an KTA-OPO pumped by a Nd:YAG laser at 1064 nm [Webb98]. The overall optical-optical conversion efficiency was >30%.

However, some problems associated with OPOs should be noted. First, the beam quality (M^2-factor) is strongly dependent on the beam quality of the pump laser. Additionally, at high signal intensities, the thermal load leads to further beam quality degradation, as the phase-matching condition is no longer fulfilled, and also the spectral purity is expected to be lowered. Second, for a suitable DIAL transmitter, an injection-seeded, (frequency stabilized) pump laser is necessary to maintain the spectral output properties of the OPO. To conclude, a DIAL system based on an OPO has more strict requirements set to the pump laser compared to a (Ti:sapphire) laser. However, the broad wavelength operation range, which is basically only limited by the transmission range of the nonlinear crystal, compensates the higher requirements set to the pump laser. A current airborne water-vapor DIAL system based on an OPO frequency converter according to the WALES specifications is described in [Wirth08].

3.2 Raman laser

The Raman effect is an inelastic scattering process (third-order nonlinear process, $\chi^{(3)}$) of photons with frequency ν_p in a material, in which frequencies higher ν_{aS} and lower ν_S are created in addition to the elastic scattered ν_p (pump) radiation:

$$\nu_{aS} = \nu_p + \nu_{Rs} \qquad \text{anti-Stokes frequency} \tag{18}$$

$$\nu_p \qquad \text{elastic Rayleigh scattering} \tag{19}$$

$$\nu_S = \nu_p - \nu_{Rs} \qquad \text{Stokes frequency}. \tag{20}$$

ν_{Rs} is a characteristic constant of the material and is called the Raman shift. This photon-phonon process is called spontaneous Raman scattering and the emitted radiation is incoherent. In the effect of stimulated Raman scattering (SRS) [Bloembergen67], the pump radiation intensity is further increased, and a previously excited atom or molecule in a energy state v or W respectively, interacts with a photon of frequency ν_S, or ν_{aS} respectively, then another photon with ν_S or ν_{As} is being emitted (stimulated emission). Here, the emitted coherent radiation is subsequently amplified, whereas the pump radiation is depleted.

$$\nu_p + \nu_{aS} = 2\nu_{aS} + \nu_{Rs} \qquad \text{anti-Stokes frequency} \tag{21}$$

$$\nu_p + \nu_S = 2\nu_{aS} - \nu_{Rs} \qquad \text{Stokes frequency.} \tag{22}$$

The total rate of Stokes created photons dn_s/dt can be described with [Penzkofer79]:

$$\frac{dn_s}{dt} = N\left(\frac{\partial\alpha}{\partial q}\right)^2 \frac{4\pi^3}{\mu_L\,\mu_S^2\,m\,c} I_L \sum_{k_s} \frac{\omega_s}{\omega_0} \left(\vec{e}_L\vec{e}_S\right)^2 \left(1 + n_s + n_v\right) \delta\left(\omega_S - \omega_L + \omega_0\right). \tag{23}$$
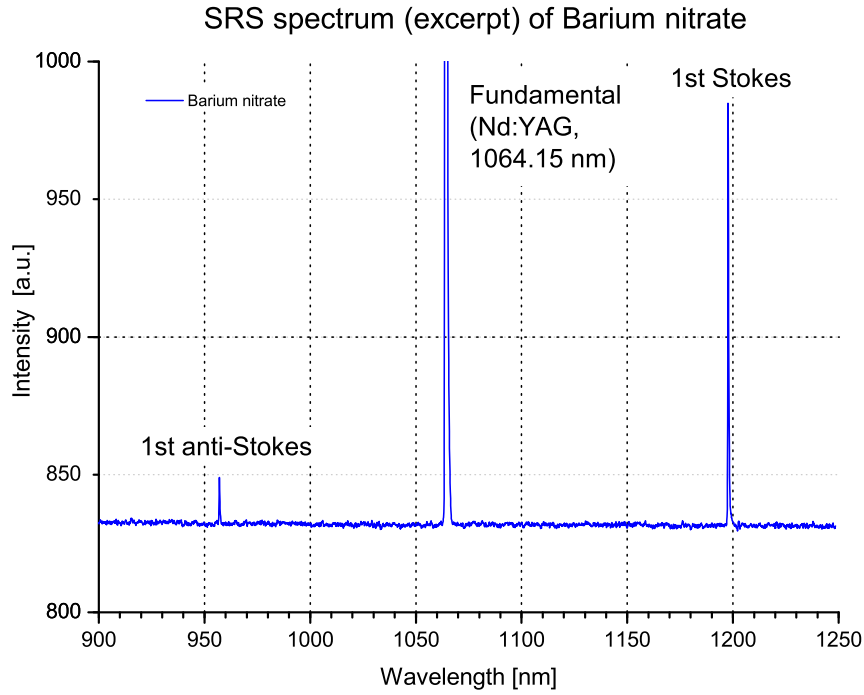
Figure 3.2: SRS spectrum (excerpt) measurement of Barium nitrate (Ba(NO$_3$)$_2$). Barium nitrate crystal provided by Optisches Institut, TU Berlin. The SRS experiment was performed in the frame of the DLR frequency converter project at IPM. 1st anti-Stokes line: 957.5 nm, 1st Stokes line: 1197.6 nm. The intensity of the anti-Stokes line is weaker, as the population of the excited level is lower compared to the ground-level population in thermal equilibrium.

In Eq. 23, N is the number density of Raman-active sites (molecules), $\partial\alpha/\partial q$ is the normal mode derivative of the polarizability tensor, μ_L and μ_S are the refractive indices at laser and Stokes frequency, respectively, and m is the reduced mass of the oscillating site (molecule). c is the speed of light, ω_S is the angular frequency of the Stokes radiation, and ω_0 is the difference of the angular frequencies of pump and Stokes. I_L is the pump laser intensity, $\vec{e}_L$ and $\vec{e}_S$ are the unit vectors for the laser and Stokes polarizations, respectively. n_S and n_v are Stokes (see above) and excited (phonon) populations, respectively. δ is a delta function. The sum is over all Stokes modes k_S. For a single Stokes mode, the summation in Eq. 23 is omitted.

Finally, the number of Stokes photons n_s for a single mode is given by [Penzkofer79]

$$n_S \;=\; \text{const.} \exp(g\,I_L\,x)\,, \qquad\qquad (24)$$

where g is the Raman gain factor, and x is the interaction length. In contrast to a laser, the intensity of the pump I_L is part of the gain expression for the amplification of n_S.

The frequency-dependent gain factor $g(\omega_s)$ is given by [Penzkofer79]

$$g(\omega_s) \;=\; N \left(\frac{\partial \alpha}{\partial q}\right)^2 \frac{4\,\pi^2}{\mu_L\,\mu_S\,c^2\,m\,\omega_0} \frac{\Gamma}{(\omega_S - \omega_L + \omega_0)^2 + \Gamma^2}\,, \tag{25}$$

where Γ is the linewidth of the Raman transition.

Figure 3.2 shows the created anti-Stokes and Stokes radiation in an performed SRS experiment. The Raman material was Barium nitrate ($Ba(NO_3)_2$, [Zverev99]). Shown are the anti-Stokes line at 957.5 nm and the Stokes line at 1197.6 nm together with the fundamental wavelength of the high-power Nd:YAG pump laser (1064.15 nm). The Raman shift of $Ba(NO_3)_2$ is 1047 cm^{-1}.

At even higher pump intensities, as the intensity of the first Stokes- or anti-Stokes radiation is further increasing, additional multiple Stokes and anti-Stokes lines of higher order i appear in the spectrum:

$$\nu_{aS,i} \;=\; \nu_p + i\,\nu_{Rs} \qquad \text{higher order anti-Stokes frequency} \tag{26}$$

$$\nu_{S,i} \;=\; \nu_p - i\,\nu_{Rs} \qquad \text{higher order Stokes frequency}\,. \tag{27}$$

In a four-wave mixing process (FWM) anti-Stokes-, pump-, and Stokes-photons interact together to create Stokes and anti-Stokes radiation:

$$2\nu_p + \nu_{aS} \;=\; \nu_S + \nu_{aS} \qquad \text{Stokes-anti-Stokes coupling}\,. \tag{28}$$

The overall process of the interaction of pump, Stokes, and anti-Stokes can be described by the four-wave mixing equations which are in the steady-state limit [Ottusch91]:

$$\frac{dA_p}{dz} \;=\; \frac{g}{2\,\omega_s}\,\omega_p\,\left(|A_a|^2 - |A_s|^2\right)\,A_p \tag{29}$$

$$\frac{dA_s}{dz} \;=\; \frac{g}{2\,\omega_s}\,\omega_s\,\left[-A_a^*\,A_p\,\exp(i\Delta z) + A_p^*\,A_s\right]\,A_p \tag{30}$$

$$\frac{dA_a}{dz} \;=\; \frac{g}{2\,\omega_a}\,\omega_s\,\left[-A_a\,A_p^* + A_p\,A_s^*\,\exp(i\Delta z)\right]\,A_p, \tag{31}$$

where $A_{p,s,a}$ are the field amplitudes, and $\omega_{p,s,a}$ are the optical frequencies of the pump, Stokes and anti-Stokes beams. g is the Raman gain coefficient at ω_s, z is the direction of pump beam propagation, and Δ is the wave-vector mismatch for the four-wave interaction of two pump photons with a Stokes and anti-Stokes photon. Also a relation regarding the wave vectors of pump, Stokes and anti-Stokes radiation ($\vec{K}_{p,S,aS}$) must be fulfilled for efficient conversion:

$$2\vec{K}_p = \vec{K}_S + \vec{K}_{As}\,. \tag{32}$$

By putting the Raman material in a resonator, the pump efficiency is increased, the operation threshold is decreased, and by suitable resonator mirror coating, the emission of a single (higher-order) Stokes or anti-Stokes Raman-line can be selected and controlled (Raman-laser [Pask03a], Fig. 3.3). A design option is to incorporate the Raman material directly into the resonator of the pump laser (intracavity SRS). Due to higher conversion efficiency, Raman lasers are usually operated in the Stokes instead of the anti-Stokes regime [He97], but also anti-Stokes Raman lasers are reported. In [Pask03b] an optical-optical conversion efficiency of 46% was achieved with a 1st-Stokes Raman laser being pumped at 1064 nm resulting in 3 W average output power at 1197 nm.

In contrast to OPOs, tuning of the output wavelength of a Raman frequency converter is not possible with a fixed pump wavelength. The output wavelength can only be tuned by shifting of the pump wavelength.
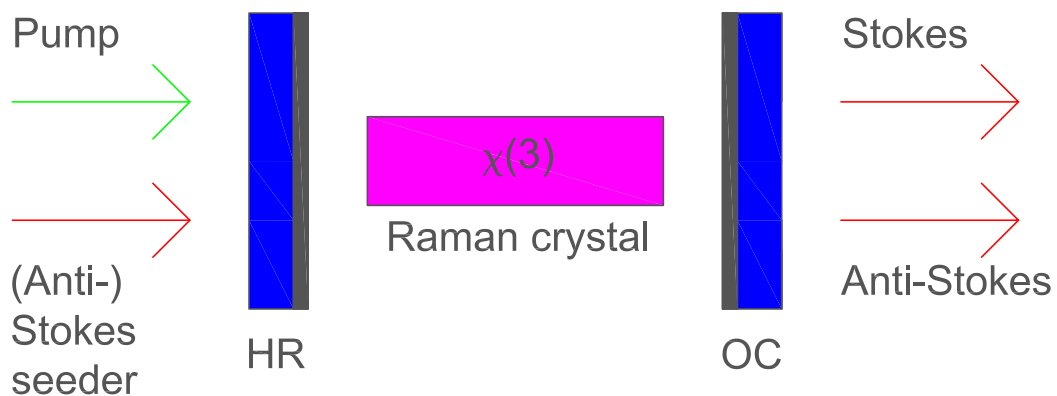
Figure 3.3: Scheme of Raman frequency converter set up.

3.3 Laser

A laser consists of an active gain medium which is activated by a suitable pumping process placed inside an optical resonator (Fig. 3.4) providing the feedback with customized output-coupling condition. In the following, only solid-state laser materials are considered, in which optically active ions (e.g. trivalent ions Nd^{3+}, Ti^{3+}, Cr^{3+}) are placed within a host material (e.g. $Y_3Al_5O_{12}$ (YAG), Al_2O_3 (sapphire), $BeAl_2O_4$). Other materials (liquid dye solutions, gas cells et cetera) are less suitable for water-vapor DIAL systems, mainly for maintenance and also for safety reasons. Another solid-state laser solution option could be to use pulsed semiconductor diode lasers, but so far pulsed diode lasers for high-average power operation are not available[2].

By the pumping process, energy is being transferred to the active ions and a population inversion is being created. Above threshold, the gain exceeds the loss and laser oscillation is being established at resonances of the cavity. Depending on the laser material, narrow-linewidth or broadband radiation is being created in a free running laser, the latter leading to tunable lasers.

Complete multimode laser operation can be described by coupled cavity and atomic rate equations [Siegman86a]:

$$\frac{dn_i(t)}{dt} = K_i\,N_2(t)\,[n_i(t)+1] - K_i\,N_1(t)\,n_i(t) - \gamma_{ci}\,n_i(t) \tag{33}$$

$$\frac{dN_2(t)}{dt} = \sum_i K_i\,n_i(t)\,[N_1(t)-N_2(t)] + \text{pumping terms} + \text{relaxation terms} \tag{34}$$

$$\frac{dN_1(t)}{dt} = -\sum_i K_i\,n_i(t)\,[N_1(t)-N_2(t)] + \text{pumping terms} + \text{relaxation terms}\,. \tag{35}$$
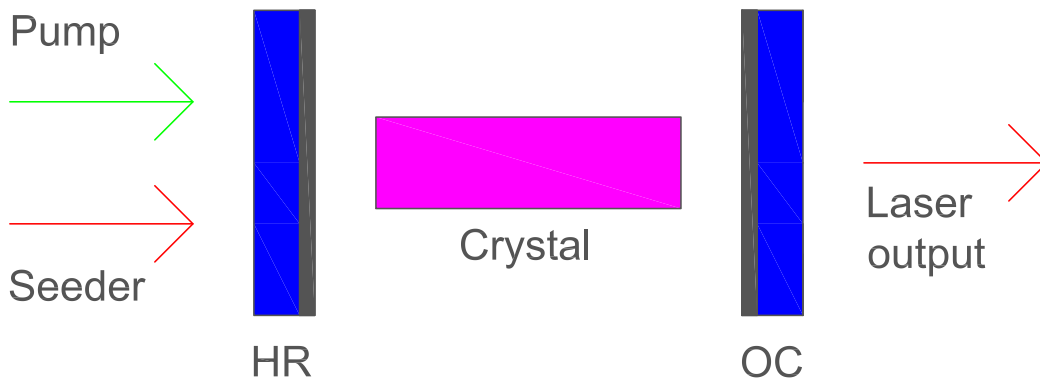
Figure 3.4: Scheme of laser frequency converter set up.

---

[2]Note: the power values given in datasheets for pulsed semiconductor diode lasers (e.g. 140 W) refer to the peak power.

In Eqs. 33-35, i is the mode number index, t is time, n_i are the cavity photon numbers, $N_{1,2}$ are the populations in lower and upper lasing level, K_i are the coupling constants, and γ_{ci} are the cavity decay rates. If only a single mode is excited, and if $N_1 \approx 0$, which can be applied in real 4-level energy systems (e.g. Ti:sapphire), then Eqs. 33-35 can be reduced to

$$\frac{dn}{dt} = K N_2(t) (n(t) + 1) - \gamma_c n(t) \tag{36}$$

$$\frac{dN_2}{dt} = R_p - K N_2(t) n(t) - \gamma_2 N_2(t), \tag{37}$$

with the pumping rate R_p.

The process leading to a decision for a further investigation of a single frequency converter is as follows. At present, the desired wavelengths can more easily created by OPOs and lasers. Raman materials are available, but the wavelengths can usually only be reached by additional adaptation of the pump wavelength. The tunability is therefore also more demanding for Raman converters.

The requirements set to pulse energy, repetition rate, and pulse length are expected to be fulfilled by all conversion techniques. High-quality crystals and optics are available.

Theoretically, the optical-optical conversion efficiency of $> 20\%$ can be fullfilled. However, for each converter they have to be experimentally demonstrated.

The pulse linewidth is not expected to be a critical parameter for all converters.

The frequency instability is primarily determined by the frequency stabilization technique. Suitable frequency stabilization techniques for single-mode, single-frequency operation are available and can be adapted to all converters. Additionally, the requirements to the pump laser are higher for the nonlinear converters (OPOs, Raman) concerning the beam profile and the energy stability. For an end-pumped laser, a moderate pump-beam profile quality ($M^2 \approx 3$) seems to be good enough to create the required inversion. The resulting beam quality of a laser is always better compared to OPOs. Special nonlinear effects, e.g. Raman beam clean-up, are not considered here.

A critical factor are the spectral properties of the frequency converter. Lasers and OPOs have demonstrated to maintain the spectral properties (spectral purity) at high pulse energies. Higher-order nonlinear effects are expected to limit the spectral characteristics of Raman frequency converters and probably also of OPOs. The polarization seems to be not a critical factor for all conversion techniques.

The boresight stability has to be determined experimentally, but it not considered to be a critical parameter for all conversion techniques.

To sum up, the more promising and suitable candidates at present are lasers and OPOs. Concerning the Raman frequency converter, more uncertainties remain, as basically all of the parameters for the requirements have not been demonstrated yet. Further experimental

investigation is necessary for Raman converters. A comparison of the transmitters is given in Tab. 3.2.

Finally, the unique properties of a laser concerning beam profile, and spectral characteristics were much more convincing compared to other conversion techniques. Based on this assessment, the TISA laser was chosen as the candidate to fulfill all requirements as a suitable candidate for a high-average power DIAL transmitter. The present assessment is also given by the fact, that this material is very well understood and can withstand high pulse energy. Other possible lasers within the 943 nm wavelength range for water-vapor detection, e.g. based on Nd:GSAG crystals (mixed garnets), are not a subject here [Kallmeyer07].

Within this work, there is strong emphasis on theoretical TISA modeling in all of its decisive factors for a high-power TISA laser, e.g. thermal lensing, spectral properties, resonator design, and performance modeling. In Ch. 4.5, a system of coupled differential equations for the description of gain-switched TISA[3] laser operation describing inversion density and photon density will be used to calculate the performance of a stable and unstable TISA laser. Thermal effects in differently shaped TISA crystals are extensively modeled in Ch. 4.2. Sta-

Table 3.2: Transmitter requirements in comparison with frequency converters (+: fulfills requirement, (+): expected to fulfill requirement, tbc: to be confirmed, uk: unknown, −: does not fulfill requirement, (−): not expected to fulfill requirement). Concerning the Raman frequency converter, only the Raman laser is taken into account. The Stokes and anti-Stokes lines of a simple Raman-shifter can also be used to create the required wavelength at the expense of the spectral properties. For the parametric converters, the pump laser is identified to have a decisive influence on all parameters.

Parameter, Unit	Value	OPO	Raman	Laser
Wavelength, nm	820	+	(+)	+
	935	+	(+)	+
Pulse energy, mJ	75	(+)	(+)	(+)
Energy instability, % RMS	< 4	+	(+)	+
Repetition rate, Hz	25	+	(+)	+
Pulse duration, ns	< 200	+	(+)	+
Conversion efficiency, %	> 20	+	(+)	+
Pulse linewidth, MHz	< 160	+	(+)	+
Frequency instability, MHz	< 60	+	(+)	+
Tunability, GHz	± 10	+	(+)	+
Spectral purity, %	> 99.7	(+)	tbc	(+)
Polarization, %	> 99	+	uk	+
Beam quality, M^2	< 3	−	(−)	+
Boresight stability, μrad	< 15	+	(+)	+

---

[3]In TISA, pumping with a ns-pump laser results in a similar situation to a Q-switched, cavity-dumped laser.

ble and unstable laser resonators are modeled in Ch. 4.3 and Ch. 4.4, respectively. Spectral narrowing by injection-seeding is presented in Ch. 4.6.2. Active laser frequency stabilization techniques for a TISA are compared and presented in Ch. 4.6.3. As the spectral purity is a critical parameter of a DIAL, it is investigated and modeled in Ch. 4.6.4, and laser noise is treated in Ch. 4.6.5.

4 Ti:Sapphire laser

4.1 Introduction and Ti:Sapphire laser crystal properties

Besides the broad tuning range of 670-1070 nm and the possibility of creating ultra-short pulses, the thermal and mechanical properties are also key features of this solid-state laser. Since the first laser demonstration in 1982 [Moulton82] and characterization [Moulton86, Albers86, Rapoport88], the titanium-doped sapphire ($Ti^{3+}:Al_2O_3$, Ti:sapphire, TISA) laser and its development is more than two decades later still a field of active research, for instance, in the field of high-resolution spectroscopy [Dupré07, Hannemann07], and the Ti:Sapphire laser has become a standard device not only in the laser laboratory.

High-quality TISA crystals are produced using the heat exchanger method (HEM [Rapoport88], Crystal Systems, USA). The crystal quality is defined as the figure of merit (FOM), which is given by the relation of the absorption coefficient α at 532 nm ($\alpha_{532,\pi}$) and 800 nm ($\alpha_{800,\pi}$) for π-polarization:

$$\text{FOM} = \frac{\alpha_{532,\pi}}{\alpha_{800,\pi}} . \tag{38}$$

High-quality crystals with FOM values of 200-1000 are available. Problems associated with Ti^{3+}-Ti^{4+}-ion pairs or other impurities leading to absorption at the lasing wavelength are solved. Annealing of the crystals under hydrogen atmosphere can improve the crystal quality. The residual Ti^{4+}-ions are then reduced to Ti^{3+}.

A detailed energy-level diagram of $Ti^{3+}:Al_2O_3$ is depicted in Fig. 4.2. The single 3d-electron ^2D of Ti^{3+} (electron configuration: $3d^1$) splits due the octahedral crystal field of the host crystal Al_2O_3 into two levels $^2T_{2g}$ (ground state) and $^2E_{2g}$ (excited state). The ground state $^2T_{2g}$ further splits into a lower level ^2E and an upper level $^2A_1$. The ground-state is further split due to spin-orbit interactions into two sets of Kramers' degenerate pairs $_2E_{3/2}$, $_2E_{1/2}$, while the $^2A_1$ splits into an $E_{1/2}$ Kramers' doublet. The excited state ^2E is mostly split by Jahn-Teller distortion into levels $E_{3/2}$, and $E_{1/2}$. The fluorescence (emission) is given by the lowest upper state and the two lower ground-states. The electronic levels are coupled to vibrations of the host crystal (electron-phonon interaction). Phonon broadening is therefore responsible for the tunability of TISA. The resulting absorption is between 400-600 nm with a maximum at 485 nm (π-polarization). The emission is between 600-1100 nm with a maximum at 760 nm (π-polarization, see Fig. 4.1). This is in contrast to other fixed wavelength solid-state lasers, e.g. Nd:YAG, where the energy levels are mostly unaffected by the vibrations of the host crystal lattice ions.

A simplified energy-level diagram of TISA is depicted in Fig. 4.3. TISA is a four-level laser system. The transitions $\text{③} \rightarrow \text{②}$, and $\text{①} \rightarrow \text{⓪}$ with lifetimes τ_{32} and τ_{10}, are fast compared

Ti:Sapphire: emission cross section for π- and σ-polarization
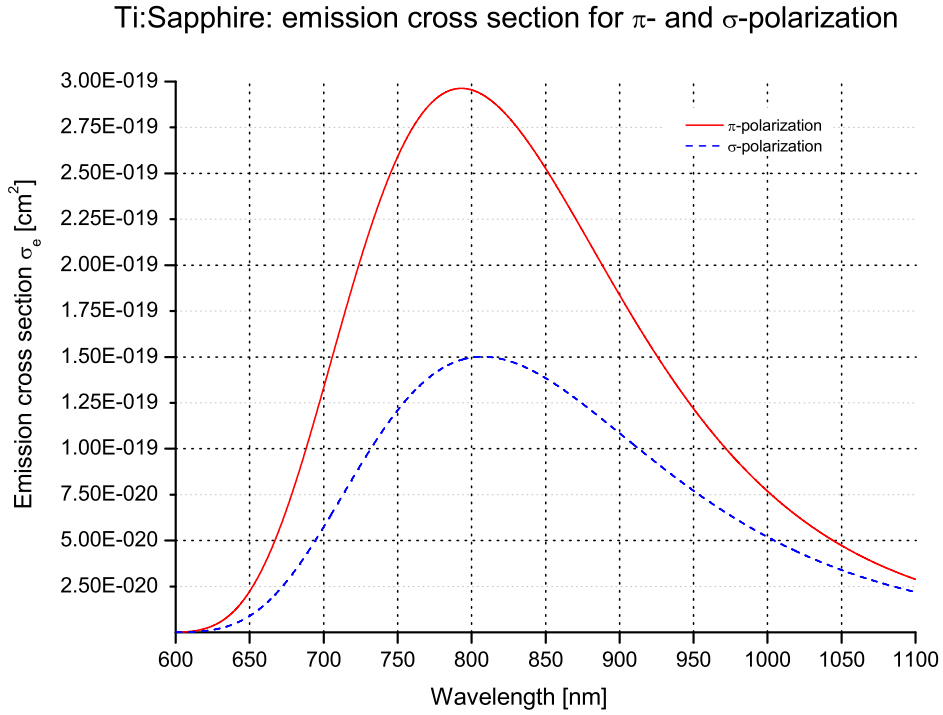
Figure 4.1: Ti^{3+}:Al$_2$O$_3$: stimulated emission cross section σ_e for π- and σ-polarization using Poisson-fit of [Eggleston88]. TISA crystals are being pumped with the polarization parallel to the c-axis of the crystal (π-polarization).
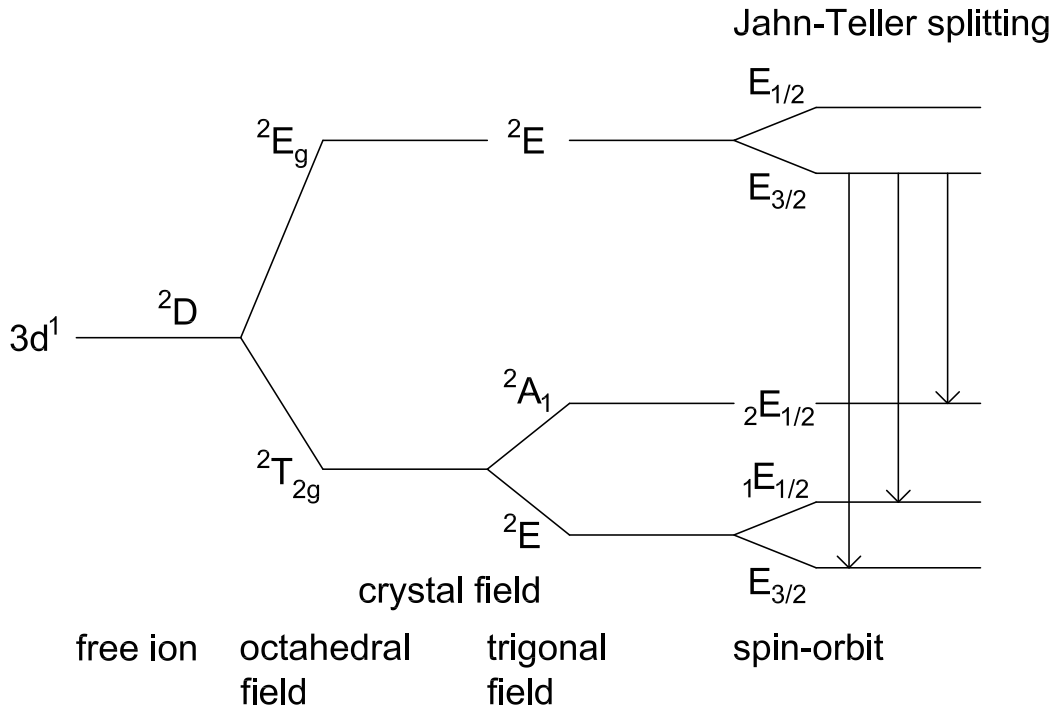
Figure 4.2: Detailed energy-level diagram of Ti^{3+}:Al$_2$O$_3$.

to the lifetime of the laser transition (fluorescence lifetime). Consequently, the populations

of the energy levels ③, and ⓪ can be neglected. The TISA energy level system is reduced to a 2-level system, considering the population inversion between upper lasing level ②, and lower lasing level ①. The quantum efficiency of TISA is ≈1 when pumped with a photon near 532 nm [Koechner99a].

The temperature dependence of the fluorescence lifetime is depicted in Fig. 4.4. The decrease in fluorescence lifetime is explained by nonradiative quenching of the excited state energy ^{2}E due to thermal activation of the upper Jahn-Teller component of the excited state $E_{1/2}$. As temperature increases, the rate of radiationless transitions increases also. Using a simple model, the total transition rate τ^{-1} of radiation and nonradiative transitions is expressed by [Albers86, Powell86]

$$\tau^{-1} = \tau_r^{-1} + \tau_{nr_0}^{-1}W_p \quad \text{[Albers86] or} \tag{39}$$

$$= \tau_r^{-1} + \beta\left[\exp(\Delta E/k_bT) - 1\right]^{-1} \quad \text{[Powell86]}, \tag{40}$$

where τ_r^{-1} is the radiative decay rate, and the second term describes the nonradiative quenching due to phonon absorption to a higher level for both model representations. In Eq. 39, $\tau_{nr_0}^{-1}$ is the nonradiative decay rate, and W_p is a function to describe the nonradiative transitions [Albers86]. In Eq. 40, β is the rate constant for the radiationless transition, ΔE is barrier for the quenching process, k_b is the Boltzmann constant, and T is the temperature [Powell86]. The spectroscopy, radiative and radiationless transitions of TISA are investigated in greater detail in [Grinberg93b, Grinberg93a, Grinberg94]

The reduced lifetime leads to a reduced quantum efficiency of about 80% at room temperature [Albers86] under cw excitation at 485 nm. [Grinberg94] describe a significant theoretical decrease in quantum efficiency for excitation below 460 nm. This is supported by PPE spec-
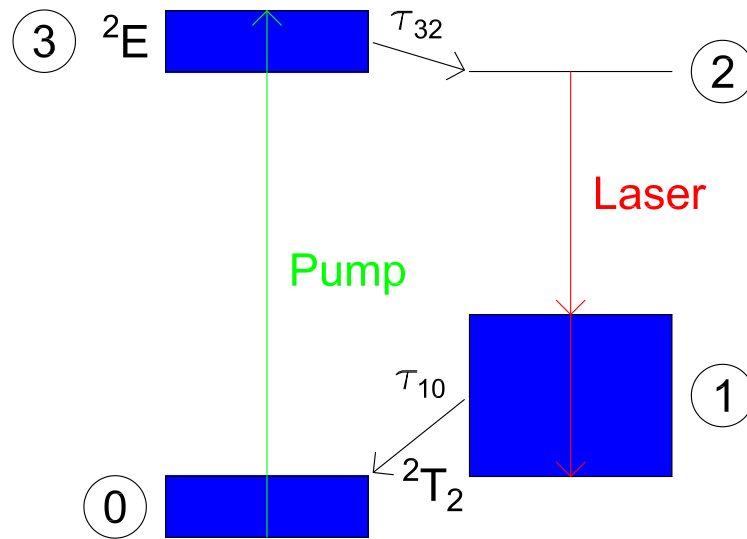
Figure 4.3: Simplified 4-level energy system of Ti^{3+}:Al$_2$O$_3$ [Saleh07].

Ti:Sapphire: temperature dependence of fluorescence lifetime
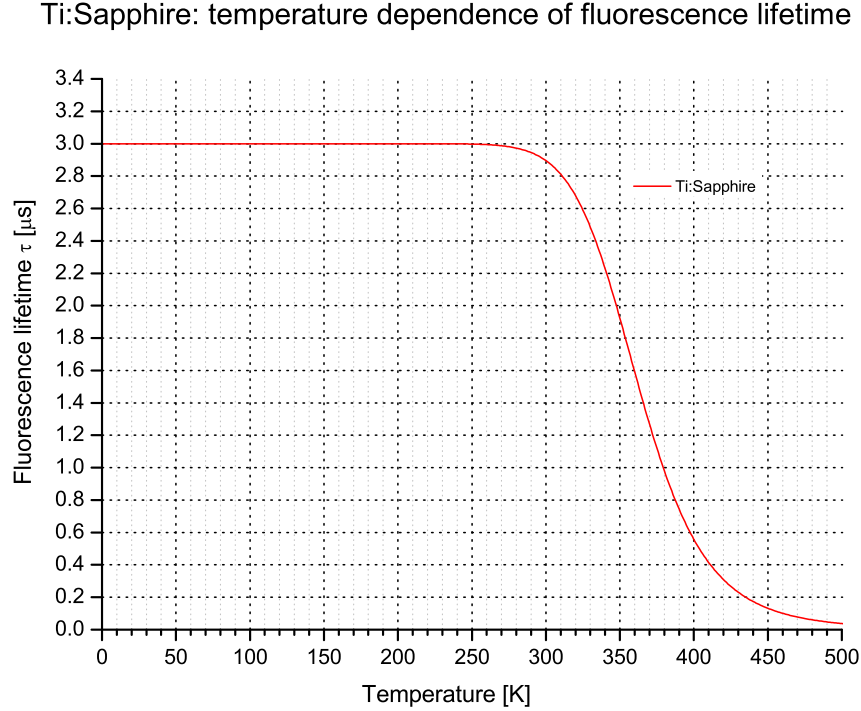
Figure 4.4: Temperature dependence of the fluorescence lifetime of Ti^{3+}:Al_2O_3 using fit of Eq. 40 [Powell86] (τ_r=3 μs, β=2.62·10^6 μs^{-1}, ΔE=4000 cm^{-1}, k_b=1.380505·10^{-23} J/K).

tra (PPE: photopyroelectric).

The reduced quantum efficiency is expected to increase the lasing threshold. Above threshold, the total fluorescence intensity can be considered as constant [Sanchez88], and laser operation with a quantum efficiency of 100% under pulsed excitation at 532 nm is expected. A performance limiting factor for laser operation can be excited state absorption (ESA). However, there is no indication for ESA concerning TISA [Eggleston88, Henderson00b]. ESA was observed in TISA for excitation below 350 nm [Huber09, Danger93], which is far away from the pumping wavelength at 532 nm. Therefore, no performance limitation due to ESA can expected.

TISA has an about 3 times higher thermal conductivity compared to Nd:YAG at room temperature [Koechner99a]. With decreasing temperature, the thermal conductivity increases (see Fig. 4.10 on page 33). Detailed thermal simulations of TISA crystals under different conditions are presented in the following subsection (Ch. 4.2).

The key TISA crystal properties are summarized in Tab. 4.1.

TISA lasers are attractive for LIDAR and DIAL applications due to their large tuning range (see above) and their spectral characteristics. They are used as injection-seeders (cw) [Wulfmeyer95, Wulfmeyer98a] or as transmitters itself (see references of Tab. 2 on

Table 4.1: Parameters of $Ti^{3+}:Al_2O_3$. Note: maximum values for the stimulated emission cross-section vary within the literature.

Parameter, Unit	Value	Comment
Fluorescence lifetime at 300 K, μs	3	temperature dependent
Quantum efficiency at 532 nm, %	≈ 100	4-level system
	≈ 80	[Albers86] (300 K, 485 nm)
Abs. cross section at 532 nm, cm^2	$(4.9 \pm 1.1) \cdot 10^{-20}$	fit, π-pol. [DeShazer88]
Sat. fluence (abs.) at 532 nm, J/cm^2	7.63	[DeShazer88]
Stim. em. cross section at 787 nm, cm^2	$3.8 \cdot 10^{-19}$	fit, π-pol. [Rapoport88]
Stim. em. cross section at 820 nm, cm^2	$2.85 \cdot 10^{-19}$	fit, π-pol. [Eggleston88]
Stim. em. cross section at 935 nm, cm^2	$1.39 \cdot 10^{-19}$	fit, π-pol. [Eggleston88]

page 7). However, for a high-average power TISA laser operating at repetition frequencies of 250 Hz to 1 kHz, and being pumped with a frequency-doubled Nd:YAG lasers with average powers 50-200 W, suitable laser designs have to be found to fulfill the requirements for a water-vapor DIAL operating in the 820-, or 935-nm wavelength regime (see Tab. 2.1).

For optimum operation of the TISA laser, four connected theoretical modules are developed within this work. The main models are a thermal module, a resonator design and optimization module, a performance module, and a spectral module. Each module provides input for the next module. The situation is depicted in Fig. 4.5 with the thermal module being the starting point in the TISA laser design cycle. Each of the modules is addressed in the following subsections.
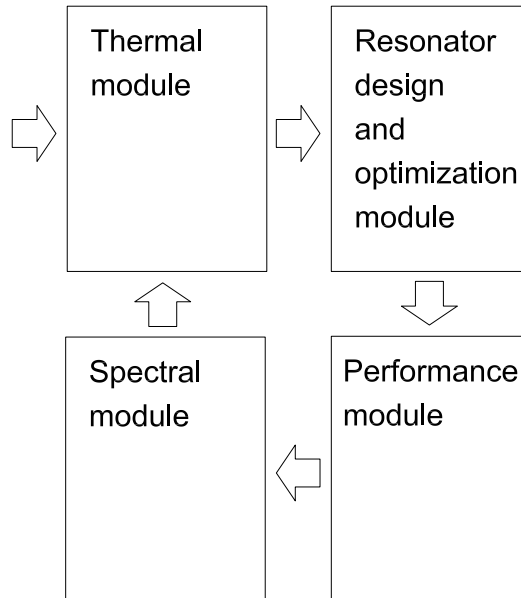
Figure 4.5: TISA laser modeling design cycle.

4.2 Thermal modeling

4.2.1 Introduction

Within the thermal module, the heat load of the TISA laser crystal is calculated by solving the heat equation using a finite element analysis (FEA) program[4]. The resulting 3-dimensional (3d) temperature and stress-strain fields for different crystal geometries, pump and boundary configurations are used to calculate the overall thermal lensing. The results are values for the focal length of the thermal lens in the sagittal and tangential plane of a Brewster-cut TISA crystal including aberrations from quadratic refraction index dependence.

The modeling procedure of a FEA program is mainly divided into five steps, which are shown in Fig. 4.6. The procedure starts with the set up of the geometry (subdomains) of the crystal and the cooler. In the next step, the physics of the model is set up. The material parameters, for instance, the thermal conductivity, the heat capacity, the mass density and the mechanical properties (Youngs modulus, Poisson ratio, thermal expansion coefficient) are assigned to the subdomains. In the corresponding thermal and structural mechanics module part, the boundary conditions between subdomains or the surrounding are choosen. In the following step, the meshing of the subdomains for the FEA solver is performed with unstructured or structured, mapped and extruded meshes. The different meshing cases are selected according to the modeling situations (see the modeling cases section in Ch. 4.2.5, page 35). The various types of meshes of the subdomains are connected using identity boundary conditions. Then the FEA solver is set up, where direct or indirect, iterative solvers or a combination of both are used to solve the heat equation. In the last modeling step, the calculated temperature field is used for postprocessing, for instance, for the visualization and the calculation of thermal lensing as well as of aberrations.

All FEA simulations presented within this work are executed using three dimensions (3d).

Set up of geometry/ subdomains (crystal, chiller)	⇨	Set up of subdomain and boundary conditions	⇨	Meshing of subdomains and connection of meshes	⇨	FEA solver set up and solving of model	⇨	Post-processing (thermal lens calc.)
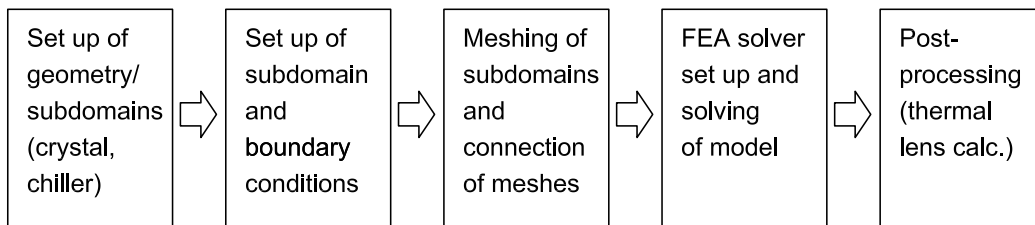
Figure 4.6: FEA thermal modeling procedure.

---

[4]COMSOL(TM) Multiphysics Version 3.2b, COMSOL AB.

4.2.2 Importance of thermal modeling

In solid-state lasers, the pump energy of flashlamps, diodes or pump lasers is absorbed by the solid-state laser material. Due to various quantum effects, a significant amount of pump energy is dumped as heat in the crystal, and does not contribute to laser emission. As a consequence, the dumped heat in the laser crystal forms a thermal lens. The beam propagation inside the laser resonator is altered and distorted.

Therefore, without the knowledge of the thermal load of the laser crystal and the amount of thermal lensing, high-power laser operation would not be possible or could lead to damage of optical parts of the resonator. The calculation and estimation of the thermal lens is the key problem in high-power laser resonator design [Koechner99c, Hodgson05c].

Previous modeling efforts did not include temperature dependent material properties, pump configurations and profiles. They did not consider the geometric situation of crystal and cooler and the boundary conditions between both and the surrounding. The work presented here closes this gap and gives new insights.

4.2.3 Heat equation and solution

The heat transfer by conduction can be described by the partial differential equation

$$\rho \, C_p \, \frac{\partial T}{\partial t} - \nabla(k\nabla T) \;\; = \;\; Q \,, \tag{41}$$

which is called the heat equation. ρ is the density, C_p the specific heat (heat capacity) at constant pressure, and k is the thermal conductivity of the material. Q is the heat source, which is described below, and $T(x, y, z, t)$ is the temperature field to be calculated. k can be expressed by a temperature dependent function turning Eq. 41 into a nonlinear partial differential equation. In case k is anisotropic, it is described by a conductivity tensor. C_p can also be expressed by a temperature dependent function. In steady-state modeling, the first term in Eq. 41 disappears.

4.2.4 Thermal model set up

The radiation of the frequency-doubled Nd:YAG pump laser is being absorbed by the TISA crystal depending on the pump configuration. The crystal itself is mounted in a Peltier-cooled aluminum cooler. The thermal contact between crystal and cooler is optimized by a gold layer (thickness: 5 μm). Fig. 4.7 shows the TISA crystal inside the cooler. The absorption process can be described by the law of Lambert-Beer. It is still valid at high pump energies as the saturation fluence E_{sat} of absorption of TISA (4-level energy system),
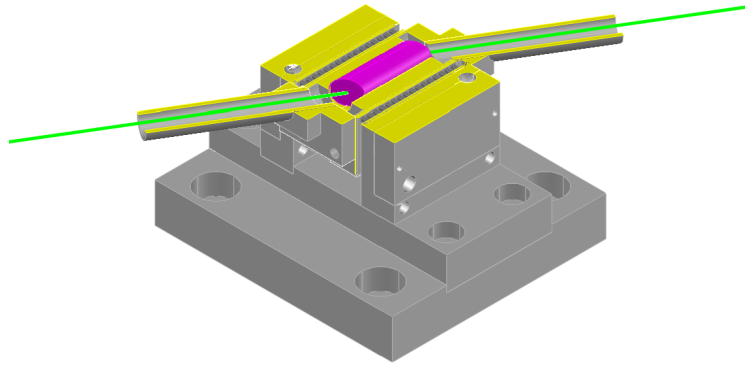
(a) Complete crystal cooler set up (half part).
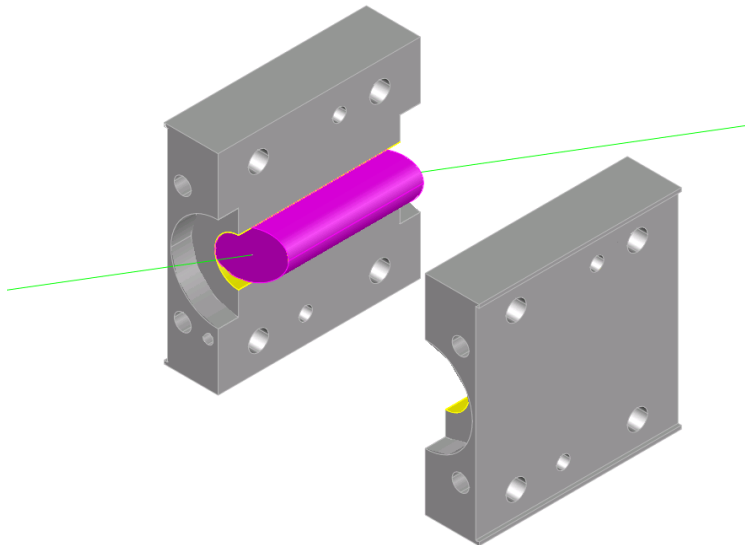
(b) Crystal cooler set up for FEA model. Gold layer: yellow.

Figure 4.7: Scheme of TISA crystal (magenta) mounted in the cooler (gray). Original cooler design by NCAR, Boulder CO, USA. Redesign at IPM, Stuttgart-Hohenheim, Germany.

which is given by

$$E_{sat} \quad = \quad \frac{h\,\nu_p}{\sigma_{abs}}\,, \tag{42}$$

is $\approx 6.9\,\mathrm{J/cm^2}$ at 532 nm and π-polarization ($\sigma_{abs}{=}5.4{\cdot}10^{-20}\,\mathrm{cm^2}$ at π-polarization and 532 nm pump wavelength [Moulton86]). In Eq. 42, h is Planck's constant, ν_p is the pump frequency, and σ_{abs} is the ground-state absorption cross-section. At a pump level of 100 mJ per pulse and a beam diameter of 1.5 mm for a pulse length of 20 ns, a peak fluence of $\approx 1.4\,\mathrm{J/cm^2}$ is reached, assuming a Gaussian pump-beam profile. Typical values of the damage threshold of TISA crystals are of the order of $1{-}10\,\mathrm{J/cm^2}$, depending mainly on pump laser beam profile quality [Canova05, Rines91]. Most likely, the TISA crystal is being damaged before reaching the saturation level of absorption. A detailed analysis of the absorption behavior of TISA is given in [DeShazer88], where a Frantz-Nodvik approach [Frantz63] is used to model the absorption characteristics.

The fraction of pump energy η_h, which is being dumped as heat inside the crystal can be expressed by

$$\eta_h \;=\; 1 - \eta_c = 1 - \frac{\nu_l}{\nu_p} = 1 - \frac{\lambda_p}{\lambda_l}\,, \tag{43}$$

where η_c is the color efficiency (Stokes efficiency), which is given by the ratio of lasing (ν_l) to pump (ν_p) frequency, or the corresponding ratio of the wavelengths (λ_p, λ_l), respectively. In Eq. 43, all transitions in the energy level system except the lasing transition are considered to contribute to heat generation. Furthermore, degeneracies of the energy levels are neglected, and no difference is being made between lasing and nonlasing conditions within this approach. Therefore, η_h represents a worst case factor. The difference between lasing and non-lasing conditions is not considered in the thermal simulation.

In the case of a plane-parallel, end-pumped crystal being pumped from both sides, a suitable expression for the spatially resolved heat source $Q(x,y,z)$ in cartesian coordinates reads[5]:

$$\begin{aligned} Q(x,y,z) \;=\; & \eta_h\,P_0\,p(x,y,z)\,\frac{\alpha}{1 - \exp(-\alpha\,L)} \\ & \left[\exp\left(-\alpha\left(z+\frac{L}{2}\right)\right) + \exp\left(\alpha\left(z-\frac{L}{2}\right)\right)\right]. \end{aligned} \tag{44}$$

In Eq. 44, P_0 is the average single-side pump power in an end-pumped geometry, $p(x,y,z)$ is the normalized pump-beam profile, α is the small-signal absorption coefficient of the TISA crystal at the pump wavelength, and L is the TISA crystal length (z-direction) with the coordinate origin being at the crystal center. In the case of a Gaussian pump profile, and a plane-parallel crystal, $p(x,y,z)$ reads

$$p_G(x,y,z) \;=\; \frac{2}{\pi\,\omega_p^2}\,\exp\left(-\frac{2\,x^2}{\omega_p^2}\right)\exp\left(-\frac{2\,y^2}{\omega_p^2}\right)\,, \tag{45}$$

---

[5]Equation 44 is derived from Eq. 3 in [Weber98] for single-side pumping.

with ω_p being the $1/e^2$-(pump-)beam radius. The factor $2/\pi\,\omega_p^2$ is a result of the normalization condition

$$\iiint p_G(x,y,z)\,dx\,dy\,dz \;=\; 1\,. \tag{46}$$

Accordingly, for a super-Gaussian pump-beam profile p_{SG}, the normalized profile reads

$$
\begin{aligned}
p_{SG}(x,y,z) \;=\;& \frac{2^{-2+\frac{1}{2m}+\frac{1}{2n}}}{\omega_x\,\omega_y\,\Gamma\left(1+\frac{1}{2m}\right)\Gamma\left(1+\frac{1}{2n}\right)} \\
& \exp\left(-2\left(\frac{x^2}{\omega_x^2}\right)^n\right)\exp\left(-2\left(\frac{y^2}{\omega_y^2}\right)^m\right),
\end{aligned}
\tag{47}
$$

where ω_x, ω_y are the $1/e^2$-beam radii in x- and y-direction, and the n,m are the super-Gaussian exponents in x- and y-direction, respectively. Γ is the Euler gamma function[6].

Note that in Eqs. 45 and 47, a z-dependence of the pump profile is neglected, as the propagation of the pump beam through the crystal is assumed to be constant.

For a Brewster-cut crystal, $Q(x,y,z)$ has to be modified to account for the Brewster angle θ_B (θ_{B*}, see Fig.4.8b, 4.8c). This is accomplished by shearing the function $Q(x,y,z)$ using the shearing matrix M_S

$$
M_S \;=\;
\begin{pmatrix}
1 & 0 & 0 \\
0 & 1 & 0 \\
0 & -\tan(\theta) & 1
\end{pmatrix},
\tag{48}
$$

which represents a shearing in the x,z-plane along the z-axis, where

$$\theta \;=\; 90° - \arctan(n) = 90° - \theta_B = \theta_{B*}\,. \tag{49}$$

θ is the shearing angle, and n the refractive index of TISA ($n\approx1.76$)[7]. Additionally, the beam diameter in y-direction is enlarged by a factor of n, resulting in an elliptic beam shape when propagating through the crystal. The overall geometric situation of an end-pumped Brewster-cut TISA is depicted in Fig. 4.8a, where ω_p is the pump-beam radius, and $\omega_x{=}\omega_p$, $\omega_y{=}n\,\omega_p$ are the beam radii inside the crystal in x-, and y-direction, respectively. The sheared, modified and normalized $Q(x,y,z)$ therefore reads in the case of a Brewster-cut

---

[6]The Euler gamma function $\Gamma(x)$ is given by: $\Gamma(x) := \int_0^{+\infty} \exp(-t)\,t^{x-1}\,dt\ \ (x>0)$.
[7]Note: $90° - \theta_B \approx \theta_{B*}$ due to dispersion, see Figs. 4.8b, 4.8c.
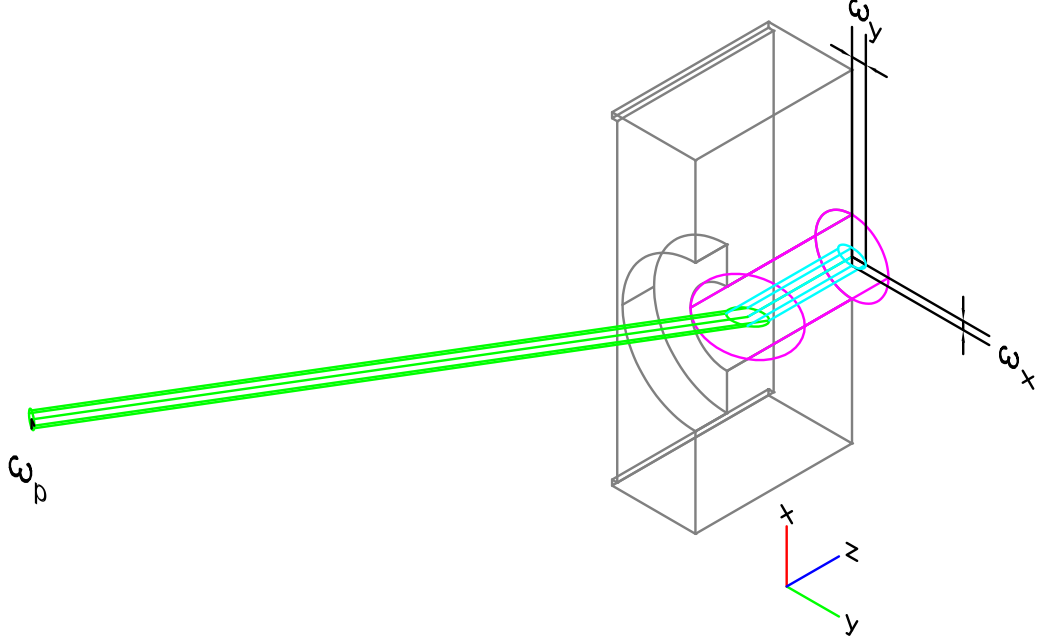
(a) Overall TISA pumping situation scheme. Shown is pumped TISA crystal (half part) with cooler (quarter part).
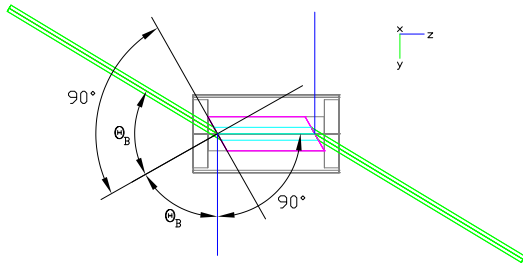
(b) Propagation of pump laser: Brewster angle air-TISA crystal at 532 nm: θ_B=60.56°
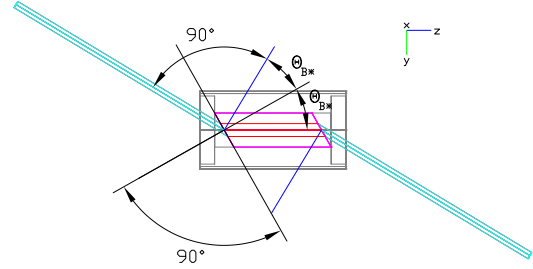
(c) Propagation of TISA laser: Brewster angle TISA crystal-air at 820 nm: θ_{B*}=29.61°

Figure 4.8: TISA crystal: detailed geometric situation of TISA crystal pumping and TISA laser. Color-code: green: pump laser; red: TISA laser; magenta: TISA crystal; blue: reflected (both pump and TISA laser); cyan: refracted (both pump and TISA laser); grey: aluminum cooler. Minimum reflection at Brewster angle for π-polarization. Additional beam separation by dispersion is not shown.

crystal pumped with a Gaussian beam profile

$$Q_{G,\theta}(x,y,z) \;=\; \eta_h\, P_0\, p_{G,\theta_B}(x,y,z)\, \frac{\alpha}{1-\exp(-\alpha\, L)} \tag{50}$$

$$\left[\exp\left(-\alpha\left(z+y\left(-\tan(\theta)\right)+\frac{L}{2}\right)\right)+\exp\left(\alpha\left(z+y\left(-\tan(\theta)\right)-\frac{L}{2}\right)\right)\right],$$

with $p_{G,\theta}(x,y,z)$ given by

$$p_{G,\theta}(x,y,z) \;=\; \frac{2}{\pi\, n\, \omega_x\, \omega_y}\, \exp\left(-\frac{2\,x^2}{\omega_x^2}\right)\exp\left(-\frac{2\,y^2}{(n\,\omega_y)^2}\right). \tag{51}$$

A plot of the heat source for a Brewster-cut crystal being pumped by 25 W from each side is shown in Fig. 4.9, where the power density is color-coded in units of W/m^3. A peak power density of 273 MW/m^3 is reached at the crystal surface center. To account for a time-dependent pump power, $Q(x, y, z)$ can be extended with a normalized function $p(t)$, describing the time-dependence of the pump power and extending the heat function to $Q(x, y, z, t)$. However, at repetition frequencies of 250-400 Hz of the pump laser, the inverse thermal relaxation time τ_{therm}^{-1}

$$\tau_{therm}^{-1} \quad = \quad \frac{4\,k}{C_p\,\rho\,r_0^2} \tag{52}$$

of a TISA rod (r_o: rod radius) is much smaller than the repetition frequency, so that a steady-state temperature profile inside the TISA crystal can be assumed. This is a common and valid approximation [Eichler93].

The thermal conductivity k, and specific heat C_p of the materials used in the thermal model are presented in Fig. 4.10 and Fig. 4.11, respectively. Both physical properties are strongly dependent on the temperature. The recommended values for the thermal conductivity of Sapphire are used inside the model, instead of different values for c-, and a-axis, as the data
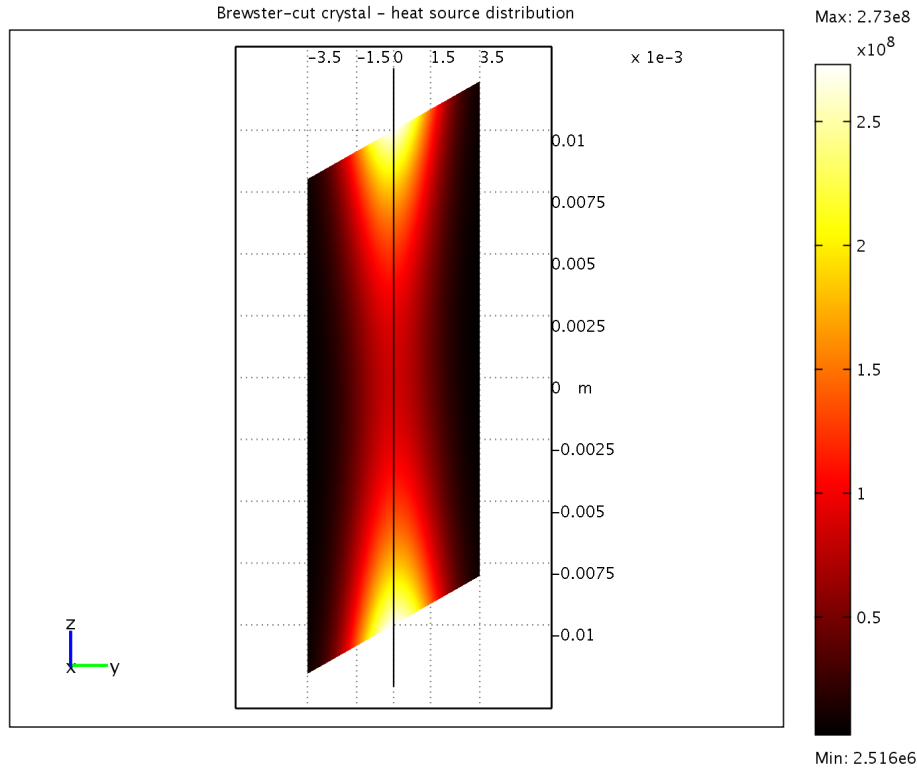
Figure 4.9: Heat-source plot (power density) of Brewster-cut crystal. Pump power: 25 W each side. $1/e^2$-pump-beam radius: 1.5 mm.
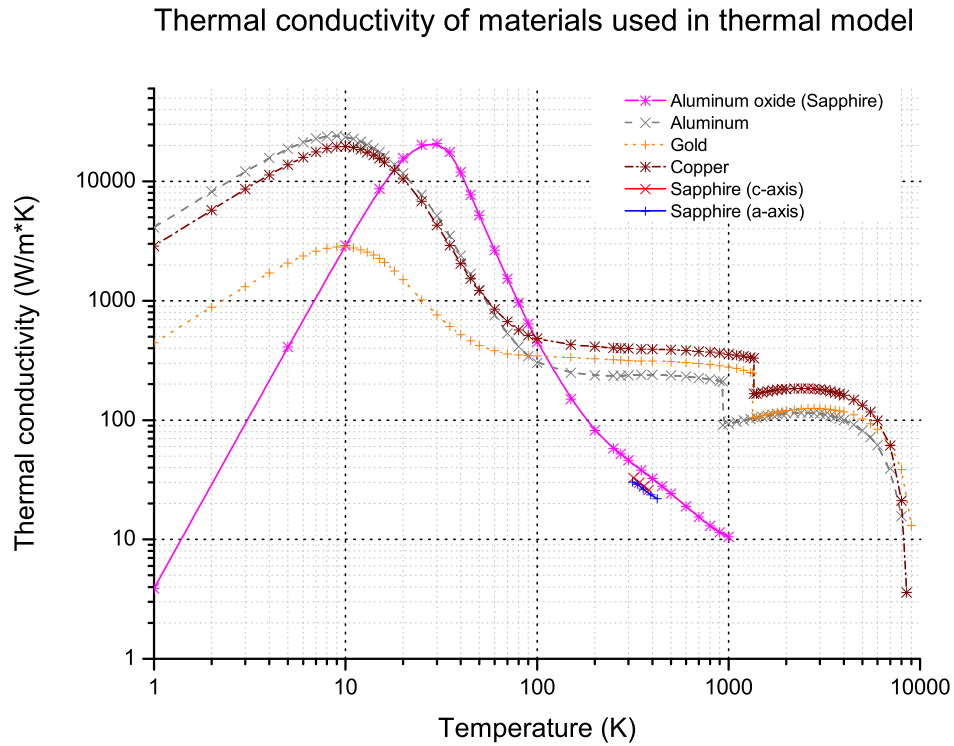
Figure 4.10: Thermal conductivity of materials used in thermal model [Touloukian70, Touloukian72c]. Discontinuity indicating phase change.
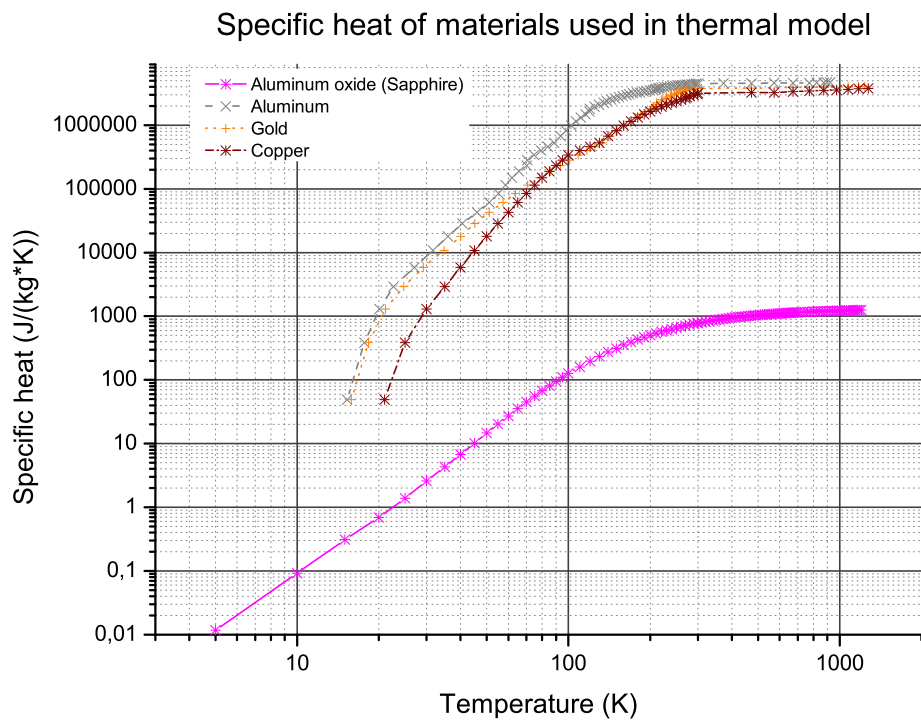
Figure 4.11: Specific heat of materials used in thermal model [Touloukian72a, Touloukian72b].

was only available for a small temperature range. The $C_p(T)$- and $k(T)$-values of gold were not used inside the (3d-) modeling. It is assumed that the thin gold layer between crystal and cooler does not change or limit the overall heat transfer between crystal and aluminum cooler significantly, and therefore the gold layer is neglected. Initially, the meshing of thin layers inside the model program frequently caused difficulties due to the large differences in scale of the subdomains and the geometric situation. This is being resolved in a newer version of COMSOL Multiphysics by adding a function for the modeling of thin layers (modeling of thermal contact resistance). However, we expect that this refinement has negligible effects on the modeling results, as the gold layer is very thin (5 μm). See Appendix C for modeling of a multiphysics model including structural mechanics effects.

Besides the expression for the heat source term $Q(x, y, z, t)$ and the material parameters of the corresponding subdomains, the boundary conditions with corresponding heat transfer coefficients (HTC) are important for the solution of the nonlinear partial differential equation (Eq. 41). The boundary conditions for the given modeling situation can be separated as follows: crystal - aluminum cooler, crystal - air, aluminum cooler - Peltier element for the cooler simulation. A suitable expression for the boundary condition is of the form[8]

$$\vec{n} \cdot (k\nabla T) \quad = \quad q_0 + h(T_{inf} - T) + C_{const}(T_{amb}^4 - T^4) \qquad \text{(heat flux)} \qquad (53)$$

to describe general, convection, and radiation heat flux. In Eq. 53, $\vec{n}$ is the normal vector, q_0 is the heat flux to the subdomain inward normal. The next two terms describe general or convection and radiation boundary types. h is the (convective) heat transfer coefficient, T_{inf} is the ambient bulk temperature, C_{const} is the radiation constant, T_{amb} is the temperature of the surrounding environment. The contribution of the radiation term has been left out in the modeling part, as the contribution is negligible. Special boundary conditions are given by

$$\vec{n} \cdot (k\nabla T) \quad = \quad 0 \qquad \qquad \text{(insulation)} \qquad (54)$$

$$T \quad = \quad T_0 \qquad \qquad \text{(prescribed temperature)} \qquad (55)$$

$$T \quad = \quad 0 \qquad \qquad \text{(zero temperature)} \qquad (56)$$

$$\vec{n} \cdot (k_1\nabla T_1 - k_2\nabla T_2) \quad = \quad \frac{k}{d}(T_1 - T_2) \qquad \text{(thin resistive layer)} . \qquad (57)$$

In Eq. 57, k and d are the thermal conductivity and the thickness of the layer, respectively. Table 4.2 lists (effective) heat transfer coefficients (HTC) for various boundary conditions together with measured effective heat transfer coefficients for the thermal contact between an Yb:YAG crystal and the cooler using various contact materials [Chénais04c]. The variation

---

[8]See [COMSOL06a] for reference and information regarding boundary conditions used in COMSOL Multiphysics.

Table 4.2: Heat transfer coefficients (HTC) for thermal model and other typical values.

Boundary	HTC, W/m²·K	typ. Range, W/m²·K
Crystal-Peltier element	15000	
Crystal-indium foil-copper heat sink	15000	[Weber98]
Crystal-water cooling	50000	
Crystal-air	10	2-25
Aluminum-air	10	2-25
Crystal-aluminum	1500	
Yb:YAG-cooler	2500	[Chénais04c]
Graphite layer	2900	[Chénais04c]
Indium foil	9000	[Chénais04c]
Heat sink grease	20000	[Chénais04c]
Silicon chip-aluminum cooler	200	

is quite large due to different experimental and geometric situations. Additionally, the surface roughness plays an important role for the thermal resistance. Further values for HTCs and the calculation of overall heat transfer coefficients are found in the specialized literature [Incropera02]. These combine the heat transfer through several surfaces of various thickness to a single HTC coefficient.

4.2.5 Thermal modeling results

In the following, different cases $\boxed{Ti}$ are shown for the FEA thermal modeling of a TISA crystal:

$\boxed{\textbf{T1}}$ Plane-parallel (PP) TISA crystal: pumped with single-side pump power of 25 W (page 37)

$\boxed{\textbf{T2}}$ PP TISA crystal: different boundary conditions using finite and infinite heat transfer coefficient (page 42)

$\boxed{\textbf{T3}}$ PP TISA crystal: temperature dependent and constant thermal conductivity k of Sapphire (page 44)

$\boxed{\textbf{T4}}$ PP TISA crystal: variable absorption coefficient of TISA (page 46)

$\boxed{\textbf{T5}}$ PP TISA crystal: variable pump-beam profile using Gaussian to super-Gaussian pump-beam profile (page 48)

$\boxed{\textbf{T6}}$ PP TISA crystal: Gaussian pump-beam profile with variable pump-beam radius (page 50)

$\boxed{\textbf{T7}}$ PP TISA crystal: time-dependent analysis - ramped pump power from 0-25 W (page 52)

T8 Brewster-cut (BR) TISA crystal: pumped with single-side pump power of 25 W (page 53)

T9 BR TISA crystal: unevenly pumped (page 55)

T10 BR TISA crystal: single-side pumped (page 58)

T11 Brewster-cut TISA crystal with undoped end-caps (BRUEC): pumped with single-side pump power of 25 W (page 60)

T12 BR TISA crystal with cooler (BRC): pumped with single-side pump power of 25 W (page 65)

T13 BRC TISA crystal: simulated Peltier-element failure at cooler (page 70)

T14 PP TISA crystal: incorporation of measured pump-beam profile (page 73)

T15 BR TISA crystal: crystal cooling with liquid nitrogen (page 79).

For each model case, a separate multiphysics model covering thermal effects[9] is set up in the COMSOL Multiphysics environment. For reference, the computer and software revisions used for the calculations are shown in Tab. 4.3. Description of the models and the parameters are listed in the corresponding tables. If not other values are given inside the simulations, the boundary conditions found in Tab. 4.4 are used. In each model, the coordinate origin is at the crystal center. The absorption of the pump laser is given along the z-axis, which is also the optical resonator axis. The TISA crystal is oriented in the y-z-plane (tangential plane, paper plane) with its c-axis normal to the z-axis (crystal coordinate system). A small-signal absorption coefficient for TISA crystals of α=1.84 cm^{-1} is used throughout simulations **T1**–**T15**, except **T4**. This value corresponds to an absorption of pump radiation of about 97.5% at a crystal length of 2 cm. Concerning the fraction of pump energy dumped as heat η_h, a value of η_h=0.351 is used in simulation **T1**–**T15**[10].

---

[9]A multiphysics model covering also structural effects is presented in Appendix C.

[10]A value of η_h=0.351 is used for a TISA laser operating at λ_l with 820 nm, and a value of η_h=0.431 is used for a laser operating at 935 nm (see Eq. 43 with λ_p=532 nm).

Table 4.3: FEA computer hardware and software specifications.

Hardware and Operating System	
Sun Java Workstation W2100Z	2x AMD Opteron 252 Processor
	8 GB RAM (ECC)
	NVIDIA Quadro FX3000
	Operating System: Fedora 7 (X86-64)
Custom-built	Intel Core 2 Quad Q6600 Processor
	8 GB RAM (non-ECC)
	NVIDIA GeForce 8800GTS
	Operating System: OpenSuSE 10.1 (X86-64)
	Linux Kernel 2.6.23.12
	Intel processor microcode data file version: 20080131
FEA Software	
FEMLAB 3.1i	Version: 3.1.0.163
	Comment: none
COMSOL 3.2b	Version: 3.2.0.304
	Available modules:
	- Structural mechanics module
	- Electromagnetics module
	- Script module
	Comment: Version used for modeling
COMSOL 3.3	Version:
	Available modules:
	- Structural mechanics
	- Electromagnetics module
	- Script module
	Comment: Version for testing only available
The use of the optimized mathematical libaries provided by the processor manufacturers is explicitly enabled to obtain the best calculation performance (Intel: MKL (Math Kernel Library), AMD: ACML (AMD Core Math Library)).	

Table 4.4: Boundary conditions for thermal models.

Boundary condition (see. Eq. 53)	h, W/m²·K	T_{inf}, K	Comment
Crystal-cooler boundary	15000	288.15	model with crystal domain only
Crystal-air	10	298.15	crystal end-face
Aluminum cooler-air	10	298.15	
Crystal-aluminum cooler	1500	-	used for testing purpose
Crystal-aluminum cooler	-	-	continuous boundary condition
Aluminum cooler-Peltier element	15000	288.15	

Plane-parallel crystal   T1

A plane-parallel TISA crystal (length: 20 mm, diameter: 7 mm) is longitudinally pumped (end-pumped) from both sides with a single-side average pump-power of 25 W and a Gaussian

pump-beam profile with a $1/e^2$-pump-beam radius of 1.5 mm. Additional model parameters and boundary conditions are given in Tab. 4.4. The end-faces of the TISA crystal are in contact with air (T_{inf}=298.15 K, h=10 W/m^2·K), and the remaining boundaries are in contact with the cooler (T_{inf}=288.15 K, h=15000 W/m^2·K). The resulting calculated temperature profile is shown in Fig. 4.12 and in Fig. 4.13 (isosurface plot). Color-coded is the temperature given in Kelvin (K).

The calculated temperature profiles along z-direction (optical axis) for different single-side pump power levels (1, 5, 10, 15, 20, and 25 W) are shown in Fig. 4.14. The calculated temperature profiles at the crystal surface ($z=\pm 0.01$ m, crystal length: 0.02 m) and at the crystal center (z=0 m) along the radius of the crystal (x-, y-directions) for the same power levels are shown in Fig. 4.15 and Fig. 4.16, respectively.

The sequence of plots showing the calculated temperature along the optical axis (z-direction) and along x-, y-directions at crystal center and surface will appear several times within the presentation of the modeling results. From now on, it will not explicitly be referred to it in the context any more and only the number of the figures will be given. Lateral dimensions are given in meters (m), and slice-, iso-surface plots are showing the color-coded temperature in Kelvin (K).

At power levels 1-5 W, the temperature changes less than 1 K along z-direction. At higher pump power levels, the temperature drops significantly and a strong temperature minimum builds up at the center of the crystal.

As expected, the maximum temperature is reached at the center of the crystal surface. But in contrast to a transversally pumped rod, the temperature profile can not be approximated by a single parabolic temperature profile along the complete crystal rod length (z-direction). The temperature profile shows a tightening-effect towards the center of the crystal. The absorption-process is following Lambert-Beers' law and the cooling of the crystal is constant along the crystal boundary surface in contact with the cooler. In consequence, an analysis based on a slice approach is necessary to calculate the beam propagation through the crystal. Using Gaussian (ABCD-matrix) beam propagation, a parabolic approximation of the temperature profile has to be executed for each slice individually along z-direction.

Figures 4.15 and 4.16 show overall higher maximum temperatures at the crystal surface and a parabolic temperature decrease within about the radius equal to the pump-beam radius. Outside this region, the temperature shows a nearly linear decrease towards the cooler boundary. This is discussed in more detail in Ch. 4.2.6.
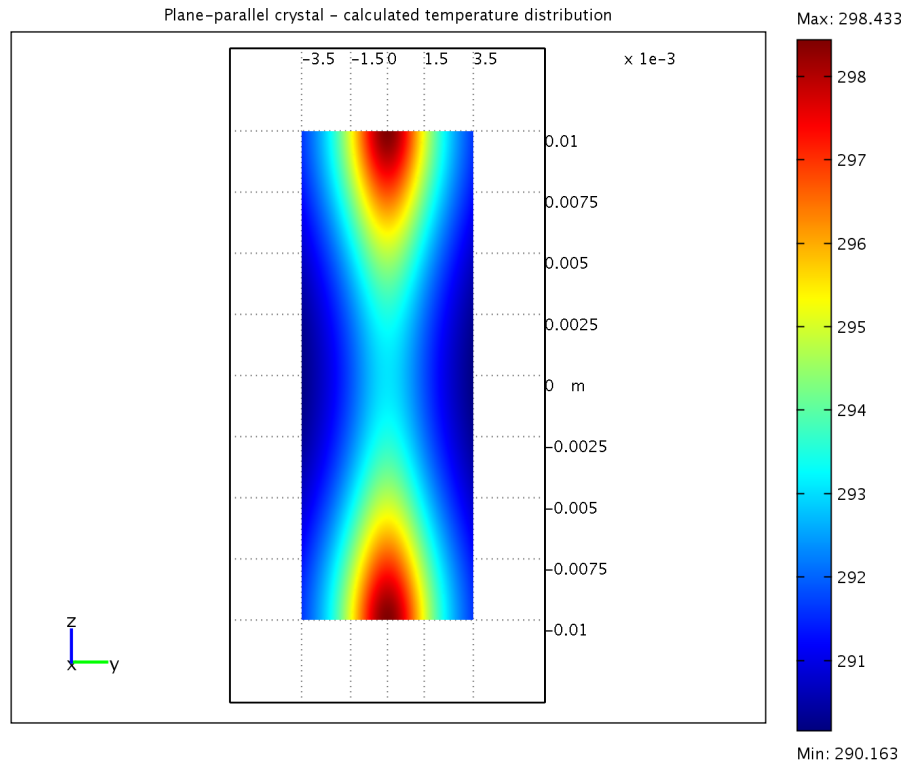
Figure 4.12: Thermal simulation of plane-parallel (PP) TISA crystal - single-side pump power: 25 W. Color-coded is the temperature given in Kelvin (K).
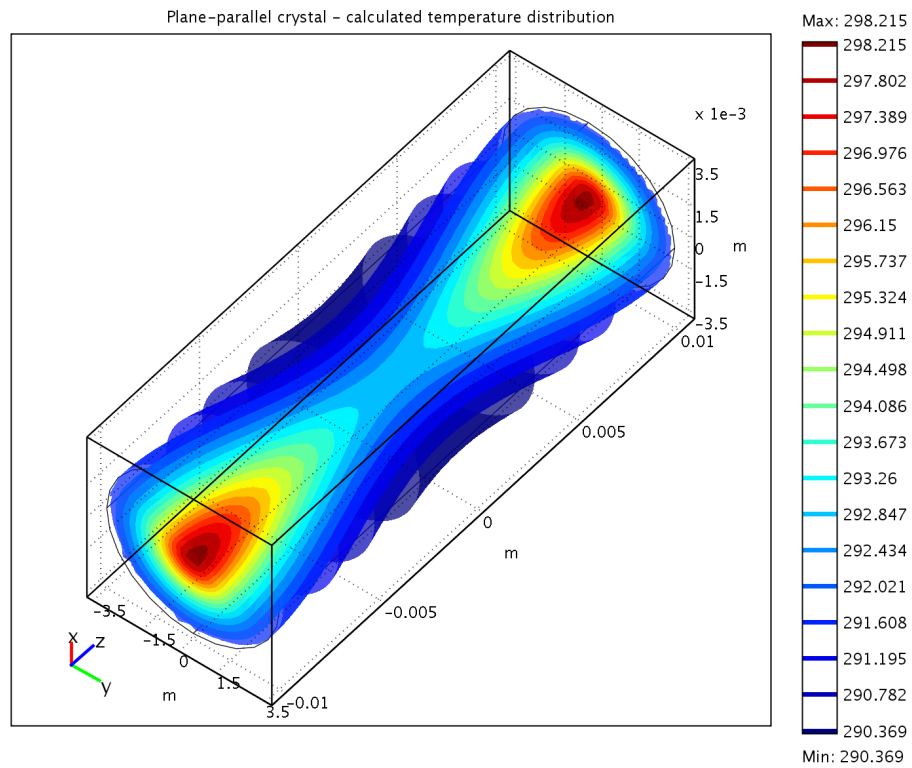
Figure 4.13: Plane parallel TISA crystal: isosurface plot of calculated temperature distribution. Single-side pump power: 25 W.
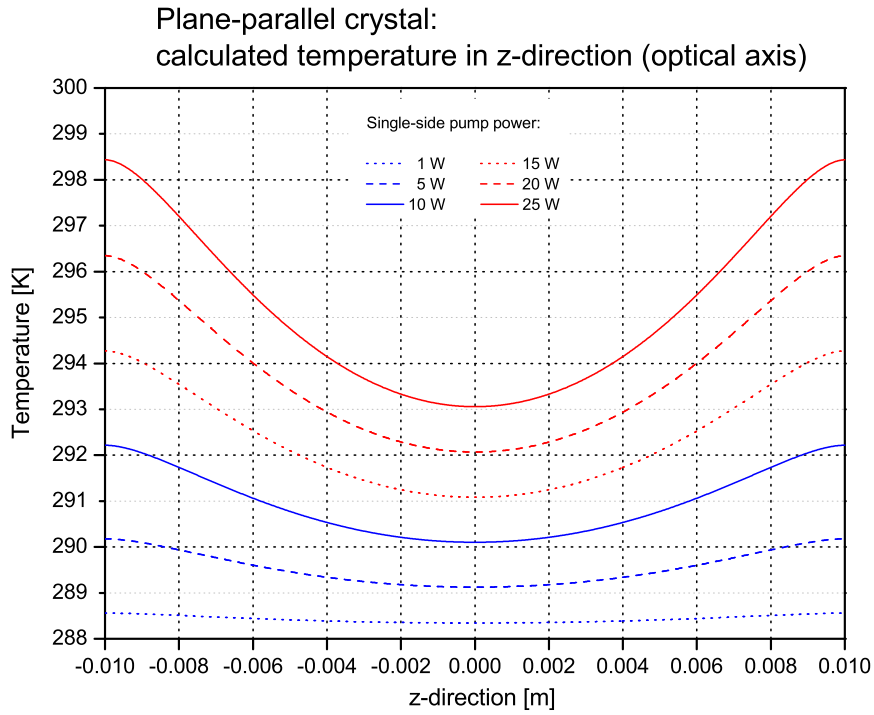
Figure 4.14: Plane-parallel TISA crystal: temperature along z-axis for various single-side pump levels.
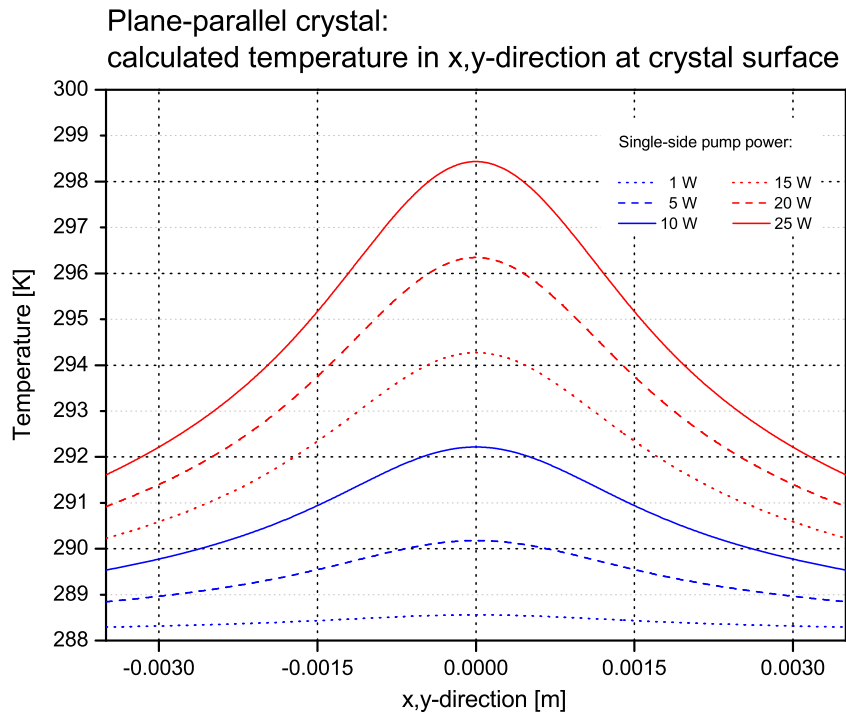
Figure 4.15: Plane-parallel TISA crystal: temperature along x-, y-axis at crystal surface for various single-side pump levels.
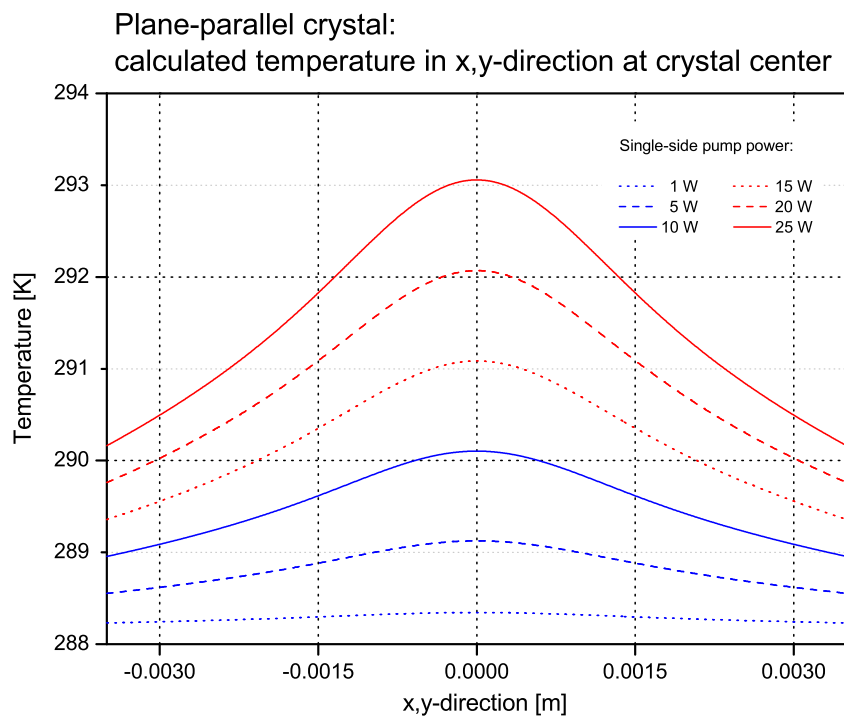
Figure 4.16: Plane-parallel TISA crystal: temperature along x-, y-axis at crystal center for various single-side pump levels.

T2 **Plane-parallel crystal - different boundary conditions**

Within this simulation, the influence of the boundary conditions is studied. The boundary conditions are critical for the solution of every differential equation. Of special interest is the boundary of the crystal in contact with the cooler and the associated heat transfer. Therefore, two simulations are carried out. One has a constant boundary condition with a given heat transfer coefficient of h=15000 W/m^2·K and a surface temperature of T_{inf}=288.15 K (HTC boundary condition). In the other simulation, the heat transfer coefficient is set to infinite and only a surface temperature of T_{inf}=288.15 K is set (constant boundary condition with prescribed temperature, Eq. 55). Figures 4.17-4.19 show the calculated temperature profiles. The difference between both is about less than 2 K within the $1/e^2$-pump-beam radius and less than 4 K at the crystal boundary.

Although the HTCs are difficult to determine, it is not recommended to run simulations with infinite HTCs which corresponds to a constant boundary temperature. First, infinite HTCs are unrealistic, as the thermal contact is always not perfect due to the surface roughness (thermal resistance). Second, a performance limitation of a cooling mechanism or device can not be determined if infinite HTCs are used.
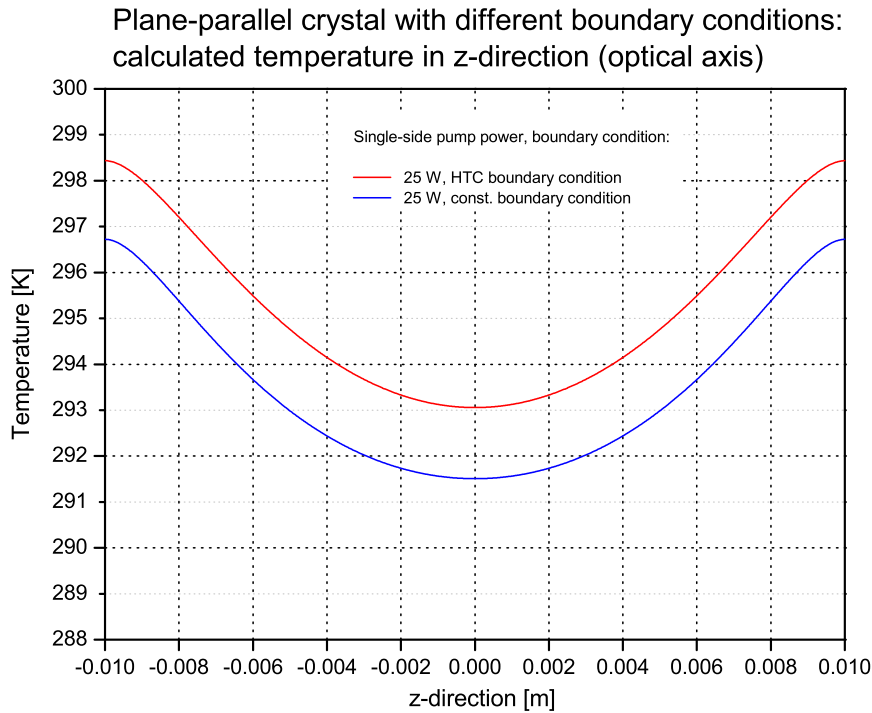
Figure 4.17: Plane-parallel TISA crystal - different boundary conditions temperature along *z*-axis.
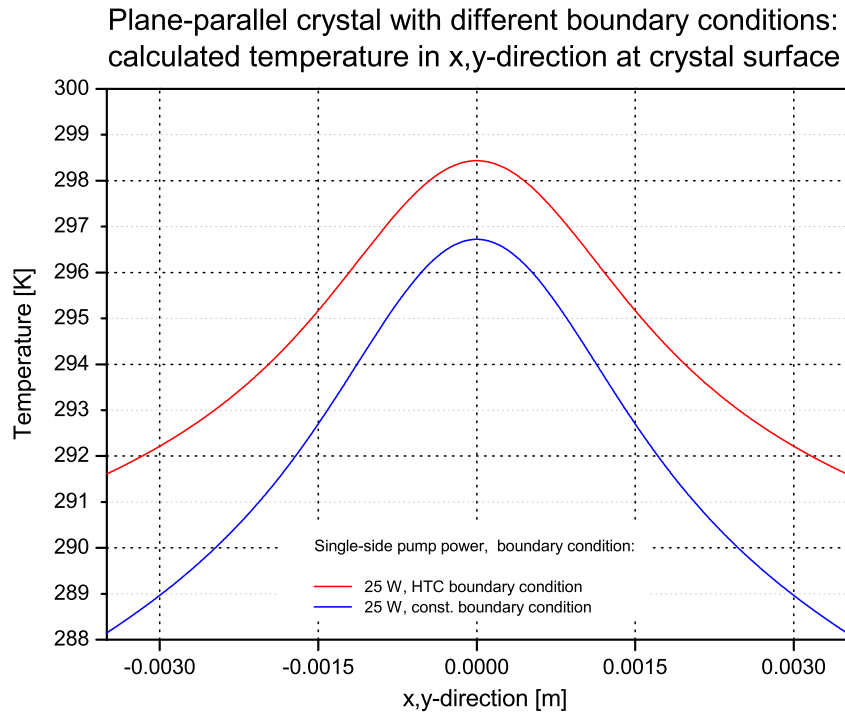
Figure 4.18: Plane-parallel TISA crystal: different boundary conditions - temperature along x-, y-axis at crystal surface for various single-side pump levels.
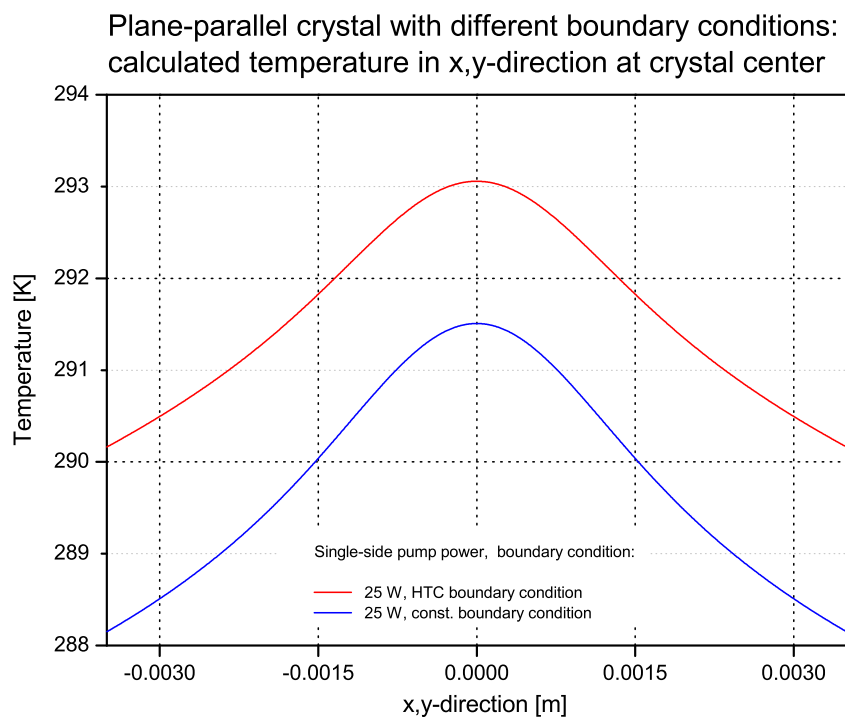
Figure 4.19: Plane-parallel TISA crystal: different boundary conditions - temperature along x-, y-axis at crystal center for various single-side pump levels.

T3 Plane-parallel crystal - temperature dependent and constant thermal conductivity of Sapphire

As the thermal conductivity of Sapphire shows a strong temperature dependence, a simulation is run with a constant thermal conductivity of Sapphire (k of Sapphire at 273.15 K), and another simulation is run with a temperature dependent thermal conductivity of Sapphire. The single-side pump power is set to 25 W with a $1/e^2$-beam radius of 1.5 mm (Gaussian pump-beam profile).

As can be seen, the temperature difference between both simulations is less than 1 K. The difference is larger at the crystal surface compared to the crystal center, indicating the decrease of the thermal conductivity of Sapphire with increasing temperature (see Fig. 4.10). As k of Sapphire was taken at 273.15 K, which is lower than the overall temperatures in the simulation with $k(T)$, the curve with constant k shows overall lower calculated temperatures, and both temperature curves intercept at a point close to the crystal boundary (Figs. 4.21-4.22).
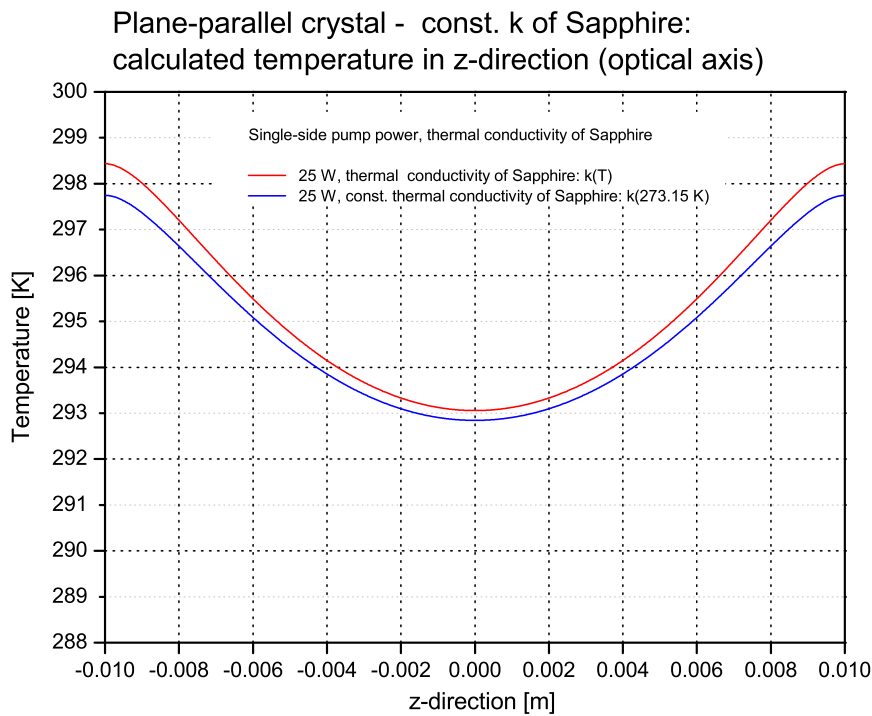
Figure 4.20: Plane-parallel TISA crystal: temperature dependent and constant thermal conductivity k of Sapphire - temperature along z-axis.
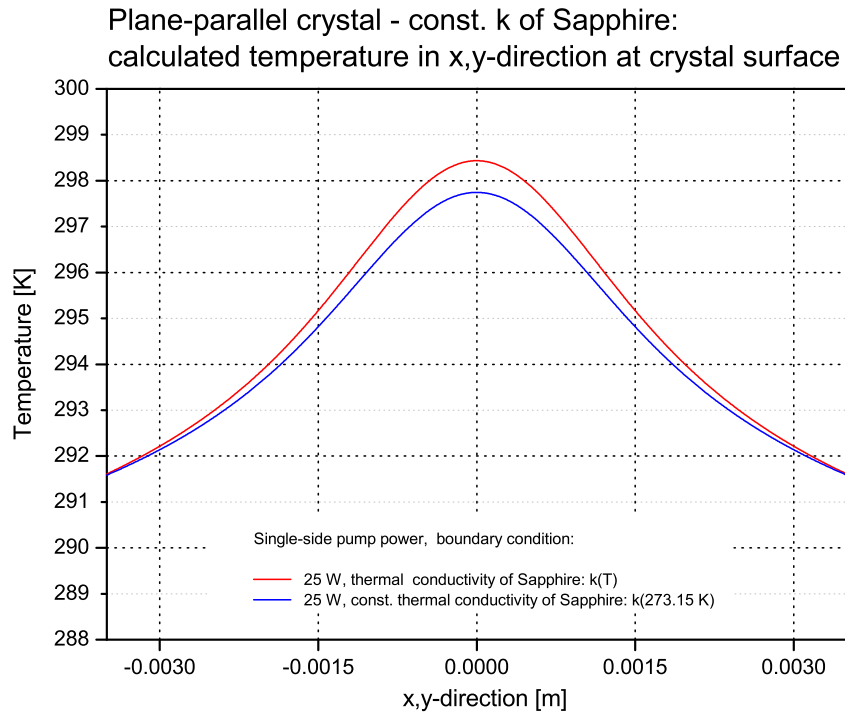
Figure 4.21: Plane-parallel TISA crystal: temperature dependent and constant thermal conductivity k of Sapphire - temperature along x-, y-axis at crystal surface.
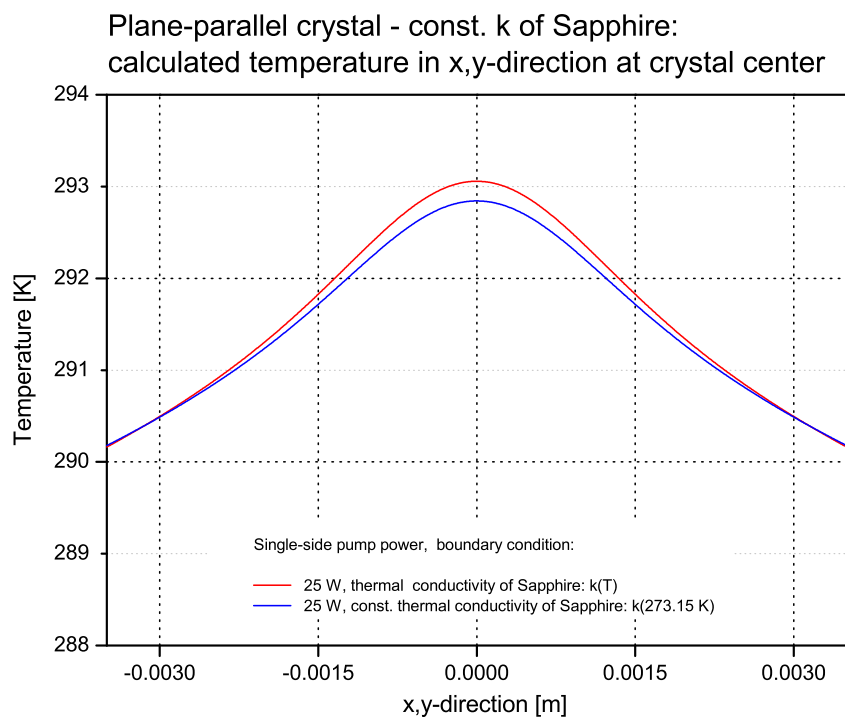
Figure 4.22: Plane-parallel TISA crystal: temperature dependent and constant thermal conductivity k of Sapphire - temperature along x-, y-axis at crystal center.

$\boxed{\textbf{T4}}$ **Plane-parallel crystal - variable absorption coefficient**

The absorption coefficient α of TISA is dependent on the overall doping concentration of Ti^{3+}-ions. For instance, if the absorption coefficient is measured and the absorption cross section of TISA σ_{abs} at the wavelength is known, then the total number density n_0 of Ti^{3+}-ions can be calculated with

$$n_0 \;\; = \;\; \frac{\alpha}{\sigma_{abs}} \, . \tag{58}$$

Typical values of the small-signal absorption coefficient α are in the range of 0.5-4.5 cm^{-1} and correspond to a doping level of ≈ 0.03-0.25% (wt.%) Titanium. For the simulation, the overall crystal length is kept constant at 2 cm. For a typical laser design, the absorption of the complete pump radiation is interesting. Therefore, the doping concentration is adjusted according to the crystal length and vice versa. In the absence of saturation of pump radiation absorption (nonlinear effect), the absorption process can be described by the law of Lambert-Beer. The simulations at different absorption coefficients of TISA show, that higher absorption coefficients lead to higher crystal surface temperatures (see Figs. 4.23, 4.24). Lower absorption coefficients result in lower overall temperatures and lower gradients at the expense of reduced absorption of pump radiation. For α=1.0 cm^{-1}, only about 86.5% of the pump power is absorbed compared to 98.2% at α=2.0 cm^{-1}.
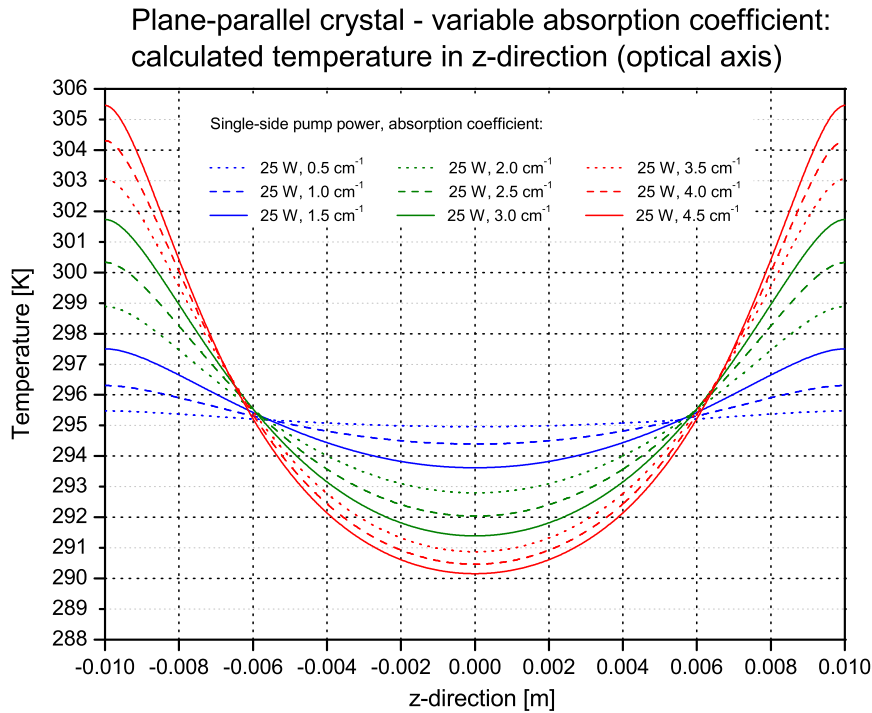
Figure 4.23: Plane-parallel TISA crystal: variable absorption coefficient of TISA - temperature along z-axis.
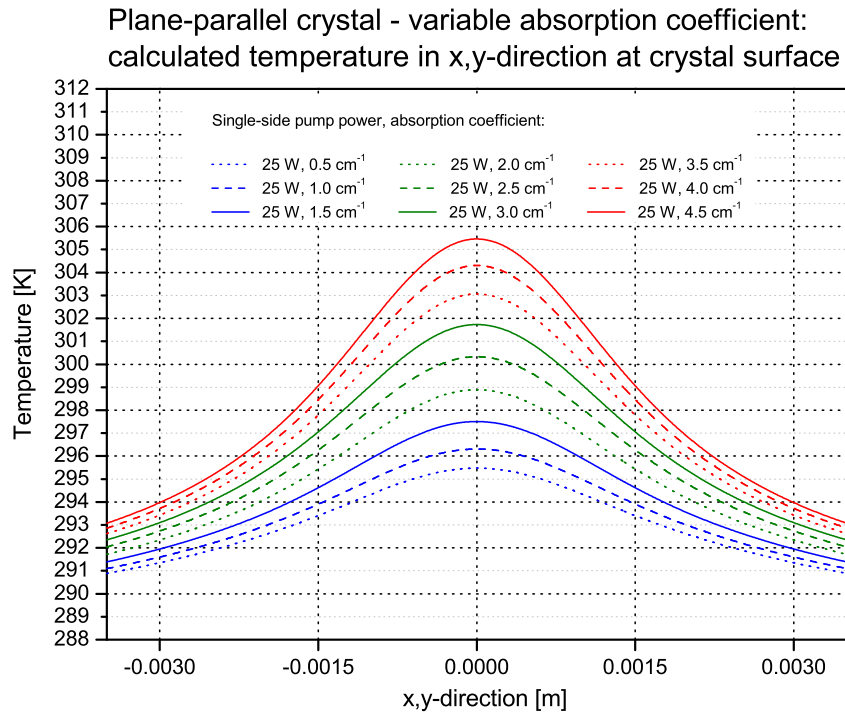
Figure 4.24: Plane-parallel TISA crystal: variable absorption coefficient of TISA - temperature along x-, y-axis at crystal surface.
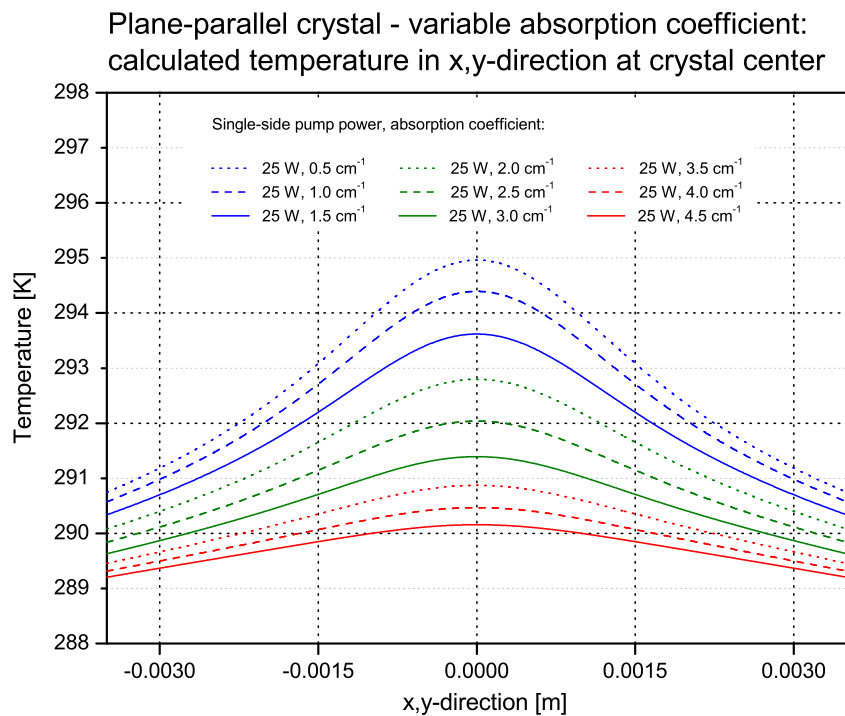
Figure 4.25: Plane-parallel TISA crystal: variable absorption coefficient of TISA - temperature along x-, y-axis at crystal center.

| T5 | **Plane-parallel crystal - variable pump-beam profile** |

An important parameter is the shape of the pump-beam profile. Inside the simulation, the pump-beam profile was varied from a pure Gaussian profile by use of Eq. 45 or Eq. 47 with $n, m=1$ to a super-Gaussian profile ($n, m=10$ in Eq. 47), which corresponds almost to a top-hat pump-beam profile.

As can be seen in Figs. 4.26-4.28, a super-Gaussian beam profile with $n, m=10$ results in lower temperatures along the z- and x-, y-directions compared to a Gaussian beam profile. The temperature difference is about 1.5 K. Outside the $1/e^2$-pump-beam radius (1.5 mm), the effect of the beam profile on the temperature profile completely vanishes. Consequently, the pump-beam profile has little effect on the overall temperature distribution in an end-pumped geometry.
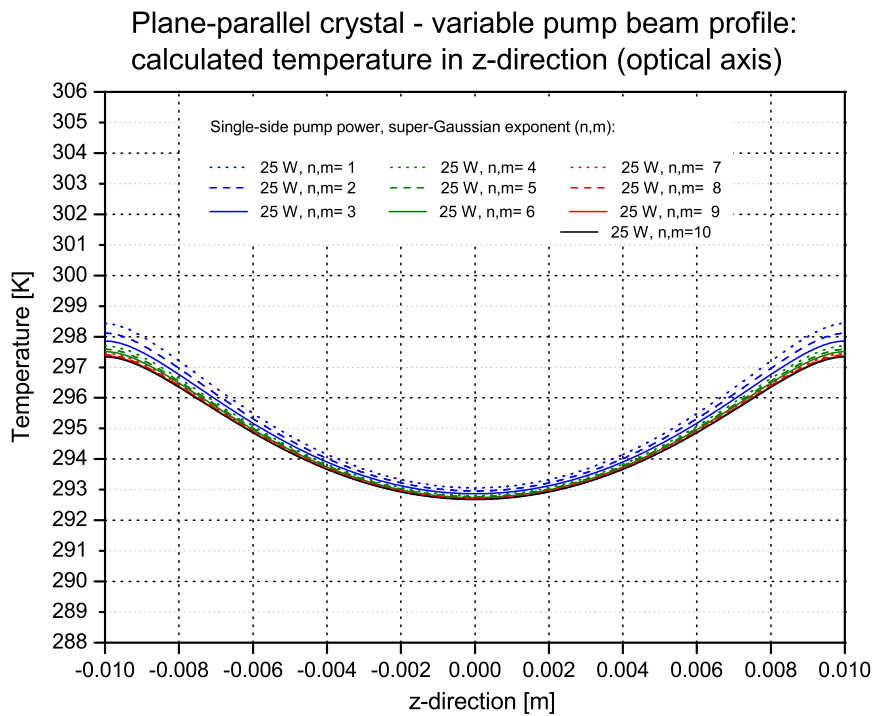
Figure 4.26: Plane-parallel TISA crystal: variable pump-beam profile - temperature along z-axis.
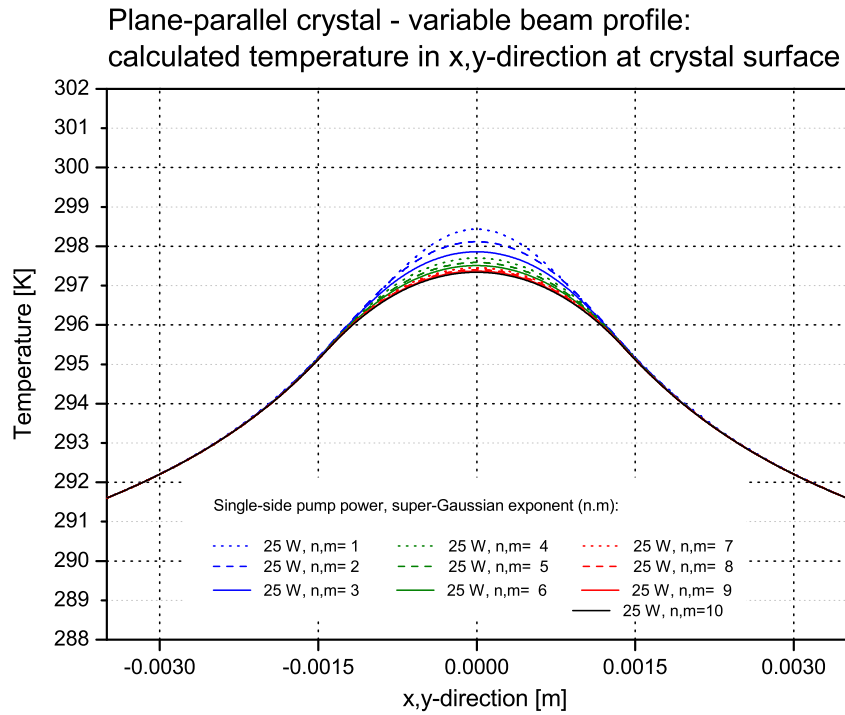
Figure 4.27: Plane-parallel TISA crystal: variable pump-beam profile - temperature along *x*-, *y*-axis at crystal surface.
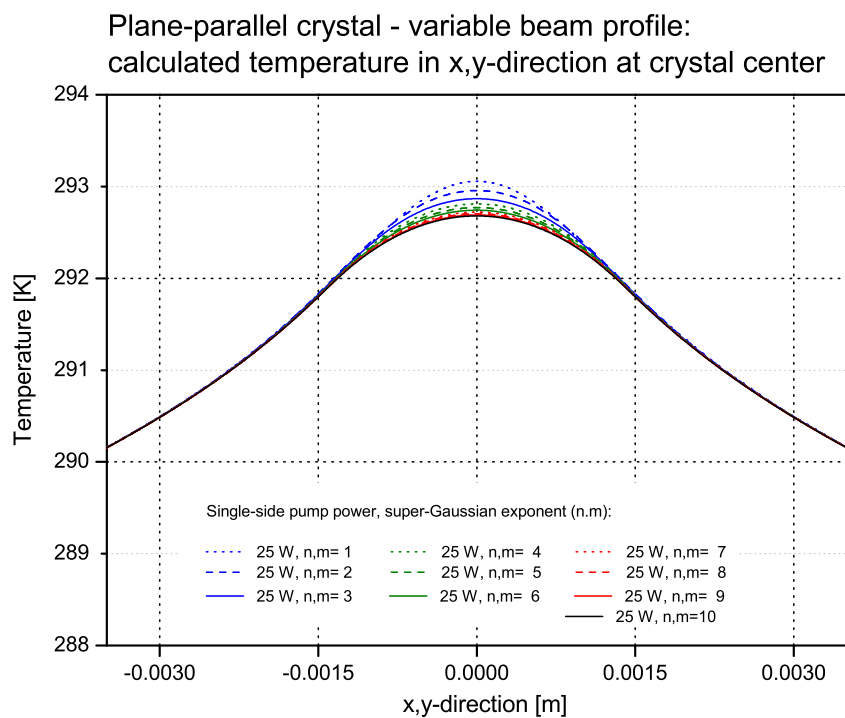
Figure 4.28: Plane-parallel TISA crystal: variable pump-beam profile - temperature along *x*-, *y*-axis at crystal center.

T6   **Plane-parallel crystal - variable pump-beam radius**

Besides the pump-beam profile, the pump-beam radius is a critical parameter for pumping crystals. The damage threshold of TISA crystals is about 3-10 J/cm^2, depending on the crystal quality. Within the thermal simulation, the $1/e^2$-beam radius of a Gaussian shaped pump beam is varied from 0.25 mm to 2.00 mm. The average pump power is 25 W for each simulation.

Figures 4.29-4.31 show that the pump-beam radius has a significant effect on the maximum temperatures. The resulting thermal lensing is therefore strongly dependent on the pump-beam radius. The simulation with the smallest pump-beam radius shows ripples and a non-centered temperature profile. This is included here intentionally to demonstrate the effect of strong gradients inside the FEA model. Obviously, the number of mesh elements is not high enough to resolve the strong gradients. In this case the mesh has to be adjusted. See Appendix B for further details about adaptive mesh refinement (AMR).
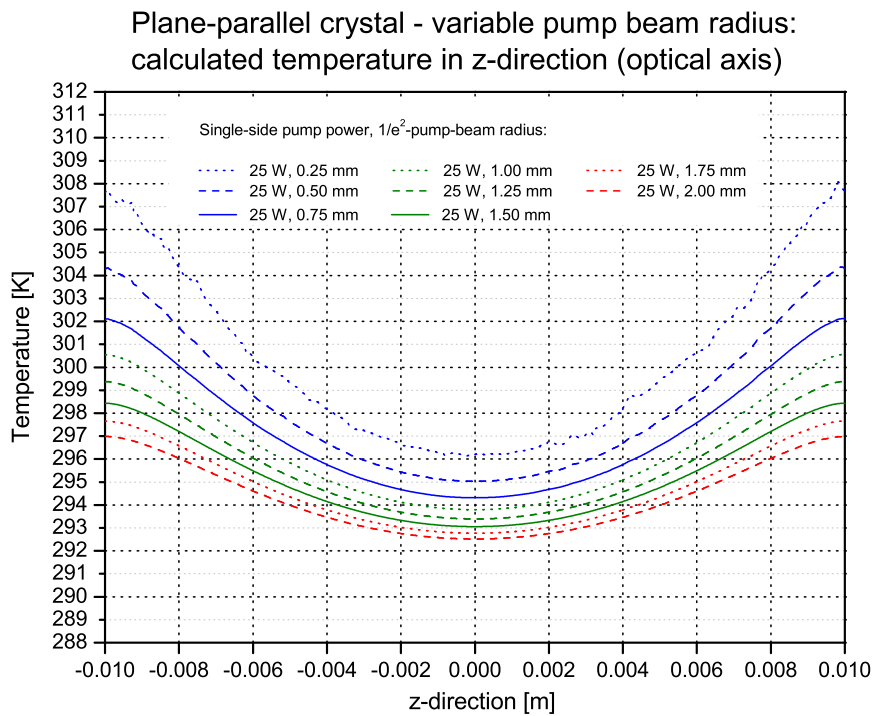
Figure 4.29: Plane-parallel TISA crystal: variable pump-beam radius - temperature along z-axis.
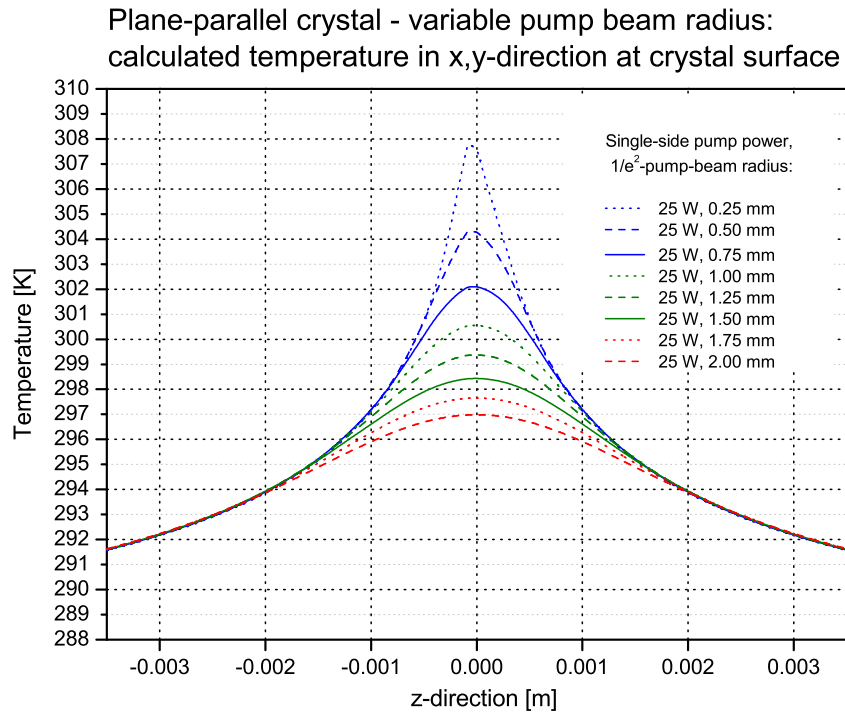
Figure 4.30: Plane-parallel TISA crystal: variable pump-beam radius - temperature along x-, y-axis at crystal surface.
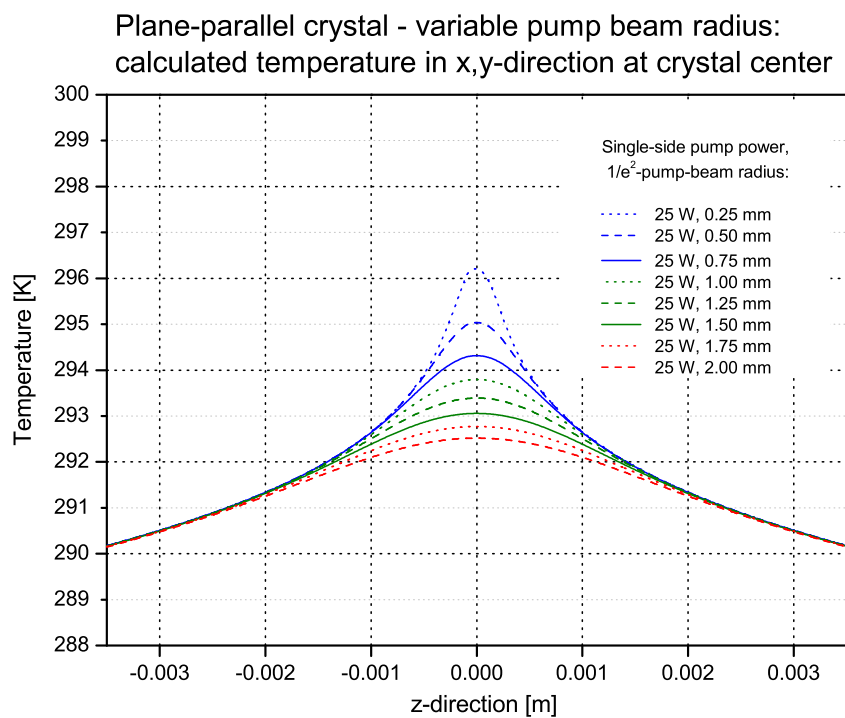
Figure 4.31: Plane-parallel TISA crystal: variable pump-beam radius - temperature along x-, y-axis at crystal center.

T7 **Plane-parallel crystal - time dependent analysis: ramped pump power**

As the pump laser is running at a high repetition frequency (250-400 Hz, see above), one can assume a constant temperature profile between each pump pulse after a certain relaxation time. The time constant at which a new constant temperature profile is established if the pump power is changed, is an interesting parameter. Within the simulation, the pump power is ramped from 0 to 25 W single-side pump power. In the simulation it is assumed, that the change in pump power happens without delay. The simulation starts with a pump power of 0 W. At t=5 s, the single-side pump power is increased to 1 W. At t=10 s, and following intervals of 5 s, the single-side pump power is increased by 5 W. The temperature is simulated at two points inside the crystal: (x, y, z)=$(0, 0, 0)$ m (crystal center) and (x, y, z)=$(0, 0, \pm 0.01)$ m (crystal surface center).

After each increase in pump power, it takes less than 2 s for a new constant temperature profile to be established. The temperature difference between crystal surface and center is increasing with higher pump power, as the temperature gradient is increased.
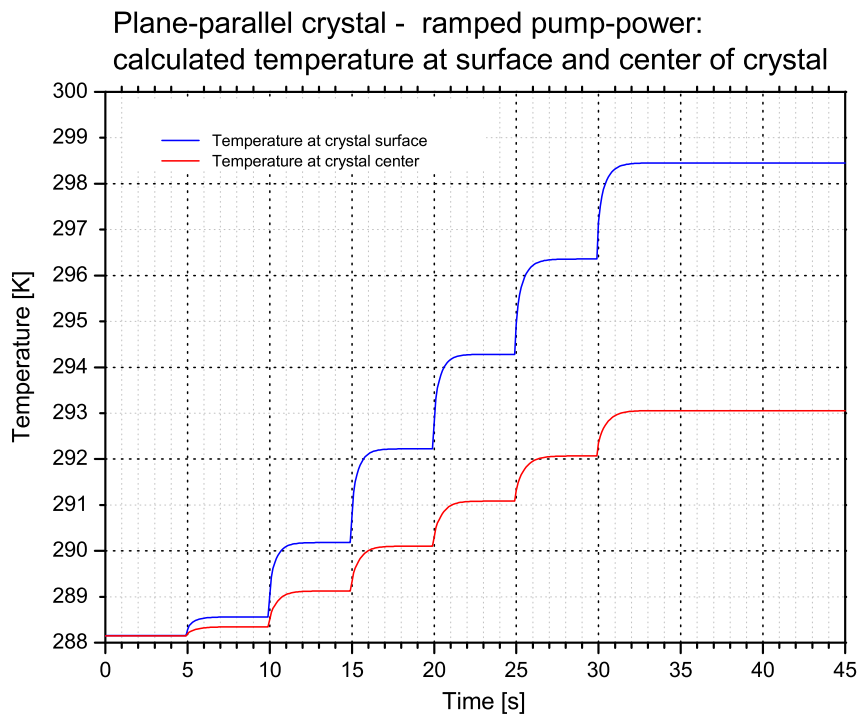
Figure 4.32: Plane-parallel TISA crystal: time dependent analysis with ramped pump power - temperature at crystal surface and crystal center.

Brewster-cut crystal

The Brewster-cut TISA crystal is oriented in the y-z-plane with its c-axis being parallel to the incident crystal plane (and in direction of the y-axis) and normal to the optical resonator axis z. The $\vec{E}$-vector of the pump beam is parallel to the c-axis (defined as p-polarization). In this coordinate system, the tangential plane is given by the y-z-plane, and the x-z-plane is the sagittal plane, respectively. As a consequence of the Brewster-cut geometry, the pump-beam radius is increased in the y-z-(tangential-)plane by a factor of n, where n is the refractive index of TISA. The resulting calculated temperature profile in shown in Figs. 4.33 and 4.34 (isosurface plot). Compared to a plane-parallel crystal being pumped at the same pump level, the maximum temperature at center of the crystal surface is decreased by about 1.4 K. The temperature profile is no longer rotational symmetric around the optical axis, which can be attributed to the Brewster-angled crystals ends in combination with the cooling. Figure 4.36 shows the temperature in x-(sagittal) and y-(tangential) direction. The increase of the beam radius in y-direction by a factor of n causes a slight temperature increase of less than 0.5 K between both directions at a single-side pump power of 25 W.
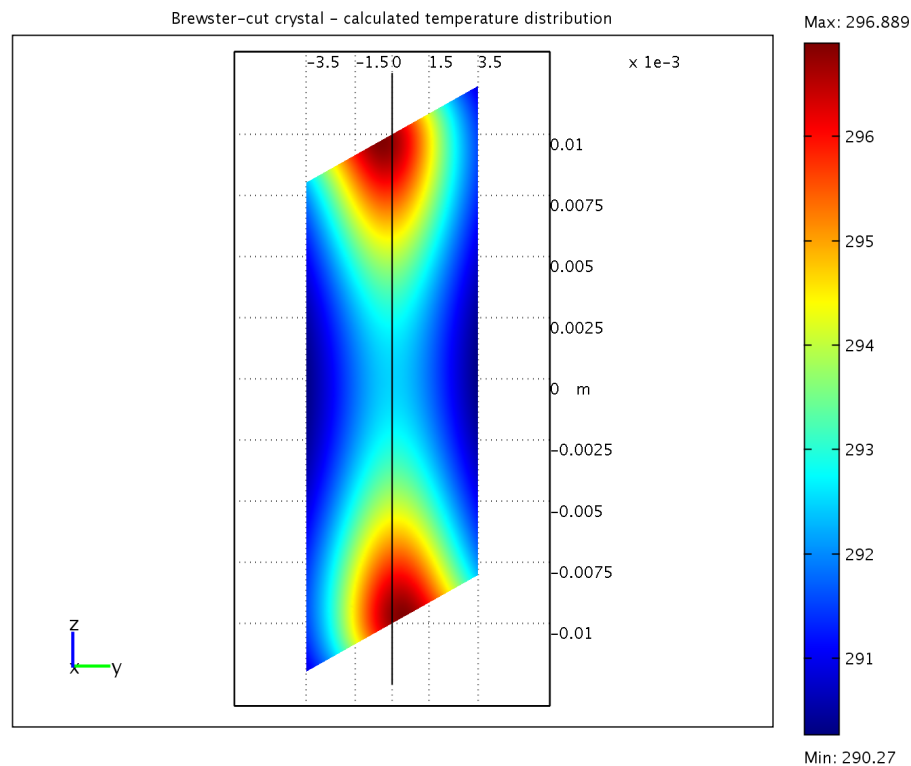
Figure 4.33: Thermal simulation of Brewster-cut TISA crystal - single-side pump power: 25 W.

Figure 4.34: Brewster-cut TISA crystal: isosurface plot of calculated temperature distribution. Single-side pump power: 25 W.
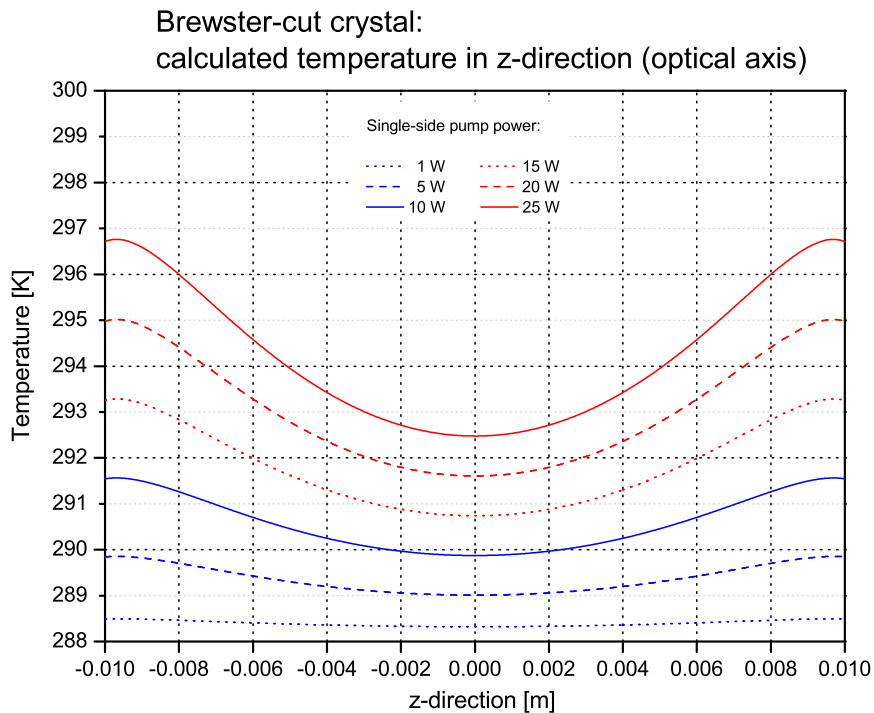
Figure 4.35: Brewster-cut TISA crystal: temperature along z-axis for various single-side pump levels.
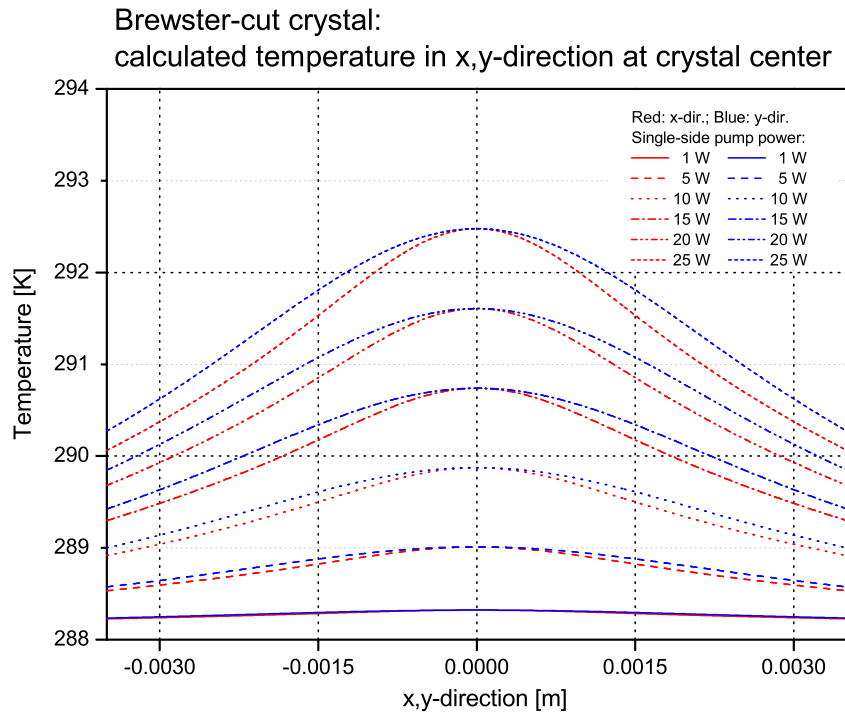
Figure 4.36: Brewster-cut TISA crystal: temperature along x-, y-axis at crystal center for various single-side pump levels.

Brewster-cut crystal - unevenly pumped $\boxed{\text{T9}}$

Within this simulation, the pump power is reduced on one side of the crystal by 10% to study the effects of nonuniform pumping. Figures 4.39-4.40 show, that the maximum temperature at the crystal surface is lowered by less than 1 K, and that the temperature profiles at the crystal center are affected by a temperature decrease of less than 0.5 K at the optical axis compared to the previous simulation $\boxed{\text{T8}}$. The heat source distribution Q and the resulting calculated temperature profile T at pump-power levels of 25 W for one side (at $-z$-direction), and 22.5 W for the other side ($+z$-direction) is depicted in Figures 4.37a, 4.37b. The resulting calculated temperature profile is again asymmetric, compared to the symmetric heat source. The asymmetric profile can be explained by the Brewster-geometry of the crystal in combination with the applied cooling. See also the previous simulation $\boxed{\text{T8}}$.

(a) Heat source Q in W/m^3.

(b) Calc. temperature distribution T in K.
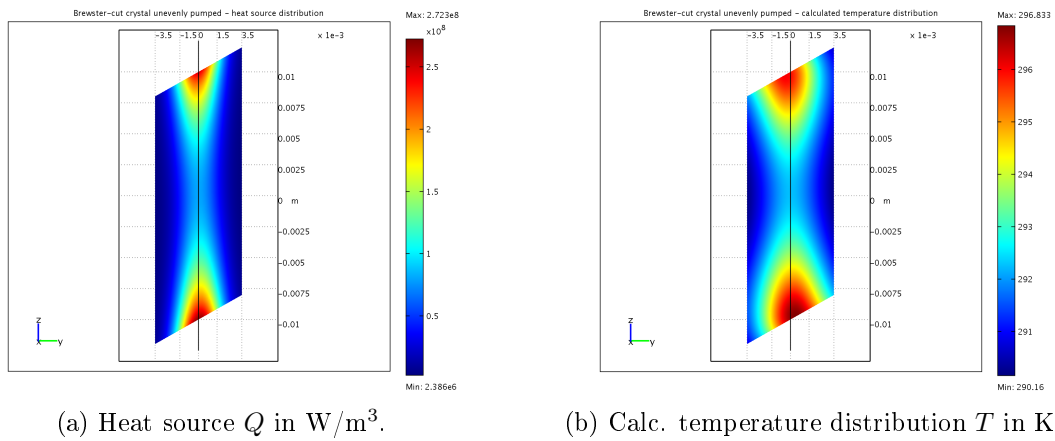
Figure 4.37: BR TISA crystal: unevenly pumped - heat source Q and calc. temperature distribution T. Single-side pump powers: 25 W, 22.5 W. Note: same color-coding for both quantities for better comparison.
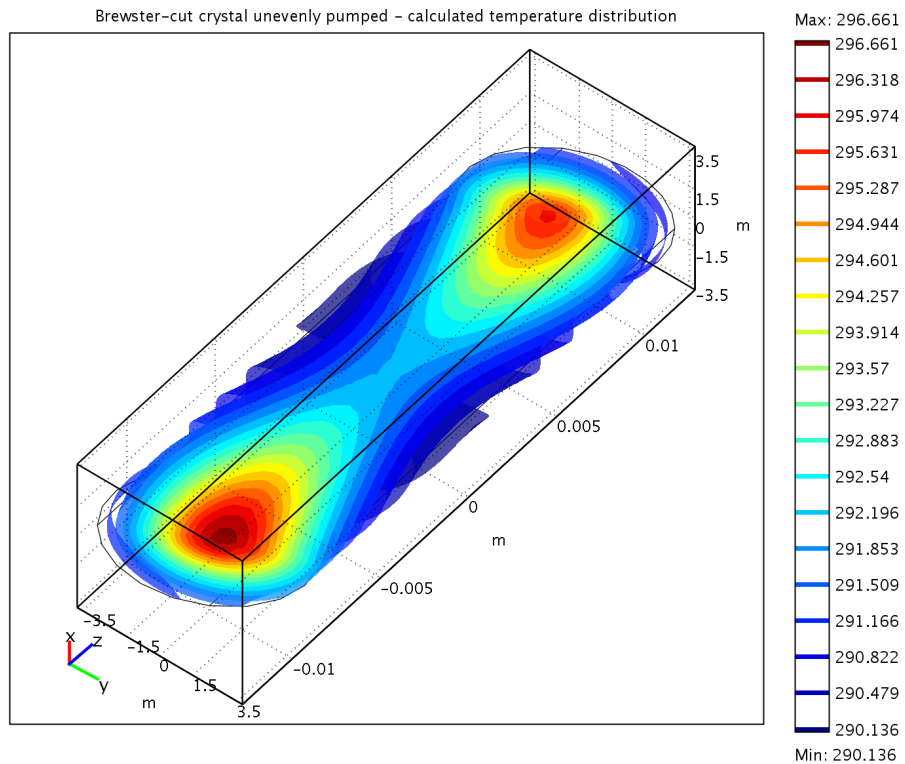
Figure 4.38: Brewster-cut crystal: unevenly pumped - isosurface plot of calculated temperature distribution. Single-side pump powers: 25 W, 22.5 W.
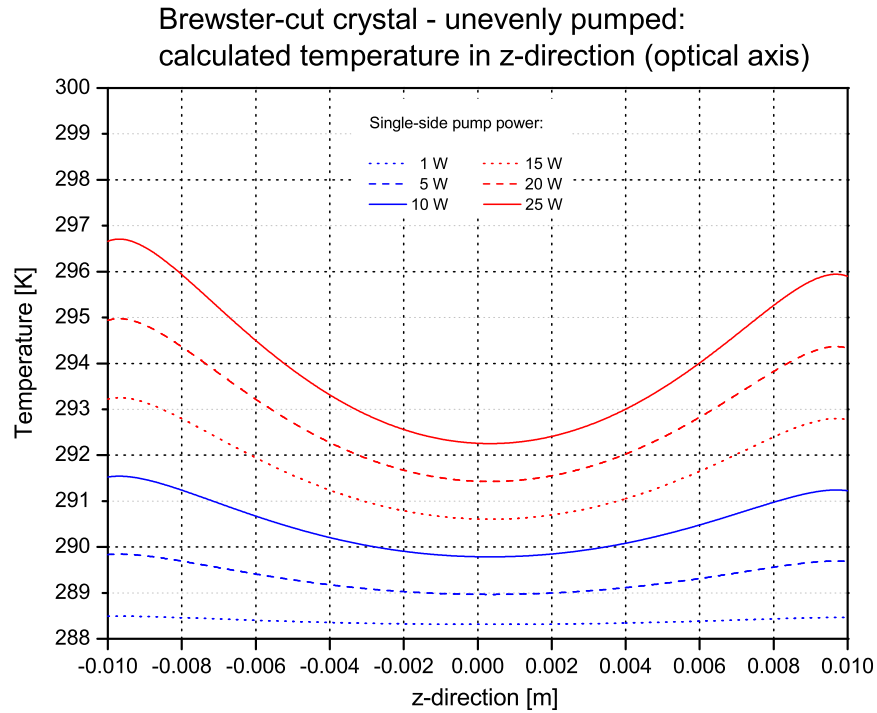
Figure 4.39: Brewster-cut crystal: unevenly pumped - temperature along z-axis for various single-side pump levels.
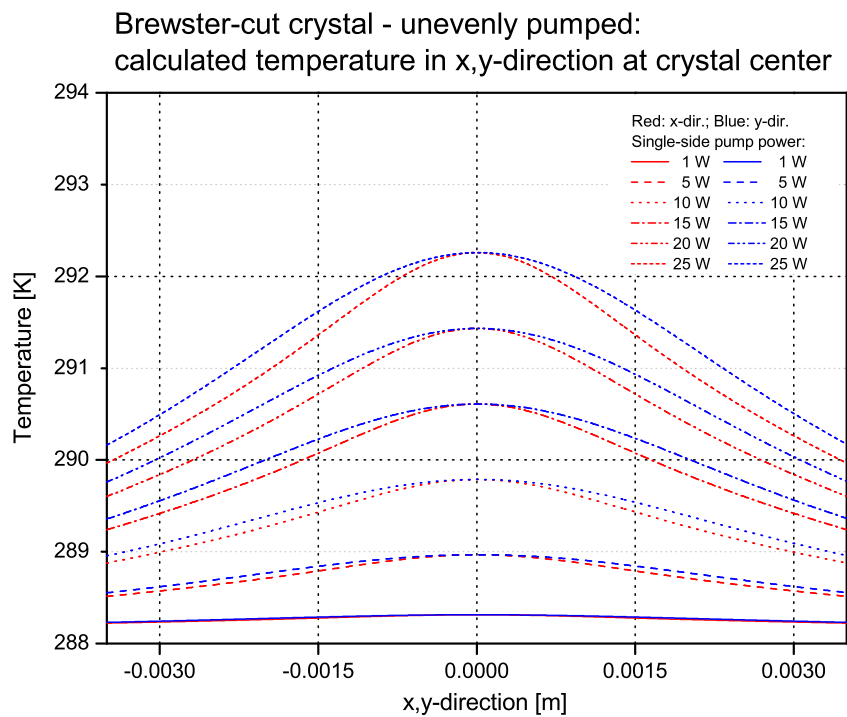
Figure 4.40: Brewster-cut crystal: unevenly pumped - temperature along x-, y-axis at crystal center for various single-side pump levels.

T10 **Brewster-cut crystal - single-side pumped**

TISA crystals are often single-side pumped. This is shown in Figs. 4.41-4.44, where the crystal with the same model conditions of T8 is being single-side pumped with 25 W. As can be seen, the temperature decreases at the unpumped surface to a level less than 1 K higher than the applied boundary condition for the crystal in contact with the cooler.

Brewster–cut crystal single–side pumped – calculated temperature distribution
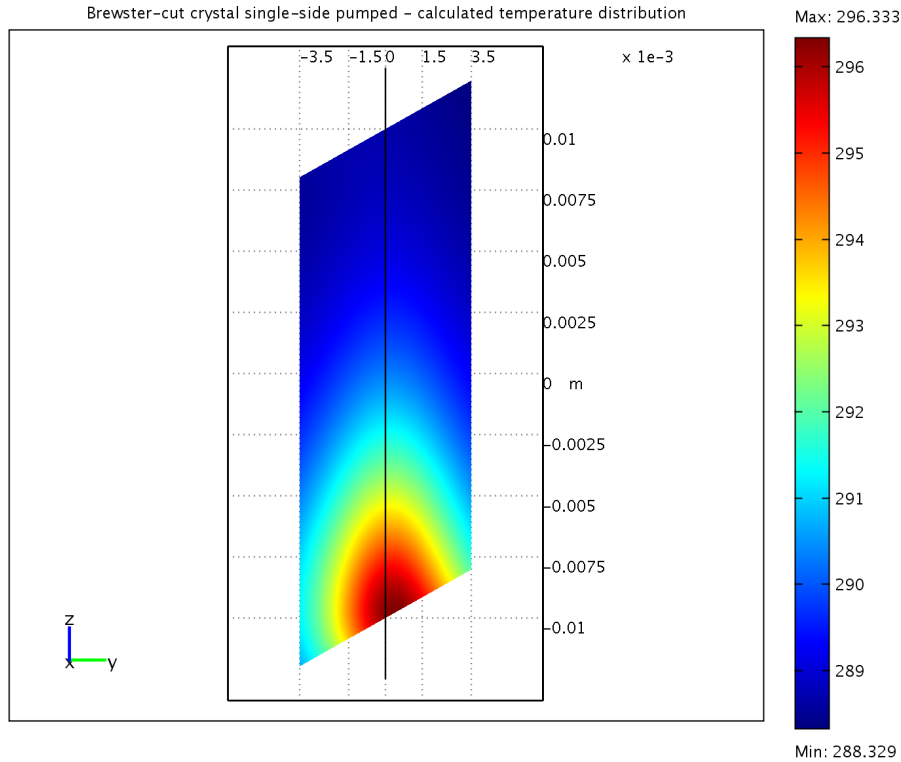
Figure 4.41: Thermal simulation of Brewster-cut crystal being single-side pumped with a power of 25 W.
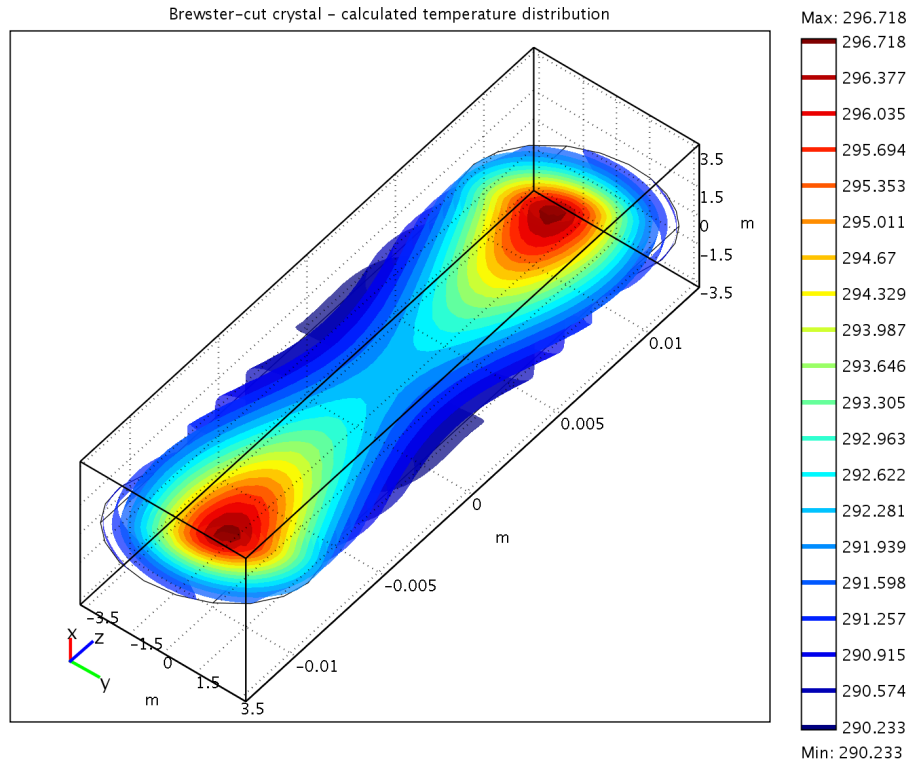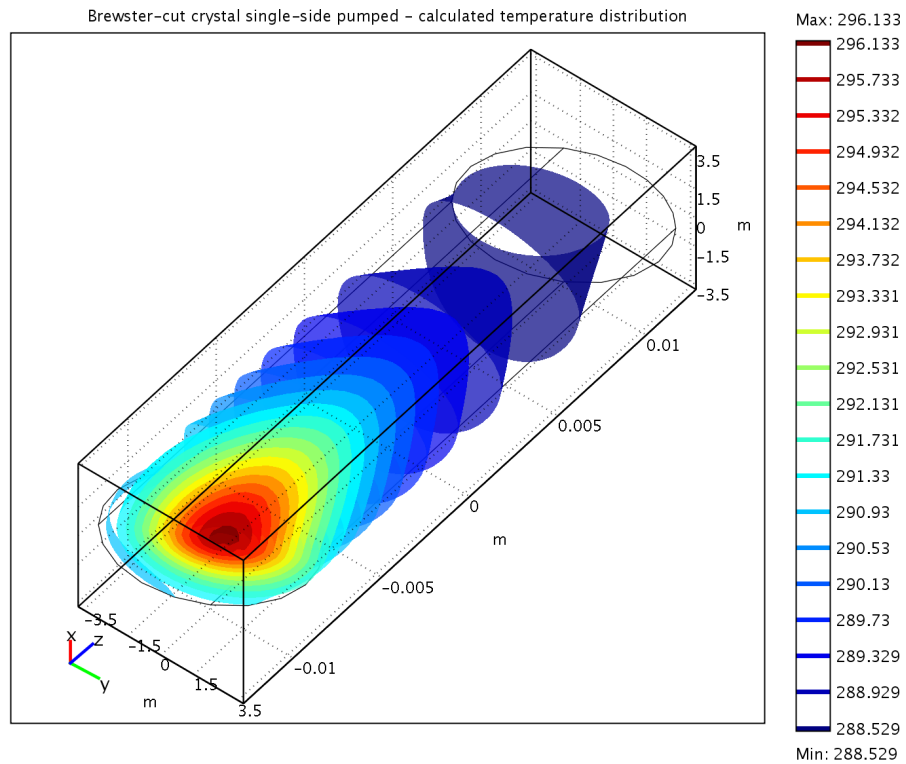
Figure 4.42: Brewster-cut crystal: single-side pumped - isosurface plot of calculated temperature distribution. Single-side pump power: 25 W.
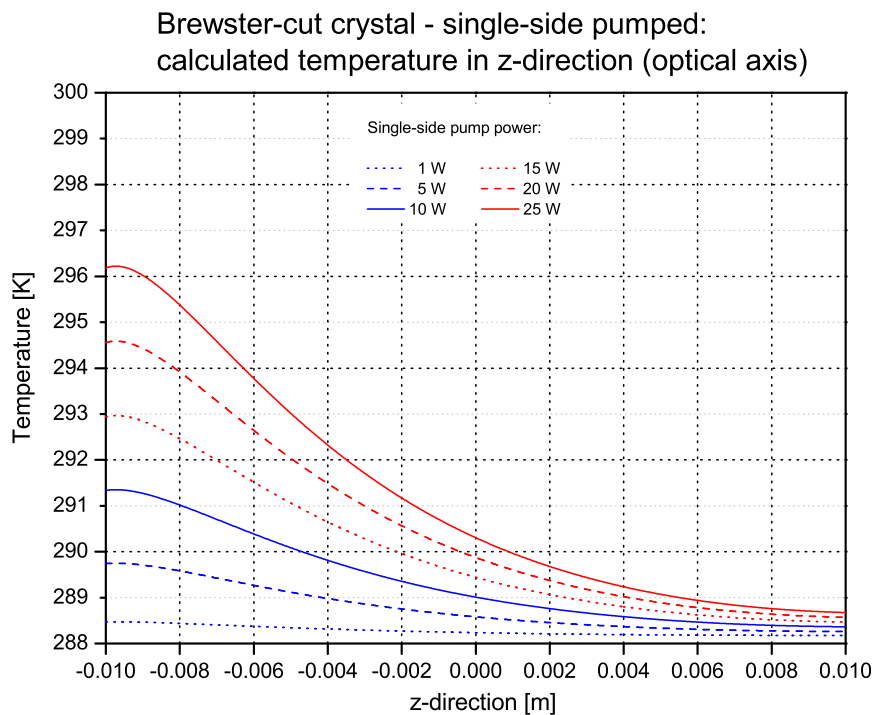
Figure 4.43: Brewster-cut crystal: single-side pumped - temperature along z-axis for various single-side pump levels.
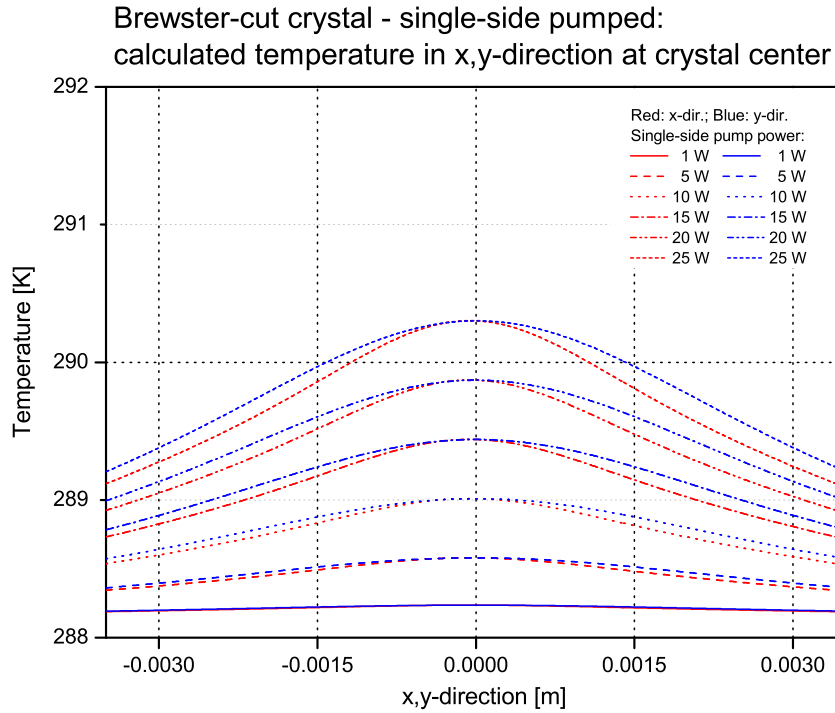
Figure 4.44: Brewster-cut crystal: single-side pumped - temperature along x-, y-axis at crystal center for various single-side pump levels.

T11 Crystal with undoped end-caps

Undoped end-caps are usually diffusion-bonded to the doped area. At IPM, TISA crystals with grown undoped end-caps are available. The undoped end-caps have been grown at FEE company, Idar-Oberstein, Germany, to TISA crystals (Crystal Systems; Doehrer). A post-annealing procedure under Hydrogen atmosphere was necessary, as Ti^{3+}-ions were oxidized to Ti^{4+} during the growth process of the undoped end-caps. However, inspection of the laser crystals indicated inhomogeneous Ti^{3+}-concentrations and color centers in the crystal after fabrication. Therefore, no later experiments have been performed with the crystals yet.

A crystal with undoped end-caps is simulated as follows. A single plane-plane domain with $\pm\,0.01$ m width is in between two Brewster-cut domains with a center length of 9 mm. Absorption of pump radiation is only given at the center domain with the heat source of a Brewster-cut crystal, but without shear. Outside the center domain, no absorption and therefore no heat source Q is given. The domains are connected through the boundaries with an continuous boundary condition. The material parameters and boundary conditions are the same as in the previous simulations. The meshed geometry is depicted in Fig. 4.45. The center domain is indicated by the space in between the two (gray) planes.

Figure 4.46 shows the calculated temperatures distribution of a crystal with undoped end-caps pumped at a single-side pump power of 25 W. Figures 4.47a, 4.47b present the resulting calculated temperature profile for isosurfaces and the crystal surface itself at a single-side

pump level of 25 W. Using undoped end-caps, an almost rotational symmetric temperature profile around the optical axis is obtained.

The resulting calculated temperature profiles along z-direction and x-, y-directions for single-side pump levels $1-25$ W are shown in Figs. 4.48 and 4.49, respectively. At pump powers above 5 W, the temperature distribution shows the same tightening effect at the crystal center (Fig. 4.48) as with previous simulations (see simulation $\boxed{\mathbf{T8}}$ and Fig. 4.35 on page 54). The zone with maximum temperature is not being found at connection between undoped and doped area: it is shifted about 2.5 mm to the center of the doped domain. The maximum temperature is decreased by more than 2 K using undoped end-caps. The temperature distribution is centered around the optical axis with slight differences in x-, y-directions due to the Brewster-effect (see above).
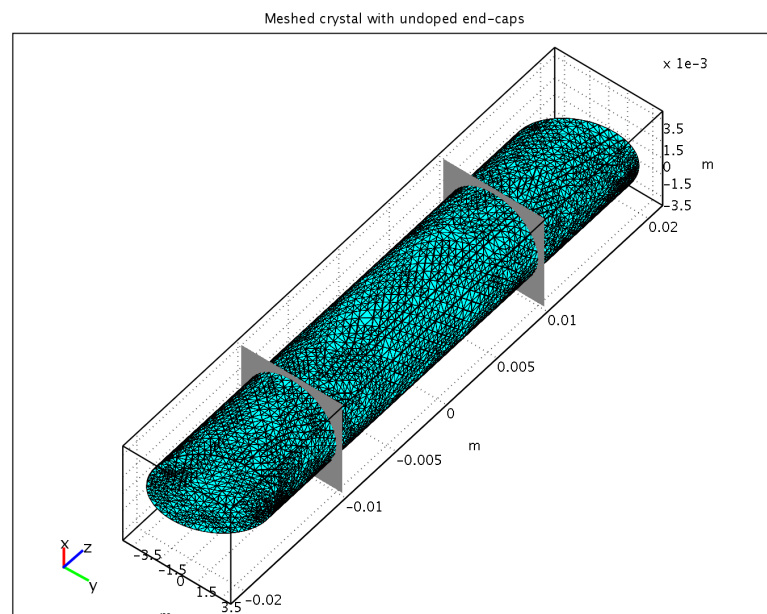
Figure 4.45: Meshed TISA crystal with undoped end-caps (Brewster-cut) (294949 elements). Absorption of pump radiation is given within the center domain, which is indicated by gray planes.
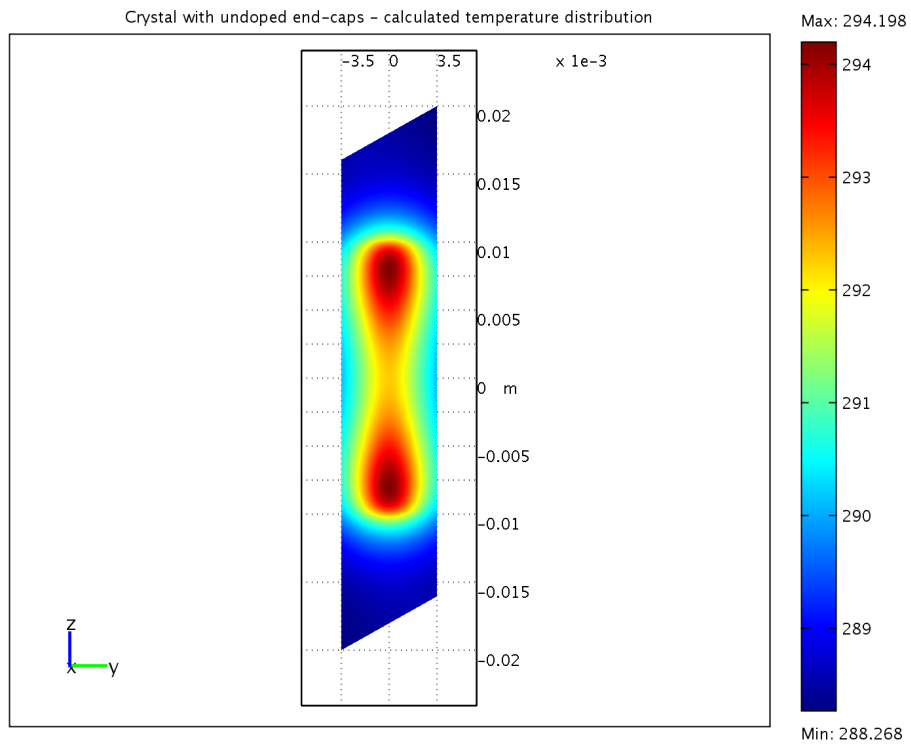
Figure 4.46: Thermal simulation of TISA crystal with undoped end-caps (Brewster-cut) - single-side pump power: 25 W.
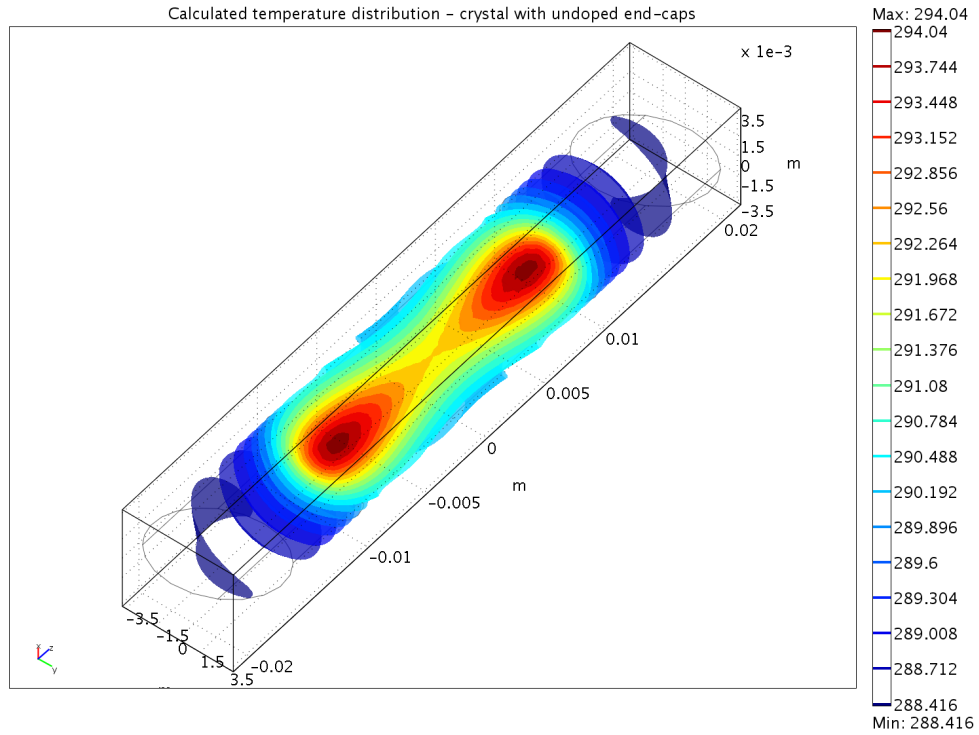
(a) Isosurfaces.
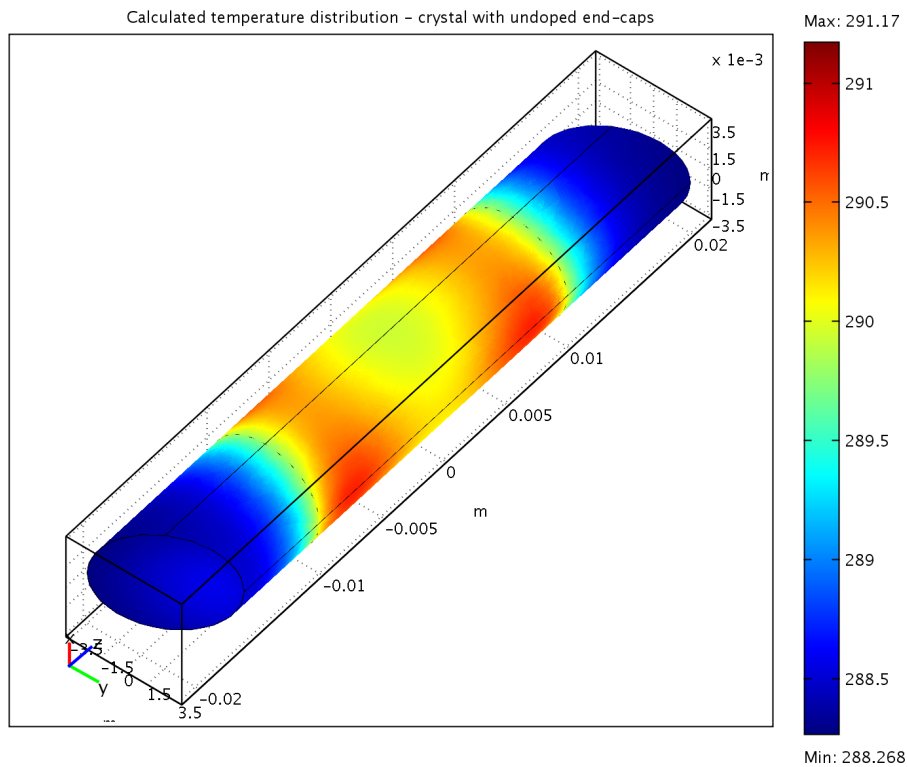
(b) Crystal boundary temperature.

Figure 4.47: Calculated temperature distribution of TISA crystal with undoped end-caps (Brewster-cut) - isosurfaces and boundary plot. Single-side pump power: 25 W. Note: different colormaps in subplots.
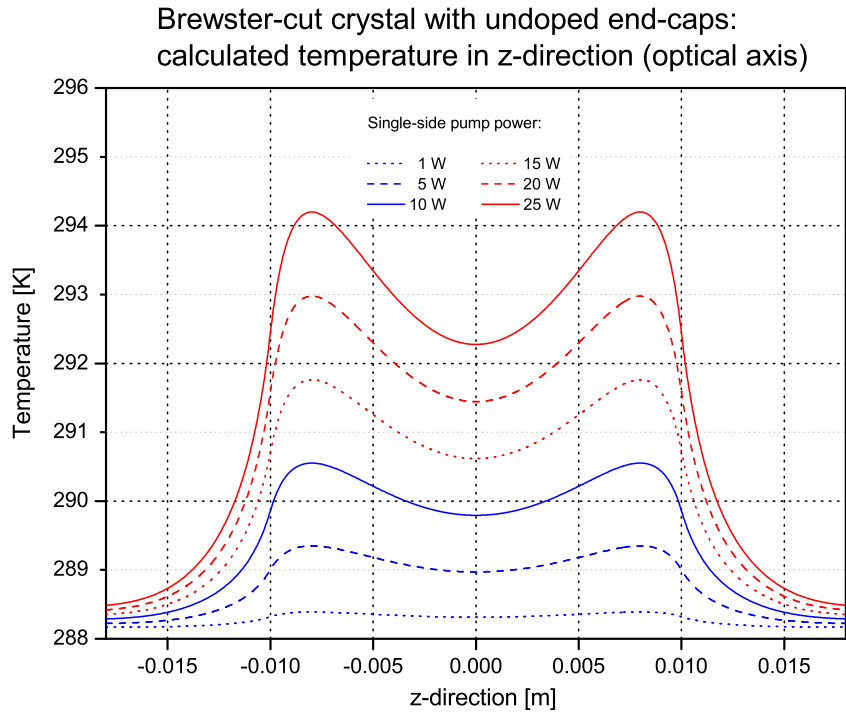
Figure 4.48: TISA crystal with undoped end-caps (Brewster-cut): temperature along z-axis for various single-side pump levels.
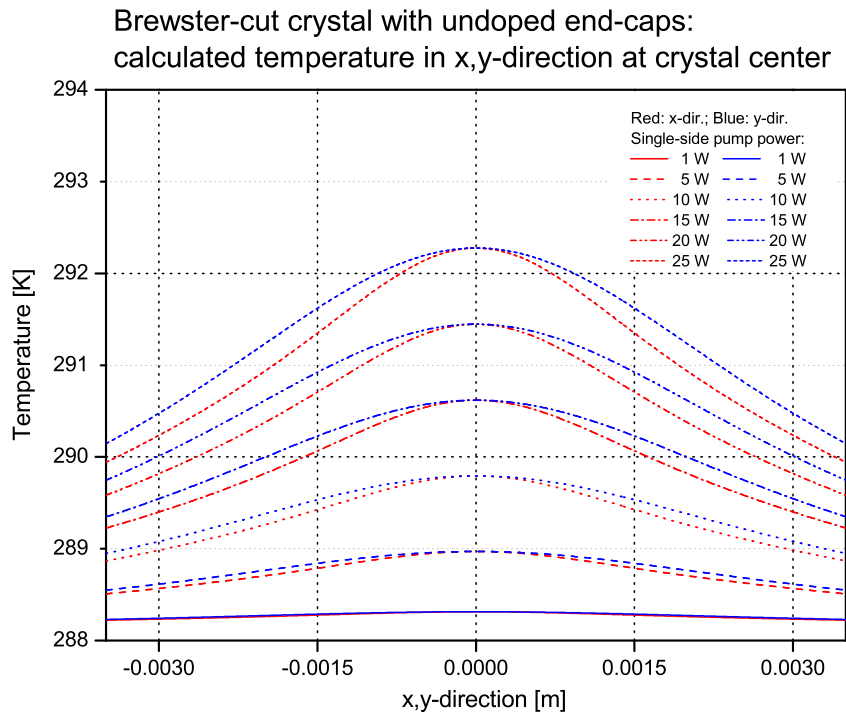
Figure 4.49: TISA crystal with undoped end-caps (Brewster-cut): temperature along x-, y-axis at crystal center for various single-side pump levels.

Incorporation of crystal cooler $\boxed{\text{T12}}$

A model of the aluminum cooler was designed in a CAD-Program[11] and imported into the FEA model. The meshed Brewster-cut crystal with cooler is depicted in Fig. 4.50. As can be seen, a complicated geometry leads to an increase in overall mesh elements at geometry edges. The boundary condition between the crystal and the cooler was first set to be continuous inside the simulation. The resulting calculated iso-surface plot is shown in Fig. 4.51a and in Fig. 4.52 as seen from top in transparent mode. In Fig. 4.51b, the same cooler is shown with the pump laser turned off. A comparison with a simulation without cooler is depicted in Fig. 4.54.

The overall parabolic shape of the temperature profile inside the pumped region is not influenced by the different simulation conditions. However, the maximum temperature is about 2 K lower compared to a simulation without cooler. Towards the crystal boundary, the same linear temperature decrease is found.

The influence of a cooler made of copper (Cu) is investigated, as copper has a higher thermal conductivity compared to aluminum (see Fig. 4.10, T>50 K). The choice of the cooler material doesn't have a significant impact (see Fig. 4.54). Therefore, a cooler design based on aluminum material is sufficient at this power level.

Figures 4.53a, 4.53b show the calculated temperature profiles for the case of a single-side (end-) pumped (SSP) TISA crystal. All other parameters are the same (single-side pump power: 25 W).

---

[11]Autodesk AutoCAD 2007.
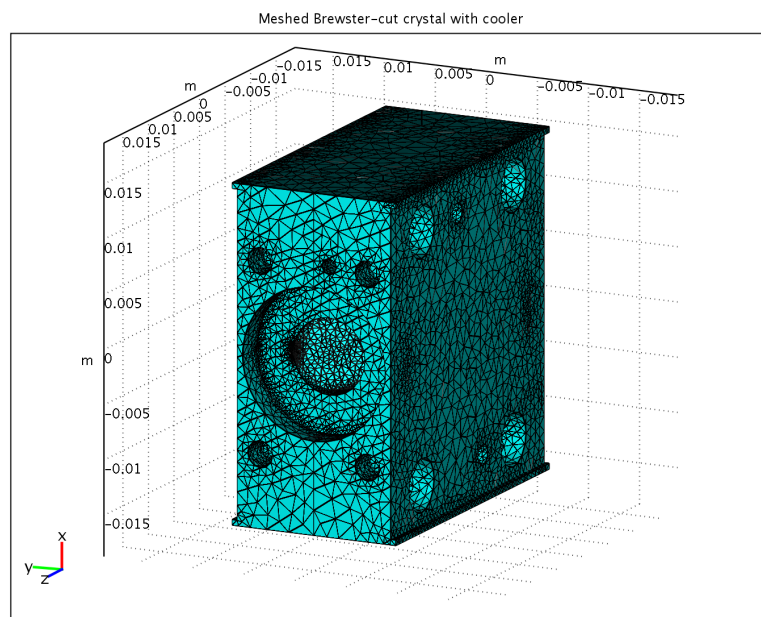
Figure 4.50: Meshed Brewster-cut TISA crystal with cooler (210177 elements).
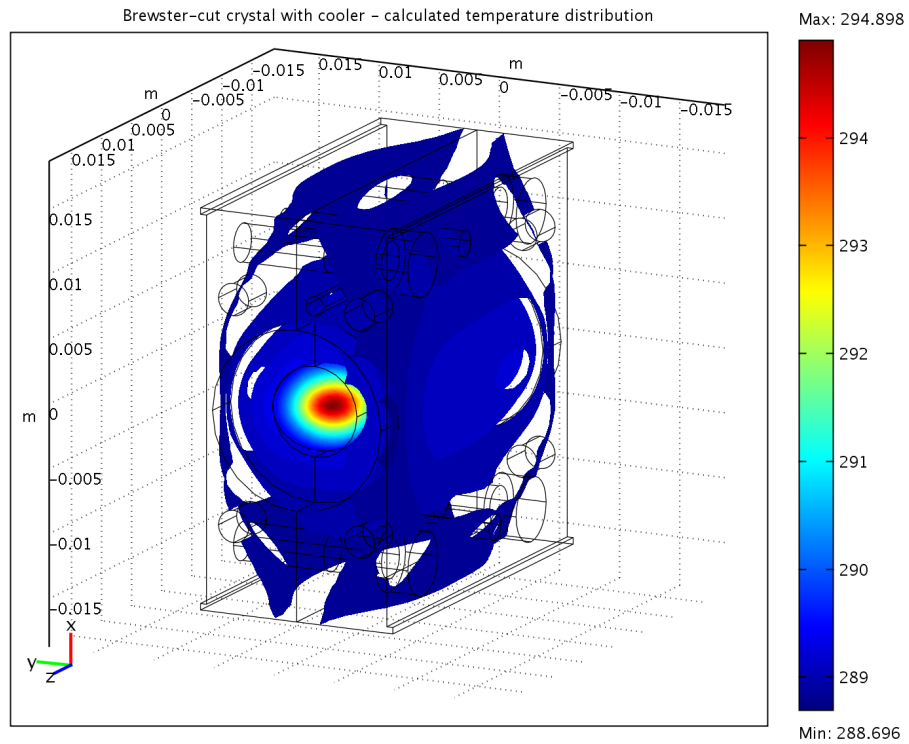
(a) Single-side pump power: 25 W.
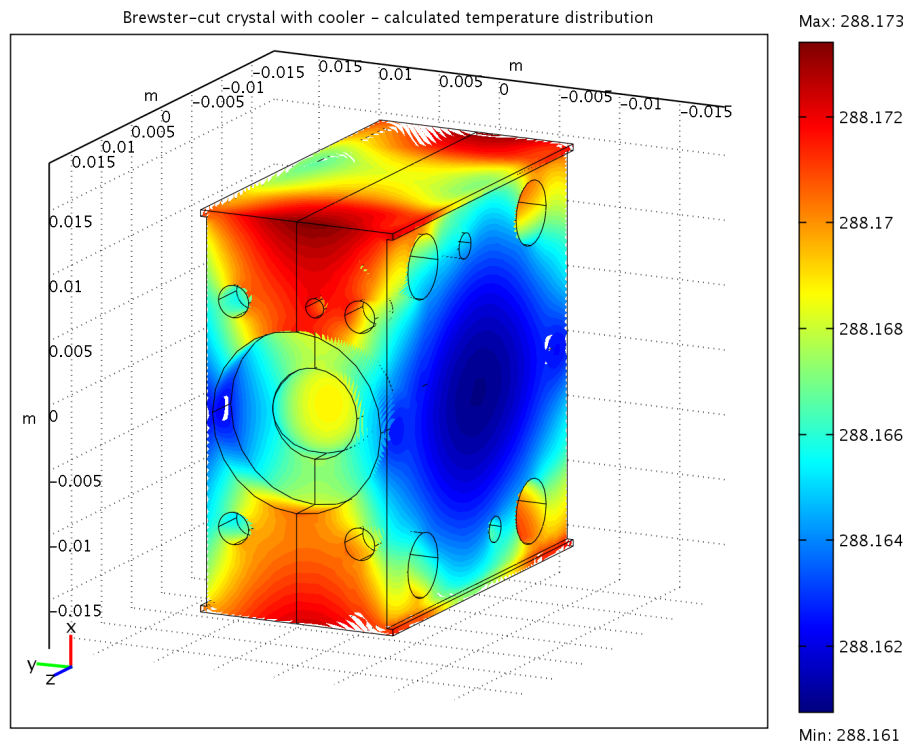
(b) Pump laser turned off.

Figure 4.51: Brewster-cut TISA crystal with cooler. Calculated temperature distribution (isosurfaces). Single-side pump power: 25 W. Note: different colormaps in subplots.
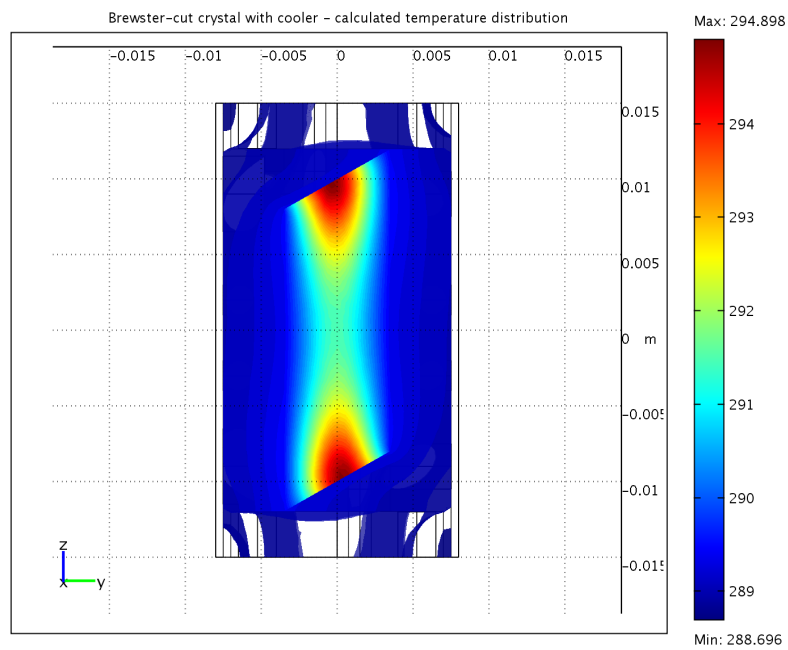
Figure 4.52: Brewster-cut TISA crystal with cooler. Calculated temperature distribution (isosurfaces, view from top). Single-side pump power: 25 W.
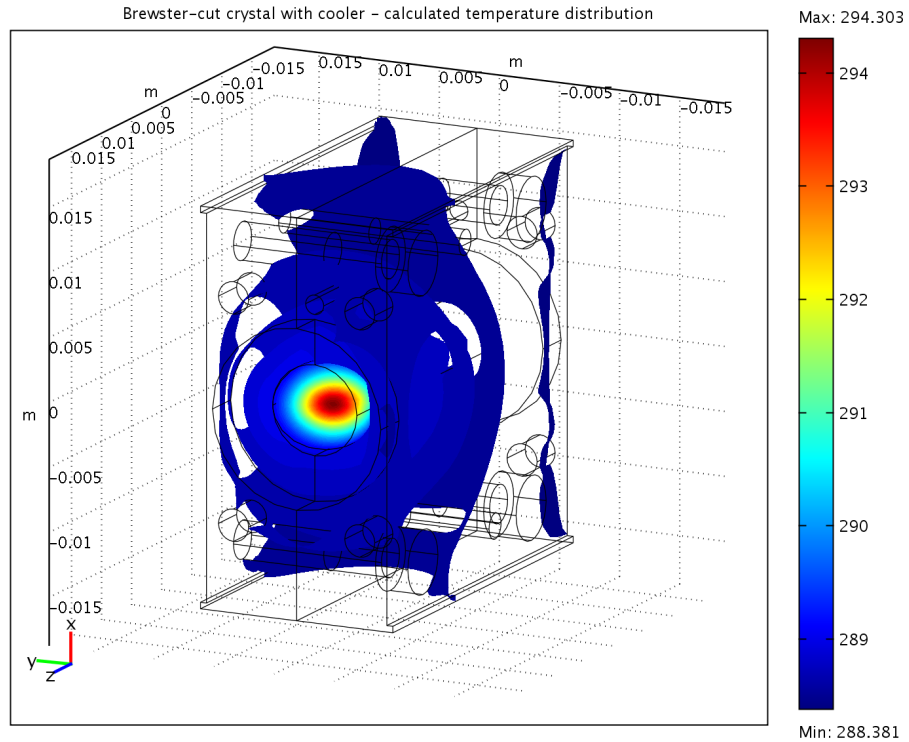
(a) 3d-view.
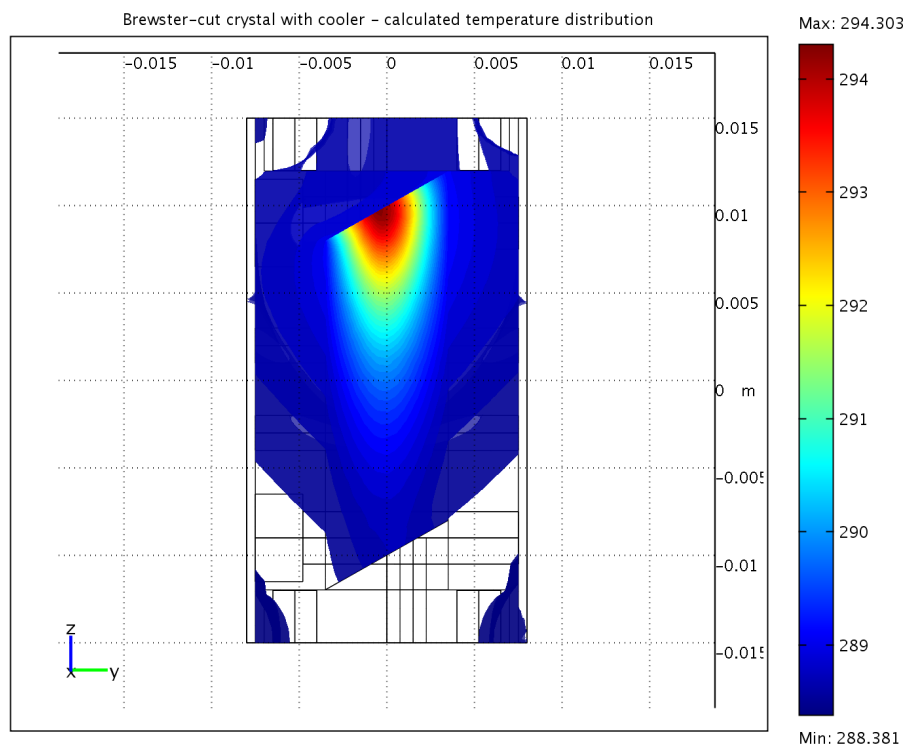
(b) View from top.

Figure 4.53: Brewster-cut TISA crystal with cooler - single-side (end-)pumped. Calculated temperature distribution (isosurfaces). Single-side pump power: 25 W.

T13 **Simulated Peltier element failure at cooler**

A Peltier-element failure is simulated by setting the heat transfer coefficient and temperature at the surface of the Peltier-element in contact with the cooler to the values given by the other surfaces in contact with surrounding air (see Tab 4.4). The defect Peltier-element is situated at the right side of the cooler (negative *y*-direction). Figure 4.55 shows, that the overall maximum temperature at the crystal surface is only slightly increased by 1.2 K. But the overall temperature distribution is becoming asymmetric, as the heat flow towards the working Peltier-element is dominating. This can be seen in Fig. 4.54.

The same situation with a Peltier element failure in the case of a single-side (end-)pumped TISA crystal is depicted in Fig. 4.56. The deformed, asymmetric temperature profile is clearly visible.

The resulting calculated optical path difference (OPD) profiles for both modeling cases are given in Ch. 4.2.6.
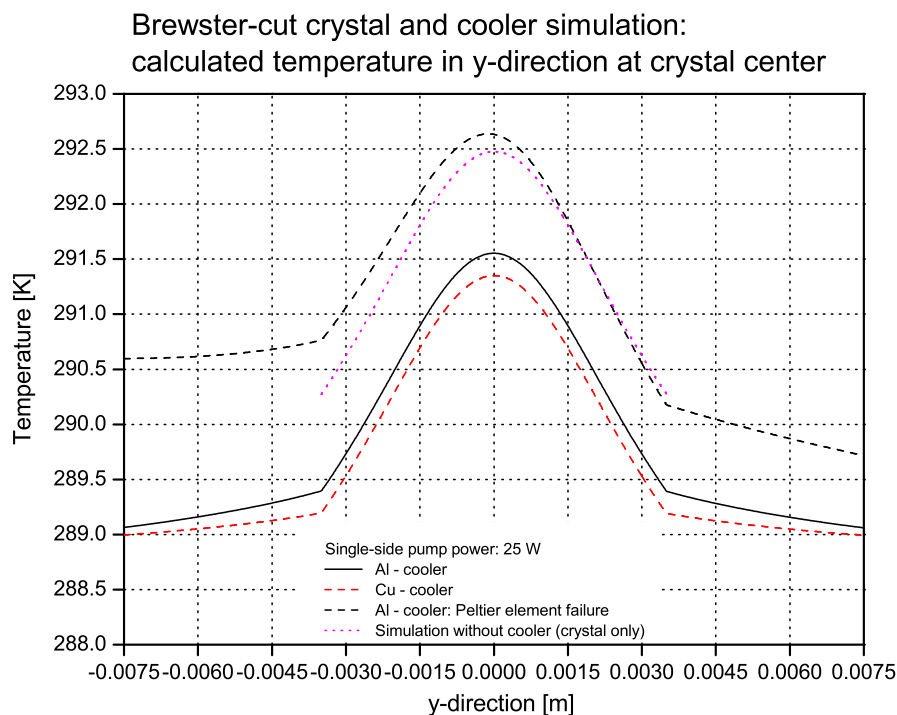
Figure 4.54: Brewster-cut TISA crystal with cooler: comparison of calculated temperature profiles.
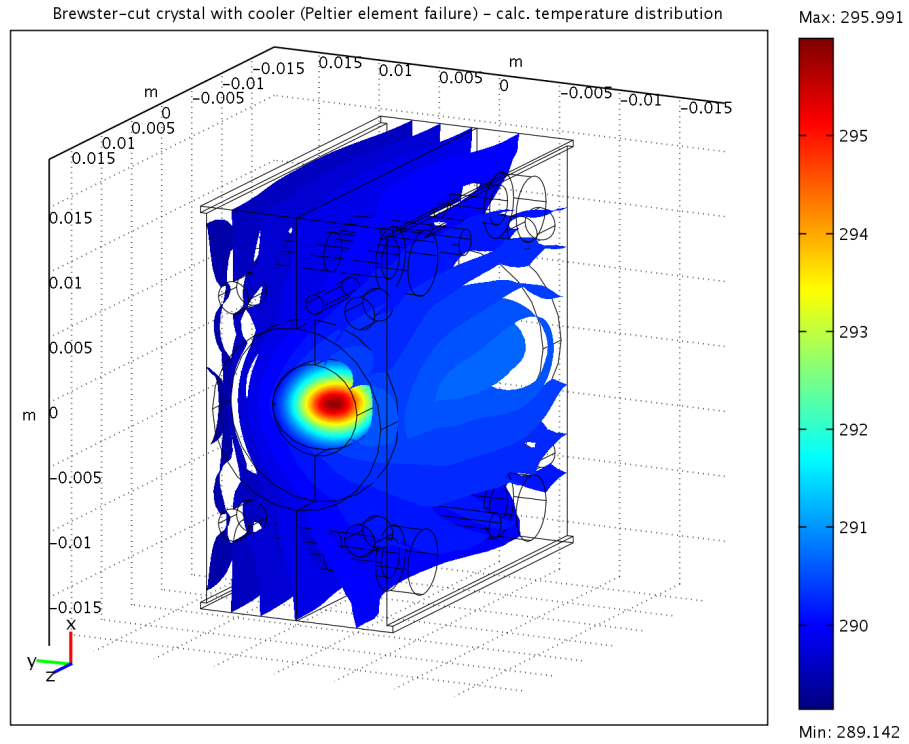
(a) 3d-view.
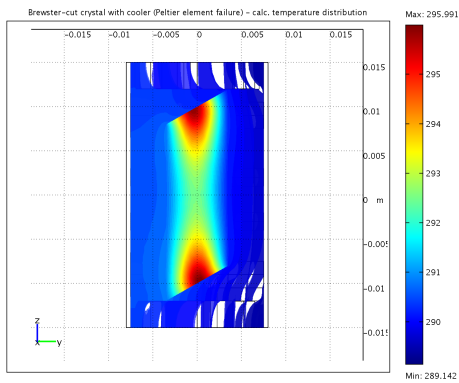
(b) View from top.
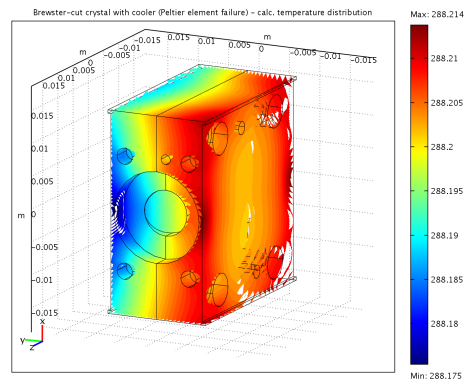
(c) Pump laser turned off.

Figure 4.55: Brewster-cut TISA crystal with cooler: simulated Peltier element failure at cooler.
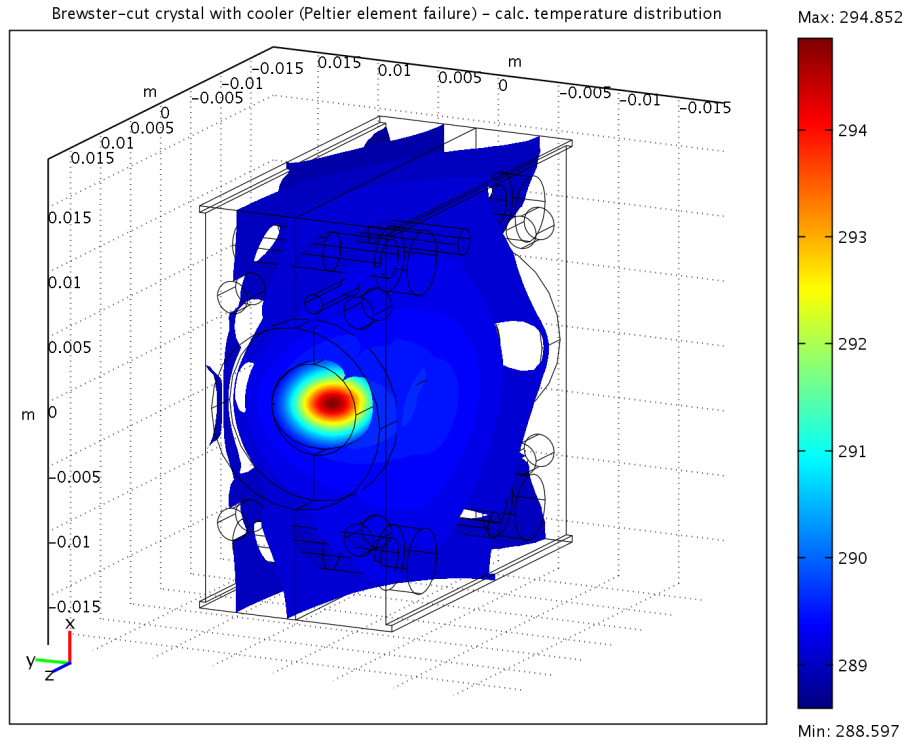
(a) 3d-view.
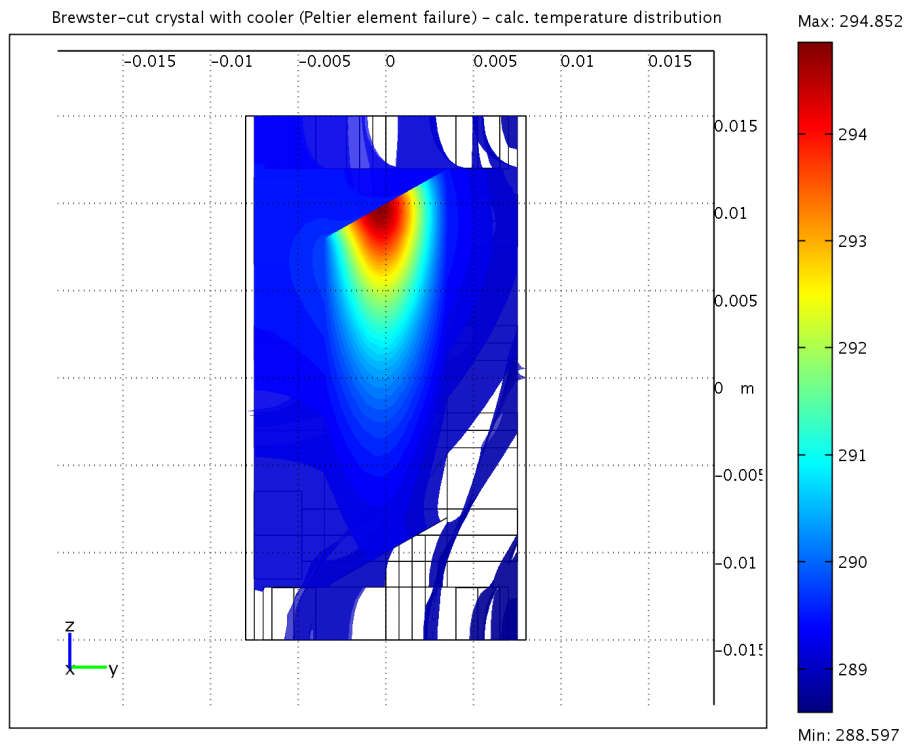
(b) View from top.

Figure 4.56: Brewster-cut TISA crystal with cooler: simulated Peltier element failure at cooler. Single-side (end-)pumped. Calculated temperature distribution (isosurfaces). Single-side pump power: 25 W.

Incorporation of measured beam profile

By incorporation of a real, measured pump-beam profile, the optical path difference and the resulting thermal lensing can be estimated and modeled for the corresponding situation of a TISA crystal pumped with any pump laser. As an example, the recorded beam profile of a frequency-doubled Nd:YAG laser with a CCD-camera (Pulnix, model TM-6EX) is shown in Fig. 4.57 at an average, (single-side) pump-power level of $\approx$14 W.

A reduction in resolution to 1/8th is necessary due to the limited amount of available computer memory (8 GB (GB: GigaByte))[12]. The beam profile is normalized, and the resulting heat equation is also adjusted to account for a non-mirrored pump-beam profile case. This means, that in the case of a double-side pumping configuration, the beam profile is mirrored in x-direction compared to the other pumping direction[13]. The modified heat source equation $Q(x, y, z)$ with a normalized pump-beam profile $p(x, y, z)$ reads then

$$Q(x, y, z) = \eta_h \, P_0 \, p(x, y, z) \frac{\alpha}{1 - \exp(-\alpha \, L)} \tag{59}$$
$$\left[p(x, y, z) \exp\left(-\alpha \left(z + \frac{L}{2}\right)\right) + p(-x, y, z) \exp\left(\alpha \left(z - \frac{L}{2}\right)\right) \right],$$
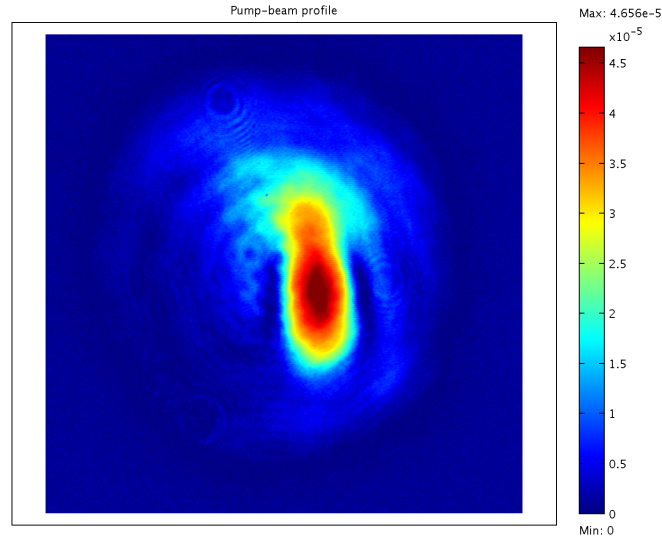
Figure 4.57: Normalized pump-beam profile of frequency-doubled Nd:YAG laser. Single-side pump power: $\approx$14 W. Resolution: 512x480 pixel.

---

[12] The constraint is to choose the number of mesh elements that high that it fits into available computer memory. Allocation of swap-space on a harddisk results in dramatic performance decrease, as the access-time is increased by a factor of at least $1 \cdot 10^6$ compared to a complete calculation in computer memory. Another general solution to memory problems is to take advantage of symmetry of the modeling geometry, and therefore to replace the modeling subdomain with only a part of the original subdomain which represents the full geometry. Additionally, an adjustment of the boundary conditions may also be necessary (insulation boundary condition).

[13] Inside this simulation, the orientation of x-, and y-directions are swapped.

with the same variables as in Ch. 4.2.4.

The beam profile is incorporated into the model by use of a structured (brigg) mesh. For this, the plane-parallel TISA crystal is divided into two (three[14]) subdomains. Outside the structured mesh for the beam profile, an unstructured mesh is used. The different mesh types are connected with a boundary identity condition. Figure 4.58 shows the resulting meshed crystal, and Fig. 4.59 shows the resulting heat-source Q with units W/m^3 at the crystal surface for a single-side pump power of 14 W.

Along the crystal length, the absorption of pump radiation is given by a total of 6 absorption zones[15]. The resulting calculated temperature profile is shown in Fig. 4.60, 4.61 for the crystal end-face and the whole crystal, respectively.

A calculation using a Brewster-cut crystal is not that straightforward due to the geometric situation. A possible solution is to take a high-resolution unstructured-meshed Brewster-cut crystal and incorporate a (sheared) beam profile.

The modeling with an incorporated pump-beam profile is stopped and the calculation of a thermal lens is not performed, as the gradients between the different meshes are too strong[16]. A further (adaptive) mesh refinement to decrease the gradients can not be performed due to the limitation in available computer memory.

However, these simulations are very powerful to assess the impact of distorted pump-beam profiles on thermal lensing and aberrations. Obviously, it is not too critical to operate pump lasers with poor beam profiles in order to achieve a smooth temperature distribution in the crystal (advantage of laser over OPO).

---

[14]The center domain is splitted into two domains for $\pm z$-directions.

[15]A higher resolution was not possible due to the given memory constraints, and a higher priority was set to the resolution of the beam profile. An ultimate model would take advantage of a full camera resolution, with $\approx$1000 absorption zones resulting in $\approx$246 million points (elements), which is by far too much for a calculation on a workstation level at present.

[16]Simulation is calculated with adaptive mesh refinement (AMR, Appendix B).
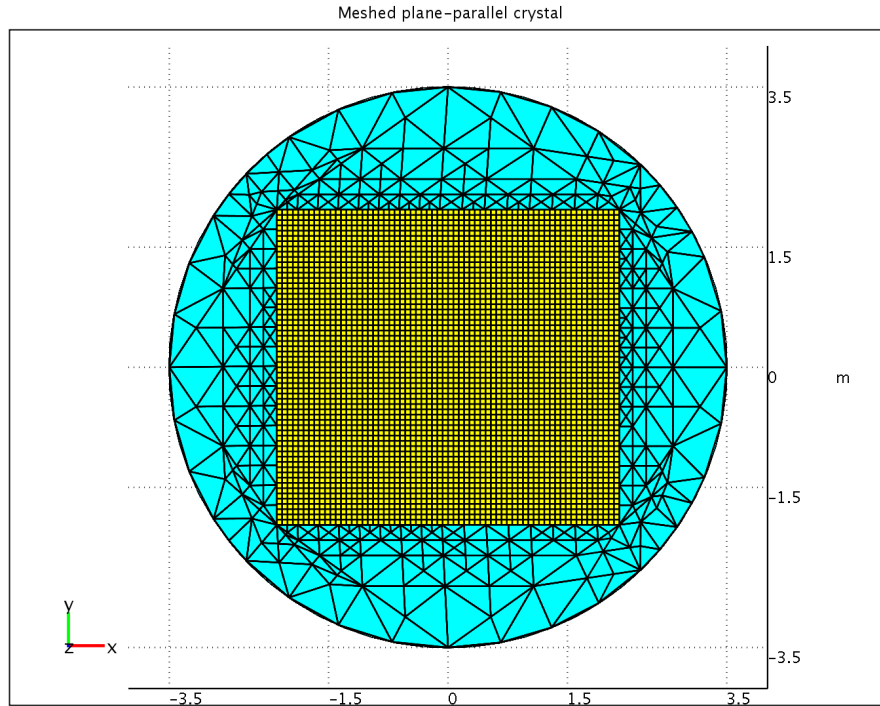
(a) End-face.
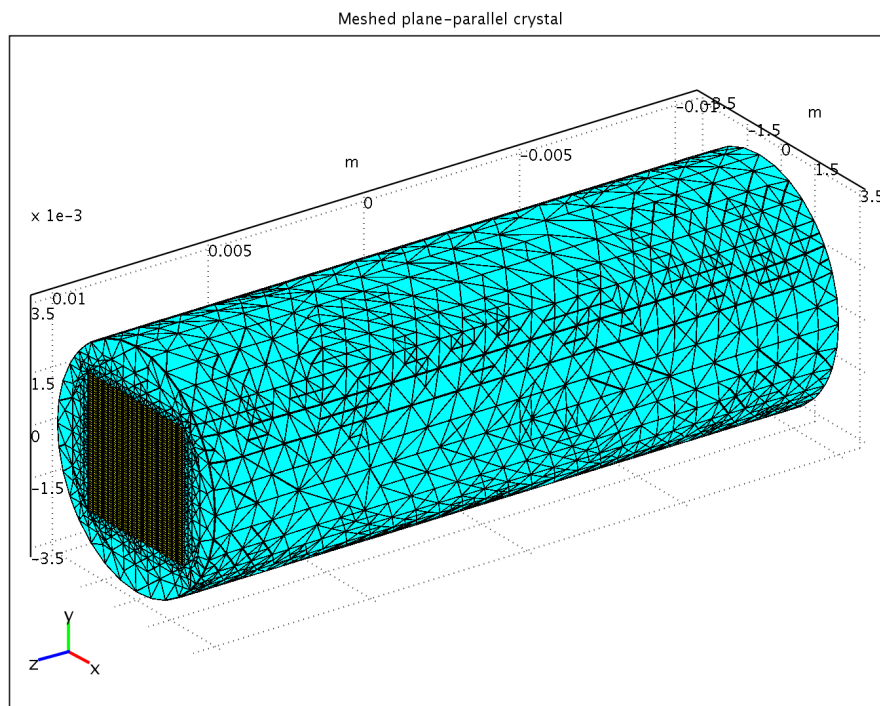
(b) Complete geometry.

Figure 4.58: Meshed plane-parallel crystal (146589 elements) - end-face and complete geometry.
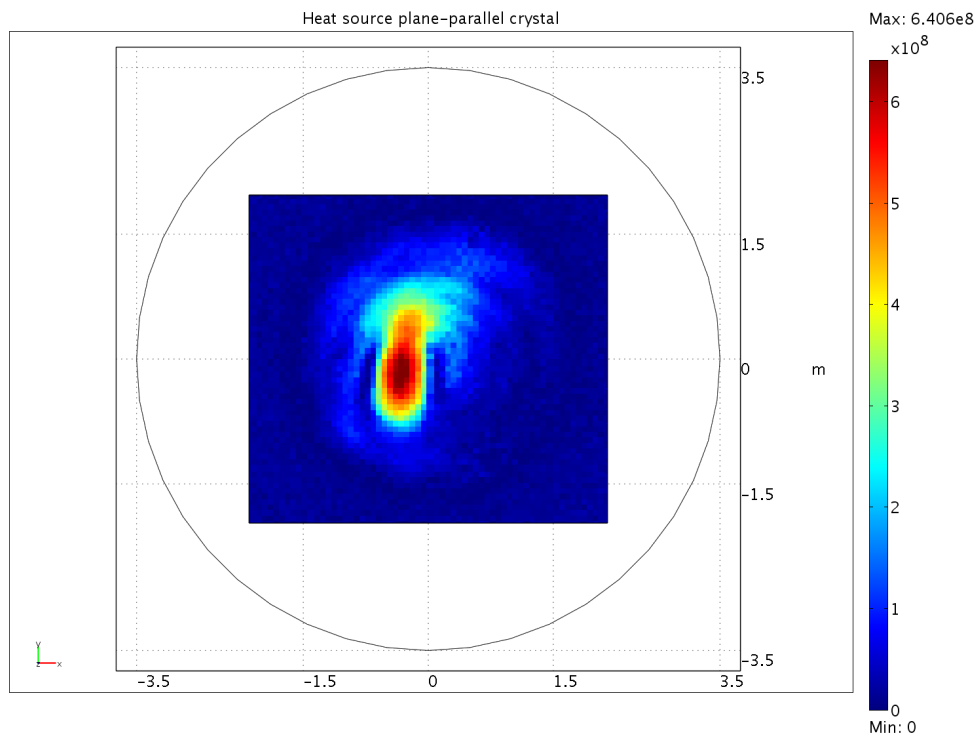
(a) End-face.
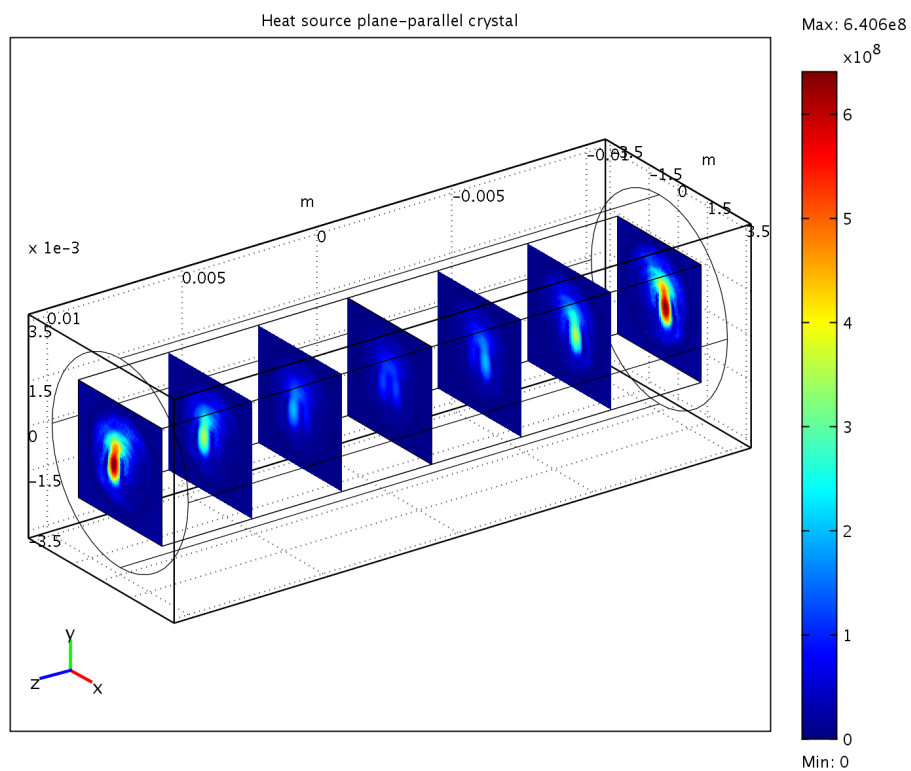
(b) Slices along crystal length.

Figure 4.59: Heat source plane-parallel crystal - end-face and slices along crystal length.
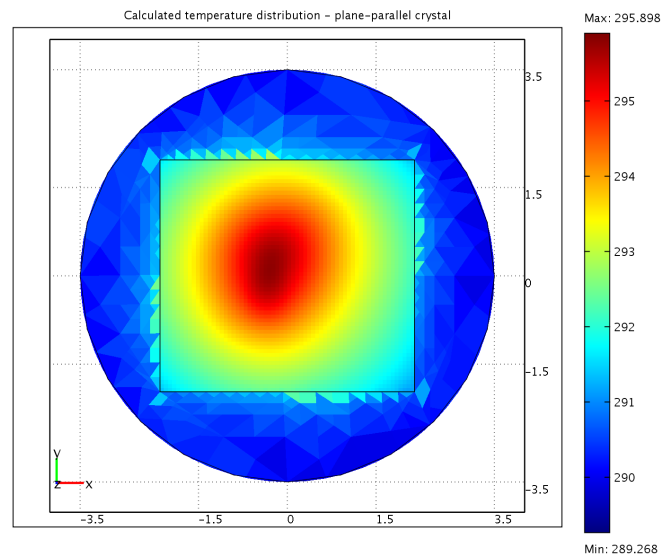
Figure 4.60: Calculated temperature distribution of plane-parallel crystal - end-face with flat shading.
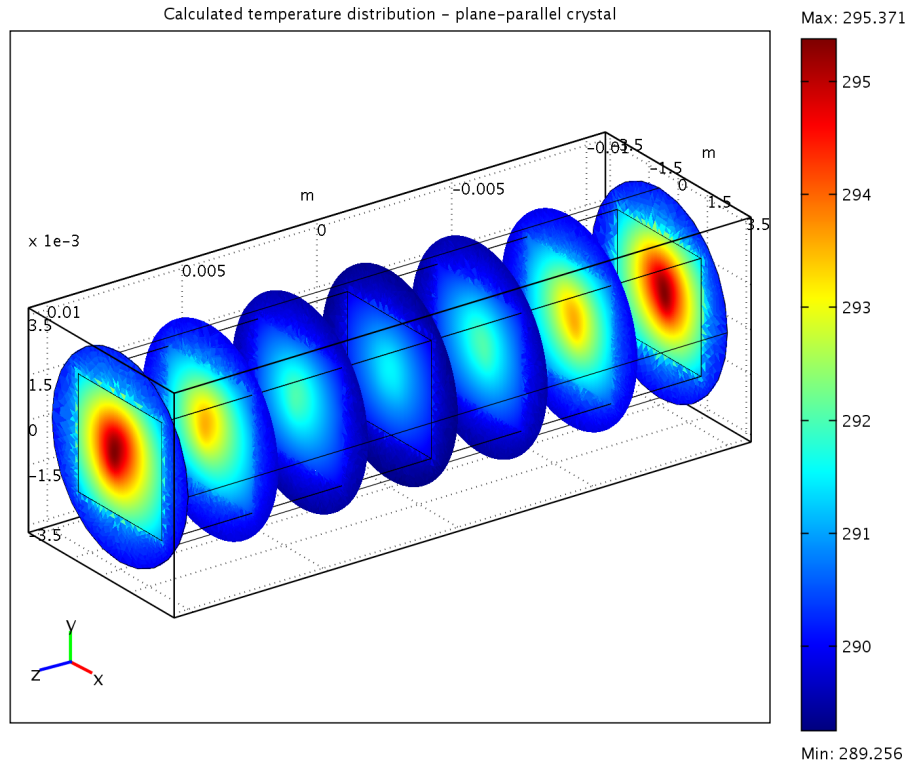
(a) Slices along crystal length.
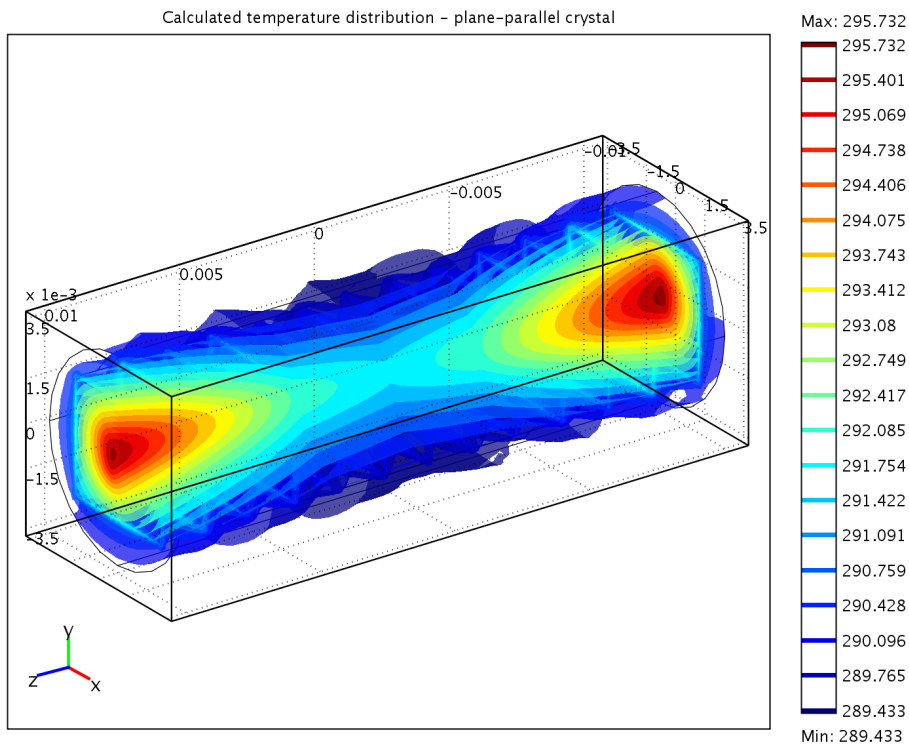
(b) Isosurfaces.

Figure 4.61: Calculated temperature distribution of plane-parallel crystal - slices along crystal length and isosurfaces.

Brewster-cut crystal - cooling with liquid nitrogen

Cooling down the crystal to the temperature of liquid nitrogen N_2 (77.35 K) is a common method to study the spectroscopy of crystals, e.g. the temperature dependence of the fluorescence lifetime. Concerning TISA, there are publications available [Schulz91, Zavelani-Rossi00], indicating that N_2-cooling can significantly improve the TISA performance and thermal lensing. Within the thermal simulation, a Brewster-cut crystal is cooled down to the temperature of liquid nitrogen. The boundary condition in contact with the cooler is set to a value of T=77.35 K, according to Eq. 55. The heat transfer between boundary and crystal is assumed to be infinite.

Figures 4.62a, 4.62b, and Figs. 4.62c, 4.62d show the resulting temperature distributions of the Brewster-cut crystal when the pump laser is turned off and on, respectively. The maximum temperature is at the crystal surface due to the heat transfer of the environment.

(a) Pump off (slice).

(b) Pump off (isosurface).

(c) Pump on (slice).

(d) Pump on (isosurface).
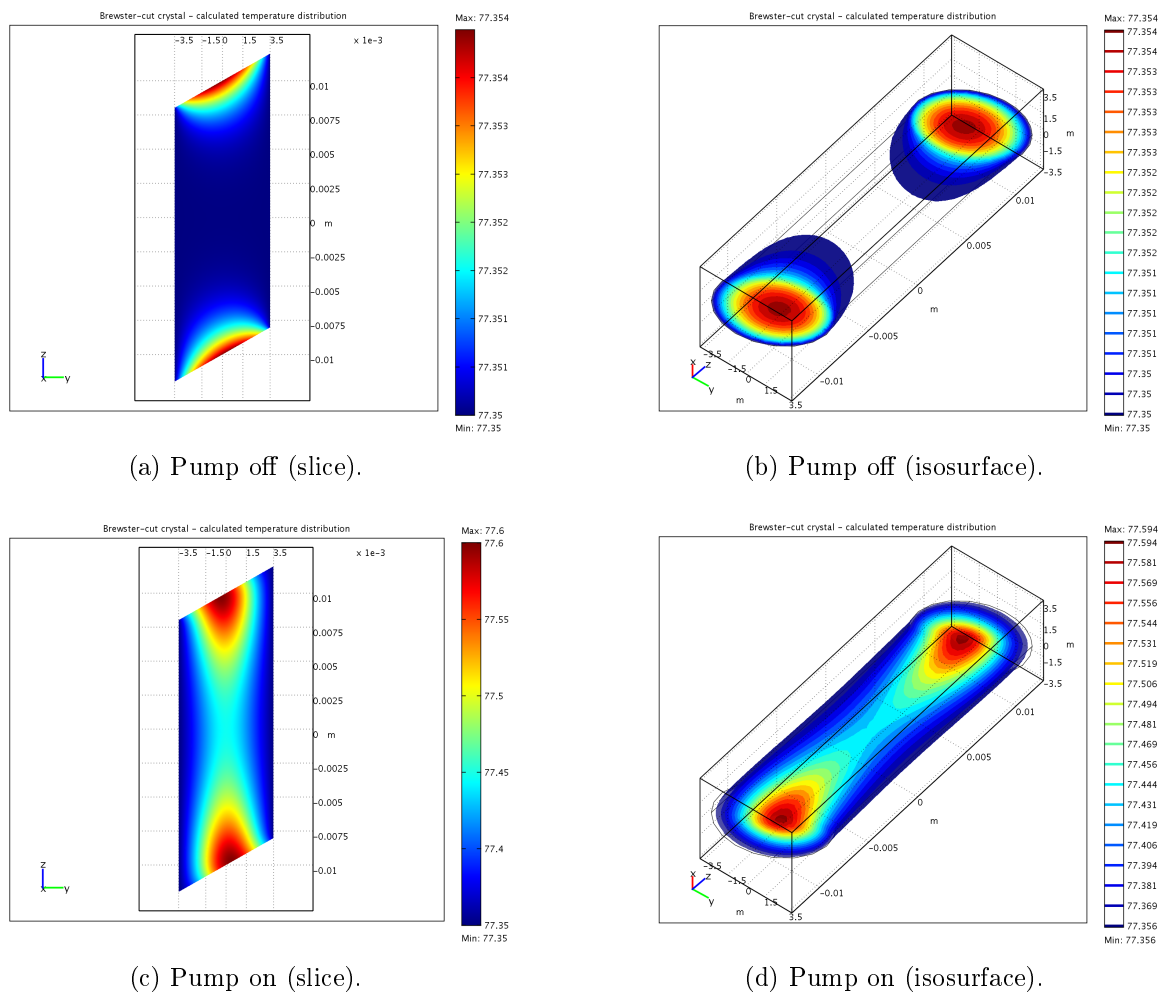
Figure 4.62: Brewster-cut TISA crystal: cooling with liquid nitrogen with pump laser turned off and on - slice and isosurface plot. Single-side pump power: 25 W.

When the the pump laser is turned on, the resulting temperature distribution shows the known tightening effect towards the crystal center (see $\boxed{\textbf{T8}}$ on page 53), with a maximum temperature of 77.602 K. This means that the maximum temperature is only by a quarter of a Kelvin higher than the cooler temperature, and therefore negligible thermal lensing can be expected at this pump level.

4.2.6 Thermal modeling analysis - calculation of thermal lensing

The calculated temperature and stress-strain fields are used to calculate the optical path difference (OPD) for a single pass through the crystal. The OPD can be expressed by [Cousins92, Pfistner94]

$$
\begin{aligned}
OPD(x,y) \;\; = \;\; & \frac{\partial n}{\partial T} \int_0^L T(x,y)\,dz \; + \; (n_0 - 1) \int_0^L \epsilon_z(x,y)\,dz \quad\quad\quad (60) \\
& + \int_0^L \sum_{i,j=1}^3 \frac{\partial n}{\partial \epsilon_{ij}} \epsilon_{ij}(x,y)\,dz \, .
\end{aligned}
$$

Equation 60 consists of three terms which contribute to the OPD. The first term represents the change of the refractive index due to the temperature change. The second term accounts to the deformation of the crystal end-caps, resulting in an overall length change of the crystal. The third term contributes to the OPD by taking account of the photoelastic effect [Nye57], where the index ellipsoid of the crystal is varied due to the stresses and strains caused by the temperature variation.

In Eq. 60, $\partial n/\partial T$ is the change of refractive index due to temperature change, L is the crystal length, $T(x,y)$ is the calculated temperature field at slice dz, and n_0 is the refractive index of sapphire. $\epsilon_z(x,y)$ is the change of length in z-direction at slice dz, $\partial n/\partial \epsilon_{ij}$ are the elasto-optical coefficients, and $\epsilon_{ij}(x,y)$ are the corresponding stress-strain components. For the change of the refractive index of sapphire with temperature, a (constant) value of $\partial n/\partial T$=13·10^{-6} K^{-1} is used, and for the thermal expansion coefficient α associated with the change of crystal length, a value of α=6·10^{-6} K^{-1} is applied for the model postprocessing.

For the thermal analysis, the first two terms in Eq. 60 are considered, as the photoelastic effect of TISA [Eilers92] and its overall contribution to the OPD is negligible, as it is for instance for Nd:YAG laser crystals [Pfistner94][17]. The availability and the errors of the photo-elastic coefficients of TISA are arguments to stop further investigation of this effect on a modeling basis.

To obtain the OPD, the calculated temperature field is extracted from the FEA calculation using a meshed grid, and the first two terms of Eq. 60 are determined. The resulting OPD

---

[17]Depolarization (loss) in Nd:YAG lasers due to the photoelastic effect [Ostermeyer06] is not considered here.

is used to calculate an averaged thermal lens for the sagittal and tangential plane using the expression for the OPD of an equivalent (concave) mirror [Frauchiger92] for each plane, representing the crystal under thermal load, given by [Pfistner94]

$$
\begin{aligned}
OPD_{\mathrm{mirror}}(r) &= OPD_0 - \frac{r^2}{R} \\
&= OPD_0 - \frac{r^2}{2f} \,,
\end{aligned}
\tag{61}
$$

where r is the radius from the center of the mirror, R the radius of curvature, and f the focal length of the (concave) mirror[18].

A parabolic interpolation over the radius of the pump beam (r in x-,y-direction) of the total OPD profile was calculated for sagittal and tangential plane to obtain the averaged focal length in sagittal f_x and tangential plane f_y, respectively[19]. The radius of approximation is the same for both directions, as the difference in the temperature profile is negligible for both directions at the pump power levels considered. Furthermore, the laser mode radius for both directions will be in the order of the pump beam radius ω_p shortly outside the crystal. Alternatively, the approximation radius r for the tangential plane can be chosen to be $n\,r$ (n: refractive index of TISA). The calculated thermal lens values for different pump powers at 935 nm and 820 nm are presented in Fig. 4.63. The resulting focal lengths show overall lower values for the focal length in sagittal plane ($f_{th,s}$) compared to tangential plane ($f_{th,t}$).

A transformation of the Brewster-crystal propagation matrix is necessary to obtain the final values for the thermal lens in sagittal and tangential planes. This transformation leads to a description of the propagation between the two principal planes. The resulting matrix is the same as the matrix of a thin lens.

The ABCD-beam propagation matrix of a Brewster-cut crystal [Huang96] under thermal load reads in sagittal plane

$$
M_s = \begin{pmatrix} 1 - \frac{l}{2nf_{th,s}} & \frac{l}{n} - \frac{l^2}{4n^2 f_{th,s}} \\ -\frac{1}{f_{th,s}} & 1 - \frac{l}{2nf_{th,s}} \end{pmatrix} ,
\tag{62}
$$

and in tangential plane

$$
M_t = \begin{pmatrix} 1 - \frac{l}{2nf_{th,t}} & \frac{l}{n^3} - \frac{l^2}{4n^4 f_{th,t}} \\ -\frac{n^2}{f_{th,t}} & 1 - \frac{l}{2nf_{th,t}} \end{pmatrix} .
\tag{63}
$$

---

[18]Note: by use of Eq. 61, aberrations are not taken into account.

[19]Another method for the calculation of the focal length of the thermal lens was given in [Wagner05], where a parabolic interpolation was done for each slice in sagittal and tangential plane, and corresponding ABCD-beam-propagation matrix was set up to calculate a focal length of the thermal lens in each plane.
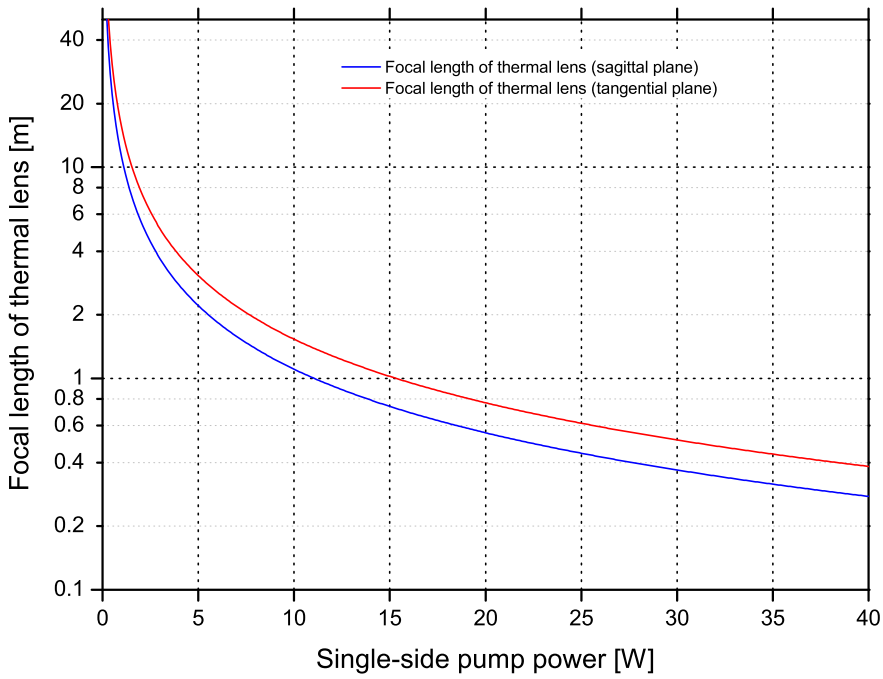
(a) 935 nm.
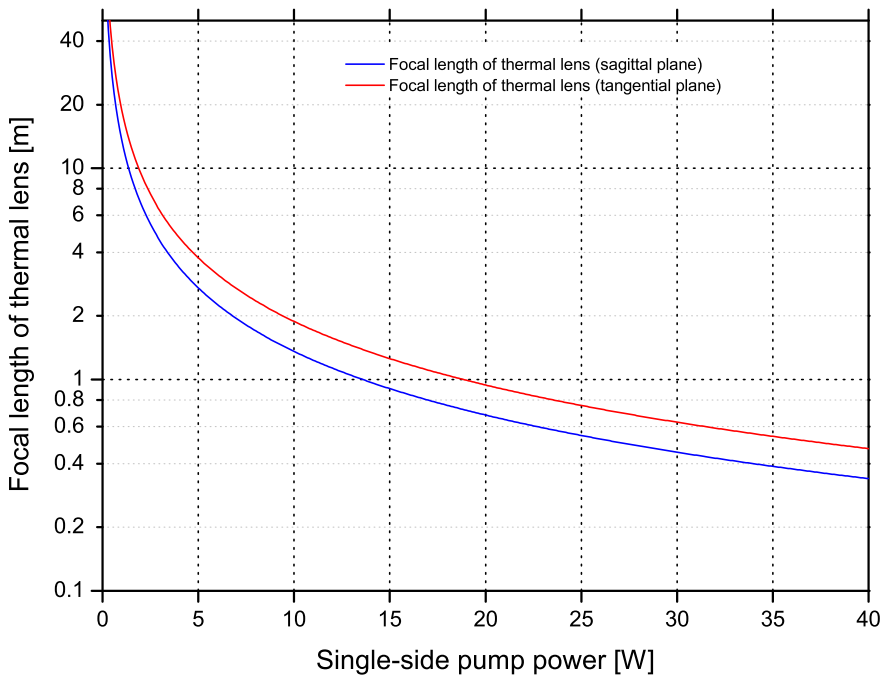
(b) 820 nm.

Figure 4.63: Calculated thermal lens (TL) for Brewster-cut TISA crystal at 935/820 nm. Calculated using a constant HTC of 15000 W/m^2·K and a $1/e^2$-pump-beam radius of 0.75 mm.

In Eq. 62, 63, l is the crystal length, and n is the refractive index of the crystal. $f_{th,\{s,t\}}$ are the focal focal lengths in sagittal and tangential plane, respectively.

The matrices of Eqs. 62, 63 are converted to describe the operation between the two principal planes. For a matrix

$$
M \;=\; \begin{pmatrix} A & B \\ C & D \end{pmatrix} \tag{64}
$$

the transformation M_T reads [Gerrard94b]:

$$
M_T \;=\; \begin{pmatrix} 1 & \frac{1-A}{C} \\ 0 & 1 \end{pmatrix} \begin{pmatrix} A & B \\ C & D \end{pmatrix} \begin{pmatrix} 1 & \frac{1-D}{C} \\ 0 & 1 \end{pmatrix} \tag{65}
$$

$$
\;=\; \begin{pmatrix} 1 & 0 \\ C & 1 \end{pmatrix}. \tag{66}
$$

Equation 66 is the matrix of a thin lens with focal length $-C^{-1}$.

The transformation of Eqs. 62, 63 yields in sagittal plane

$$
M_{T,s} \;=\; \begin{pmatrix} 1 & 0 \\ -\frac{1}{f_{th,s}} & 1 \end{pmatrix}, \tag{67}
$$

and tangential plane

$$
M_{T,t} \;=\; \begin{pmatrix} 1 & 0 \\ -\frac{n^2}{f_{th,t}} & 1 \end{pmatrix}. \tag{68}
$$

The resulting focal lengths $f_{T,th,\{s,t\}}$ are shown in Fig. 4.64. Selected values for the resulting overall focal length in sagittal and tangential plane are presented in Tab. D.1 of Appendix D, page 197. Tables D.2 and D.3 show the focal lengths for a $1/e^2$-pump-beam radius of 0.9 mm and 1.05 mm, respectively. The pump power is given as the sum of both sides. A comparison with the model of [Innocenzi90] is added to all figures. [Innocenzi90] give an expression for the focal length f of an end-pumped solid-state lasers with

$$
f \;=\; \frac{\pi\, K_c\, \omega_p^2}{P_{ph}\,(dn/dT)} \left(\frac{1}{1 - \exp\left(-\alpha\, l\right)} \right), \tag{69}
$$

where K_c is the thermal conductivity of the laser material, P_{ph} is the fraction of pump power that results in heating, dn/dT is the change of the refractive index of sapphire with temperature, and ω_p is the $1/e^2$-pump-beam radius. α is the absorption coefficient of the crystal, and l is the crystal length (2 cm). The model assumes single-side pumping. For the comparison with the FEA calculated focal lengths of the thermal lens, P_{ph} is set to $P_{ph}=2\,P\,\eta_h$

(see Eq. 43), where P is the single-side pump power for the case of dual-side pumping. As an
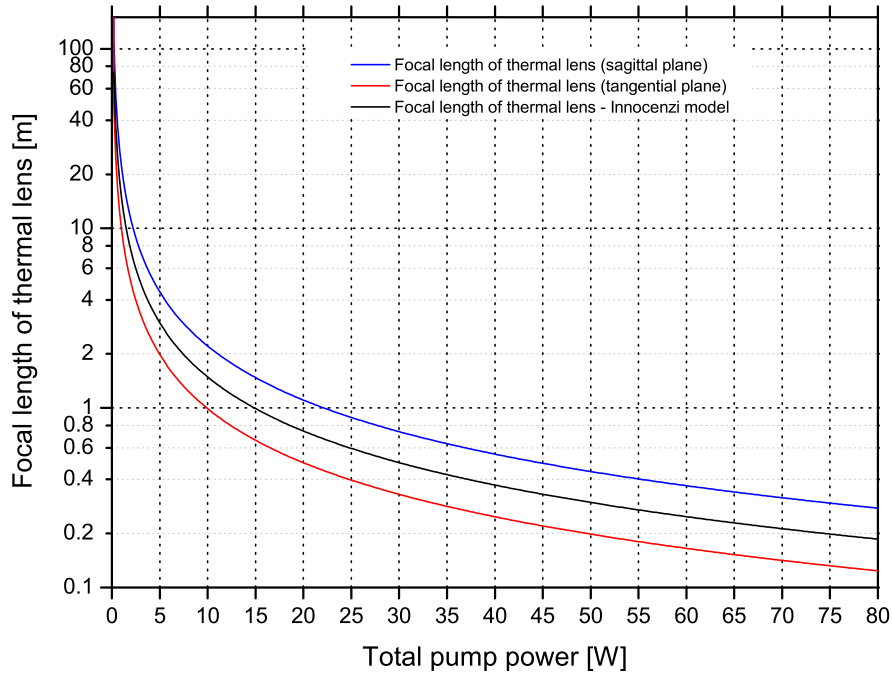
(a) 935 nm.
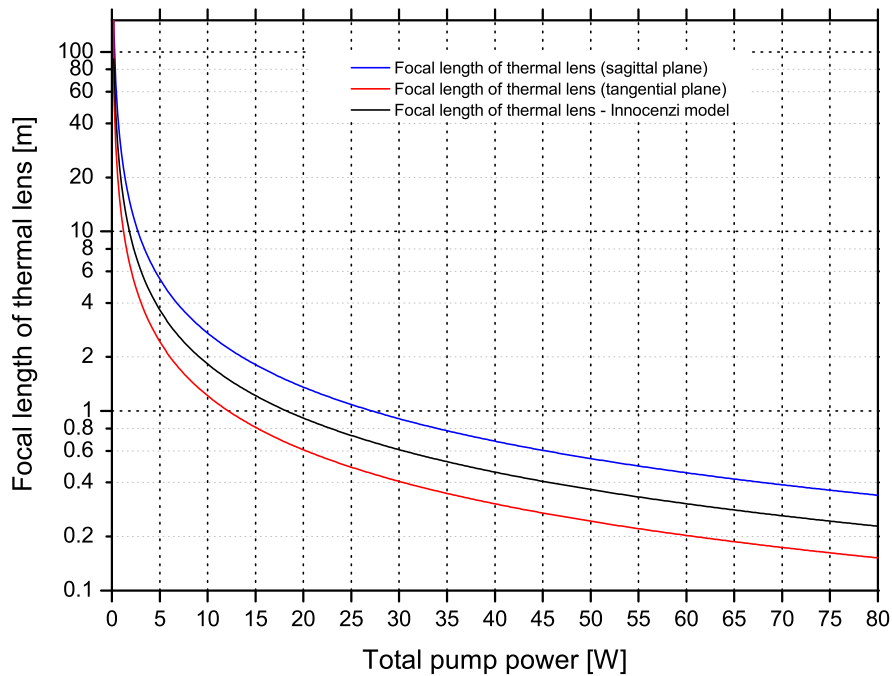
(b) 820 nm.

Figure 4.64: Calculated thermal lens (TL) for Brewster-cut TISA crystal at 935/820 nm after principal planes transformation. Comparison with model of [Innocenzi90]

example, the resulting calculated OPD profile for a dual-side pumped (DSP) Brewster-cut TISA crystal with cooler simulation (BRC) $\boxed{\textbf{T12}}$ is shown in a 3D-view and contour view in Fig. 4.65a, and Fig. 4.65b, respectively. The astigmatism (tangential plane: $(y\text{-}z)$-plane, sagittal plane: $(x\text{-}z)$-plane) is clearly visible. The resulting OPD profiles of the simulation with the Peltier-element failure $\boxed{\textbf{T13}}$ is shown in Fig. 4.66. The overall OPD for this case is higher, which means stronger thermal lensing, and the OPD profile is even more asymmetric in y-direction and shifted towards the side with the Peltier element failure. Most likely, this results in increased astigmatism, laser power loss, or even complete stop of laser operation or optical damage due to the change in beam propagation.

Figures 4.67-4.68 show the calculated OPD-profiles of a single-side pumped (SSP) Brewster-cut crystal with cooler (BRC). The OPD profile is almost symmetric for this case. For the simulated Peltier-element failure, the OPD profile is almost not deformed compared to dual-side pumped (DSP) case. This can be explained, as the Peltier-element situated in negative y-direction is out of operation, and as the temperature profile is shifted in the positive z-direction towards the negative y-direction.

Figure 4.64 shows, that the Innocenzi model can only give a coarse estimation of the thermal lens. The developed FEA model and post-processing methods developed within this work give a more detailed view of the expected thermal lensing.

The parabolic approximation of the temperature profile and therefore the refractive index profile bases on least squares analysis [Wagner05][20]. This analysis is done for each slice along the crystal length (z-direction) and for x-,y-directions independently. Using ABCD-matrix formalism, the resulting focal length of the thermal lens and the beam progation in sagittal and tangential planes is calculated. The approximation radius is chosen as the $1/e^2$-radius of the pump-beam profile, where a Gaussian beam profile is assumed. This radius is chosen based on the expected mode radius of the laser. Nevertheless, the optimum approximation radius can be calculated as follows. The least squares approximation of

$$A\,\vec{x} \;=\; \vec{b} \tag{70}$$

is given by (in MATLAB notation)

$$\vec{x} \;=\; A \setminus \vec{b}, \tag{71}$$

where A is the coefficient matrix, $\vec{b}$ the vector with observations, and $\vec{x}$ the solution vector (determined by the Moore-Penrose pseudoinverse). If $\vec{x}_1$ is a solution, then the residual $\vec{r}$ is

---

[20]Expansion and stress-strain contributions to the thermal lensing are neglected in this analysis.

given by

$$\vec{r} = A\,\vec{x}_1 - \vec{b}. \tag{72}$$

However, the relative residual $\|\vec{r}\|/\|\vec{b}\|$[21] is not a measure for the quality of the approximation. If A is a quadratic and regular matrix, then the approximation quality can be estimated by the following relation

$$\frac{\|\vec{x} - \vec{x}_1\|}{\|\vec{x}\|} \;\leq\; \text{cond}(A)\,\frac{\|\vec{r}\|}{\|\vec{b}\|}\,, \tag{73}$$

where cond(A) is the (spectral) condition number of the matrix. Therefore, the best approximation is found for a small matrix condition number together with a small relative residual. For the non-quadratic case, the same criteria is used to estimate the approximation quality. The approximation to the resulting temperature profile and therefore the refractive index profile for different approximation radii is depicted in Figs. 4.69a, 4.69b for the case of a plane-parallel TISA crystal pumped with 25 W single-side pump power and a $1/e^2$-beam radius of 1.5 mm at crystal surface and center, respectively. As can be seen, the approximation works best for a radius of 0.42 mm (surface) and 0.22 mm (center). This optimum radius is calculated by use of Eq. 73, and the plots showing the matrix condition number times the relative radius versus the approximation radius are given in Figs. 4.70a and 4.70b. At minimum, the best approximation radius is found. Moreover, the best approximation radius is different for each slice along the crystal, and therefore a compromise has to be reached for the calculation of the thermal lensing. Although a much bigger approximation radius (1.5 mm) is selected due to the laser mode, the approximation is still appreciable (Figs. 4.69a, 4.69b).

The influence of the effective heat transfer coefficient (HTC) between crystal and cooler is investigated. At a constant single-side pump power of 19 W (η_h=43.1%, 935 nm), which corresponds to the maximum available power of the pump laser at IPM[22], the heat transfer coefficient is varied in the FEA simulation (Fig. 4.71). The focal lengths do not change anymore at a certain level, and therefore the value of the effective heat-transfer coefficient can be used to adjust the model to thermal lens measurements[23] or to determine HTCs. However, the HTC (crystal-cooler) of the present TISA cooler is not expected to affect the model.

It should be noted, that the method of using the OPD has several advantages compared to the first method presented in [Wagner05]. First, the OPD method does not use single

---

[21]$\|.\|$ denotes the L^2 norm.

[22]See [Ostermeyer05a, Ostermeyer05b] for details about the frequency-doubled Nd:YAG pump laser. The system has been further optimized during the last years.

[23]For a discussion of HTCs, see [Incropera02].

slices and a parabolic approximation for each slice. For the case of a Brewster-cut crystal, where the temperature profile is not rotational symmetric around the optical axis, the parabolic approximation of the temperature profile is not appropriate, especially at slices near to the crystal surfaces. Second, the calculation of the OPD is based on summing up all contributions of thermal, expansion and stress-strain contributions using a meshed grid which extracts the calculated temperature field out of the FEA calculation. An analysis can be performed for a single or a combination of each contributions. Moreover, the thermal, expansion, and stress-strain part are separated and the contribution of each part to the total OPD can be estimated.

Overall, the method using the OPD is therefore better suited for 3d-modeling, and the results can later immediately be compared with measurements of a wavefront sensor or with probe lasers [Schiller09]. Nevertheless, if expansion and stress-strain contributions can be neglected, the method in [Wagner05] can be used for the calculation of values for the resulting thermal lensing in a simple astigmatic analysis.
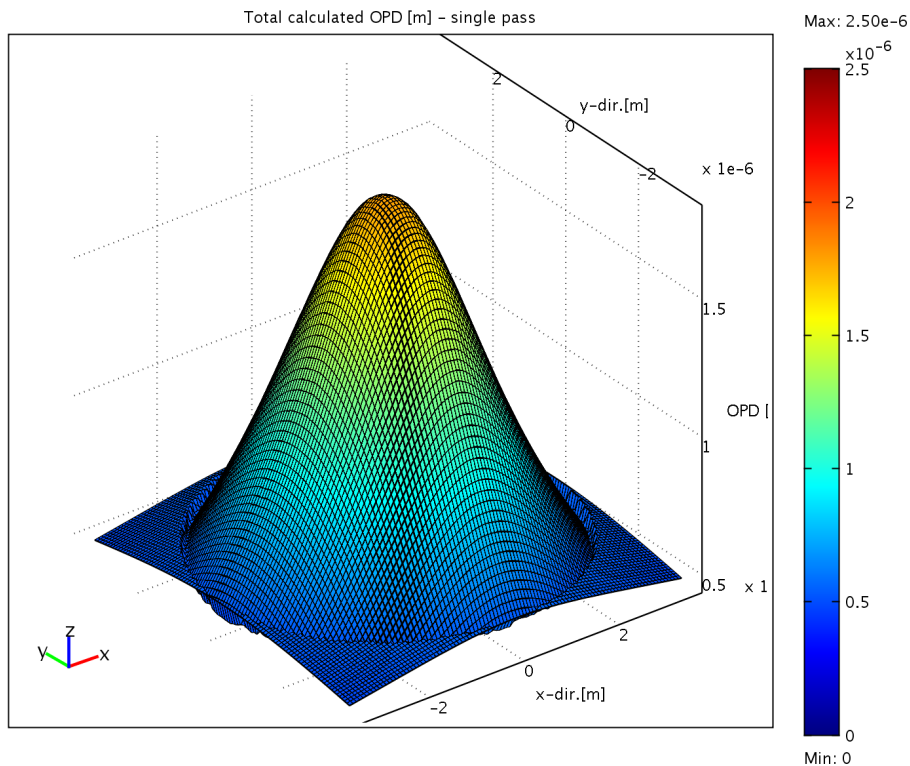
(a) OPD for BRC TISA crystal - 3D view.
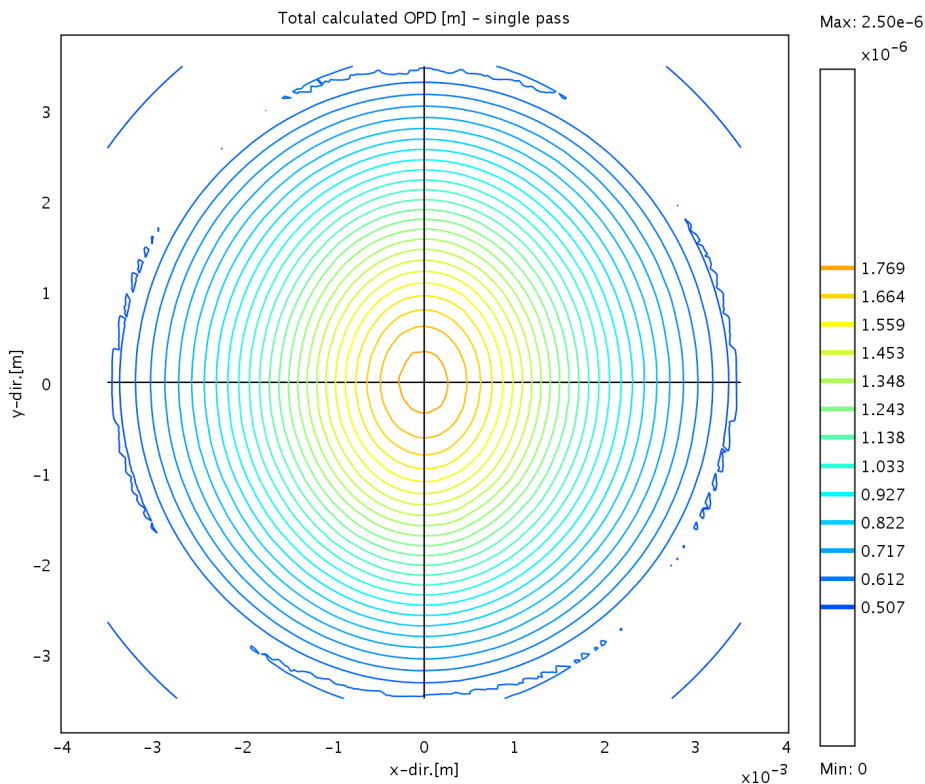
(b) OPD for BRC TISA crystal - contour.

Figure 4.65: Optical path difference (OPD) in m for dual-side pumped (DSP) Brewster-cut
TISA crystal with cooler (BRC) - 3D and contour view.
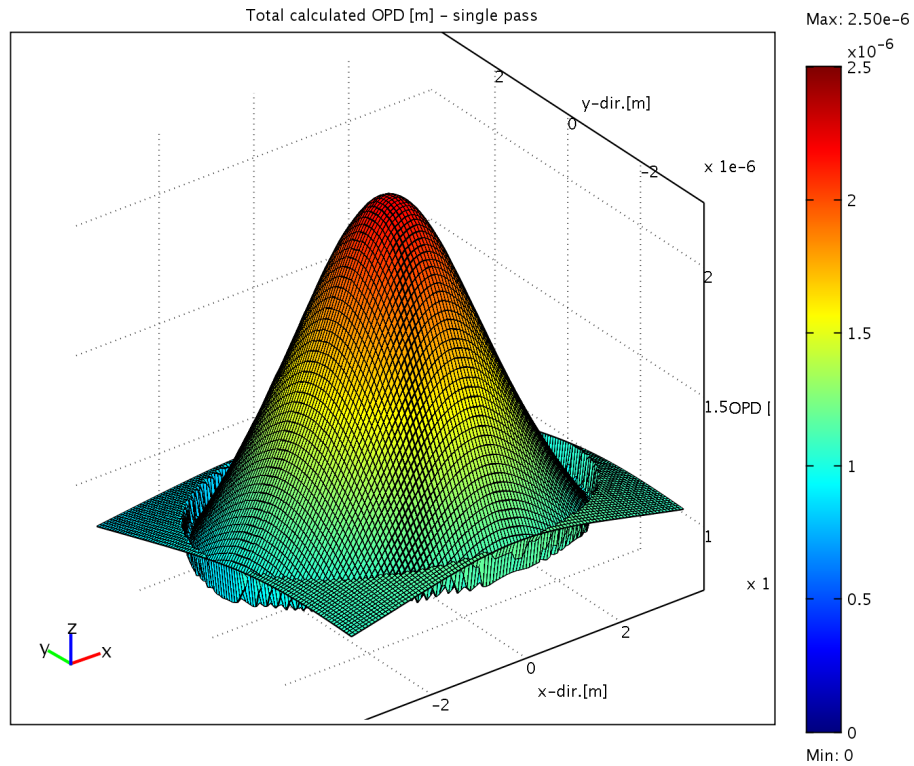
(a) OPD for BRC TISA crystal with Peltier element failure - 3D view.
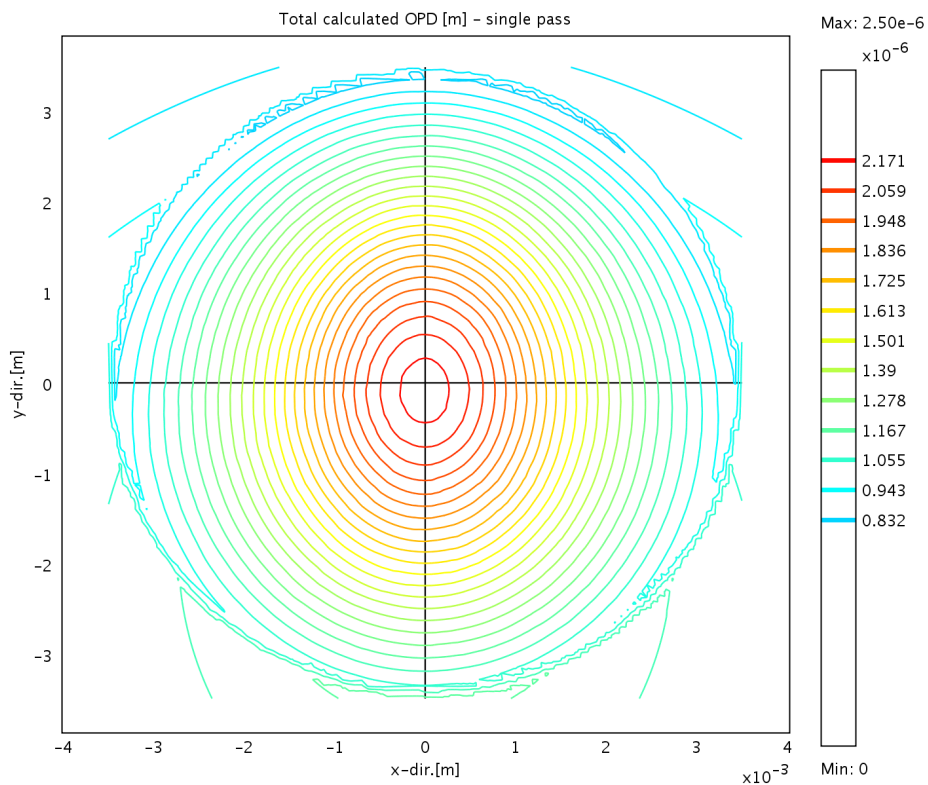
(b) OPD for BRC TISA crystal with Peltier element failure - contour.

Figure 4.66: Optical path difference (OPD) in m for dual-side pumped (DSP) Brewster-cut TISA crystal with cooler (BRC) and Peltier element failure - 3D and contour view.
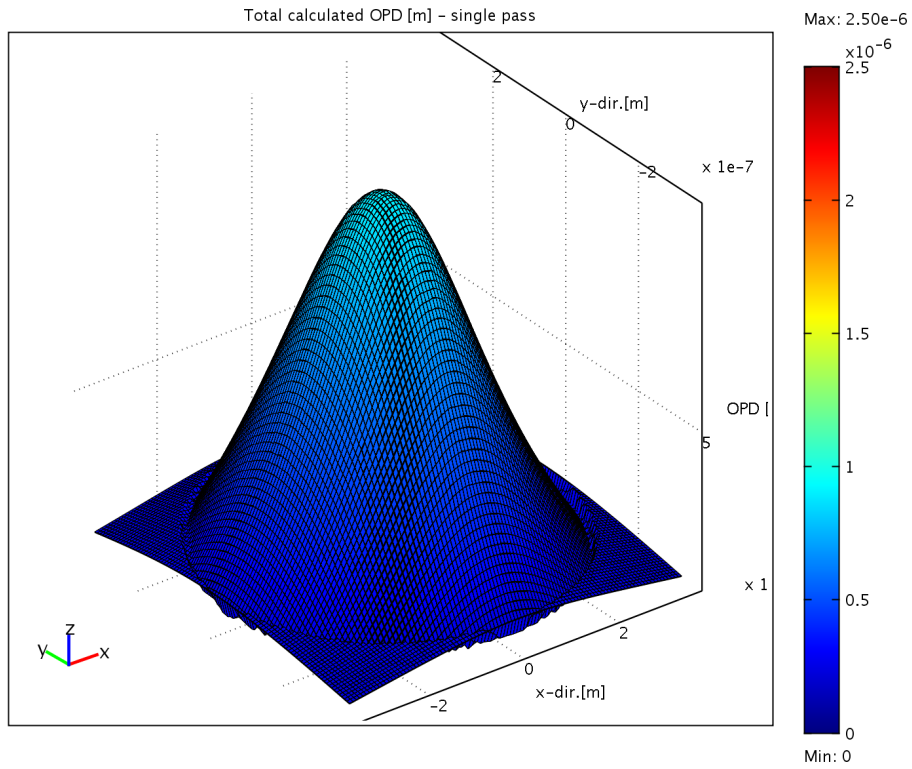
(a) OPD for BRC TISA crystal - 3D view.
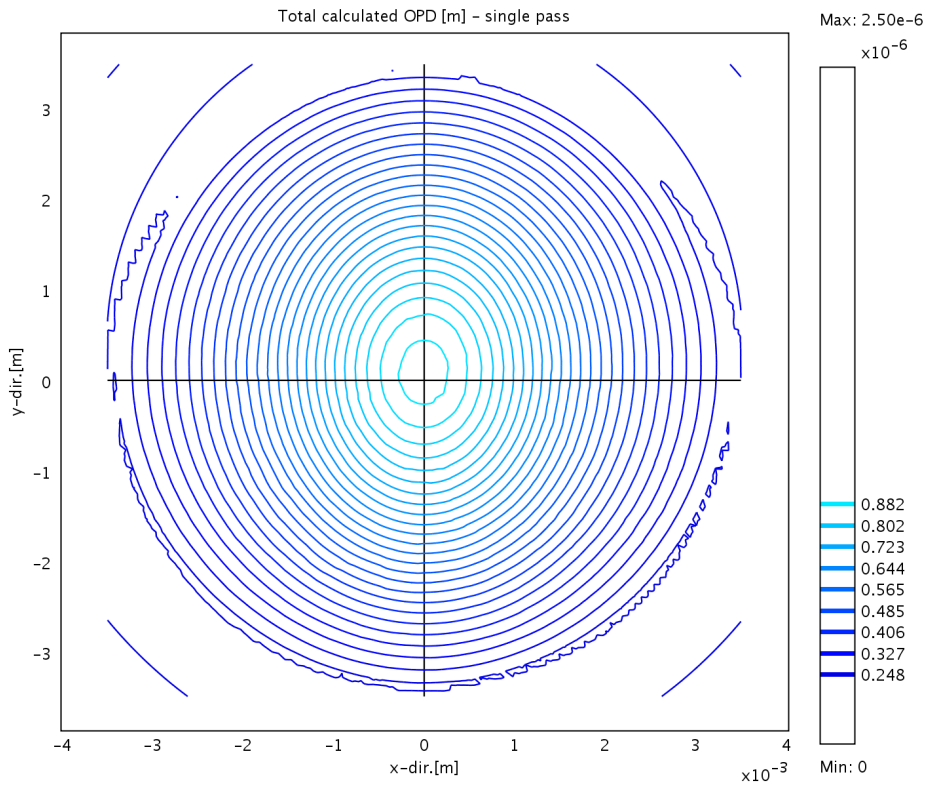
(b) OPD for BRC TISA crystal - contour.

Figure 4.67: Optical path difference (OPD) in m for single-side pumped (SSP) Brewster-cut TISA crystal with cooler (BRC) - 3D and contour view.
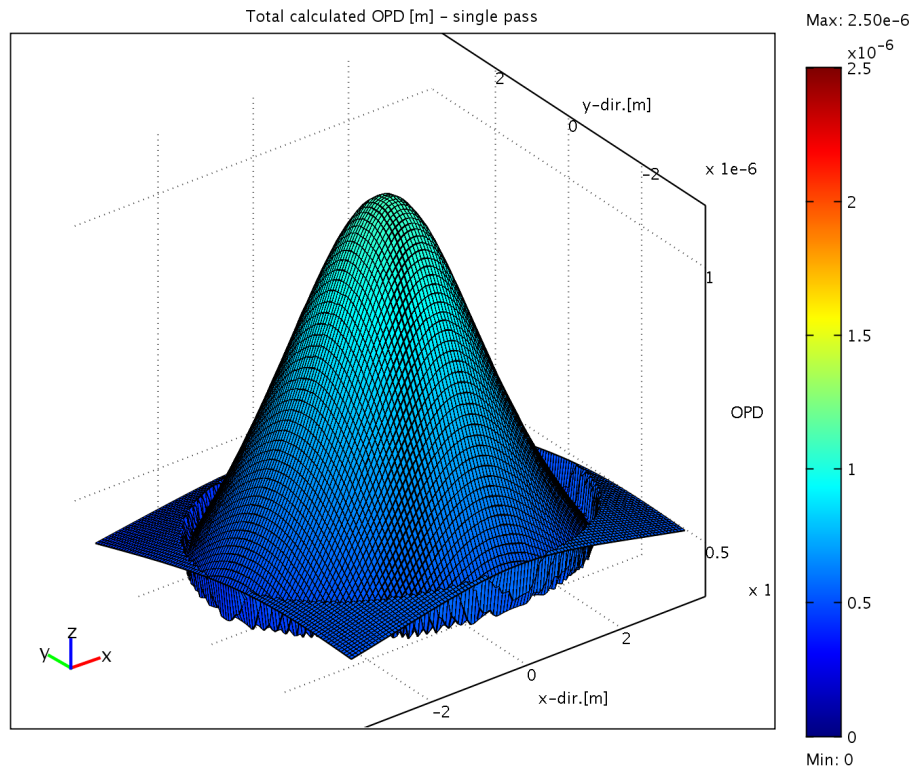
(a) OPD for BRC TISA crystal with Peltier element failure - 3D view.
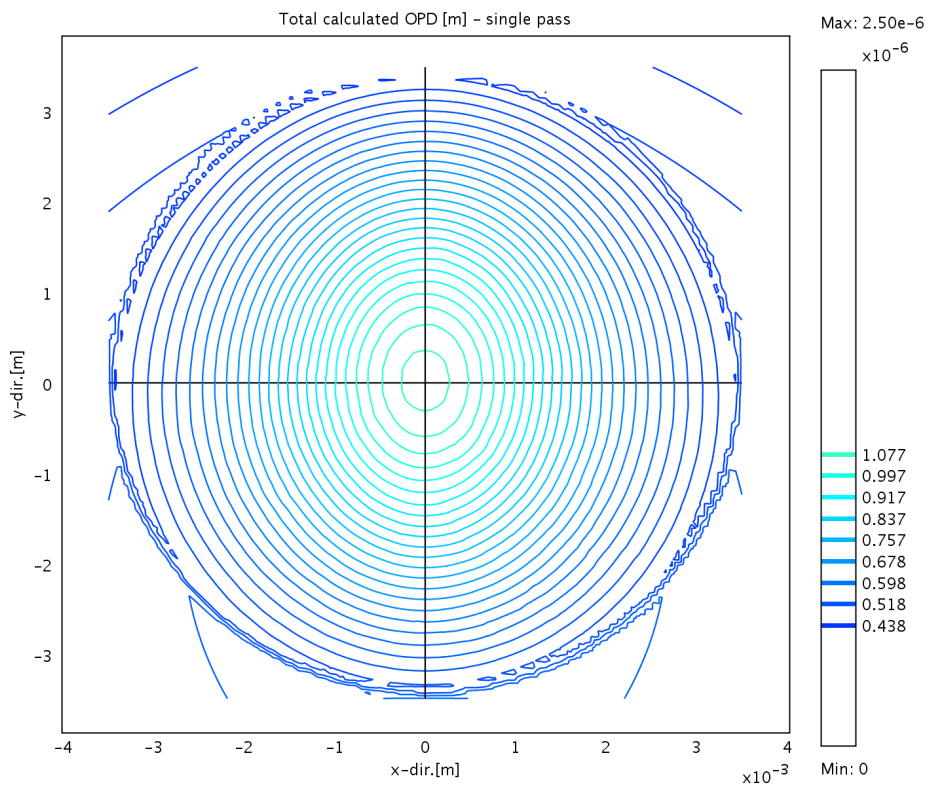
(b) OPD for BRC TISA crystal with Peltier element failure - contour.

Figure 4.68: Optical path difference (OPD) in m for single-side pumped (SSP) Brewster-cut TISA crystal with cooler (BRC) and Peltier element failure - 3D and contour view.

(a) Crystal surface.
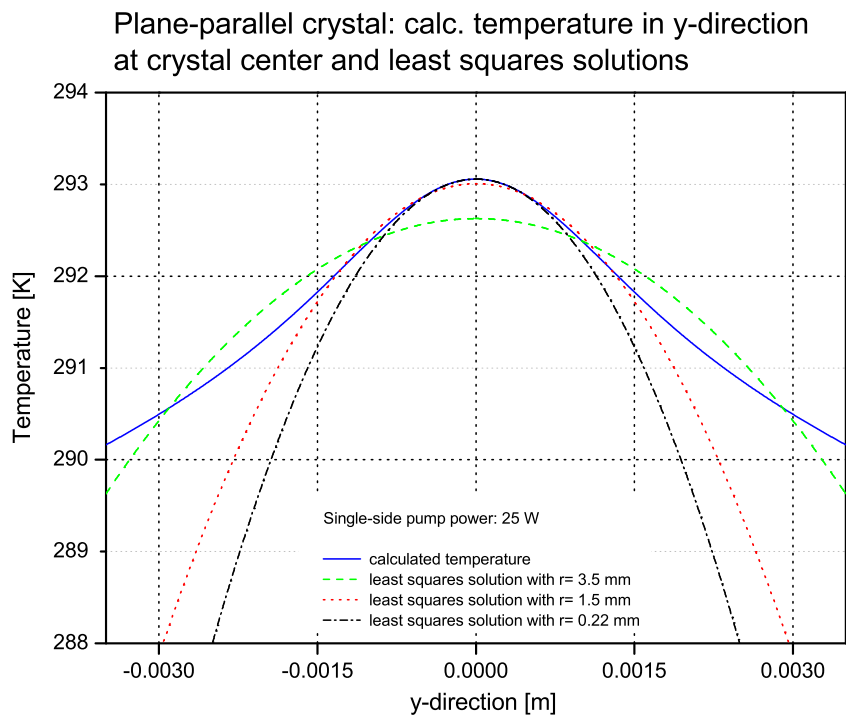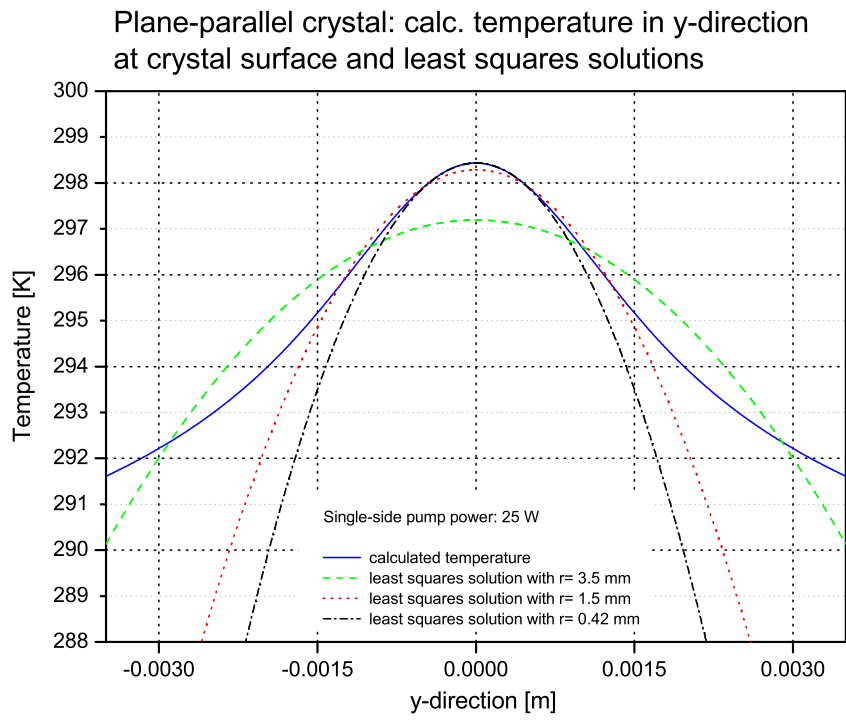
(b) Crystal center.

Figure 4.69: Plane-parallel TISA crystal - least squares approximation of temperature profile for variable approximation radius including optimum least squares radius for parabolic approximation at crystal surface and center.

(a) Crystal surface ($** = 0.00042$ m).

(b) Crystal center ($* = 0.00022$ m).
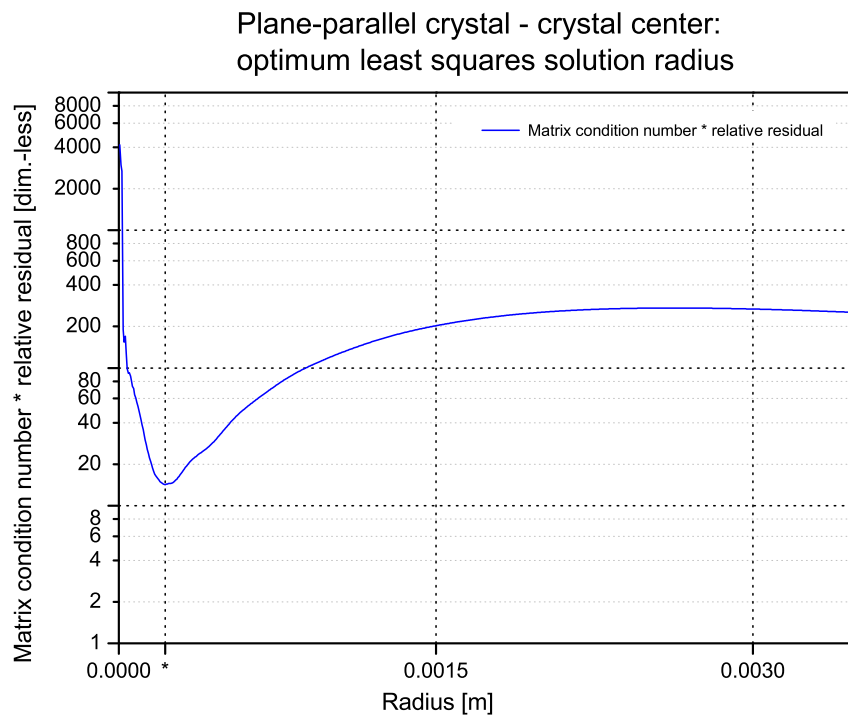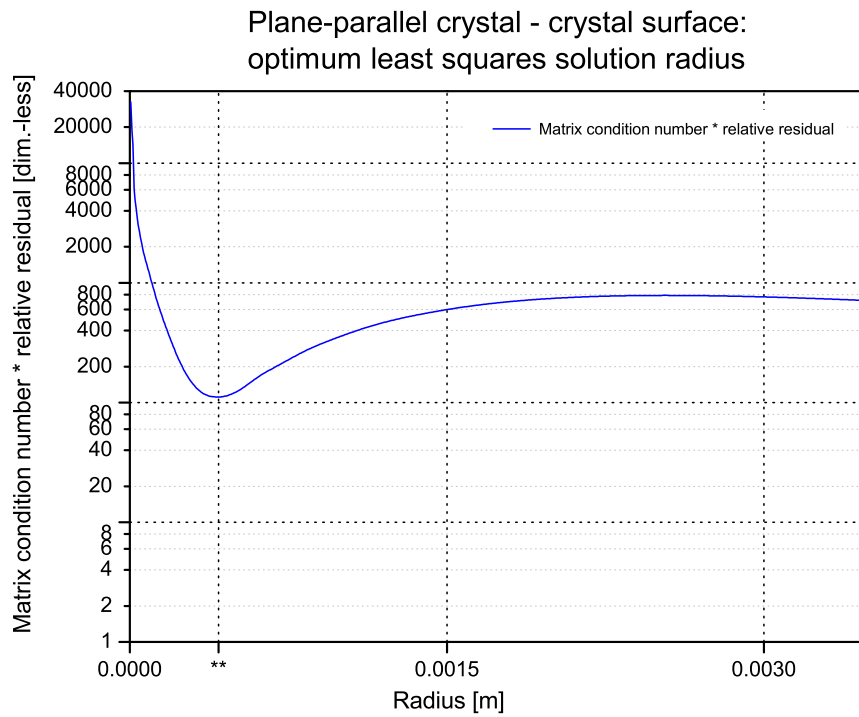
Figure 4.70: Plane-parallel TISA crystal - optimum least squares approximation radius at crystal surface ($**$) and center ($*$). Shown is matrix condition number $\cdot$ relative residual versus least squares approximation radius r.
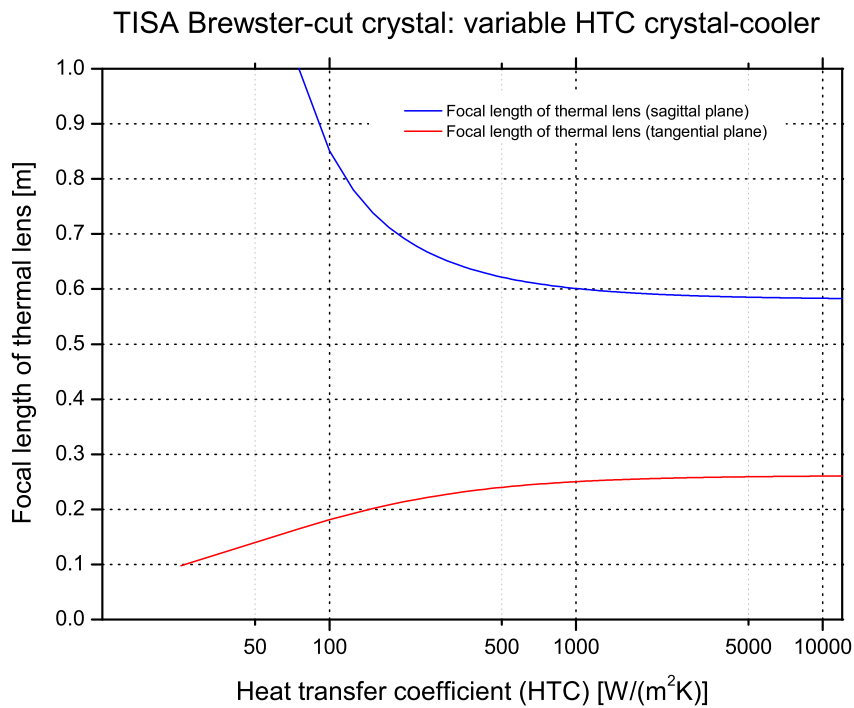
Figure 4.71: Calculated thermal lens for Brewster-cut crystal - constant single-side pump power of 19 W and variable heat transfer coefficient (HTC) crystal-cooler (935 nm, see Fig. 4.64a).

4.2.7 Thermal modeling discussion

A comparison of the FEA calculated focal lengths and measured focal lengths of an experiment[24] is presented in Figs. 4.72-4.73. The thermal lens measurements were performed with a probe laser at 820 nm. The experimental data was added to the plots of the 935 nm and 820 nm FEA model cases. A $1/e^2$-pump-beam radius of $\approx$1.05 mm was used for the measurement.

Figure 4.73b shows, that a smaller $1/e^2$-pump-beam radius of 0.75 mm of the FEA model has to be used for the comparison with the experiment. This can be explained, as the experimental values were determined under non-lasing conditions. The amount of heat deposited in the crystal is therefore higher. The FEA model assumes lasing conditions. The fraction of pump energy dumped as heat is given by Eq. 43. Additionally, the pump-beam shape was not pure Gaussian and symmetric, and therefore a more precise pump-beam radius could not be determined. This can explain the remaining difference in sagittal plane.

The model of [Innocenzi90] provides values, which are in between sagittal and tangential plane values of the FEA model. This also applies for the experimental values.

To sum up, the radius of the pump-beam has a decisive influence on the FEA model results. The pump-beam radius should be determined more precisely in the future. Additionally, the laser stability criteria can be used to determine the thermal lens under lasing conditions. In addition, more experimental results are required for comparison.

A comparison of the model can be made with a wavefront sensor (Shack-Hartmann wavefront sensor) [Ito02]. Unfortunately, a wavefront sensor is not available at IPM. Recently, [Ramanathan06] performed simulations and OPD measurements at a fs-TISA cooled to liquid nitrogen. They have found excellent agreement between FEA simulations and experimental results. This supports the overall FEA simulation strategy, instead of finding suitable approximation formulas [Chénais04a, Chénais04b]. In a previous study, it has been shown that the thermal effects can be controlled and disappear at a certain temperature [Zavelani-Rossi00] when cooling down the TISA crystal (cryogenic cooling).

The calculated temperature profiles can be used to calculate histograms. Figures 4.74-4.75a show the temperature histograms of simulation $\boxed{\textbf{T8}}$. A single histogram is obtained by processing the temperature at about 2.7 million equally spaced points within a 1.5 mm radius of the crystal domain. The bins of the histograms are 0.1 K in width. The temperature histograms are dominated by two peaks at the lowest and highest temperature. The histrograms are broadened with increasing pump-power. Figure 4.75b shows the temperature histograms at a power level of 25 W, with a reduced $1/e^2$-beam radius of 0.75 mm, and an increased absorption coefficient α=3.68 cm^{-1}. The histograms can be used to calculate a weighted mean crystal temperature. The calculated weighted mean temperatures of simulation $\boxed{\textbf{T8}}$

---

[24]Experimental data courtesy of [Schiller09].
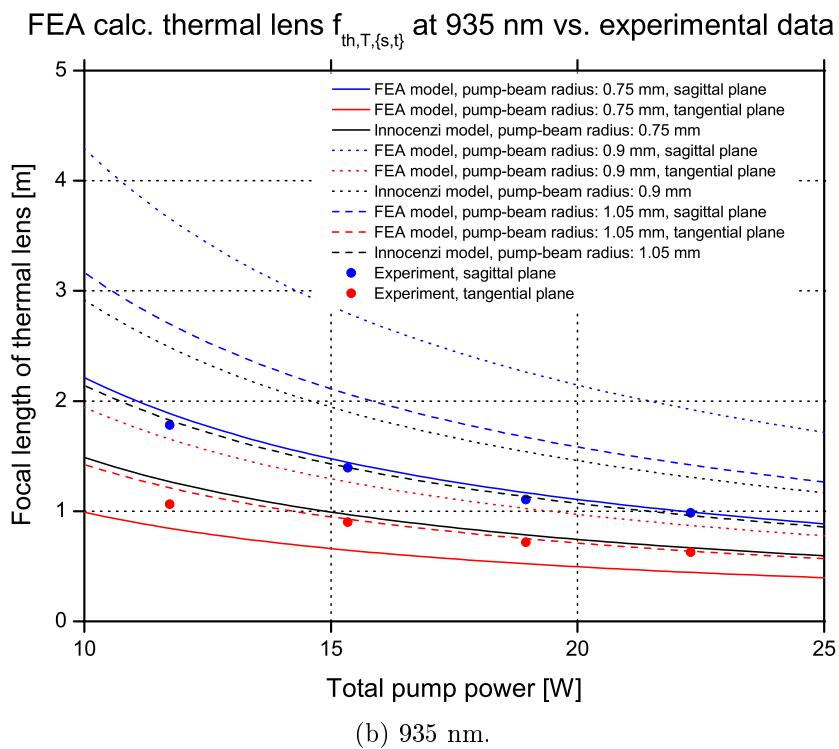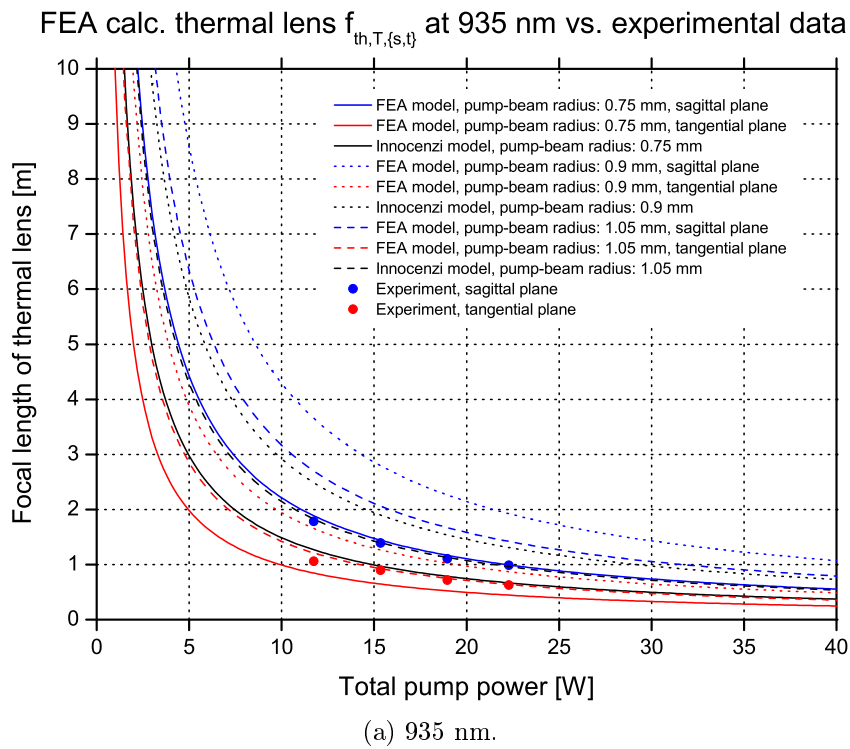
(a) 935 nm.

(b) 935 nm.

Figure 4.72: FEA calculated thermal lens vs. experiment - 935 nm. Note: experimental data of 820 nm case.

are listed in Tab. 4.5. If necessary, they can be incorporated in the performance model of Ch. 4.5, e.g., by an efficiency factor η_T (see Appendix A, page 187), to account for thermal effects inside the crystal.

FEA calc. thermal lens f$_{th,T,\{s,t\}}$ at 820 nm vs. experimental data

(a) 820 nm.

FEA calc. thermal lens f$_{th,T,\{s,t\}}$ at 820 nm vs. experimental data
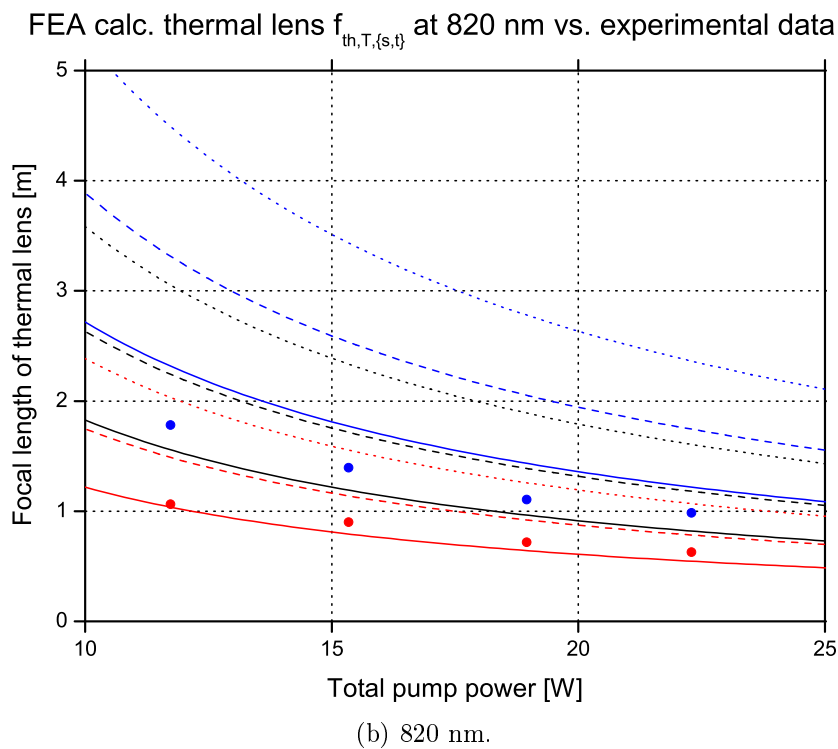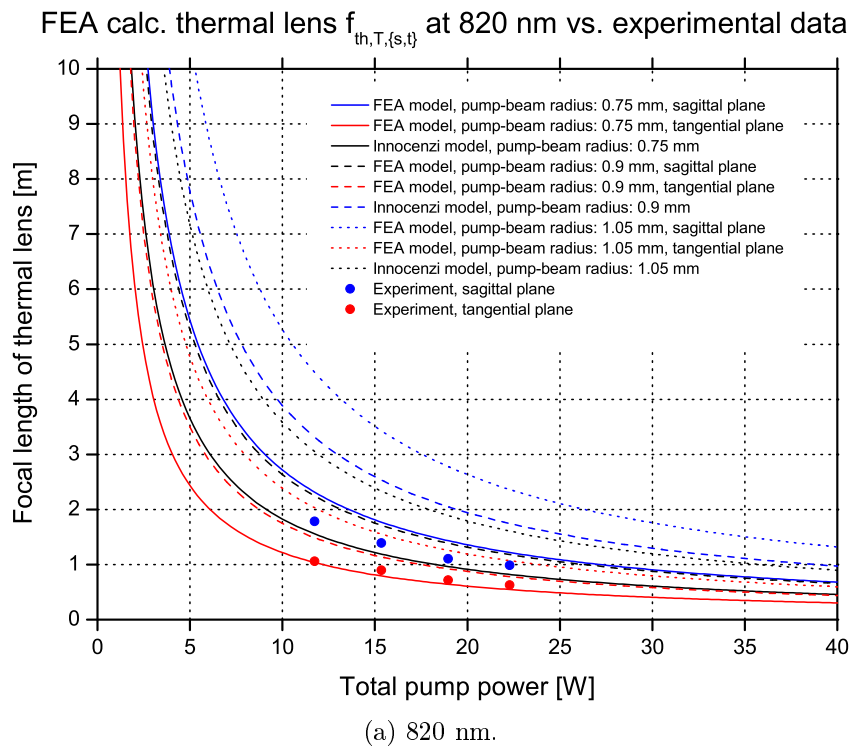
(b) 820 nm.

Figure 4.73: FEA calc. thermal lens vs. experiment - 820 nm.

However, the influence of the thermal load to the TISA laser performance is expected to be negligible. No performance limitation due the TISA crystal itself (fluorescence lifetime, 4-level system) can be expected. This issue is also discussed in the performance modeling

Table 4.5: Calculated weighted mean crystal temperatures of simulation $\boxed{\textbf{T8}}$.

Parameter, unit	Parameter, unit	Comment
Single-side pump power, W	Weight. mean temp., K	
1 W	288.4	
5 W	289.3	
10 W	290.5	
15 W	291.6	
20 W	292.8	
25 W	294.0	
25 W	295.4	Fig. 4.75b (B)
25 W	293.9	Fig. 4.75b (C)

section (Ch. 4.5, page 129) and Ch. 4.1 (page 21). However, the calculated mean temperature can help to estimate the quantum efficiency of other laser materials.

It is recommended to extend the overall thermal simulation strategy, as an adaptation of the parameters inside the FEA simulations to other solid-state laser materials and pump configurations is straightforward. Possible improvements, which still can be performed are:

- increase model resolution to include a higher resolved pump-beam profile

- compare FEA simulations with measurements of a wavefront sensor

- use different cooling temperatures (cryogenic cooler)

- perform efficiency tests of different cooler designs.
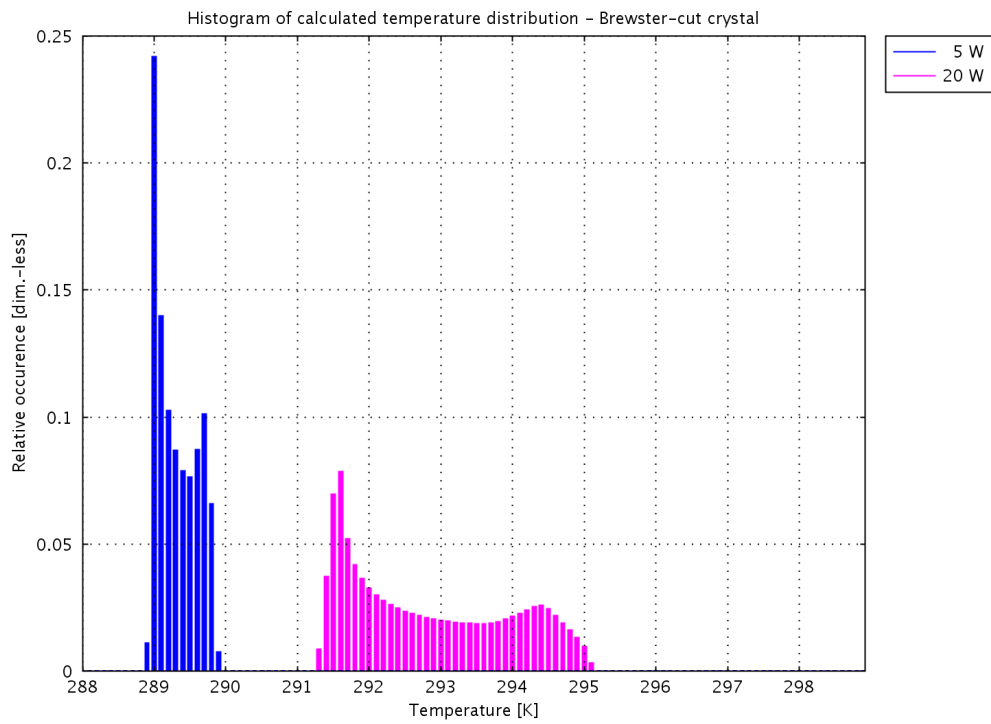
(a) 5 W, 20 W.
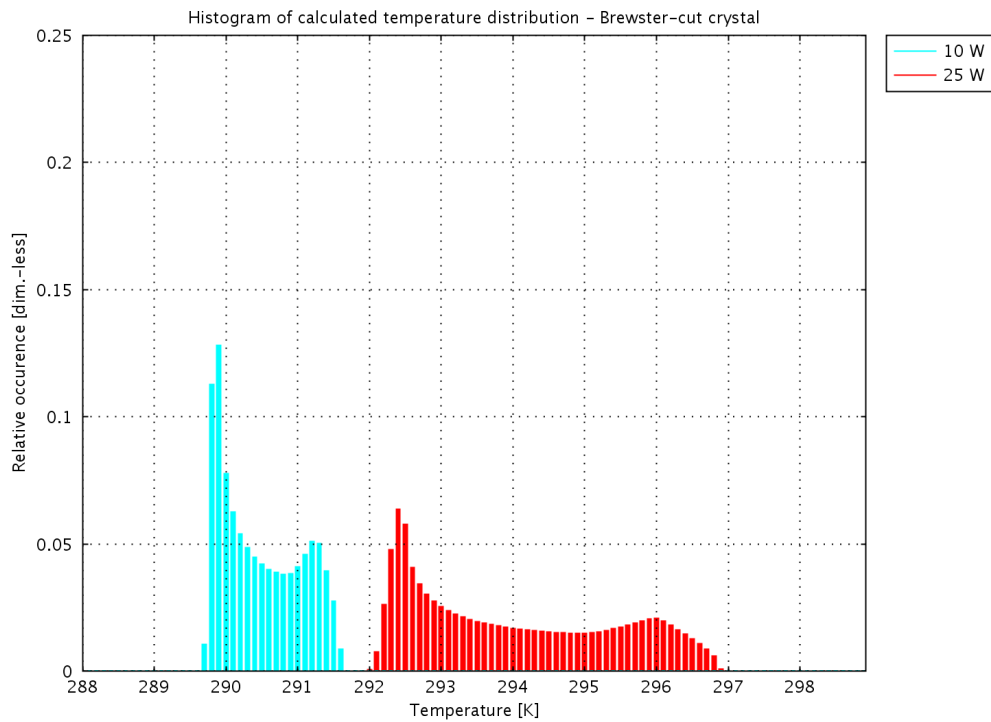
(b) 10 W, 25 W.

Figure 4.74: Histograms of calculated temperature profiles (Brewster-cut TISA crystal) of simulation **T8**. Bin width of histograms: 0.1 K. Single-side pump power: (a): 5 W, 20 W, (b): 10 W, 25 W.
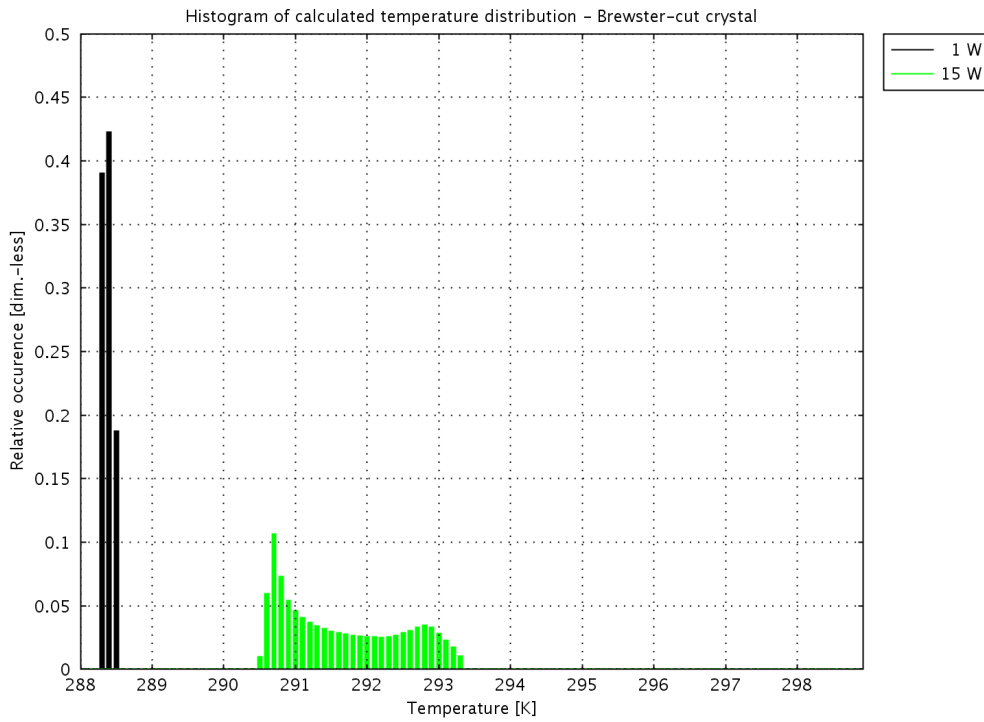
(a) 1 W, 15 W.
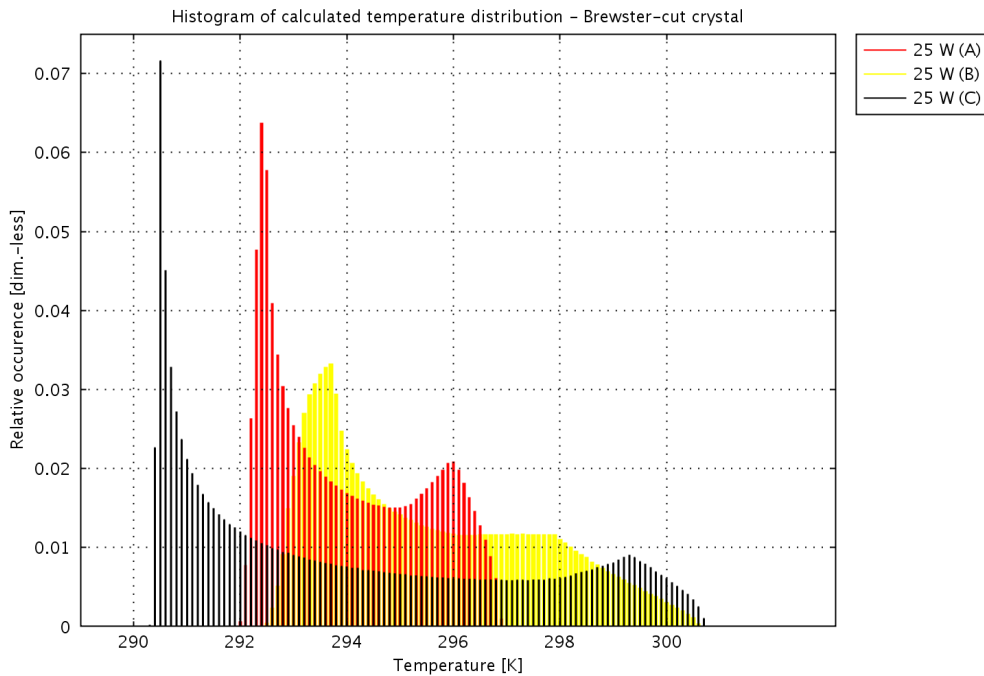
(b) (A): 25 W; (B): same as (A), but with reduced pump-beam radius 0.75 mm; (C): same as (A), but with TISA absorption coefficient α=3.68 cm^{-1}.

Figure 4.75: Same as Fig. 4.74. Single-side pump power: (a) 1 W, 15 W (b) (A) 25 W; (B): same as (A), but with reduced pump-beam radius 0.75 mm; (C): same as (A), but with TISA absorption coefficient α=3.68 cm^{-1}.

4.3 Stable resonator

4.3.1 Introduction

Laser resonators can be divided into two classes: stable and unstable resonators. They are classified through the eigenvalues $\lambda_{1,2}$ of the corresponding 2×2-beam-propagation matrix

$$M \;=\; \begin{pmatrix} A & B \\ C & D \end{pmatrix} \tag{74}$$

of the resonator (ABCD-round-trip matrix of the resonator). A resonator is called stable, if the eigenvalues are complex *and* the absolute value of the real part of the dominant eigenvalue is in the interval $[0,1)$. *All* of the eigenvalues of a stable resonator matrix are *always* complex valued. In fact, the eigenvalues of an unstable resonator matrix *can* be pure real valued. Accordingly, a resonator is called (positive or negative) unstable, if the absolute value of the real part of the dominant eigenvalue is greater than 1. A resonator with eigenvalues of 1 is operating on its stability limit.

If all matrix elements of M are real, the distinction between stable and unstable resonators can be made via the matrix trace $(A+D)$:

$$\begin{aligned} \text{stable resonator:} & -1 < \tfrac{A+D}{2} < 1 \\ \text{positive unstable resonator:} & \quad \tfrac{A+D}{2} > 1 \\ \text{negative unstable resonator:} & \quad \tfrac{A+D}{2} < -1 \,. \end{aligned} \tag{75}$$

As the properties of a stable resonator are extensively discussed in the literature (see e.g. [Hodgson05b]), they will not be repeated here.

In the following, we will briefly present a stable TISA ring resonator design.

4.3.2 Design modeling

The stable resonator laser design modeling procedure is based on the Gaussian beam propagation [Kogelnik65, Kogelnik66] and the concept of the dynamically stable resonator [Lörtscher75, Magni86, Metcalf87, Kortz81]. Additional astigmatism together with compensation and corresponding stability regions for stable resonators have been analyzed in [Wang94]. The properties of the dynamically stable resonator in a DIAL system are discussed in [Wulfmeyer98a]. The design criteria for a dynamically stable resonator are as follows:

 – large stability zone(s)

 – large beam radii, particularly at the crystal

– a low misalignment sensitivity.

4.3.3 Resonator selection

A suitable stable resonator TISA laser design is depicted in Fig. 4.76. The TISA crystal is end-pumped from both sides through dichroic mirrors. The remaining parts of resonator consist of a half-wave plate (L/2) in combination with the Faraday rotator (FR) to ensure unidirectional wave propagation. The birefringent filter (BF) is used for coarse wavelength selection. The resonator is seeded through the output coupler (OC). Additional parts for the active frequency stabilization are not shown in the figure. The cylindrical lens (L) is used to minimize the thermally induced astigmatism of the crystal.
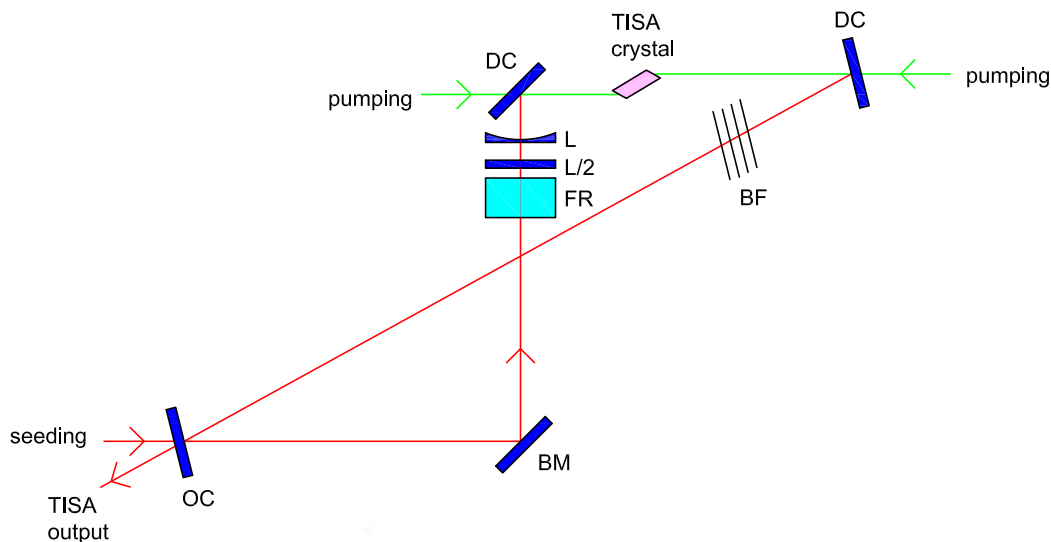
Figure 4.76: Stable resonator (SR) TISA laser set up (DC: Dichroic mirror, BM: bending mirror, FR: Faraday rotator, L: cylindrical lens, L/2: half-wave plate aligned to 45° retardation, BF: birefringent filter).

4.3.4 Beam propagation modeling

For the beam propagation of a stable resonator, usual ABCD-matrix analysis can be applied. The astigmatism introduced by curved mirrors and of the Brewster-cut crystal including thermal lensing can be taken into account in the ABCD matrix formalism [Hanna69, Kogelnik72]. The calculated focal lengths of the thermal lens can also be incorporated into the matrix formalism [Huang96, Georgiev92, Wulfmeyer98a, Magni86]. Due to the (symmetric) ring resonator, the stability zones of a dynamically stable ring resonator merge together resulting in a single zone of doubled width. However, the width of the zone is still dependent on the overall thermal lensing, and therefore the width of the zone decreases with increasing thermal lensing.

The beam propagation inside the resonator is separated into sagittal and tangential planes due to the astigmatism introduced by Brewster-cut crystal and thermal lensing. The corresponding stability zones are the same for both planes. However, additional astigmatic elements, e.g., cylindrical lenses, inside the resonator to adjust the beam propagation lead to separation of the stability zones [Schiller09].

The beam propagation and the stability zone for a stable TISA resonator design at 935 nm, and 820 nm is depicted in Figs. 4.77 and 4.78, respectively. Starting point of the beam propagation is the first principal (crystal) plane. The resonator parameters can be found in the caption of the corresponding figures. The stability zones of Figs. 4.77b and 4.78b indicate, that the current stable resonator design is not suitable for focal lengths of the thermal lens below ≈0.4 m. Here, the resonator is on the stability limit.

A simulation was set up inside the GLAD software package [GLAD, Lawrence92] to further investigate the stable TISA laser at 935 nm and 820 nm. Figures. 4.79 and 4.80 show the Gaussian mode (beam) profiles in intensity as burnpattern, and tangential and sagittal slices at the crystal and the waist for the stable resonator TISA at 935 nm, respectively. Figures 4.81 and 4.82 present the beam profiles at the same positions for the TISA laser at 820 nm.

The beam intensity is given in units of W/cm^2 for a total average (integrated) intracavity circulating power of 1 W. Assuming a TISA pulse length of ≈40 ns and a repetition frequency of the TISA laser of 250 Hz, the resulting peak power densities are as follows. For the TISA laser at 935 nm we can expect a peak power of ≈14 MW/cm^2 at the crystal and ≈38 MW/cm^2 at the waist position. For the TISA at 820 nm, a peak power of ≈16 MW/cm^2 is reached at the crystal and ≈34 MW/cm^2 at the waist position. For an intracavity circulating power of, e.g., 20 W, the previous given values have to be multiplied with a factor of 20 accordingly. However, the TISA pulse length is expected to be much shorter than 40 ns at this power level (see Fig. 4.101 on page 139, Fig. 4.116 on page 152). Intracavity peak power densities of ≈1 GW/cm^2 and above can be expected for this case. This can be critical

for optical components and therefore other resonator configurations or concepts with larger mode volumes have to be found for this power level.
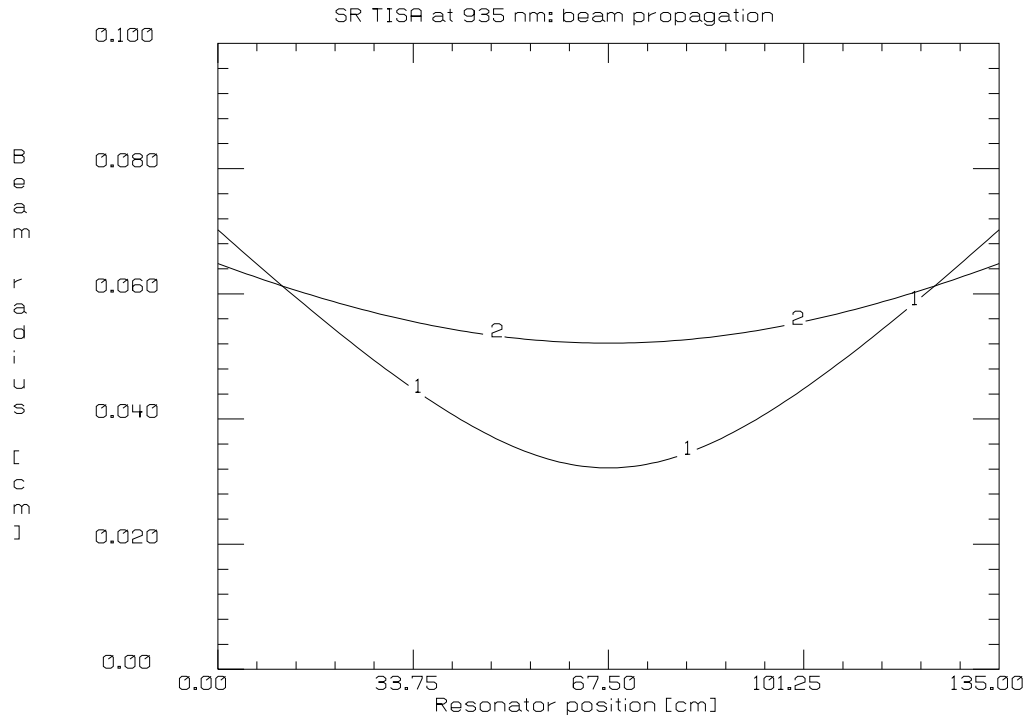
(a) Beam propagation through resonator. 1: tangential plane, 2: sagittal plane.
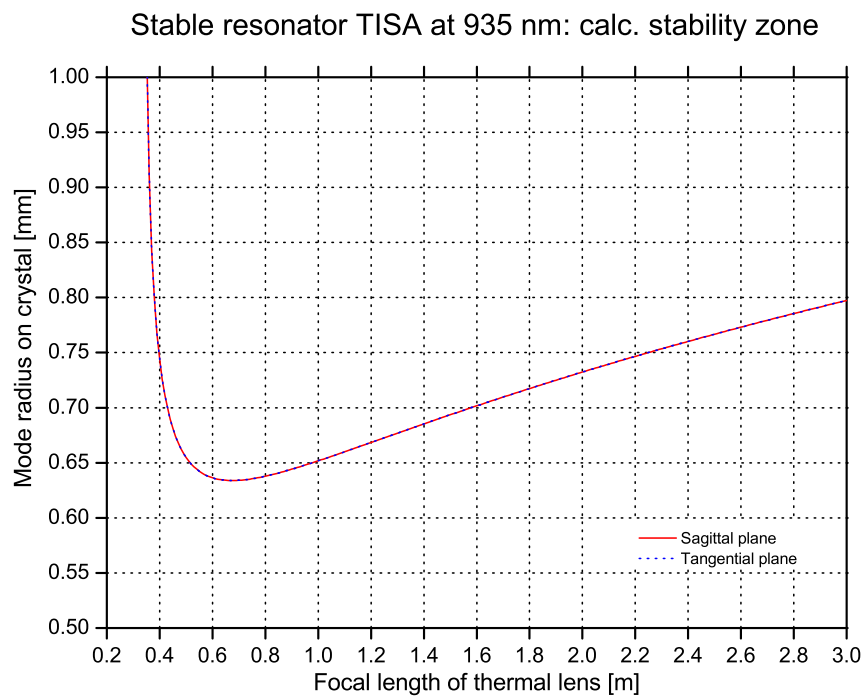
(b) Stability zone(s).

Figure 4.77: Stable resonator TISA laser at 935 nm: beam propagation and stability zone for sagittal and tangential planes. Resonator length: 1.35 m, thermal lens for Brewster-cut crystal at a total pump-power level of 23.2 W (see Tab. D.1): $f_{th,T,s}$=0.95414 m (sagittal plane), $f_{th,T,t}$=0.42721 m (tangential plane).
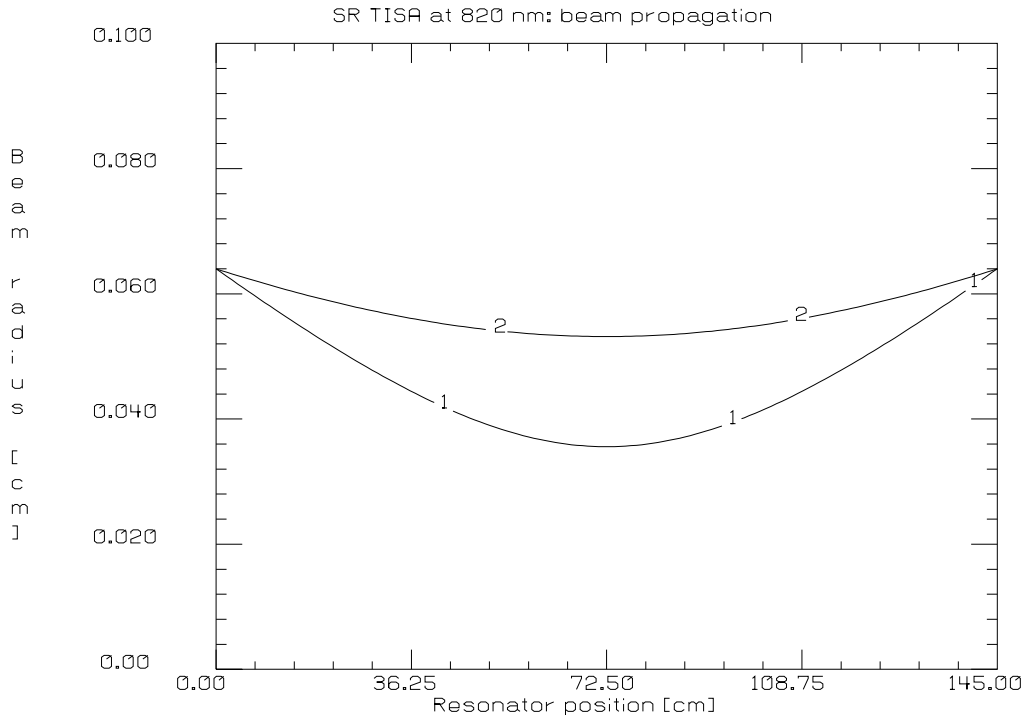
(a) Beam propagation through resonator. 1: tangential plane, 2: sagittal plane.
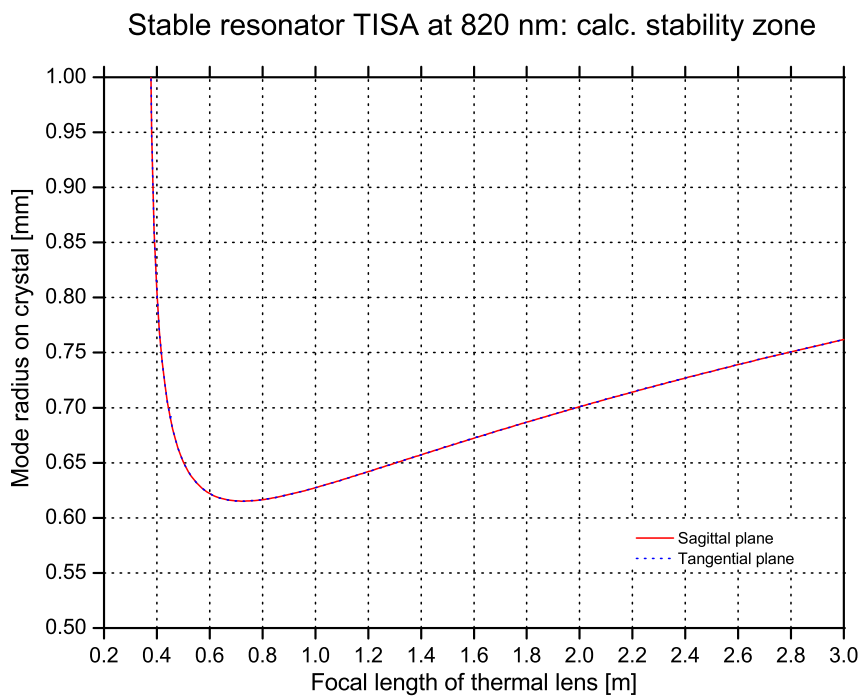
(b) Stability zone(s).

Figure 4.78: Stable resonator TISA laser at 820 nm: beam propagation and stability zone for sagittal and tangential planes. Resonator length: 1.45 m, thermal lens for Brewster-cut crystal at a total pump-power level of 23.2 W (see Tab. D.1): $f_{th,T,s}$=1.17160 m (sagittal plane), $f_{th,T,t}$=0.52468 m (tangential plane).
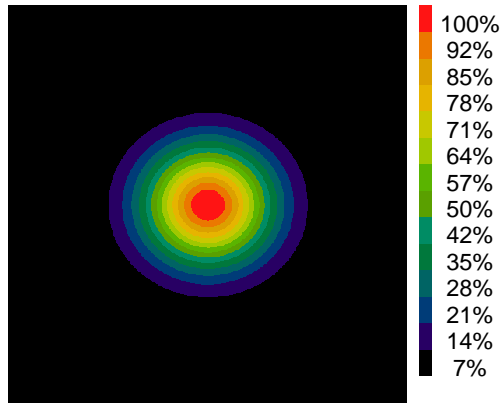
935 nm SR TISA: burnpattern at crystal
intensity, Beam   1
range: 0.000E+00,   1.400E+02,
x-limits: -1.600E-01,   1.597E-01,
y-limits: -1.597E-01,   1.600E-01,
PLOT 4, Sat Mar 07 10:09:07 2009, 3570

(a) Burnpattern at crystal.
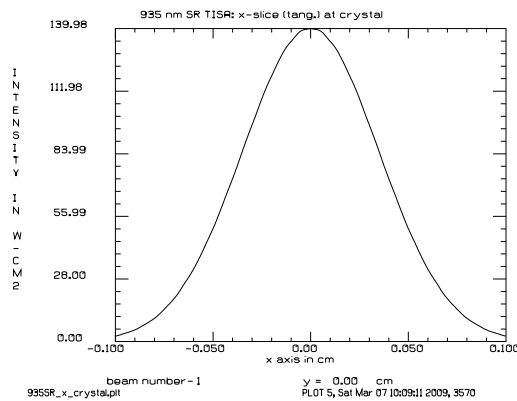
(b) Intensity tang. plane at crystal.
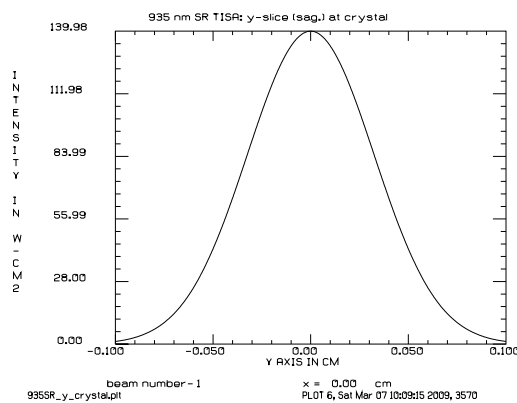
(c) Intensity sag. plane at crystal.

Figure 4.79: SR TISA laser at 935 nm: GLAD simulation at crystal position: (a) intensity (burnpattern) at crystal (W/cm^2), (b) intensity tangential plane (x-slice) at crystal (W/cm^2), (c) intensity sagittal plane (y-slice) at crystal (W/cm^2). Total (integrated) power of beam: 1 W.
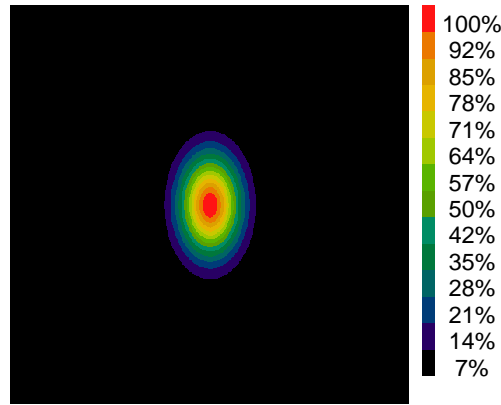
935 nm SR TISA: burnpattern at waist
intensity, Beam   1
range: 0.000E+00,   3.816E+02,
x-limits: -1.600E-01,   1.597E-01,
y-limits: -1.597E-01,   1.600E-01,
PLOT 1, Sat Mar 07 10:08:04 2009, 3570

(a) Burnpattern at waist.
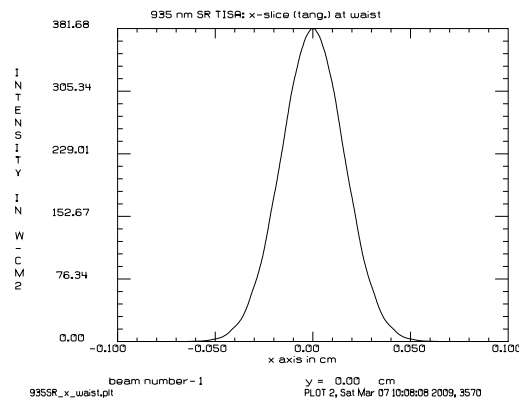
(b) Intensity tang. plane at waist.
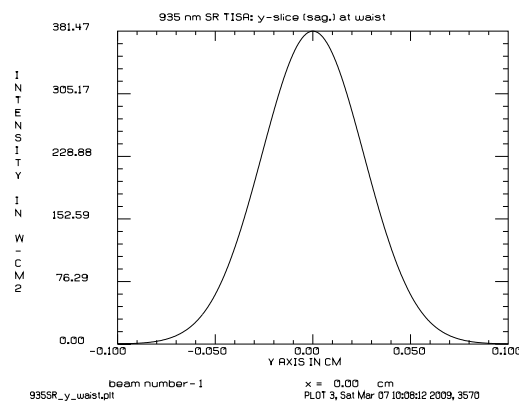
(c) Intensity sag. plane at waist.

Figure 4.80: SR TISA laser at 935 nm: GLAD simulation at waist position: (a) intensity (burnpattern) at waist (W/cm^2), (b) intensity tangential plane (x-slice) at waist (W/cm^2), (c) intensity sagittal plane (y-slice) at waist (W/cm^2). Total (integrated) power of beam: 1 W.
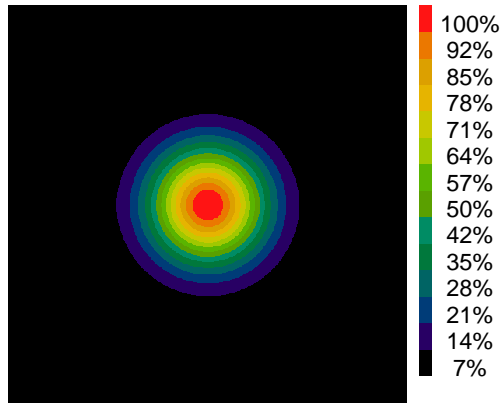
820 nm SR TISA: burnpattern at crystal
intensity, Beam   1
range: 0.000E+00,   1.554E+02,
x-limits: -1.600E-01,   1.597E-01,
y-limits: -1.597E-01,   1.600E-01,
PLOT 4, Sat Mar 07 11:08:11 2009, 3570

(a) Burnpattern at crystal.
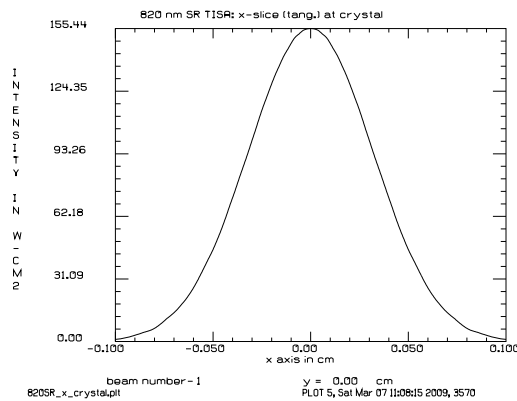
(b) Intensity tang. plane at crystal.
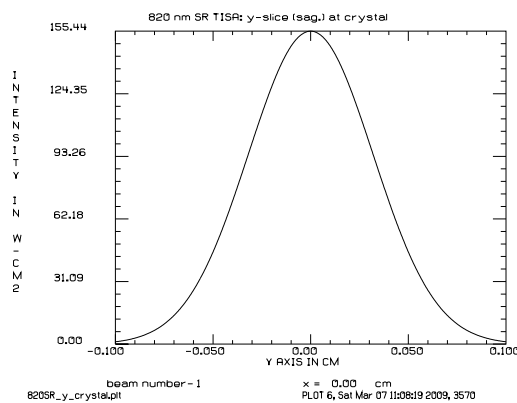
(c) Intensity sag. plane at crystal.

Figure 4.81: SR TISA laser at 820 nm: GLAD simulation at crystal position: (a) intensity (burnpattern) at crystal (W/cm^2), (b) intensity tangential plane (x-slice) at crystal (W/cm^2), (c) intensity sagittal plane (y-slice) at crystal (W/cm^2). Total (integrated) power of beam: 1 W.

820 nm SR TISA: burnpattern at waist
intensity, Beam   1
range: 0.000E+00,   3.361E+02,
x-limits: -1.600E-01,   1.597E-01,
y-limits: -1.597E-01,   1.600E-01,
PLOT 1, Sat Mar 07 11:07:04 2009, 3570
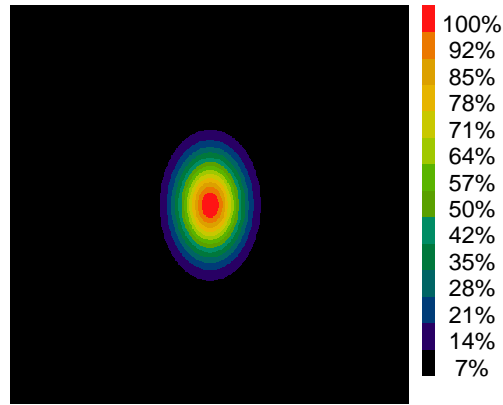
(a) Burnpattern at waist.
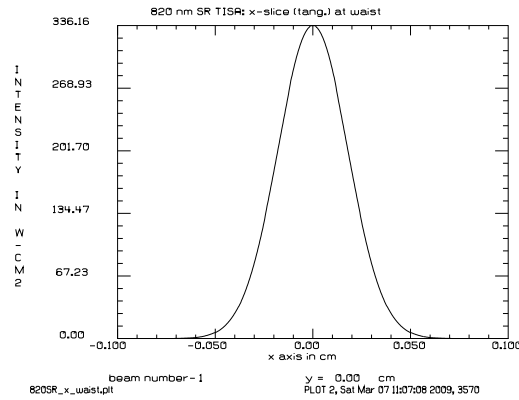
(b) Intensity tang. plane at waist.
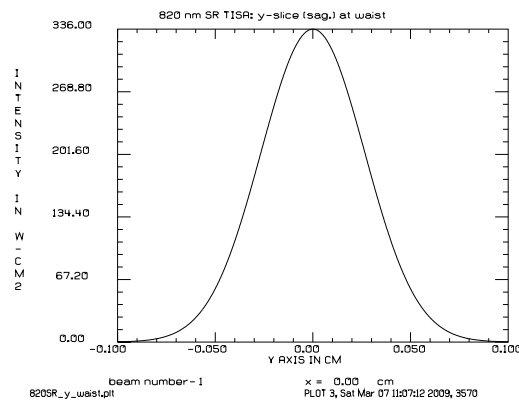
(c) Intensity sag. plane at waist.

Figure 4.82: SR TISA laser at 820 nm: GLAD simulation at waist position: (a) intensity (burnpattern) at waist (W/cm^2), (b) intensity tangential plane (x-slice) at waist (W/cm^2), (c) intensity sagittal plane (y-slice) at waist (W/cm^2). Total (integrated) power of beam: 1 W.

4.4 Unstable resonator

4.4.1 Introduction

The unstable resonator was first presented by A.E. Siegman in 1965 [Siegman65]. Since then, the modeling and development efforts around this resonator type show that unstable resonators offer more design flexibility and are still the choice for high-power lasers. This is mainly due to the fact that the mode volume can be adjusted more easily compared to a stable resonator design. Almost any commercially available high-power Nd:YAG laser is based on an unstable MOPA[25] resonator design. Moreover, the unstable resonator has more scientific potential, as many designs factors are not fully understood, and the structure of the eigenmodes is assumed to have fractal character [Karman98, New01]. However, a few more design factors have to be taken into account compared to a dynamically stable resonator.

In this chapter, a TISA laser resonator design based on an unstable resonator is developed and presented. It is demonstrated that the unstable resonator design procedure is a straightforward process. The motivation for an unstable TISA resonator design is given by the fact that the highest optical-optical efficiency ever reported for a TISA laser has been achieved with an unstable resonator [Rines90, Rines91]. For the first time, the thermal load of an end-pumped TISA crystal at various power levels is taken into account in the unstable resonator design procedure. This is in contrast e.g. to transversally pumped Nd:YAG unstable resonator designs, where the thermal load of the crystals is constant due to flashlamp or diode pumping[26]. The corresponding results of the performance calculations for the unstable resonator TISA laser are presented in Ch. 4.5.4 and Ch. 4.5.6.

4.4.2 Design modeling

Unstable resonators are primarily characterized by their magnification M and the output coupling condition (loss). A Gaussian beam, when being injected into an unstable optical resonator, is magnified until it is coupled out. In contrast to a stable resonator, the beam propagation is not being reproduced after each round-trip. Compared to a stable resonator, the beam radii of different transverse modes do not change, and the (transverse) modes exhibit different diffraction losses[27]. In principle, an unstable resonator oscillates in a single transverse mode, as other modes cannot reach threshold.

Unfortunately, due to diffraction at the output coupler, the mode structure and beam propagation has to be calculated by solving the diffraction integral using numerical methods.

---

[25]MOPA: Master oscillator power amplifier.

[26]The difference in thermal load between lasing and non-lasing is not considered here.

[27]Transverse modes without azimuthal structure. Circular symmetry is assumed. For the same case of stable resonators, the mode structure is given by Gauss-Laguerre polynomials.

The description of unstable resonators using geometrical beam propagation is still valid, as it represents an upper limit for the beam propagation and a lower limit for the overall losses. In the following, the treatment will be limited to positive branch unstable resonators (PBUR), as they have 0 or 2 internal focii. Therefore, negative branch unstable resonators (NBUR), which have at least 1 internal focus are not considered here, although the negative unstable resonator offers the possibility for spatial filtering and better discrimination of one propagation direction. In a (ring) resonator, this can be achieved by incorporation of an intracavity aperture.

The loss factor V per round-trip[28] of an unstable resonator describes the power fraction that stays inside the resonator and is given by[29]

$$V = \frac{1}{|M|^2} .$$

(76)

The output coupling is achieved by a mirror with a variable reflectivity profile (VRM) to minimize diffraction effects[30]. This type of mirror has a reflectivity profile (in intensity) $R(x)$ along the radius x of the mirror according to

$$R(x) = R_0 \exp\left[-2(x/\omega_m)^n\right] ,$$

(77)

where R_0 is the center reflectivity, ω_m is the $1/e^2$-radius of the intensity profile, and n is the super-Gaussian order. The corresponding field reflectivity profile $\rho(x)$ is given by

$$\rho(x) = R(x)^{1/2}$$

(78)

$$= \rho_0 \exp\left[-(x/\omega_m)^n\right] .$$

(79)

The profile of the fundamental mode in the near-field has the same super-Gaussian structure as the output coupler. Figure 4.83 shows reflectivity profiles for variable super-Gaussian orders ($n=2,\ldots,10$). For simplicity, the following geometrical approximation treatment and results are given for a strip resonator [Morin97]. The results for a spherical resonator are given at the end of this subsection. The intensity profile of the outcoupled beam is given by [Morin97]

$$I_{out}(x) = (1 - \rho(x)^2)|V_0(x)|^2$$

(80)

$$= |V_0(0)|^2(1 - R_0 \exp\left(-2(x/\omega_m)^n\right) \exp\left(-2(|x|/\omega_i)^n\right) ,$$

---

[28]V can be seen as the equivalent output coupler reflectivity R of a stable resonator.
[29]Hard-edge mirror assumed.
[30]The corresponding loss factor V for the VRM output coupler is given by Eq. 111 (Ch. 4.5.4, page 141).
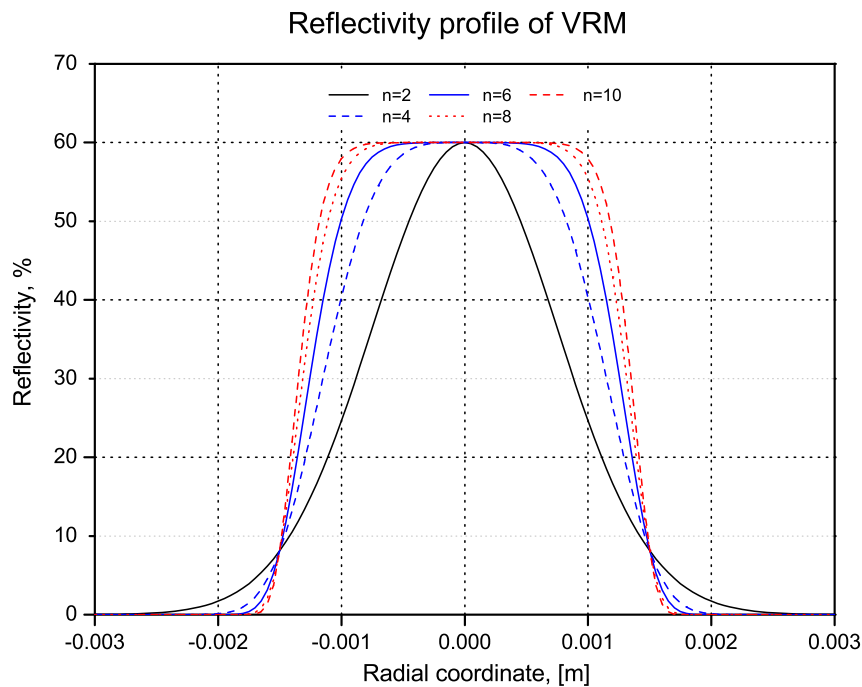
Figure 4.83: Variable reflectivity mirror (VRM): reflectivity profiles for super-Gaussian orders $n=2, \ldots, 10$. Center reflectivity: $R_0=60\%$, $1/e^2$-radius (intensity): $\omega_m=1.5$ mm.

with the fundamental mode field $V_0(x)$ given by

$$V_0(x) = V_0(0) \exp(-(|x|/\omega_i)^n). \tag{81}$$

$V_0(0)$ is the fundamental mode field at the origin, ω_i is the $1/e^2$-radius of the mode in front of the VRM with

$$\omega_i = (|M_g|^n - 1)^{1/n} \omega_m. \tag{82}$$

M_g is the geometric magnification.

The central dip in the intensity profile can be avoided by adjusting the center reflectivity R_0 according to

$$R_0 \leq 1/|M_g|^n. \tag{83}$$

An example is given in Fig. 4.84, where the output intensity profile is shown, and R_0 is varied from $15, \ldots, 90\%$ for $M=1.6$. The optimum R_0 is given by $R_{0,opt}=5.96\%$.

The beam propagation for a single round-trip in resonator can be described by the ABCD-
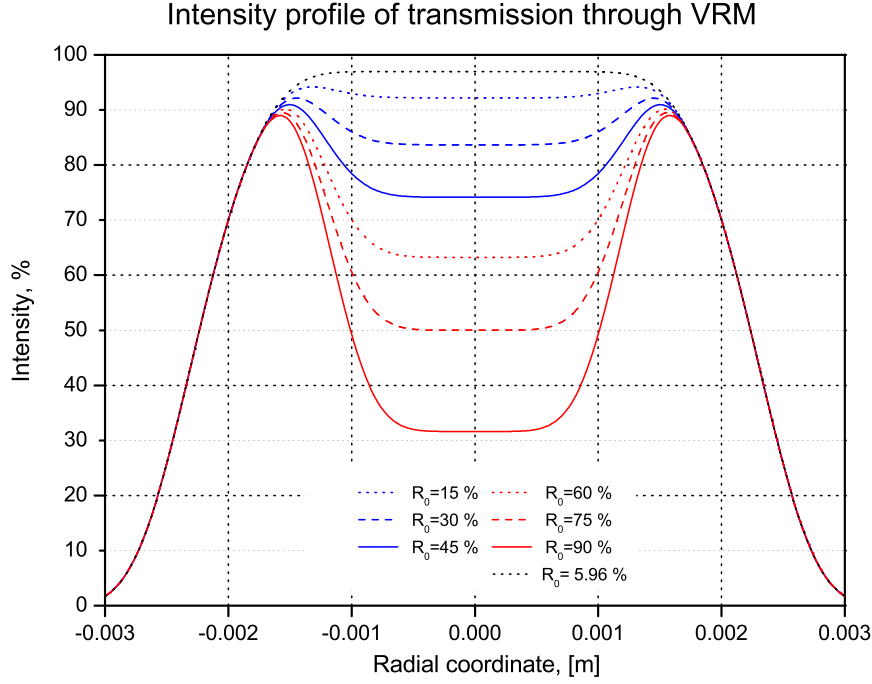
Figure 4.84: Outcoupled beam intensity profile at VRM for R_0=15,...,90%, M=1.6, ω_m=ω_i=1.5 mm. $R_{0,opt}$=5.96%.

matrix formulation of the Huygens integral [Siegman76, Morin97]

$$
E(x_1) \;=\; \left(\frac{j}{B\,\lambda}\right)^{1/2} \int_{-\infty}^{+\infty} E_0(x_0) \exp\left[-j\frac{\pi}{B\,\lambda}\left(A\,x_0^2 - 2\,x_0\,x_0 + D\,x_1^2\right)\right] dx_0 , \quad (84)
$$

where $E(x_1)$, $E_0(x_0)$ are the output and input fields, respectively, and A, B, C, D are the elements of the corresponding beam propagation matrix. Transformation of Eq. 84 to the corresponding eigenvalue equation of an unstable resonator with a VRM mirror results in

$$
\gamma_n V_n(x_1) \;=\; \left(\frac{j}{M_g\,B\,\lambda}\right)^{1/2} \int_{-\infty}^{+\infty} \frac{R(x_1/M_g)V_n(x_1/M_g)}{M_g^{1/2}} \exp\left[-\frac{j\pi(x_0 - x_1)^2}{M_g\,B\lambda}\right] dx_0 , (85)
$$

with eigenvalues γ_n, $M_g \equiv x_1/x_0$ (n: transverse mode index), and the field given by

$$
E_n(x) \;=\; V_n(x)\exp\left[-j\frac{\pi\,x^2}{\lambda R_m}\right] . \quad (86)
$$

R_m is the radius of curvature of the magnifying wave[31]. Equation 85 reduces in the case of the geometrical approximation ($\lambda \to 0$) to

$$
\gamma_n V_n(x) \;=\; \frac{R(x/M_g)V_n(x/M_g)}{M_g^{1/2}} . \quad (87)
$$

---

[31]The demagnifying wave transforms itself in a magnifying wave in unstable resonators.

The eigenvalue of the fundamental mode is given by

$$|\gamma_0| = \frac{|R(0)|}{|M_g|^{1/2}}, \tag{88}$$

and the corresponding feedback to the mode is

$$|\gamma_0|^2 = \frac{|R(0)|^2}{|M_g|}. \tag{89}$$

General solutions to Eq. 87 are

$$V_n(x) = x^n V_0(x), \tag{90}$$

with corresponding eigenvalues

$$\gamma_n = \frac{\gamma_0}{M_g^n}. \tag{91}$$

The discrimination D between the lowest two order modes is

$$D = \frac{|\gamma_0|^2}{|\gamma_1|^2} = M_g^2. \tag{92}$$

Therefore, the magnification should be chosen as high as possible to obtain a good mode discrimination.

For the special case of a output intensity profile without central dip (Eq. 83), the maximum achievable feedback for a strip resonator is given by

$$|\gamma_0|^2 \leq 1/|M_g|^{n+1}. \tag{93}$$

Compared to a strip resonator, the feedback to the fundamental mode of the spherical resonator reads [Morin97]

$$|\tilde{\gamma}_{0,0}|^2 = \frac{|R(0)|^2}{|M_g|^2}. \tag{94}$$

Therefore, it is smaller compared to the strip resonator (Eq. 89). Consequently, the maximum achieveable feedback of a spherical resonator under flat-top condition (Eq. 83) is

$$|\tilde{\gamma}_{0,0}|^2 \leq 1/|M_g|^{n+2}. \tag{95}$$

4.4.3 Resonator selection

For the positive-branch unstable resonator (PBUR) design, the basic ring-resonator design found in [Freiberg74, Anan'ev69] is used. It is an asymmetric confocal unstable ring resonator (ACURR). The set-up is depicted in Fig. 4.85. The advantages of this design are the confocality condition and the asymmetric ring configuration. The confocality condition results in high energy extraction of the gain media and a collimated output beam in one propagation direction. The asymmetric ring provides different propagation characteristics in clockwise (CW) and counterclockwise (CCW) propagation directions, allowing discrimination of one propagation direction by incorporation of an aperture. However, several improvements are necessary to modify the design for high-power operation, as thermal lensing in the gain media, astigmatism of mirrors and Brewster surfaces have to be considered. The design point and additional considerations for the unstable laser are as follows.

The TISA crystal is pumped by 40 W average power (20 W each side). This results in significant thermal lensing and additional astigmatism due to the Brewster-cut crystal (see Ch. 4.2.5, 4.2.6). The magnification of the unstable resonator is chosen as high as possible for effective mode discrimination, as additional spectral narrowing elements (birefringent filter, etalon, etc.) have to be avoided. For spectral narrowing, the resonator will be injection-seeded through the output-coupler. Therefore, the magnification is set at a value of M=1.6, also due to the results achieved by [Rines90] with a center reflectivity of R_0=60% and super-Gaussian order of n=6 [Morin97], even though the output beam transmission simulation shows a central dip. The feedback was considered to have higher importance. The super-Gaussian order with n=6 was chosen for better energy extraction compared to a
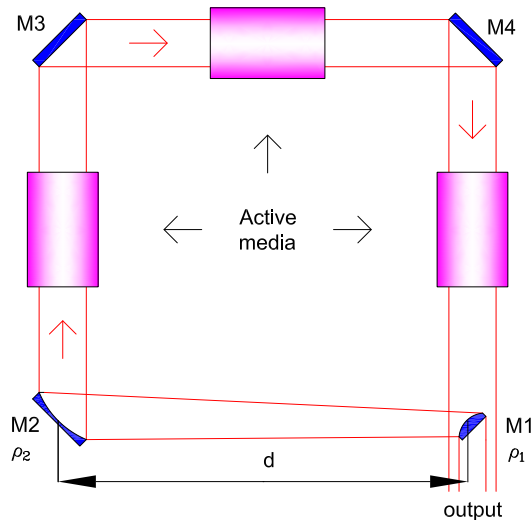
Figure 4.85: Asymmetric confocal unstable ring resonator. Confocality condition: $\rho_1 + \rho_2 = 2d$ (ρ_i: radius of curvature). Shown is CW (clockwise) propagation direction with collimated output at output coupler (M1).

pure Gaussian-profile. An even higher super-Gaussian order shows additional ripples in the free space output beam propagation simulation and the outcoupled beam. The design point magnification was chosen intentionally that high, as the condition of a flat-top beam profile is being more fulfilled with the increase of thermal load.

The process stages leading to the final setup are explained in the following. First, the ABCD-matrix of the unstable resonator[32] (asymmetric confocal unstable ring resonator) of the type shown in Fig. 4.85 was set up. The distances, and mirror curvatures are varied in a combinatorial approach to find the desired magnification M=1.6. Suitable configurations are extracted out of the solutions, using the constraints given by the confocality and asymmetric condition.

Another approach finding an optimum configuration using an advanced algorithm for global minimization [Duan93] failed due to the nature of the problem: a single optimum configuration is not available, as there are several optimum solutions in the parameter space.

In a third attempt, the method of Lagrange multipliers was used to find a configuration. With this method, the solution for a starting configuration is almost identified at once. In the next step, the thermal lens of the Brewster-cut crystal at maximum pump-power[33], compensating cylindrical lenses, and the mirror astigmatism are added to the configuration of the ABCD beam propagation matrix (see Ch. 4.4.4). Further optimization is done for the position of the cylindrical lenses. These steps are carried out for both sagittal and tangential planes.

To minimize the astigmatism at the output coupler, the angle is reduced by adding two additional (flat) mirrors to the configuration. The overall strategy in finding an optimum configuration for a given design point shows the potential for future investigations, as the optimization of end-pumped unstable resonator configurations has not been done before. However, further setup development by application of advanced optimization methods were not made due to time constraints.

The unstable TISA resonator configuration for a complete set up including seeding is depicted in Fig. 4.86. The pump power of the frequency-doubled Nd:YAG laser can be adjusted with the combination of half-wave plate (L/2) and thin film polarizer (TFP). The telescope (T) for the pump optimizes the pump-beam radius for the TISA crystal (pump-beam radius: 0.75 mm). The pump beam is splitted 50:50% with the beam splitter (BS) to pump the TISA crystal through the dichroic mirrors (short-wave pass mirrors) from both sides.

The TISA resonator itself contains the variable reflectivity output coupler (VRM, plano-convex mirror, radius of curvature rcc=$-$1.6 m, R_0=60%, n=6, ω_m=1.5 mm), the curved mirror M (plano-concave mirror, rcc=$+$2.0 m), and additional cylindrical lenses (L) for both sagittal (x) and tangential (y) planes. The resonator is injection-seeded through the VRM

---

[32]Assumption: paraxial ray theory can be applied.
[33]Maximum pump-power: 40 W (200 mJ, 250 Hz).

Figure 4.86: Unstable resonator TISA laser set up (BM: bending mirror, L/2: half-wave plate, TFP: thin film polarizer, BD: beam dump, T: telescope, BS: beam splitter, DC: dichroic beam splitter (short-wave pass), VRM: variable reflectivity mirror (plano-convex, rcc=-1.6 m =ρ_1, R_0=60%, n=6, ω_m=1.5 mm), M: plano-concave mirror (rcc=2.0 m =ρ_2), L: negative cylindrical lens in x-, y-direction (x: sagittal, y: tangential), FI: Faraday isolator, FC: fiber coupler, ECDL IS: External cavity diode laser injection seeder). See Fig. 4.87 for further details about the unstable TISA resonator.
Note: the confocality condition without thermal load, cylindrical lenses, and astigmatism introduced by optical elements results in a magnification of M=$1 - (2d/\rho_1)$=$1 - (\rho_1 + \rho_2)/\rho_1$=1.25 for this resonator set up. Alternatively, calculation of the eigenvalues of the beam propagation matrix (Eq. 97 in Ch. 4.4.4) with corresponding values for the variables yields the same result.

output-coupler. The external cavity diode laser is protected from feedback by use of a Faraday isolator. The ECDL seeder is connected with a single-mode fiber and a fiber coupler (FC).

4.4.4 Beam propagation modeling

The beam propagation for the unstable resonator was modeled using Gaussian beam ABCD-matrix formalism[34] and diffraction propagation with the GLAD software package[35].
The overall 4×4-ABCD-matrix for a single resonator round-trip was set up and accounts for astigmatism in sagittal and tangential planes introduced by mirrors, Brewster surfaces and thermal lensing (simple astigmatic treatment). The scheme of the unstable ring resonator is

---

[34]Wolfram Mathematica 5.2/6.0 was used.
[35]GLAD: General laser analysis and design (Applied Optics Research, GLAD 5.0.)

depicted in Fig. 4.87. Additionally, a gain aperture matrix (Gaussian, subscript GA) at the crystal and a matrix for the representation of the VRM is incorporated (Gaussian reflectivity profile). The starting point for a resonator round-trip is at the VRM mirror (output coupler).
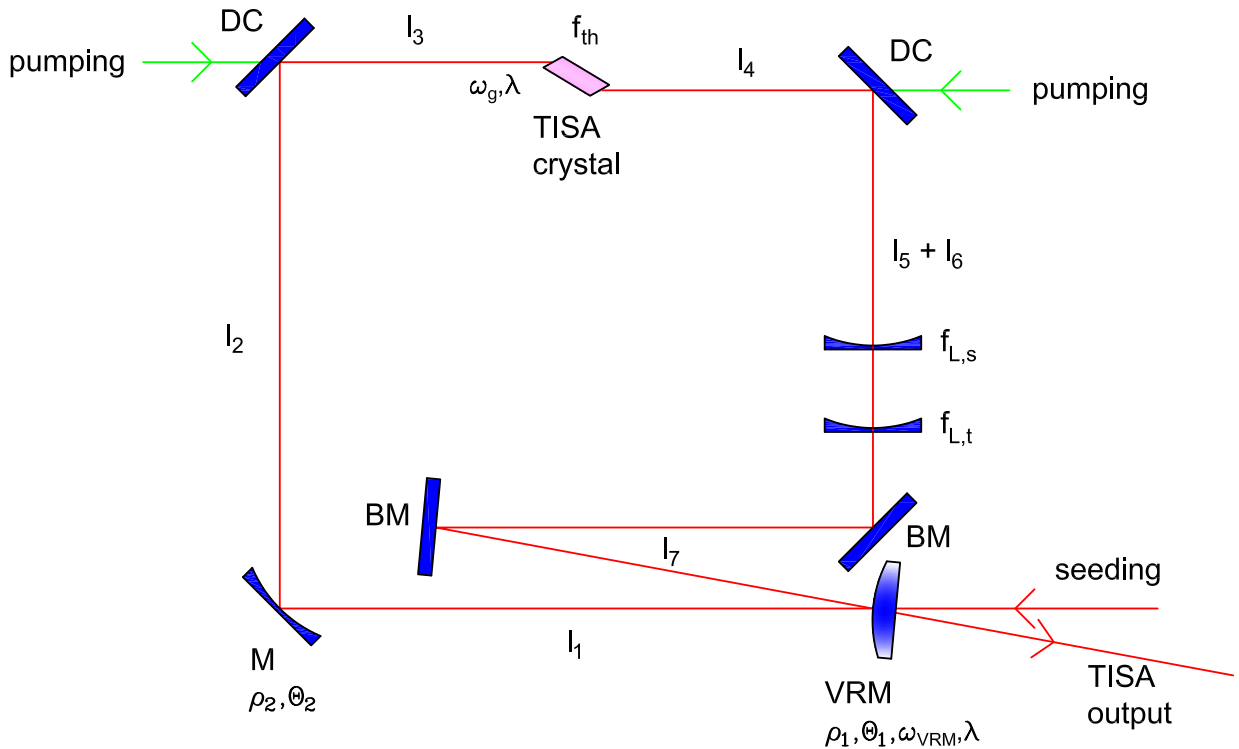
Figure 4.87: Scheme of unstable resonator TISA laser set up. Values used for beam propagation modeling: l_1=0.2 m, l_2=0.17 m, l_3=0.1 m, l_4=0.1 m, $l_{5,s}$=0.2 m, $l_{5,t}$=0.04 m, $l_{6,s}+l_{7,s}$=0.215 m, $l_{6,t}+l_{7,t}$=0.375 m, θ_1=8°, θ_2=45°, ρ_1= − 1.6 m, ρ_2=2.0 m, $\omega_{VRM,\{s,t\}}$=0.0015 m, $\omega_{g,\{s,t\}}$=0.001 m, n=1.76, l=0.02 m, λ={935, 820} nm, $f_{th,\{s,t\}}$: values according to FEA calculations.

The 4×4 matrix in CW propagation direction M_{CW} reads as follows:

$$M_{CW} = M_{FS(l_7)} M_{FS(l_6)} M_{L(f_{s,t})} M_{FS(l_5)} M_{FS(l_4)} M_{TH(ft_{FEA})} M_{GA(\omega_g)} \quad (96)$$

$$M_{FS(l_3)} M_{FS(l_2)} M_{M(\rho_2,\theta_2)} M_{FS(l_1)} M_{VRM(\rho_1,\theta_1,\omega_1)}$$

$$= \begin{pmatrix} 1 & 0 & l_{7,s} & 0 \\ 0 & 1 & 0 & l_{7,t} \\ 0 & 0 & 1 & 0 \\ 0 & 0 & 0 & 1 \end{pmatrix} \begin{pmatrix} 1 & 0 & l_{6,s} & 0 \\ 0 & 1 & 0 & l_{6,t} \\ 0 & 0 & 1 & 0 \\ 0 & 0 & 0 & 1 \end{pmatrix} \begin{pmatrix} 1 & 0 & 0 & 0 \\ 0 & 1 & 0 & 0 \\ -\frac{1}{f_{L,s}} & 0 & 1 & 0 \\ 0 & -\frac{1}{f_{L,t}} & 0 & 1 \end{pmatrix}$$

$$\begin{pmatrix} 1 & 0 & l_{5,s} & 0 \\ 0 & 1 & 0 & l_{5,t} \\ 0 & 0 & 1 & 0 \\ 0 & 0 & 0 & 1 \end{pmatrix} \begin{pmatrix} 1 & 0 & l_4 & 0 \\ 0 & 1 & 0 & l_4 \\ 0 & 0 & 1 & 0 \\ 0 & 0 & 0 & 1 \end{pmatrix}$$

$$\begin{pmatrix} 1-\frac{l}{2nf_{th,s}} & 0 & \frac{l}{n}-\frac{l^2}{4n^2 f_{th,s}} & 0 \\ 0 & 1-\frac{l}{2nf_{th,t}} & 0 & \frac{l}{n^3}-\frac{l^2}{4n^4 f_{th,t}} \\ -\frac{1}{f_{th,s}} & 0 & 1-\frac{l}{2nf_{th,s}} & 0 \\ 0 & -\frac{n^2}{f_{th,t}} & 0 & 1-\frac{l}{2nf_{th,t}} \end{pmatrix}$$

$$\begin{pmatrix} 1 & 0 & 0 & 0 \\ 0 & 1 & 0 & 0 \\ -\frac{j\lambda}{\pi(\omega_{g,s})^2} & 0 & 1 & 0 \\ 0 & -\frac{j\lambda}{\pi(\omega_{g,t})^2} & 0 & 1 \end{pmatrix} \begin{pmatrix} 1 & 0 & l_3 & 0 \\ 0 & 1 & 0 & l_3 \\ 0 & 0 & 1 & 0 \\ 0 & 0 & 0 & 1 \end{pmatrix}$$

$$\begin{pmatrix} 1 & 0 & l_2 & 0 \\ 0 & 1 & 0 & l_2 \\ 0 & 0 & 1 & 0 \\ 0 & 0 & 0 & 1 \end{pmatrix} \begin{pmatrix} 1 & 0 & 0 & 0 \\ 0 & 1 & 0 & 0 \\ -\frac{2\cos(\theta_2)}{\rho_{2,s}} & 0 & 1 & 0 \\ 0 & -\frac{2}{\rho_{2,t}\cos(\theta_2)} & 0 & 1 \end{pmatrix} \begin{pmatrix} 1 & 0 & l_1 & 0 \\ 0 & 1 & 0 & l_1 \\ 0 & 0 & 1 & 0 \\ 0 & 0 & 0 & 1 \end{pmatrix}$$

$$\begin{pmatrix} 1 & 0 & 0 & 0 \\ 0 & 1 & 0 & 0 \\ -\frac{2\cos(\theta_1)}{\rho_{1,s}}-\frac{j\lambda}{\pi(\omega_{VRM,s})^2} & 0 & 1 & 0 \\ 0 & \frac{2}{\rho_{1,t}\cos(\theta_1)}-\frac{j\lambda}{\pi(\omega_{VRM,t})^2} & 0 & 1 \end{pmatrix}. \quad (97)$$

The analogue matrix M_{CCW} for CCW-direction is not given here[36]. In Eq. 97, M_{FS} is the matrix of free space propagation with length l_i, M_{VRM} is the matrix of the VRM mirror, M_M is the matrix for a curved mirror, and M_{TH} is the matrix of the Brewster-cut crystal under thermal load (thermal lens) [Huang96]. ρ_i, θ_i, and ω_i denote radii of mirror curvature, angle of incidence, and aperture radius, respectively. Subscripts s and t denote sagittal

---

[36] CCW-direction 4×4-beam-propagation matrix M_{CCW}: reverse matrix order of Eq. 97, except starting point (VRM mirror matrix).

and tangential variable values. The value for the thermal lensing in sagittal and tangential planes are incorporated into the 4×4-matrix beam propagation to obtain the magnifications in sagittal and tangential plane.

The design idea is to have the same magnification for both sagittal and tangential planes at the design point. Therefore, the focal lengths of the cylindrical lenses for sagittal and tangential plane together with their positions have to be adjusted. Strictly speaking, lens combinations have to be incorporated for each plane instead of a single lens to aim the magnification together with a collimated output at the design point. As a experimental starting point however, it is more important to obtain the same magnifications in both planes at the design point.

For the calculation of the output power of the unstable resonator, the mean value of the magnifications of sagittal and tangential plane at the corresponding pump power level is used to obtain an effective magnification M_{eff}. This effective magnification M_{eff} is used inside the loss term in the rate equation modeling (Ch. 4.5.4, Ch. 4.5.6). The calculated magnification versus the pump pulse energy is depicted in Fig. 4.88 for the unstable resonator parameters found in Tab. 4.11 (page 143), and Tab. 4.16 (page 154) for 935 nm and 820 nm, respectively. The resulting propagation of the super-Gaussian distribution output can be estimated using the results found in [Parent92].

The injection seeding of unstable resonators is less complicated due the magnification behavior of the resonator. If the injected beam is collimated and has a radius less than the fundamental mode radius, the following magnification at consecutive round-trips within the resonator will ensure perfect overlap with the resonator mode. Therefore, in contrast to a stable resonator design, explicit mode matching of the injection seeder and the cavity mode is not necessary. Due to the mode characteristics of the unstable resonator and the applied seeding, additional spectral narrowing elements as birefringent filter (BF) or etalons are not planned for the present set up. Nevertheless, they can be easily incorporated if really necessary. Unidirectional propagation is also ensured by injection-seeding, and therefore the combination of half-wave plate aligned to 45° retardation and Faraday rotator (45°) is not necessary.

The GLAD software package [GLAD, Lawrence92] was used for modeling the beam propagation of the unstable resonator. The results are presented in the following.

The resonator setup used inside GLAD is depicted in Fig. 4.89. This simplified resonator set up was used due to time constraints. A more detailed modeling can be done in the future. However, the simulation gives a first impression of the expected beam propagation. The GLAD modeling results are shown in Figs. 4.90-4.94. Figures 4.90a, 4.90b show the reflectivity of the VRM and the corresponding transmission mask for the output coupling, respectively. Figures 4.90c-4.90f show the converged mode in front of the VRM after 10
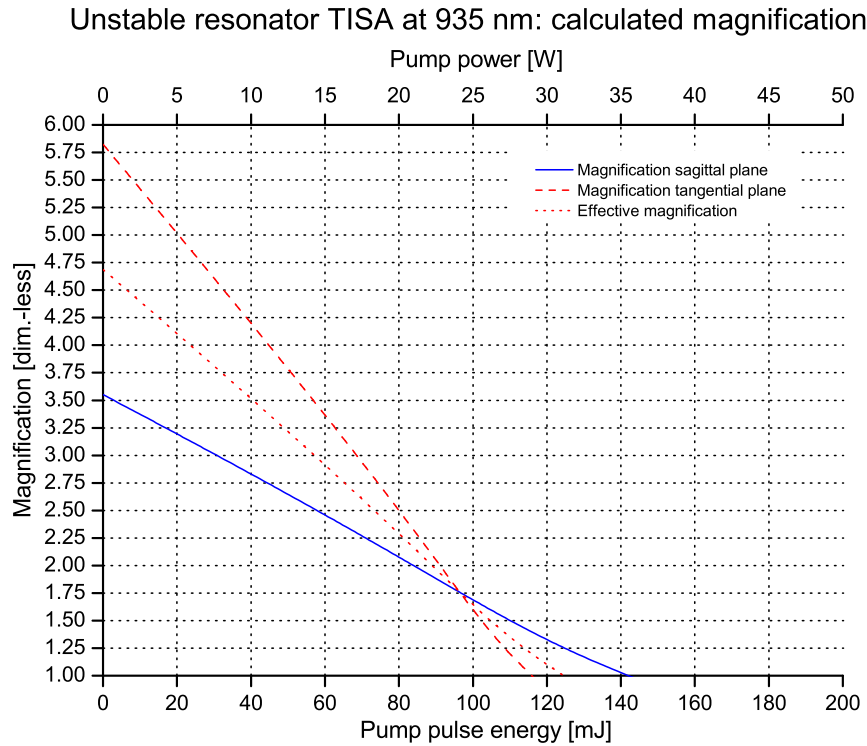
(a) Unstable resonator TISA laser at 935 nm.
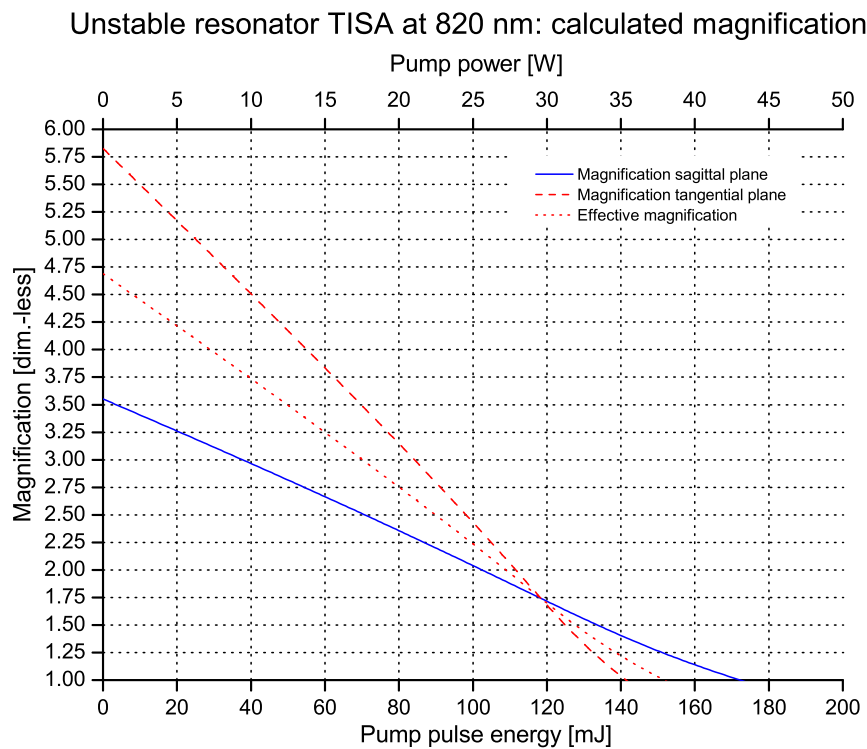
(b) Unstable resonator TISA laser at 820 nm.

Figure 4.88: Calculated magnification versus pump-pulse energy for unstable resonator TISA laser using Eq. 97 and parameters of Tab. 4.11, 4.16 for 935, 820 nm.
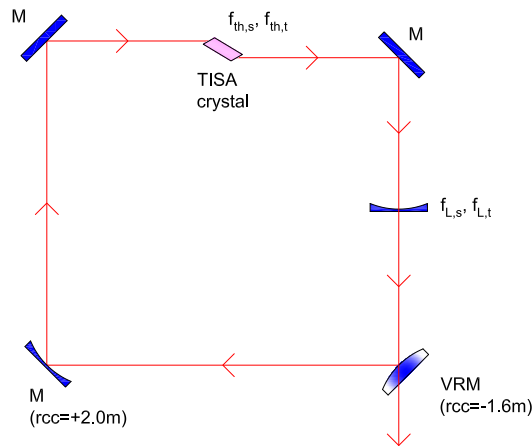
Figure 4.89: Scheme of unstable resonator TISA laser set up inside GLAD model. Resonator length: 0.8 m, TISA crystal resonator position: 0.5 m (cw-direction), thermal lens: $f_{th,T,s}$=1.2 m; $f_{th,T,t}$=0.4 m, cylindrical lens position: 0.7 m, $f_{L,s}$= − 0.772 m, $f_{L,t}$= − 0.183 m. VRM mirror: R_0=60%, ω_m=0.0015 m, super-Gaussian exponent (GLAD) *sgxp*=3. Magnification: ≈ 1.6 (both planes). Resulting beam propagation (cw-direction) shown in Fig. 4.91e.

resonator round-trips (cavity passes) in 3d, as burnpattern, and in slices of tangential and sagittal plane. The GLAD model was initialized using the GLAD command *resonator/set*, where a suitable starting mode radius is selected.

Figures 4.91a-4.91d show the outcoupled beam of the unstable resonator in 3d, burnpattern, and tangential and sagittal plane slices, respectively. The resulting beam propagation of the unstable resonator is depicted in Fig. 4.91e. The magnification character is clearly visible. The highly astigmatic and focused far-field is shown in Fig. 4.91f. The resulting outcoupled beam for the experiment is expected to be astigmatic. This could not yet be fully modeled inside GLAD, as the tranmission mask could not be turned according to the angle of the VRM.

Figures 4.92-4.94 show the unstable resonator mode evolving out of spontaneous emission noise. The figures show the cavity mode at different resonator round-trips (cavity passes) in front of the VRM. As can be seen, it takes about 14 passes to obtain an energy-stable mode. The convergence was determined by a energy criteria with the GLAD command *gain/converge/test*. Compared to a stable resonator, the unstable resonator showed faster convergence. This means, that less resonator round-trips were necessary for (energy) convergence. Whether this can be attributed to the better mode discrimination of unstable resonators is currently under investigation.

To conclude, the GLAD simulation shows that further development of the set up is necessary. To obtain a collimated output, a lens combination for both sagittal and tangential planes has to be found.
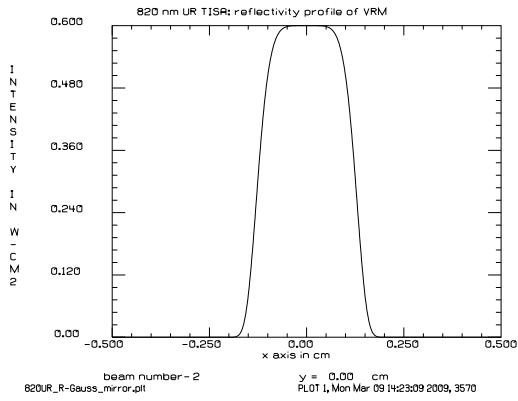
(a) Reflectivity of VRM.
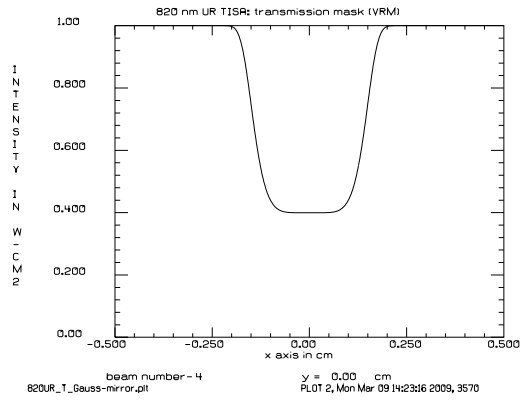
(b) Transmission mask of VRM.
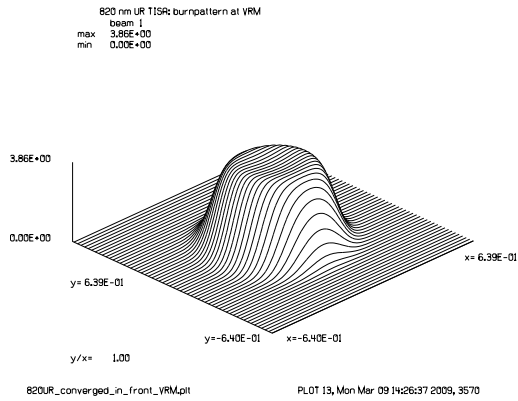
(c) Intensity of converged mode in front of VRM - 3d.
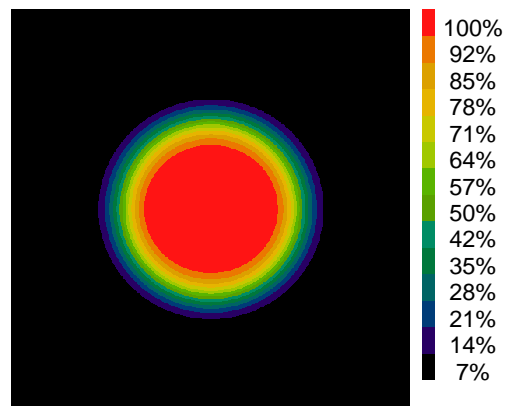
(d) Intensity of converged mode in front of VRM - burnpattern.
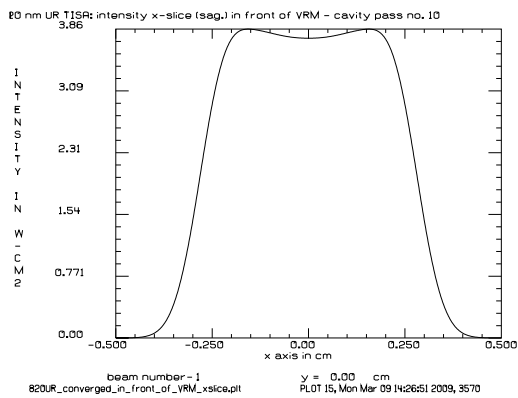
(e) Intensity of converged mode: tang. plane in front of VRM (x-slice).
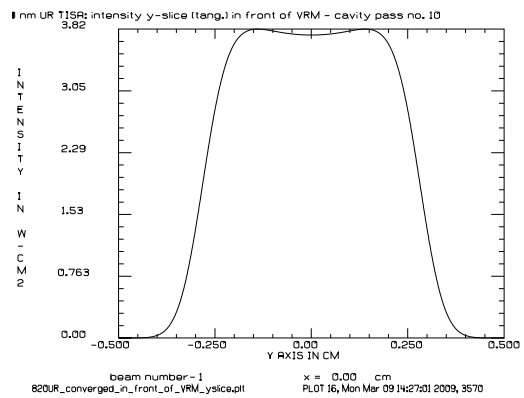
(f) Intensity of converged mode: sag. plane in front of VRM (y-slice).

Figure 4.90: UR TISA at 820 nm: GLAD modeling results, part 1.
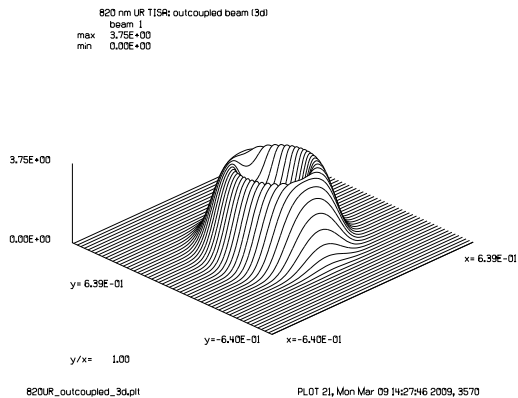
(a) Outcoupled beam - 3d.
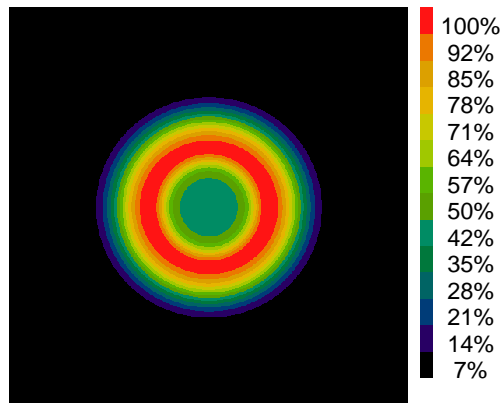
(b) Outcoupled beam - burnpattern.
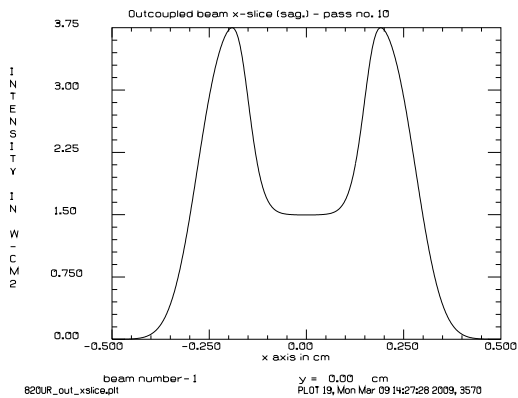
(c) Intensity of outcoupled beam: tang. plane in front of VRM (x-slice).
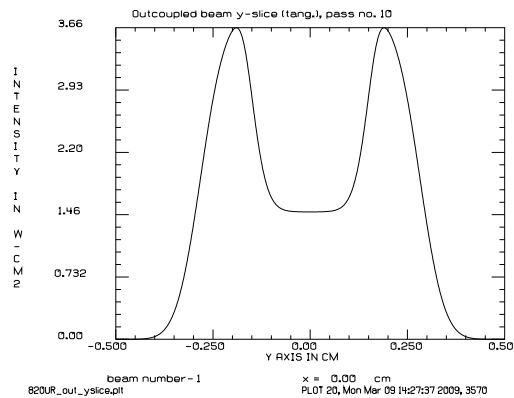
(d) Intensity of outcoupled beam: sag. plane in front of VRM (y-slice).
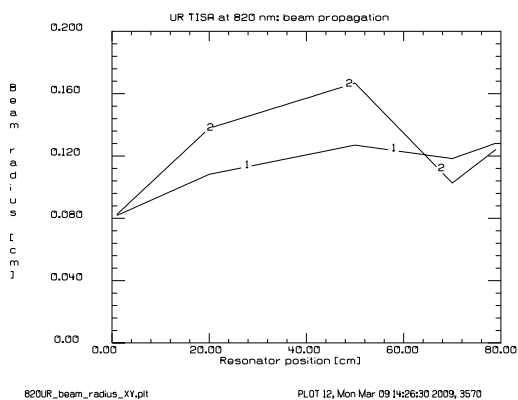
(e) Beam propagation through resonator: 1: tangential plane, 2: sagittal plane.
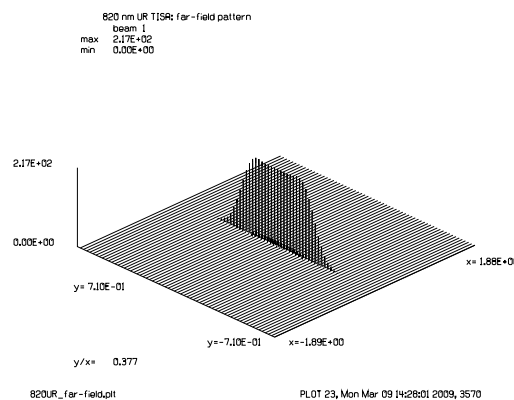
(f) Far-field - 3d

Figure 4.91: UR TISA at 820 nm: GLAD modeling results, part 2.
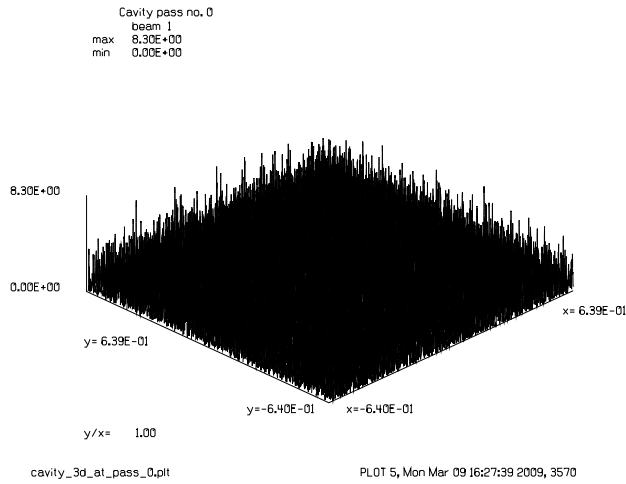
(a) Cavity pass 0 - mode 3d.
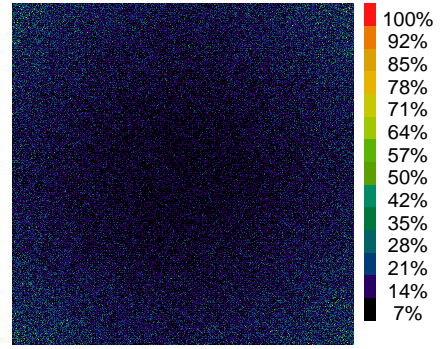
(b) Cavity pass 0 - mode burnpattern.
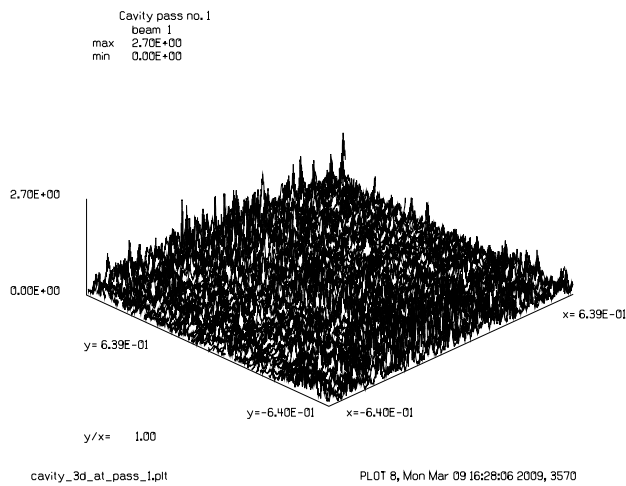
(c) Cavity pass 1 - mode 3d.
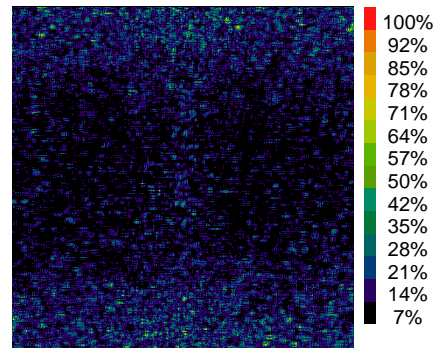
(d) Cavity pass 1 - mode burnpattern.
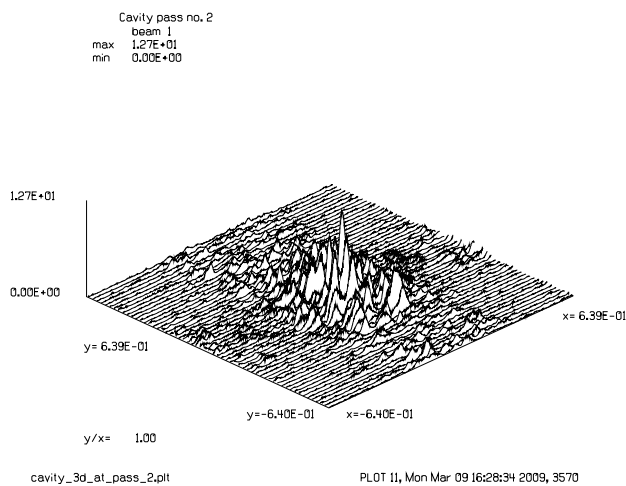
(e) Cavity pass 2 - mode 3d.
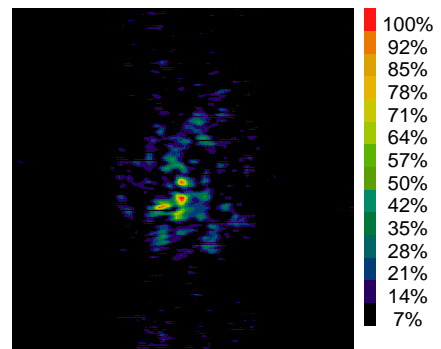
(f) Cavity pass 2 - mode burnpattern.

Figure 4.92: UR TISA at 820 nm: GLAD simulation showing cavity mode out of noise in front of VRM at resonator round-trips (cavity passes) 0, 1, and 2.
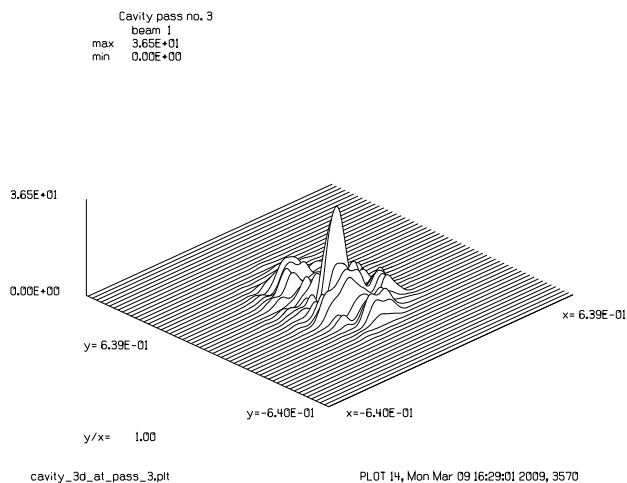
(a) Cavity pass 3 - mode 3d.
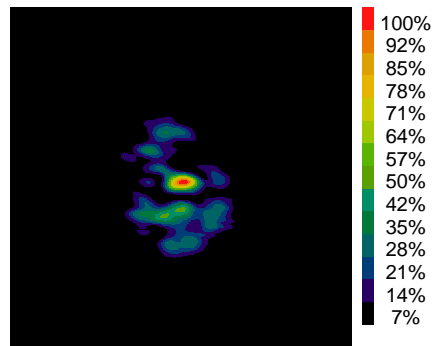
(b) Cavity pass 3 - mode burnpattern.
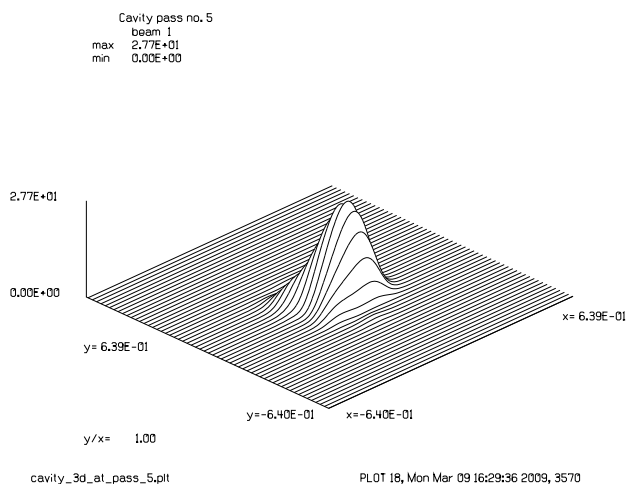
(c) Cavity pass 5 - mode 3d.
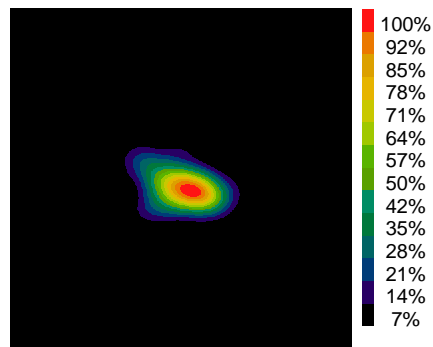
(d) Cavity pass 5 - mode burnpattern.
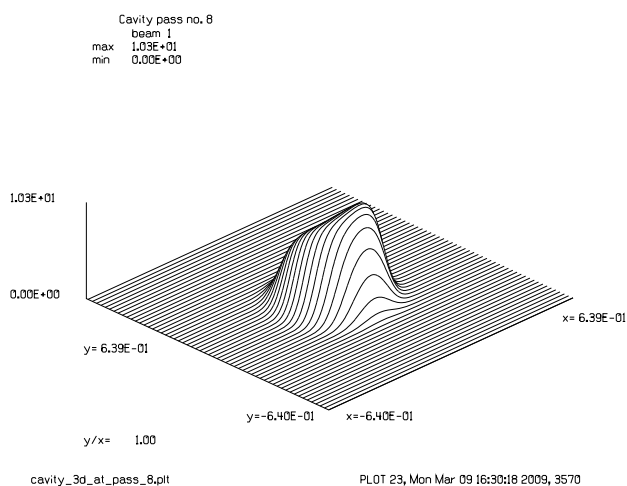
(e) Cavity pass 8 - mode 3d.
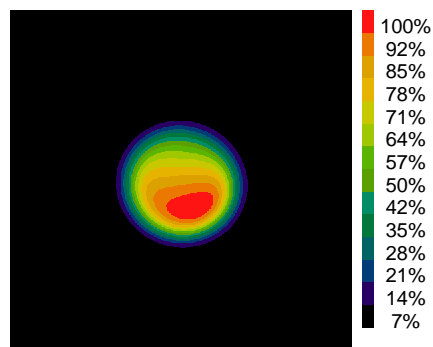
(f) Cavity pass 8 - mode burnpattern.

Figure 4.93: UR TISA at 820 nm: GLAD simulation showing cavity mode out of noise in front of VRM at resonator round-trips (cavity passes) 3, 5, and 8.
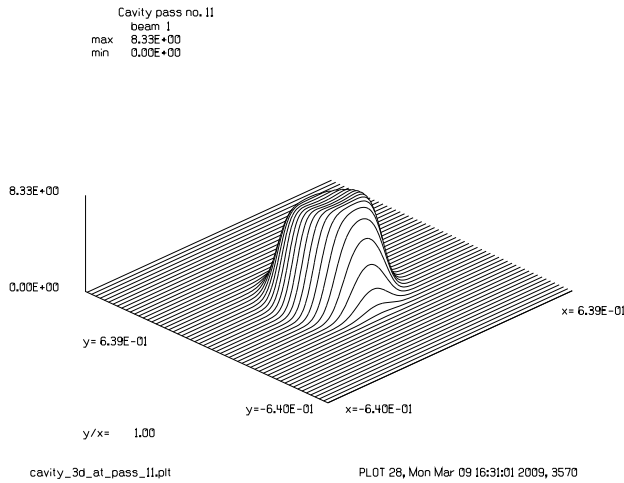
(a) Cavity pass 11 - mode 3d.
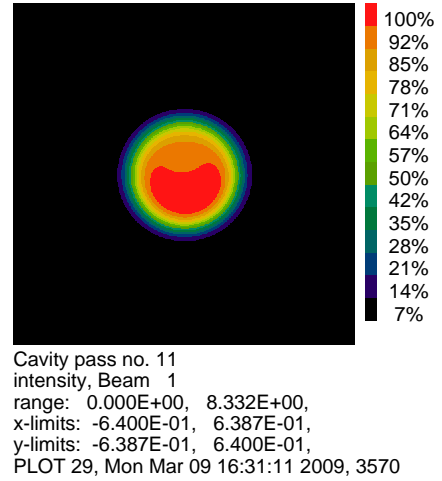
(b) Cavity pass 11 - mode burnpattern.
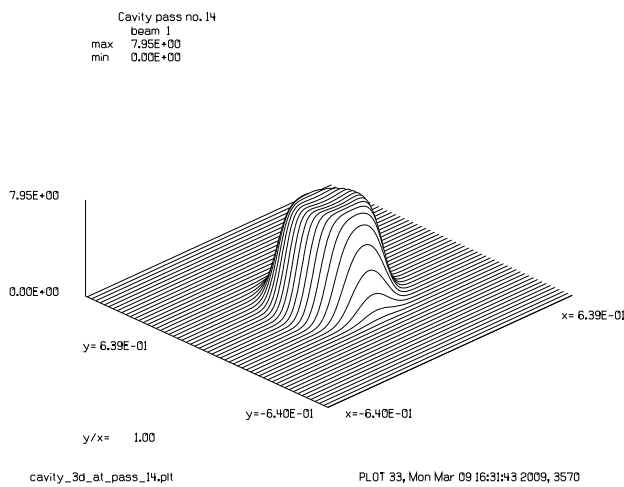
(c) Cavity pass 14 - mode 3d.
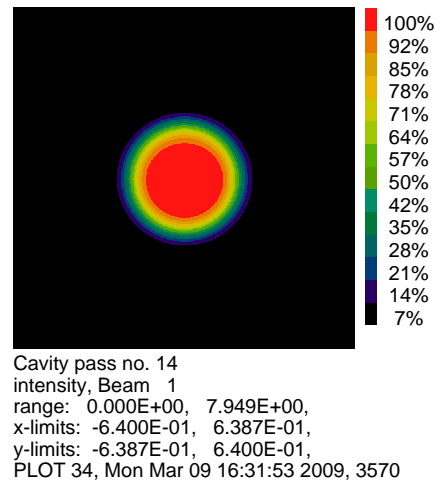
(d) Cavity pass 14 - mode burnpattern.

Figure 4.94: UR TISA at 820 nm: GLAD simulation showing cavity mode out of noise in front of VRM at resonator round-trips (cavity passes) 11, and 14.

4.5 Performance modeling

4.5.1 Introduction

In a laser, the pump radiation is absorbed by the material which has suitable energy transitions to achieve the inversion. Complete operation can be described with the cavity laser equations [Siegman86a, Siegman86c]. We limit the consideration to a solid-state laser material having 3 or 4 energy levels. Degeneracies of the energy levels are not taken into account. The TISA 4-level energy system is reduced to a 2-level energy system, where the populations of upper and lower lasing levels are considered. The laser rate equations are given by [Hodgson05a]

$$\frac{d\Delta N(t)}{dt} \;=\; W\left(N_0 - \Delta N(t)\right) - \frac{\Delta N(t)}{\tau} - \frac{\sigma_0\, c\, \Delta N(t)\, q(t)}{A\, L} \tag{98}$$

$$\frac{dq(t)}{dt} \;=\; \frac{\sigma_0\, c\, l\, \Delta N(t)}{L}\left(q(t) + 1\right) - \frac{q(t)}{\tau_c}\,, \tag{99}$$

where $\Delta N(t)$ and $q(t)$ describe the inversion density and the photon number, respectively. In Eq. 98, W is the pumping rate, N_0 is the doping concentration, and τ is the fluorescence lifetime of TISA (see Fig 4.4, page 24). $\Delta N(t)/\tau$ represents the spontaneous emission. The $+1$ in Eq. 99 is the extra noise photon due to the spontaneous emission. A is the pumped area of the crystal, and L is the resonator length. A suitable expression for $W_p(t)$ is given by [Saito01]

$$W_p(t) \;=\; \eta_Q\, \frac{P(t)}{h\, \nu_p\, V}\,, \tag{100}$$

where η_Q is the quantum efficiency of TISA with $\eta_Q \approx 1$ for pumping TISA near 532 nm. h is Planck's constant, ν_p is the pump photon energy, and V is the pumped volume. $P(t)$ is the temporal shape of the pump pulse.

Conveniently, the photon number q in Eq. 99 is replaced with a photon density number ϕ

$$\phi \;=\; \frac{q}{A\, L}\,. \tag{101}$$

4.5.2 Laser performance model

The initial conditions for the gain-switched, cavity dumped TISA laser are similar to initial conditions of a Q-switched laser. Consequently, the Q-switch-model approach can be applied. The applied TISA performance model is a set of two coupled nonlinear differential equations of first order, describing the photon density $\phi(t)$, and the inversion density $n(t)$ of the

system [Degnan89, Degnan98, Coyle95, Guerra94, Guerra99, Koechner99b].

$$\frac{dn(t)}{dt} \;=\; -\gamma\,c\,\sigma_e\,n(t)\,\phi(t) \tag{102}$$

$$\frac{d\phi(t)}{dt} \;=\; \phi(t)\left[c\,\sigma_e\left(\frac{l}{l'}\right)n(t) - \frac{\epsilon}{t_r}\right]. \tag{103}$$

In Eqs. 102 and 103, γ is the inversion reduction factor, c is the speed of light, σ_e is the stimulated emission cross section at the lasing wavelength, and l is the laser crystal length. The resonator length is given by l', and ϵ/t_r is the term describing the total loss rate per round-trip. $t_r = l'/c$ is the cavity round-trip time of a ring resonator. The term ϵ/t_r can be written as

$$\frac{\epsilon}{t_r} \;=\; \frac{c}{l'}\left[L + \ln\left(\frac{1}{R}\right)\right], \tag{104}$$

where L is the dissipative loss of the cavity and R is the reflectivity of the output coupler. For the stimulated emission cross section, values according to [Eggleston88] are used inside the modeling (see Fig. 4.1 on page 22).

The inversion reduction factor accounts for the slow or fast depletion of the lower laser level due to thermalization effects and level degeneracies. A value of the inversion reduction factor of $\gamma=1$ accounts for fast depletion with a negligible lifetime in the lower laser level, and a value of $\gamma=2$ is used for slow depletion, meaning that the lower laser level lifetime can influence the overall performance. As TISA is considered to be an almost ideal 4-level-system, a value of $\gamma=1$ is used throughout the modeling inside this work.

The spontaneous emission is not explicitly included in the differential equation system of Eqs. 102, 103. The spontaneous emission can not be omitted below threshold, but in the case considered here, operation above and several times above threshold is assumed. However, the spontaneous emission is not completely omitted, as it is included in the initial condition for the photon density, which is given below.

The solution of the coupled nonlinear differential equations is calculated with a computer algebra system[37] using numerical methods (Runge-Kutta algorithm). The equations are modified to account for the ring resonator, and the pumped and the resonator volume are adjusted for the elliptical pumped volume of the TISA crystal (increase by a factor of n (=refractive index of sapphire at Brewster angle) and astigmatic beam propagation resulting in a not symmetric round beam propagation. The photon density is therefore stretched to an elliptically shaped resonator volume, which is increased by a factor of n. Compared to a completely symmetrical round pumped volume and beam propagation, the influence of using a complete elliptical adapted equation system shows minor influence in the performance calculations and

---

[37]Wolfram Mathematica 5.2/6.0 was used to solve the nonlinear differential equation system of first order.

can be omitted. However, it represents are more detailed analysis and corresponds better to the situation and therefore it is being used in the complete performance analysis. The initial conditions of the inversion density $n(0)$, and photon density $\phi(0)$ for the solution of the differential equation system are given by

$$n(0) \;=\; \left(\frac{E_{ST}}{E_L}\right)/V \tag{105}$$

$$\phi(0) \;=\; \frac{n(0)\,A\,l\,\frac{l'}{c\,\tau_f}\,\frac{d\Omega}{4\,\pi}}{A\,l'}\,. \tag{106}$$

In Eq. 105, E_{ST} is the stored pump laser energy, which itself is a product of efficiency factors (see Appendix A) and the pump-pulse energy E_{pump}, E_L is the laser photon energy, and V is the pumped volume of the TISA crystal. In Eq. 106, A is the pumped area of the crystal, $d\Omega$ is the solid angle of the initial spontaneous emission (typically 1 mrad (sr)), and τ_f is the fluorescence lifetime of the upper laser level.

A frequently ambiguity and source of erroneous calculations found in the literature is to use the energy of the pump photons E_P for the initial inversion density [Elsayed03, Afzal94] (Eq. 105), instead of the energy of the lasing photons E_L [Degnan98, Kay05]. It is quite obvious that one is interested in how many lasing photons can be theoretically created out of the stored pump laser energy E_{ST}, which represents the initial inversion density and the total upper limit of lasing photons available given by the stored laser energy E_{ST}[38].

The resulting output pulse energy of the laser E_{out} can be found by integrating the photon density at the output coupler with reflectivity R with

$$E_{out} \;=\; \frac{h\,\nu_L\,V'}{t_r}\,\ln\left[\frac{1}{R}\right]\int_0^\infty \phi(t)\,dt\,, \tag{107}$$

where V' is the resonator (mode) volume. An example is given in Fig. 4.95, where the inversion density and the photon density evolution is shown with details given in the figure caption. Besides the output pulse energy and slope efficiency, extraction efficiency, total laser efficiency, pulse length, pulse linewidth, pulse built-up time, and optimum output coupler reflectivity can be calculated with this analysis. An even more extended analysis is done in Ch. 4.6.4 to calculate the spectral purity of the laser output.

In the following sections, the performance of stable and unstable TISA lasers operating at 935 nm (see Tab. 4.6) and 820 nm (see Tab. 4.7) is calculated by solving the differential equation system of Eqs. 102, 103 and the initial conditions of Eqs. 105, 106. The resonator parameters together with other parameters for the simulation can be found in the corre-

---

[38]The fit to experimental data is then usually done by adjusting the inversion reduction factor γ and/or by replacing the spectroscopic stimulated emission cross-section σ_e by an effective stimulated emission cross section $\sigma_{e,eff}$ given by $\sigma_{e,eff}=f_a\,\sigma_e$ (f_a: Boltzmann occupation factor).
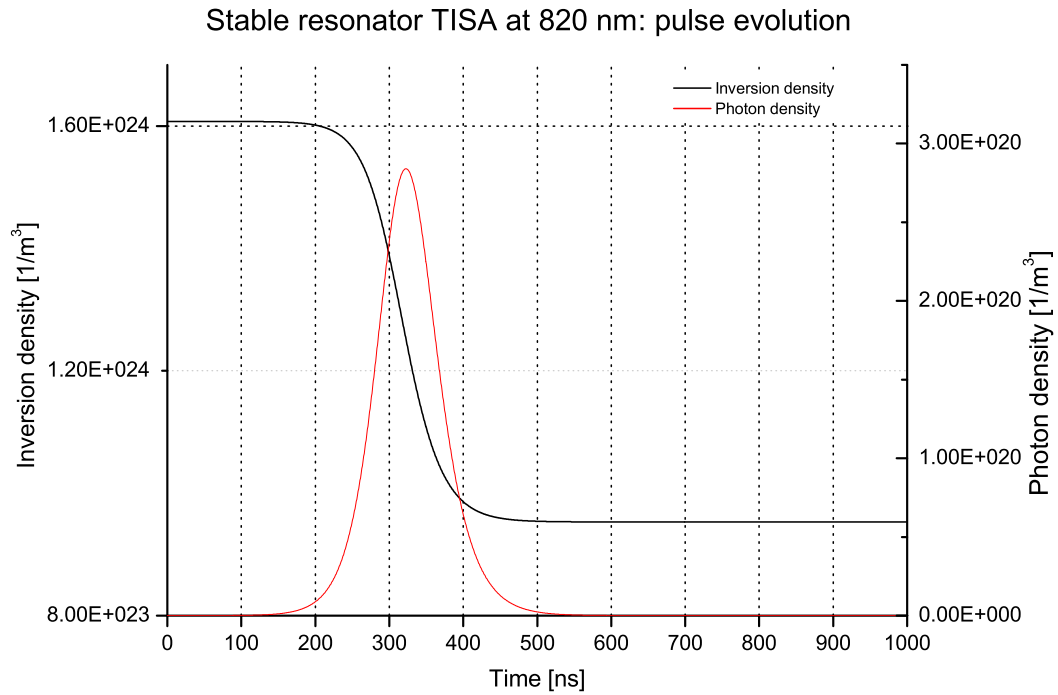
Figure 4.95: Inversion density and photon density evolution (rate equation). Selected values: pump pulse energy: 50 mJ, output coupler: 50%, calculated output pulse energy: 4.8 mJ, pulse-length: 95 ns (FWHM, full-width at half maximum), pulse built-up time: 323 ns. In this case, lasing threshold is at 39 mJ.

sponding tables of the sections.

Table 4.6: Performance modeling result matrix of 935 nm SR/UR TISA laser simulation.

Wavelength	Laser parameter	Stable resonator		Unstable resonator	
		abbrev.	page	abbrev.	page
935 nm	Optimum output coupler, R_{opt}	935nm SR R_{OPT}	136	-	-
	Output pulse energy, E_{out}	935nm SR E_{out}	137	935nm UR E_{out}	144
	Slope efficiency, η_{slope}	935nm SR η_{slope}	137	935nm UR η_{slope}	144
	Extraction efficiency, η_{extr}	935nm SR η_{extr}	138	935nm UR η_{extr}	145
	Total laser efficiency, η_{total}	935nm SR η_{total}	138	935nm UR η_{total}	145
	Pulse length, τ_p	935nm SR τ_p	139	935nm UR τ_p	146
	Linewidth, LW	935nm SR LW	139	935nm UR LW	146
	Pulse built-up time, $PBUT$	935nm SR $PBUT$	140	935nm UR $PBUT$	147

Table 4.7: Performance modeling result matrix of 820 nm SR/UR TISA laser simulation.

Wavelength	Laser parameter	Stable resonator abbrev.	page	Unstable resonator abbrev.	page
820 nm	Optimum output coupler, R_{opt}	820nm SR R_{OPT}	149	-	-
	Output pulse energy, E_{out}	820nm SR E_{out}	150	820nm UR E_{out}	155
	Slope efficiency, η_{slope}	820nm SR η_{slope}	150	820nm UR η_{slope}	156
	Extraction efficiency, η_{extr}	820nm SR η_{extr}	151	820nm UR η_{extr}	156
	Total laser efficiency, η_{total}	820nm SR η_{total}	151	820nm UR η_{total}	157
	Pulse length, τ_p	820nm SR τ_p	152	820nm UR τ_p	157
	Linewidth, LW	820nm SR LW	152	820nm UR LW	158
	Pulse built-up time, $PBUT$	820nm SR $PBUT$	153	820nm UR $PBUT$	158

4.5.3 Results for 935 nm - stable resonator

The results of the TISA laser modeling for a stable resonator at 935 nm (WALES) are presented in the following. The corresponding parameters for the resonator, pump conditions, and TISA parameters can be found in Tab. 4.8. Model input parameters are the TISA crystal and resonator length, the radius of the pump beam, where a top-hat profile is assumed, the pump pulse energy together with the repetition rate, the pump and laser wavelength, the stored energy in the upper laser level, the stimulated emission cross section at the lasing wavelength (for π-polarization), the fluorescence lifetime, and the output coupler reflectivity. A dissipative loss is introduced to account for mirror and cavity losses. The inversion reduction factor γ was discussed in the last section (Ch. 4.5). γ is set to a value of γ=1 in all performance calculations. The stored energy can be described by a product of efficiency factors ([Coyle95], Appendix A on page 187). The basic resonator parameters are not changed inside stable and unstable resonator modeling cases.

The calculations start with the determination of the optimum output coupler reflectivity for different pump power levels. The results is shown in Fig. 4.96. The value of R_{opt} is independent of the inversion reduction factor γ, but the maximum achieveable output energy varies within γ^{-1}. Lower pump-pulse energies require a higher degree of output coupler reflectivity. The calculations are continued with the R_{opt}-value for a pump pulse energy of 150 mJ[39] (R_{opt}=74.5%). The resulting output pulse energy for the optimum output coupler and an 85% output coupler is shown for variable dissipative losses (L={0.02, 0.04, 0.06}) in Fig. 4.97. As expected, the higher output coupler reflectivity results in a lower lasing

Table 4.8: Parameters of stable resonator TISA laser simulation at 935 nm.

Parameter, Unit	Value	Comment
TISA crystal length, cm	2	
Ring resonator length, cm	150	
Pump beam radius, mm	0.75	top-hat pump beam profile
Pump wavelength, nm	532	
Pump pulse length, ns	25	
Pump pulse energy, mJ	$0-1000$	
Repetition rate, Hz	250	according to pump laser
Stored pump pulse energy, %	42.5	E_{st}; see Appendix A, [Coyle95]
Lasing wavelength, nm	935	
Stim. emission cross section, cm^2	$1.39 \cdot 10^{-19}$	at 935 nm for π-polarization
Fluorescence lifetime, μs	3.15	at 300 K
Output-coupler reflectivity, %	74.5	variable; R_{opt} at 150 mJ
Dissipative loss, %	$2-6$	variable
Inversion reduction factor γ, dim.-less	1	

---

[39]Available pump pulse energy of pump laser at IPM: 150 mJ (average power: 37.5 W, 250 Hz).

Table 4.9: Stable resonator TISA laser simulation at 935 nm: optimum output coupler (OC) reflectivities R_{opt} for different pump pulse energies.

Pump pulse energy, mJ	Optimum OC, %	Output pulse energy, mJ
25	93.8	7.4
50	88.9	17.3
100	81.1	37.9
150	74.5	58.8
200	68.9	79.8
300	59.3	121.9
400	51.4	164.2
500	44.9	206.5

Stable resonator TISA at 935 nm: calculated optimum output coupler
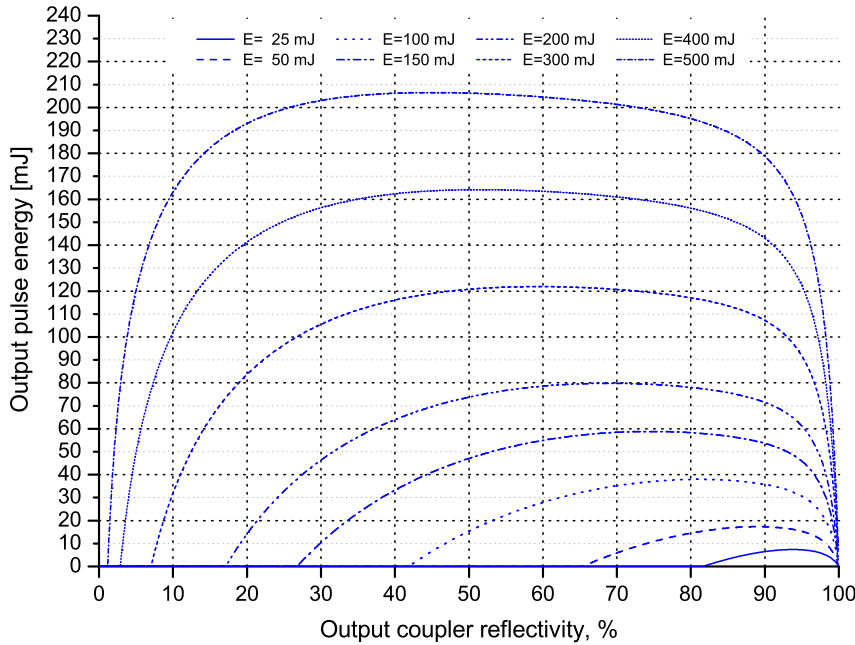
935nm
SR
R_{opt}

Figure 4.96: Stable resonator TISA laser at 935 nm: calculated optimum output coupler.

threshold. The extraction efficiency is shown in Fig. 4.99. The extraction efficiency is 92.2% (R_{opt}=74.5%, L=0.02) at a pump pulse energy of 150 mJ. A total laser efficiency of 38.9% can be reached (Fig. 4.100). The TISA output pulse length and the pulse linewidth are shown in Figs. 4.101 and 4.102. The linewidth is calculated assuming a Fourier-transform-limited linewidth $\Delta\nu$ of the TISA laser pulse with Gaussian pulse shape and full width at half maximum (FWHM) pulse duration $\Delta\tau$:

$$\Delta\nu \quad = \quad \frac{2\ln 2}{\pi\Delta\tau}. \tag{108}$$

Pulse length and corresponding linewidth are within the specifications found in Tab. 2.1.
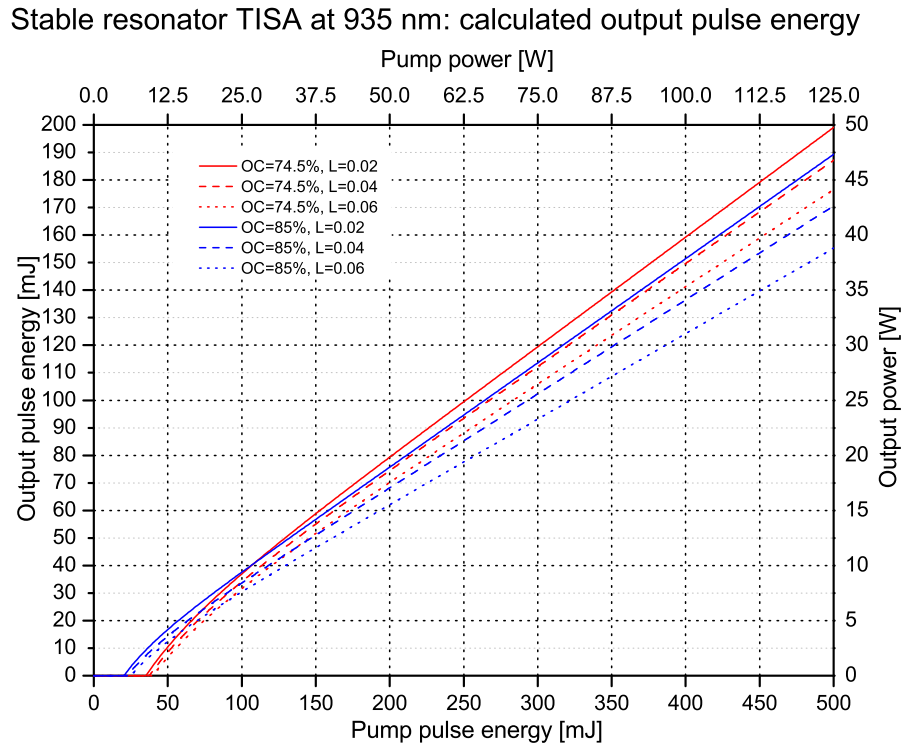
Figure 4.97: Stable resonator TISA laser at 935 nm: calculated output pulse energy.

935nm
SR
E_{out}
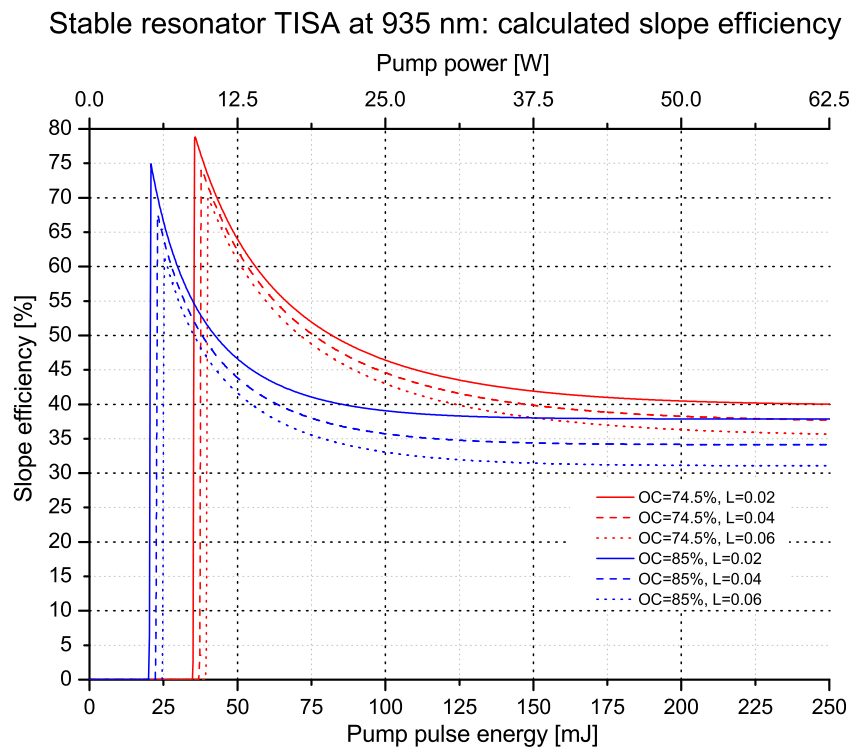
Figure 4.98: Stable resonator TISA laser at 935 nm: calculated slope efficiency.

935nm
SR
η_{slope}

The calculated pulse built-up time is shown in Fig. 4.103. At a pump pulse level of 150 mJ, the pulse built-up time is around 80 ns, which are about 16 resonator round-trips (5 ns for

Stable resonator TISA at 935 nm: calculated extraction efficiency
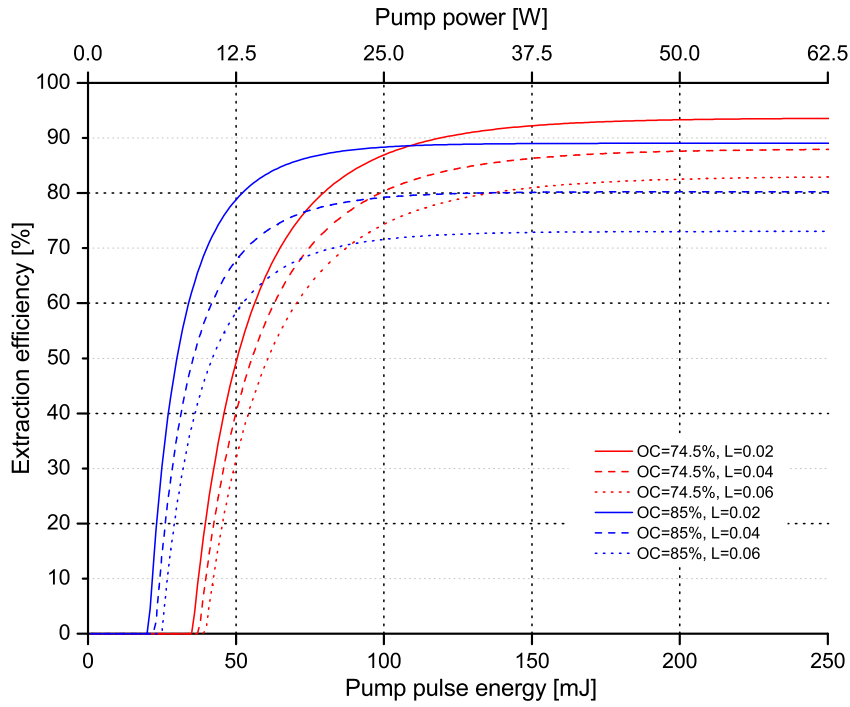
Figure 4.99: Stable resonator TISA laser at 935 nm: calculated extraction efficiency.

935nm
SR
η_{extr}

Stable resonator TISA at 935 nm: calculated total laser efficiency
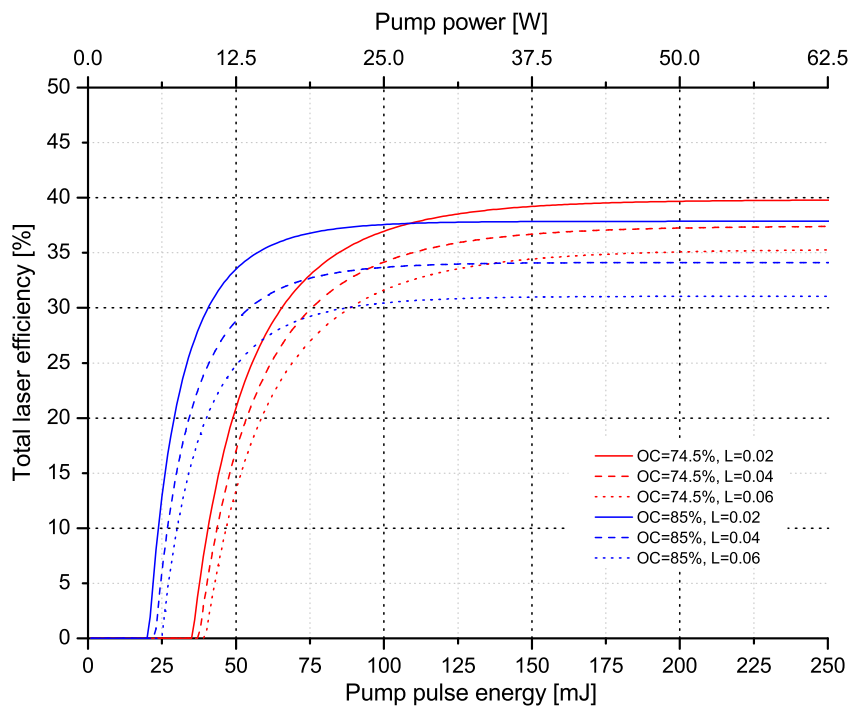
Figure 4.100: Stable resonator TISA laser at 935 nm: calculated total laser efficiency.

935nm
SR
η_{total}

each round-trip). Table 4.10 summarizes the results for the 935-nm stable resonator TISA laser.

Stable resonator TISA at 935 nm: calculated pulse length
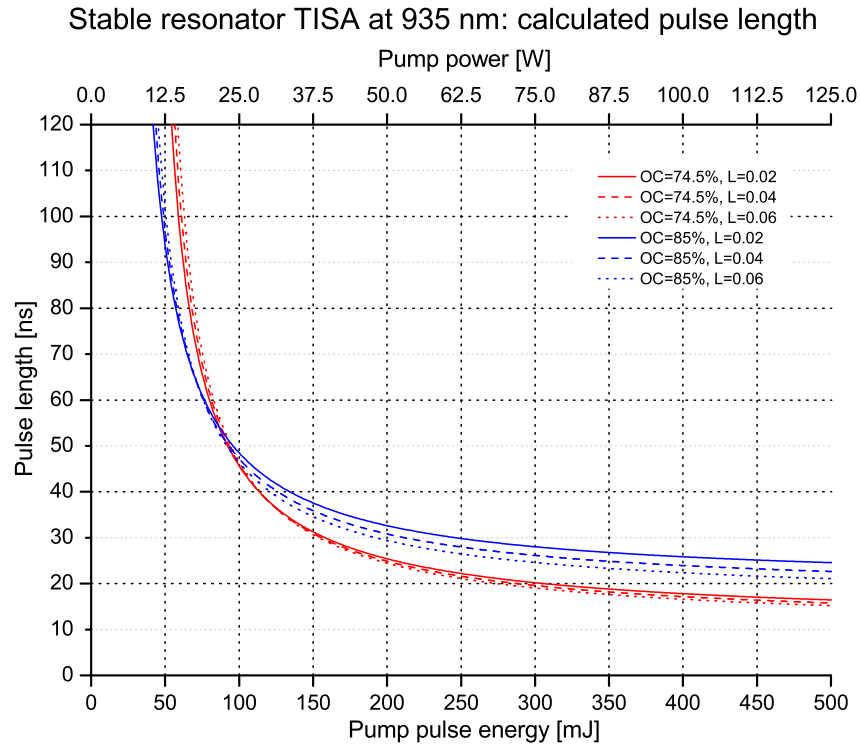
Figure 4.101: Stable resonator TISA laser at 935 nm: pulse length.

935nm
SR
τ_p

Stable resonator TISA at 935 nm: calculated linewidth
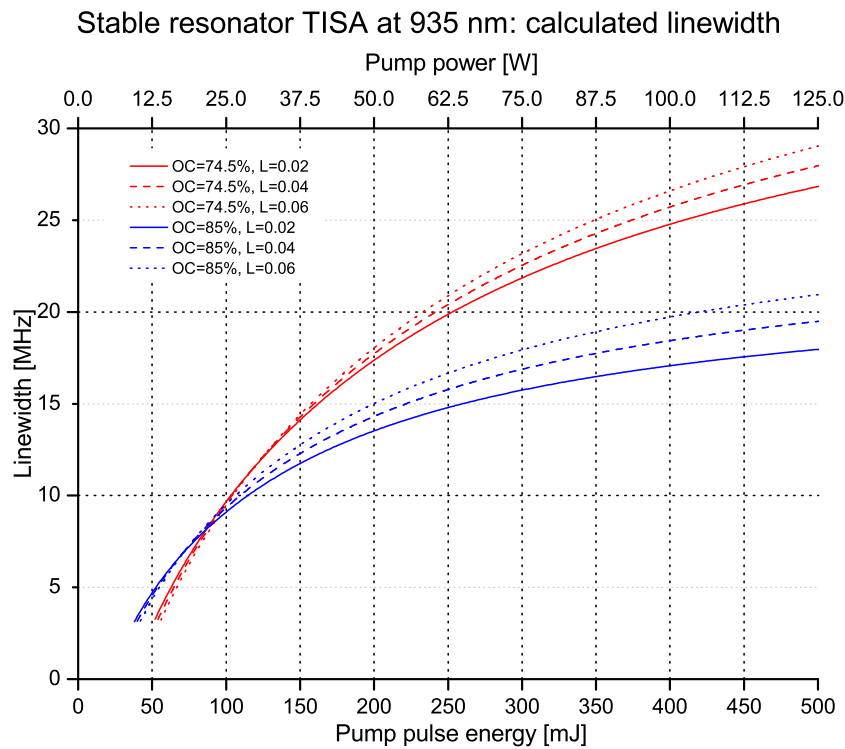
Figure 4.102: Stable resonator TISA at 935 nm: linewidth.

935nm
SR
LW
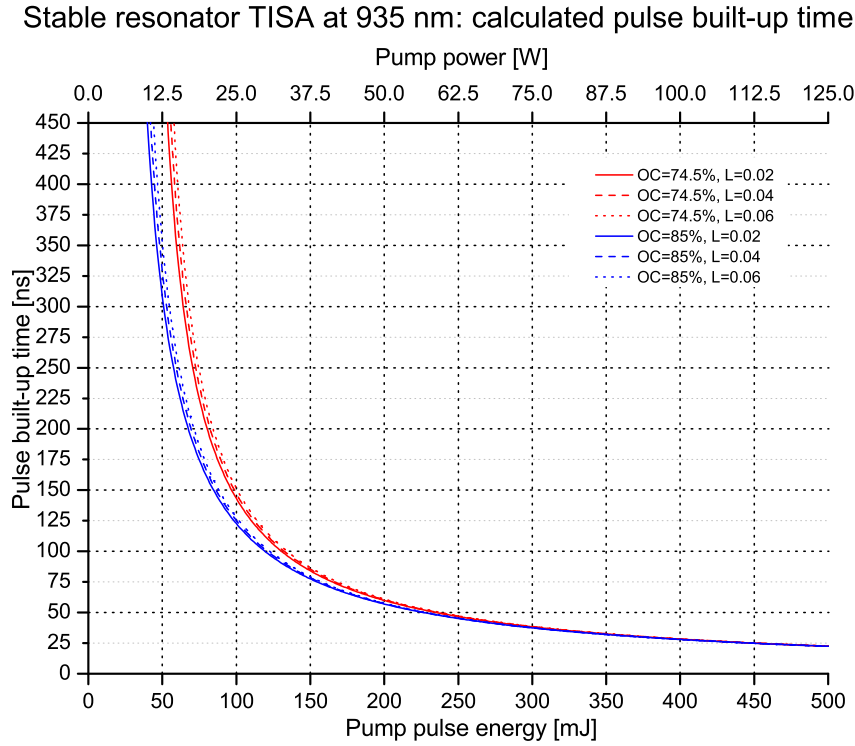
Figure 4.103: Stable resonator TISA at 935 nm: pulse built-up time.

935nm
SR
PBUT

Table 4.10: Modeling results for SR TISA laser simulation at 935 nm. Results are given for (maximum) pump pulse energy of 150 mJ and a dissipative loss of L=0.02.

Parameter, Unit	Value	Comment
Optimum OC (R_{opt}), %	74.5	at 150 mJ pump-pulse energy
Output pulse energy, mJ	58.4	
Slope efficiency, %	41.9	
Threshold energy, mJ	$\approx$36	
Extraction efficiency, %	92.2	
Excitation efficiency, %	42.2	
Total laser efficiency, %	38.9	
Pulse length, ns	31.3	
Linewidth, MHz	14.1	FT limit
Pulse built-up time, ns	84.1	$\approx$16$-$17 round-trips

4.5.4 Results for 935 nm - unstable resonator

For the performance modeling of the unstable resonator, an effective magnification M_{eff} is calculated with

$$M_{eff} = \frac{M_x + M_y}{2} \tag{109}$$

out of the 4×4-beam-propagation matrix instead of treating sagittal and tangential planes independently. The calculation of M_{eff} is performed for each pump-power level, as the thermal lens changes the total magnification and therefore the resonator loss.

The loss per round-trip ΔV of an unstable resonator with magnification M and a super-Gaussian (VRM) output coupler with center reflectivity R_0 is given by [DeSilvestri88a, DeSilvestri88b]

$$\Delta V = 1 - \frac{R_0}{M^2}, \tag{110}$$

which is independent of the super-Gaussian order n in the geometric approximation. The loss factor V (see Eq. 76 on page 112) of the VRM, which can be seen as the corresponding mirror reflectivity of a stable resonator is given by

$$\begin{aligned} V &= 1 - \Delta V \\ &= \frac{R_0}{M^2}. \end{aligned} \tag{111}$$

Consequently, the resonator loss term of Eq. 104 in the performance model is modified for the unstable resonator laser to

$$\frac{\epsilon}{t_r} = \frac{c}{l'} \left[L + \ln\left(\frac{1}{R_0}\right) + \ln\left(M_{eff}^2\right) \right], \tag{112}$$

to adjust the total resonator loss by the additional resonator loss given by the (effective) magnification M_{eff} of the unstable resonator (see Eq. 76) and the VRM center reflectivity R_0. The loss term ϵ/t_r is therefore a function of the (effective) magnification as a result of the thermal lens power at the corresponding pump-power level (Eq. 112). This is in contrast to a stable resonator, where one can assume a constant resonator loss term ϵ/t_r for each pump-power level, as the total loss is given by dissipative losses and the loss at the output coupler. Furthermore, in an end-pumped geometry resonator (e.g. TISA laser), the thermal load, thermal lens, beam propagation, magnification, and therefore the overall resonator loss changes significantly compared to a side-pumped geometry resonator (e.g. Nd:YAG laser), where a constant heat load and thermal lens due to the flashlamps or diodes can be assumed. To sum up, it is more challenging to design an unstable resonator laser in an end-pumped

geometry compared to a side-pumped design. However, extended FEA thermal modeling can support the design procedure and serves as a suitable tool.

In the calculation for the the output energy of the unstable resonator TISA laser, the mirror reflectivity R in Eq. 107 is therefore replaced by the loss factor V of the VRM output coupler of the unstable resonator $R \equiv R_{eff} = R_0/M_{eff}^2$ to yield an effective output coupler reflectivity R_{eff} of the VRM.

All subsequent performance results for the unstable resonator are valid until the effective magnification is greater than 1 ($M_{eff}>1$), which means that the resonator is (positive) unstable. Therefore, all subsequent performance plots for the unstable resonator end at a pump-power value according to $M=1$ (stability limit). This can be seen in the corresponding magnification plots for M_{eff} in Ch 4.4.2 (page 122). For a TISA laser at 935 nm, the limit for $M_{eff}=1$ is at a pump-power level of $\approx$124 mJ, and for a TISA laser at 820 nm, the limit is at $\approx$151 mJ. The design magnification of $M=1.6$ and the magnification of the resonator set up $M=1.25$ due to the confocality condition serve as points of orientation. The pump pulse level to reach $M_{eff}=1.25$ is at $\approx$114 mJ for a TISA laser at 935 nm, and $\approx$138 mJ for a TISA laser at 820 nm (see Fig. 4.88).

The parameters for the performance modeling of the unstable TISA laser at 935 nm are shown in Tab. 4.11. The performance calculation results are depicted in the subsequent Figs. 4.104-4.110. Compared to a stable resonator, the end-pumped unstable resonator TISA laser shows a limited operation regime together with a high sensitivity to the pump-power level. This is evident in all calculated performance parameters and can be explained, as the losses at low pump-power levels (high magnification) are large (see Eq. 110). However, as the pump power increases, the overall losses become significantly smaller, and the unstable resonator performs better. Table 4.12 summarizes the results for the 935 nm unstable resonator TISA laser. A total laser efficiency of 23.5% can be reached (Fig. 4.107).

Table 4.11: Parameters of unstable resonator (UR) TISA laser simulation at 935 nm.

Parameter, Unit	Value	Comment
TISA crystal length, cm	2	
Ring resonator length, cm	98.5	
Pump beam radius, mm	0.75	top-hat pump-beam profile
Pump wavelength, nm	532	
Pump pulse length, ns	25	
Pump pulse energy, mJ	$0-1000$	
Repetition rate, Hz	250	according to pump laser
Stored pump pulse energy, %	42.5	E_{st}; see Appendix A, [Coyle95]
Lasing wavelength, nm	935	
Stim. emission cross section, cm^2	$1.39 \cdot 10^{-19}$	at 935 nm for π-polarization
Fluorescence lifetime, μs	3.15	at 300 K
Center reflectivity R_0 of VRM, %	60	
Effective magnification M_{eff}, dim.-less	$1-5$	according to beam propagation
Effective output-coupler reflectivity, %	R_0/M_{eff}^2	
Dissipative loss, %	$2-6$	variable
Inversion reduction factor γ, dim.-less	1	

Table 4.12: Modeling results for UR TISA laser simulation at 935 nm. Results are given for (maximum) pump pulse energy of 120 mJ corresponding to an effective magnification of M_{eff}=1.1 and a dissipative loss of L=0.02.

Parameter, Unit	Value	Comment
Effective magnification M_{eff}, dim.-less	1.1	
Center reflectivity R_0 of VRM, %	60.0	
Output pulse energy, mJ	28.2	
Slope efficiency, %	349.0	
Threshold energy, mJ	$\approx$113.6	
Extraction efficiency, %	55.3	
Excitation efficiency, %	42.5	
Total laser efficiency, %	23.5	
Pulse length, ns	38.3	
Linewidth, MHz	11.5	FT limit
Pulse built-up time, ns	142.7	$\approx$ 44 round-trips
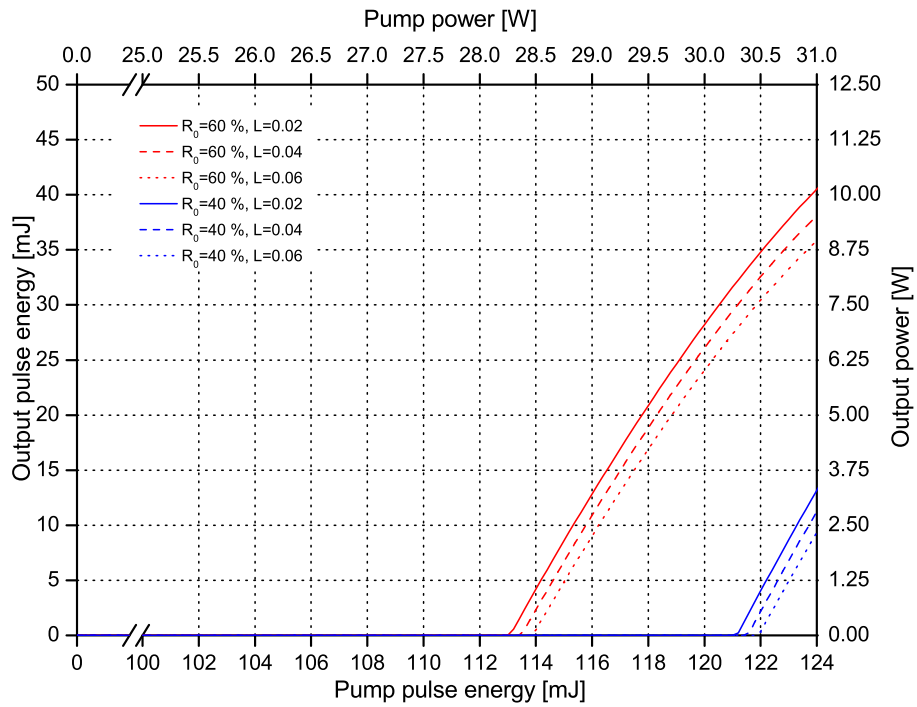
Figure 4.104: Unstable resonator TISA laser at 935 nm: calculated output pulse energy.

935nm
UR
E_{out}
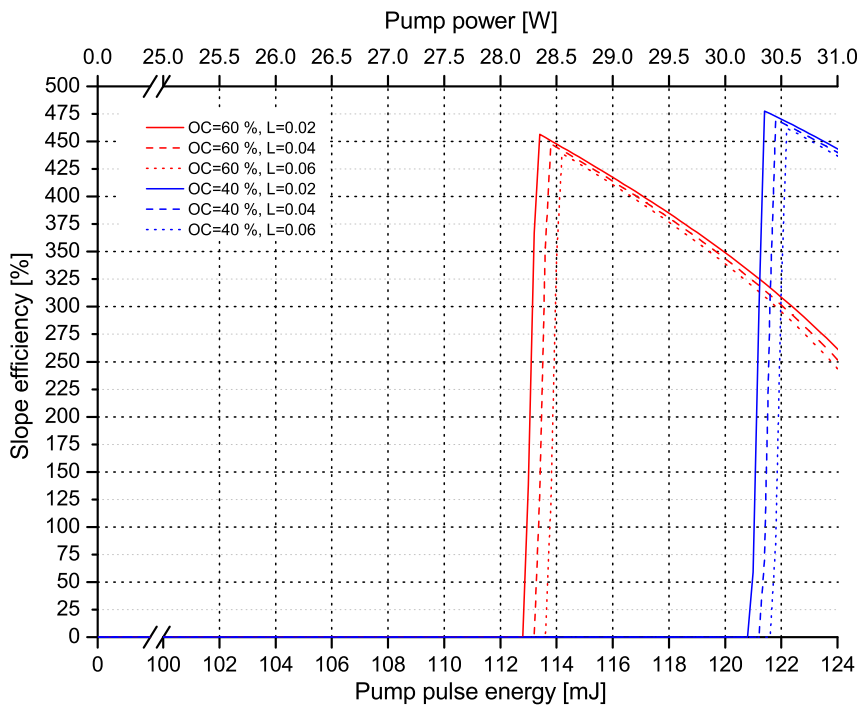
Figure 4.105: Unstable resonator TISA laser at 935 nm: calculated slope efficiency.

935nm
UR
η_{slope}

Unstable resonator TISA at 935 nm: calculated extraction efficiency
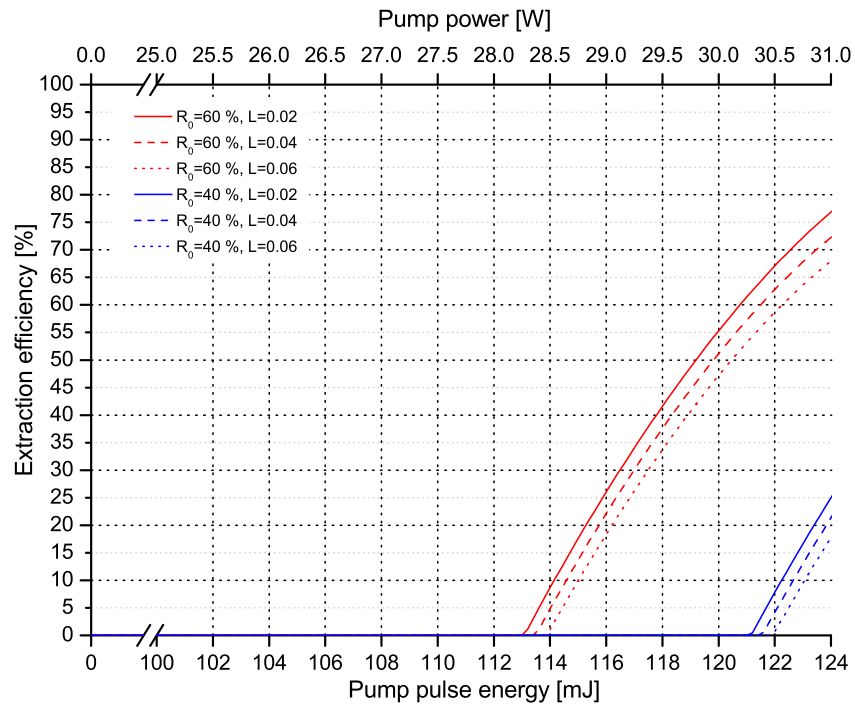
Figure 4.106: Unstable resonator TISA laser at 935 nm: calculated extraction efficiency.

935nm
UR
η_{extr}

Unstable resonator TISA at 935 nm: calculated total laser efficiency
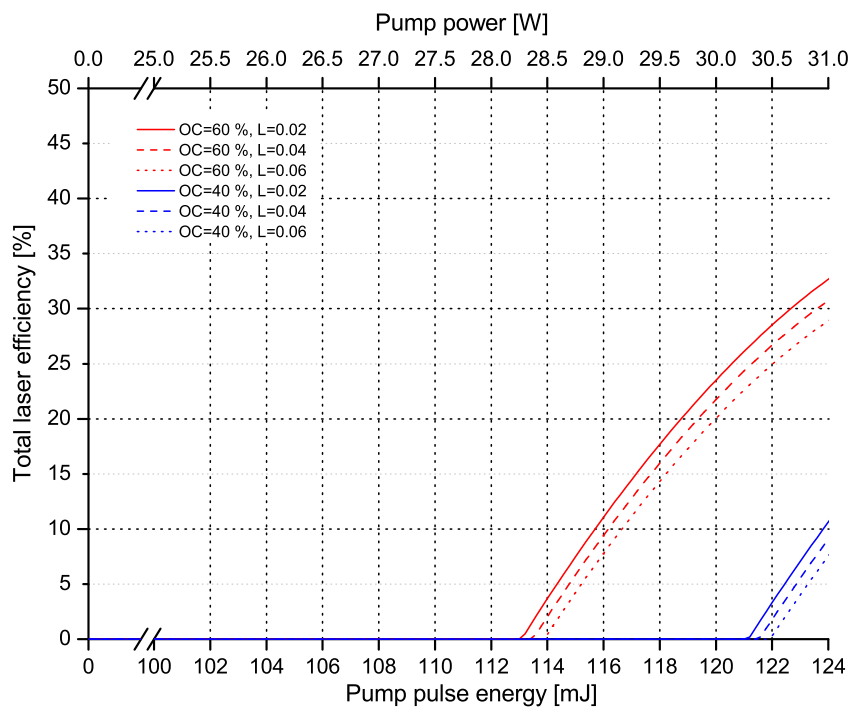
Figure 4.107: Unstable resonator TISA laser at 935 nm: calculated total laser efficiency.

935nm
UR
η_{total}

Unstable resonator TISA at 935 nm: calculated pulse length
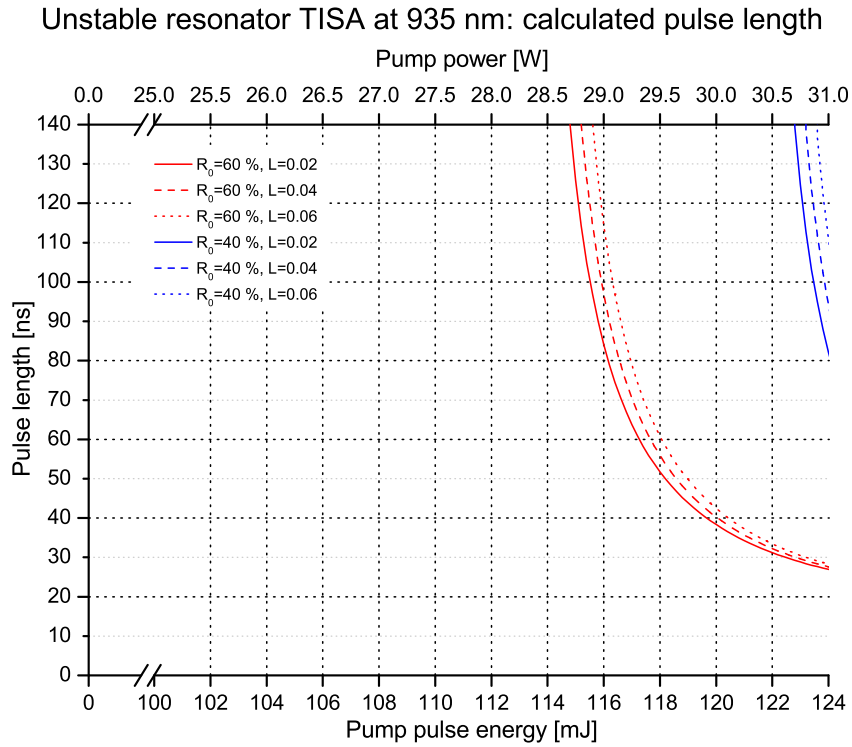
Figure 4.108: Unstable resonator TISA laser at 935 nm: pulse length.

935nm
UR
τ_p

Unstable resonator TISA at 935 nm: calculated linewidth
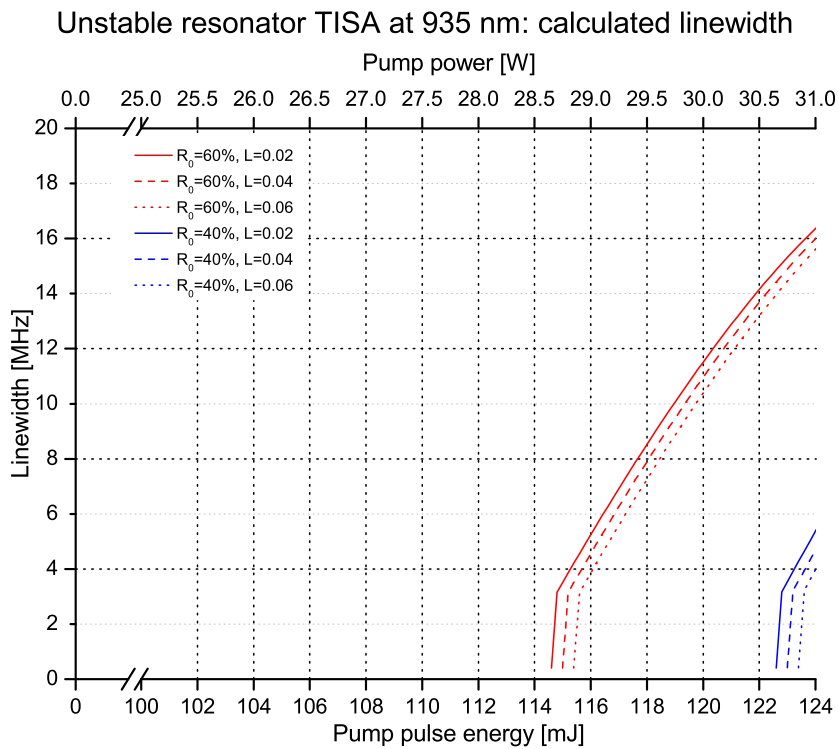
Figure 4.109: Unstable resonator TISA laser at 935 nm: linewidth.

935nm
UR
LW
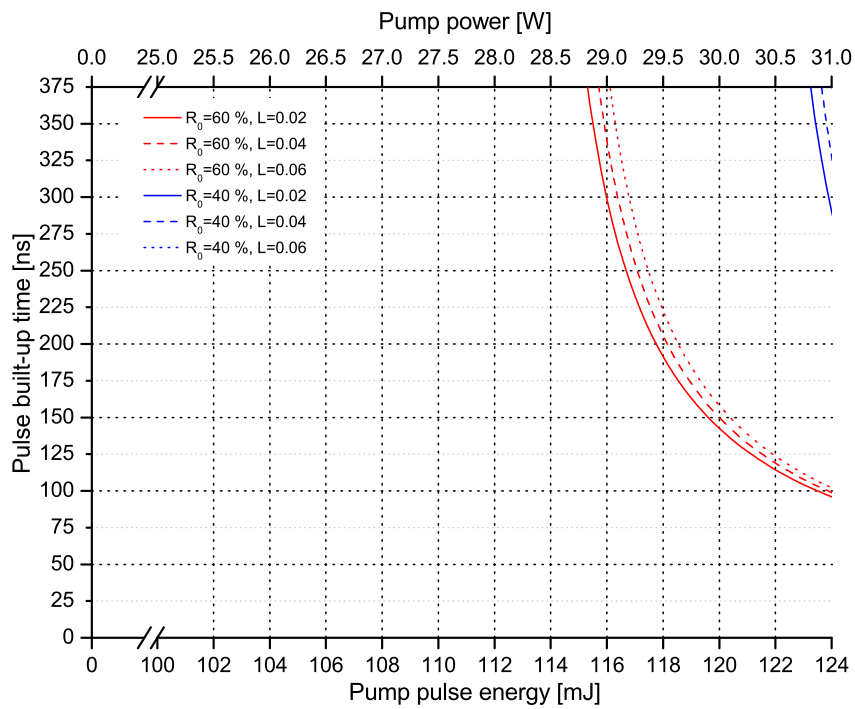
Figure 4.110: Unstable resonator TISA laser at 935 nm: pulse built-up time.

935nm
UR
PBUT

4.5.5 Results for 820 nm – stable resonator

In the following, the results for a stable resonator TISA laser operating at 820 nm are presented. The parameters for the simulation can be found in Tab. 4.13. The resulting optimum output coupler reflectivities for different pump pulse energies are listed in Tab. 4.14 and shown in Fig. 4.111. The calculations are continued with the optimum output coupler set for a pump pulse energy of 150 mJ, which is 58.6%.

In Figs. 4.112-4.118, the TISA output pulse energy, extraction efficiency, pulselength and linewidth are presented. Table 4.15 summarizes the results for the 820 nm stable resonator TISA laser. A total laser efficiency of 46.4% can be reached (Fig. 4.115).

A calculation for the complete TISA wavelength range for different OC reflectivities is shown Figs. 4.126a-4.126c in Ch. 4.5.7.

Table 4.13: Parameters of stable resonator TISA laser simulation at 820 nm.

Parameter, Unit	Value	Comment
TISA crystal length, cm	2	
Ring resonator length, cm	150	
Pump beam radius, mm	0.75	top-hat pump beam profile
Pump wavelength, nm	532	
Pump pulse length, ns	25	
Pump pulse energy, mJ	$0-1000$	
Repetition rate, Hz	250	according to pump laser
Stored pump energy, %	48.5	E_{st}; see Appendix A, [Coyle95]
Lasing wavelength, nm	820	
Stim. emission cross section, cm^2	$2.85 \cdot 10^{-19}$	at 820 nm for π-polarization
Fluorescence lifetime, μs	3.15	at 300 K
Output-coupler reflectivity, %	58.6	variable; R_{opt} at 150 mJ
Dissipative loss, %	$2-6$	variable
Inversion reduction factor, dim.-less	1	

Table 4.14: Stable resonator TISA laser simulation at 820 nm: optimum output coupler (OC) reflectivities R_{opt} for different pump pulse energies.

Pump pulse energy, mJ	Optimum OC, %	Output pulse energy, mJ
25	88.7	9.9
50	80.7	21.7
100	68.3	45.6
150	58.6	69.6
200	50.7	93.7
300	38.5	141.9
400	29.6	190.3
500	22.9	238.6

Table 4.15: Modeling results for SR TISA laser simulation at 820 m. Results are given for (maximum) pump pulse energy of 150 mJ and a dissipative loss of L=0.02.

Parameter, Unit	Value	Comment
Optimum OC (R_{opt}), %	58.6	at 150 mJ pump-pulse energy
Output pulse energy, mJ	69.6	
Slope efficiency, %	48.1	
Threshold energy, mJ	$\approx$31	
Extraction efficiency, %	95.7	
Excitation efficiency, %	48.5	
Total laser efficiency, %	46.4	
Pulse length, ns	15.8	
Linewidth, MHz	27.9	FT limit
Pulse built-up time, ns	39.7	$\approx$ 8 round-trips

Stable resonator TISA at 820 nm: calculated optimum output coupler
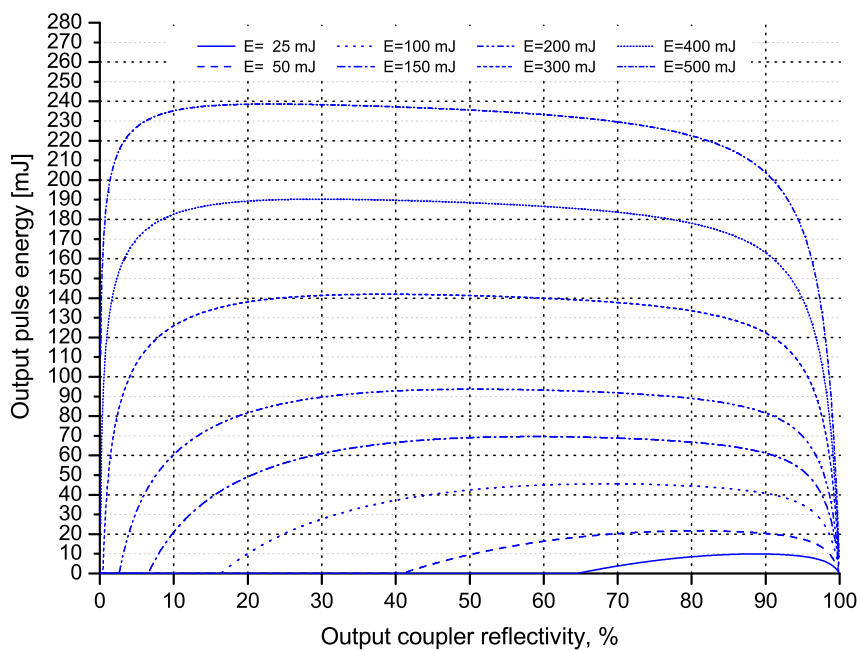
Figure 4.111: Stable resonator TISA laser at 820 nm: calculated optimum output coupler.

820nm
SR
R_{opt}
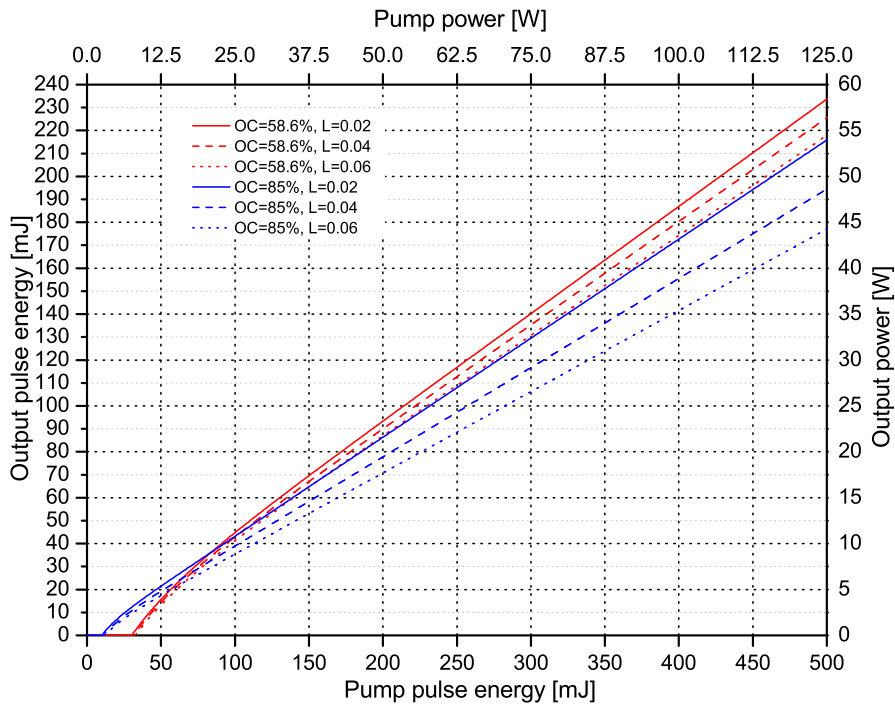
Figure 4.112: Stable resonator TISA laser at 820 nm: calculated output pulse energy.

820nm
SR
E_{out}
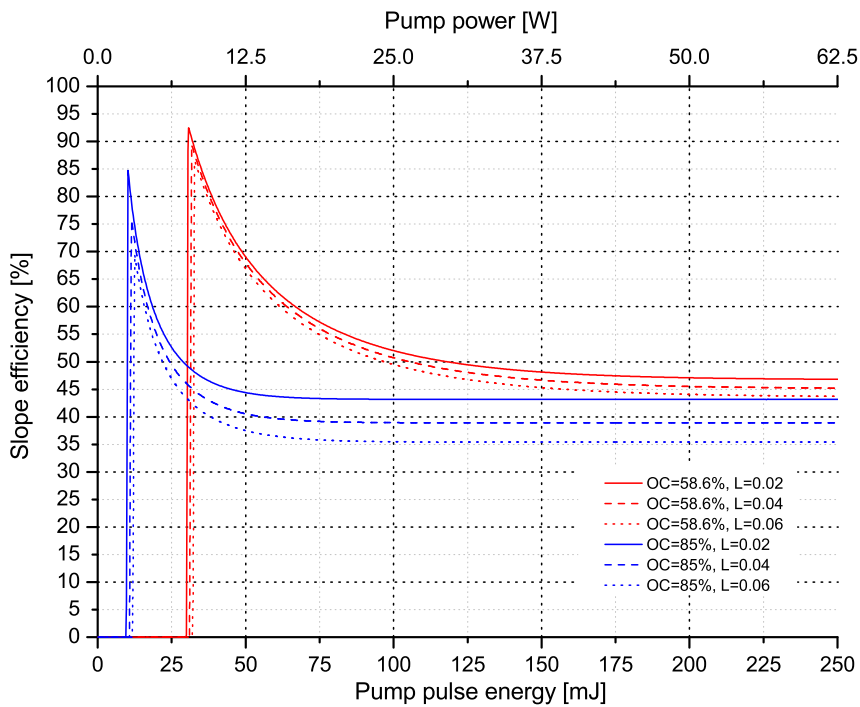
Figure 4.113: Stable resonator TISA laser at 820 nm: calculated slope efficiency.

820nm
SR
η_{slope}

Stable resonator TISA at 820 nm: calculated extraction efficiency
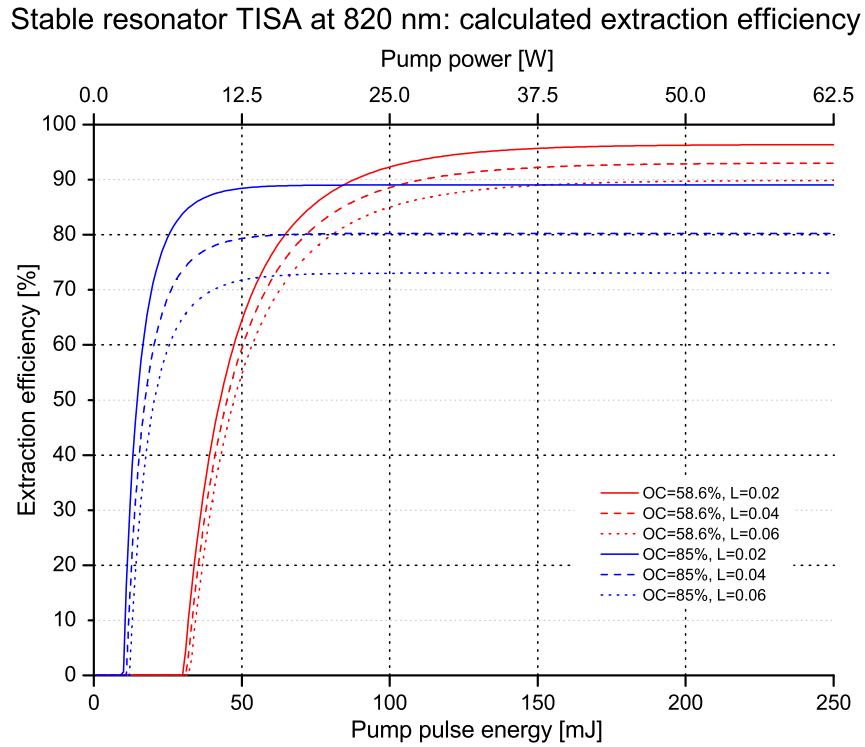
Figure 4.114: Stable resonator TISA laser at 820 nm: calculated extraction efficiency.

820nm
SR
η_{extr}

Stable resonator TISA at 820 nm: calculated total laser efficiency
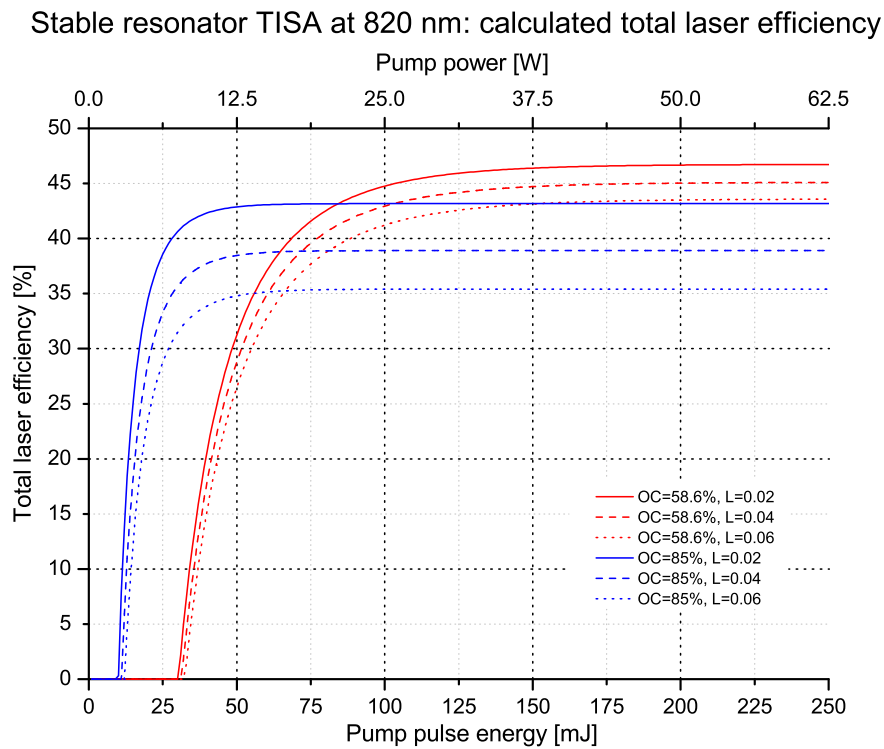
Figure 4.115: Stable resonator TISA laser at 820 nm: calculated total laser efficiency.
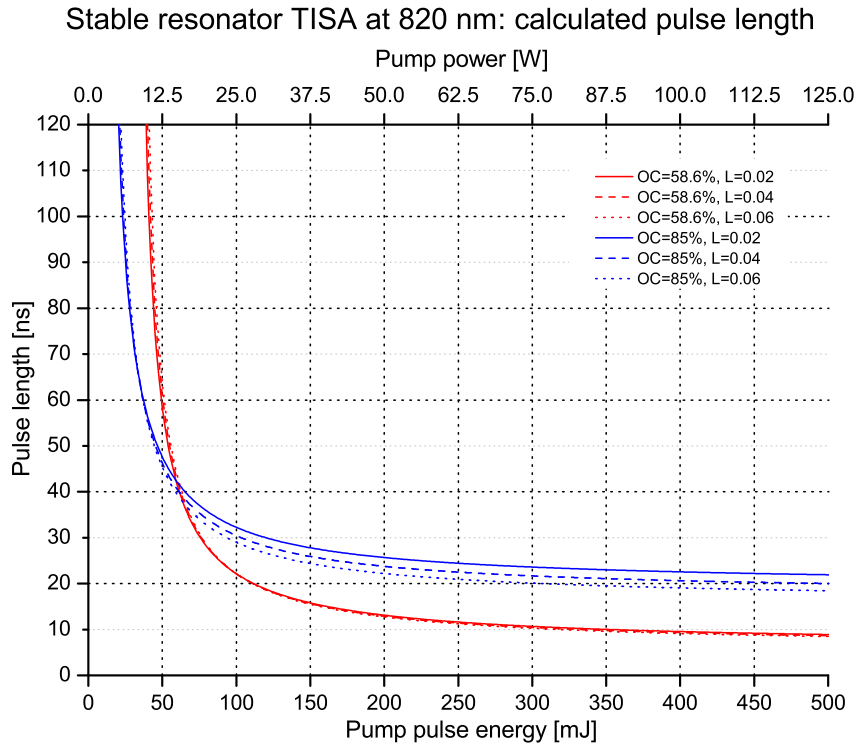
820nm
SR
η_{total}

Figure 4.116: Stable resonator TISA laser at 820 nm: pulse length.

820nm
SR
τ_p
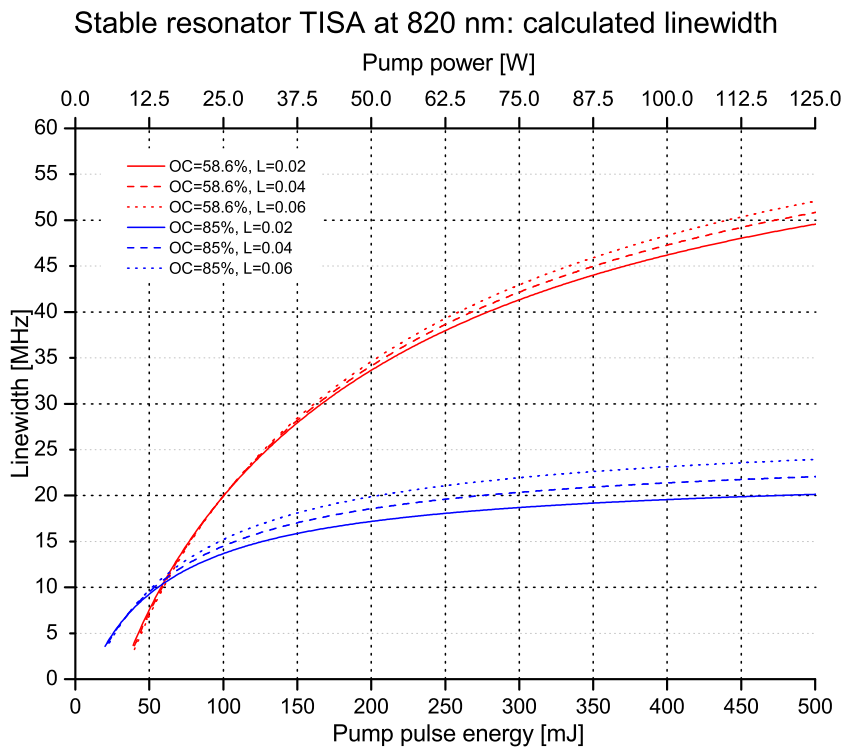
Figure 4.117: Stable resonator TISA laser at 820 nm: linewidth.

820nm
SR
LW
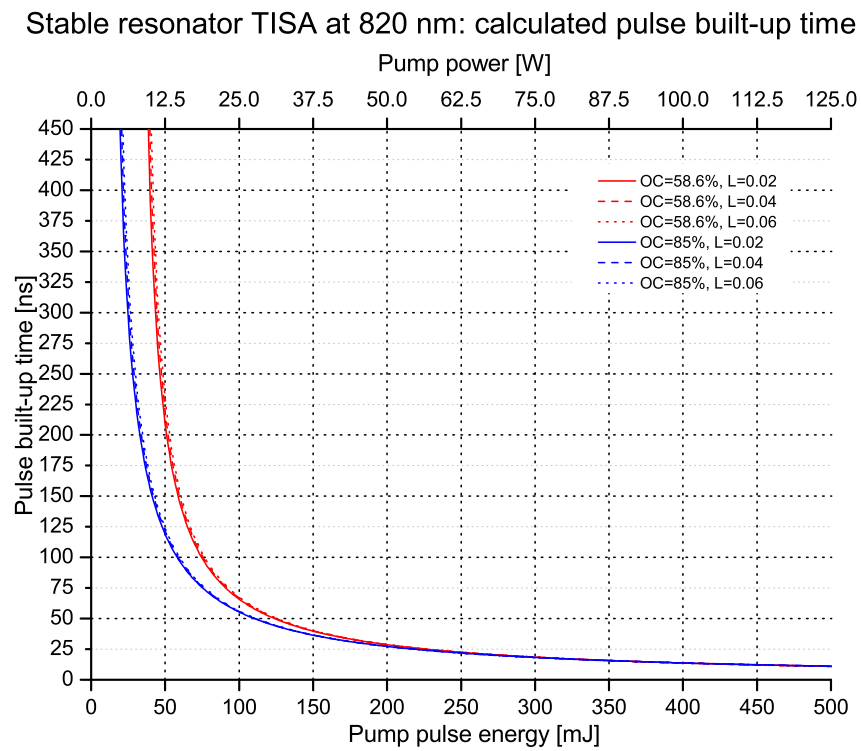
Figure 4.118: Stable resonator TISA laser at 820 nm: pulse built-up time.

820nm
SR
PBUT

4.5.6 Results for 820 nm - unstable resonator

The results for the 820 nm unstable TISA laser are presented in the following. The parameters for the simulation can be found in Tab. 4.16.

The corresponding calculated laser performance parameters are shown in Figs. 4.119-4.125. Again, the unstable resonator shows a limited and highly sensitive operation regime concerning the pump-pulse energy. The width of the operation zone is about 45 mJ. A stable pump laser is therefore required. As already pointed out in Ch. 4.5.4, this behavior can be explained with the sensitivity of end-pumped TISA lasers to thermal lensing, and as consequence with a strongly varying loss (magnification) as a result of the changing beam propagation.

Table 4.17 lists the results of the 820 nm unstable TISA laser performance calculations. A total laser efficiency of 42.8% can be reached (Fig. 4.122).

Table 4.16: Parameters of unstable resonator TISA laser performance simulation at 820 nm.

Parameter, Unit	Value	Comment
TISA crystal length, cm	2	
Ring resonator length, cm	98.5	
Pump beam radius, mm	0.75	top-hat pump-beam profile
Pump wavelength, nm	532	
Pump pulse length, ns	25	
Pump pulse energy, mJ	$0-1000$	
Repetition rate, Hz	250	according to pump laser
Stored pump pulse energy, %	48.5	E_{st}; see Appendix A, [Coyle95]
Lasing wavelength, nm	820	
Stim. emission cross section, cm^2	$2.85 \cdot 10^{-19}$	at 820 nm for π-polarization
Fluorescence lifetime, μs	3.15	at 300 K
Center reflectivity R_0 of VRM, %	60	
Effective magnification M_{eff}, dim.-less	$1-5$	according to beam propagation
Effective output-coupler reflectivity, %	R_0/M_{eff}^2	
Dissipative loss, %	$2-6$	variable
Inversion reduction factor γ, dim.-less	1	

Table 4.17: Modeling results for UR TISA laser simulation at 820 nm. Results are given for pump pulse energy of 138.4 mJ corresponding to an effective magnification of M_{eff}=1.25 and a dissipative loss of L=0.02.

| Parameter, Unit	Value	Comment
Effective magnification M_{eff}, dim.-less	1.25	
Center reflectivity R_0 of VRM, %	60.0	
Output pulse energy, mJ	59.3	
Slope efficiency, %	121.0	
Threshold energy, mJ	≈107.2	
Extraction efficiency, %	88.4	
Excitation efficiency, %	48.4	
Total laser efficiency, %	42.8	
Pulse length, ns	10.7	
Linewidth, MHz	41.2	FT limit
Pulse built-up time, ns	35.5	$\approx 10-11$ round-trips
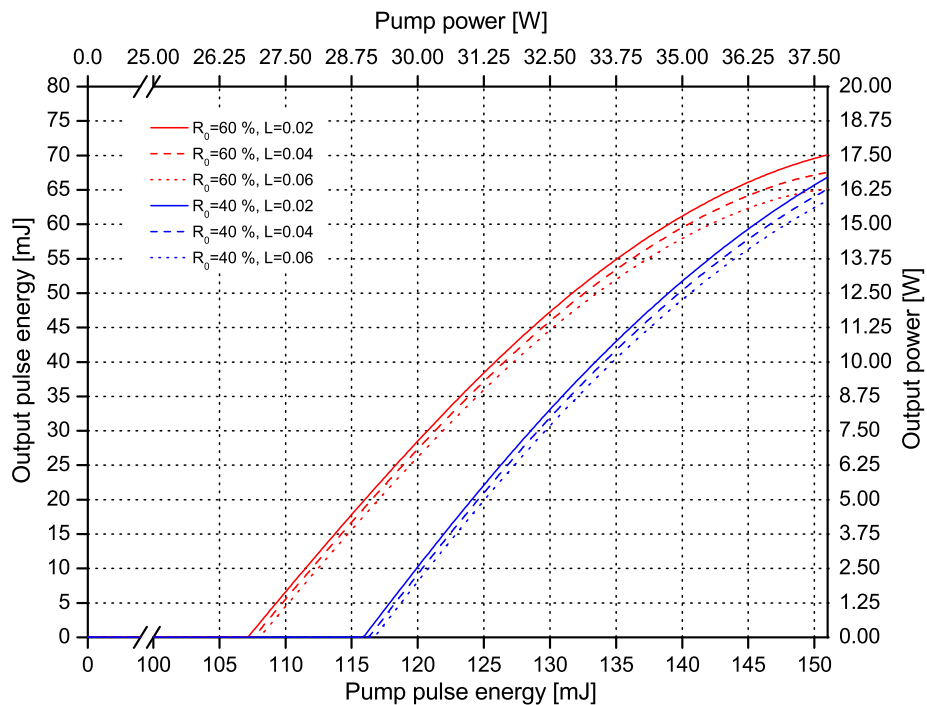
Figure 4.119: Unstable resonator TISA laser at 820 nm: calculated output pulse energy.

820nm
UR
E_{out}

Unstable resonator TISA at 820 nm: calculated slope efficiency
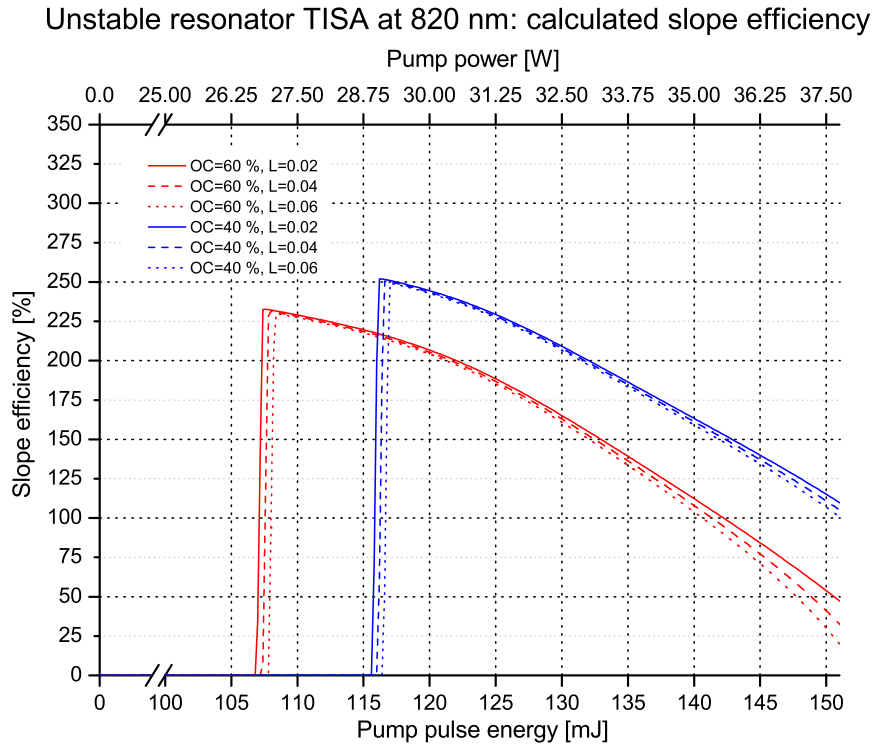
Figure 4.120: Unstable resonator TISA laser at 820 nm: calculated slope efficiency.

Unstable resonator TISA at 820 nm: calculated extraction efficiency
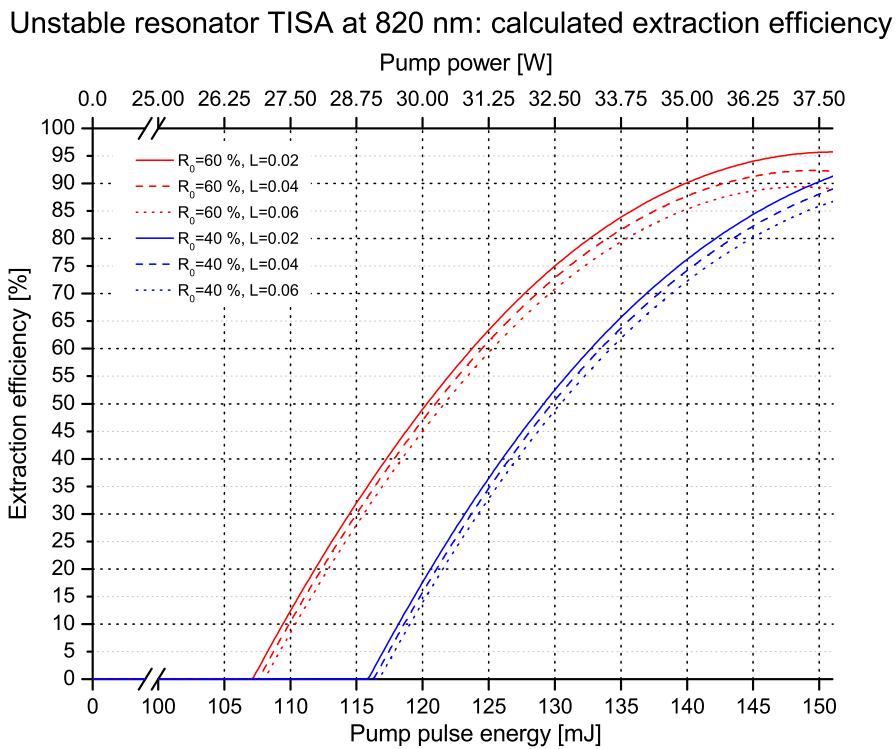
Figure 4.121: Unstable resonator TISA laser at 820 nm: calculated extraction efficiency.
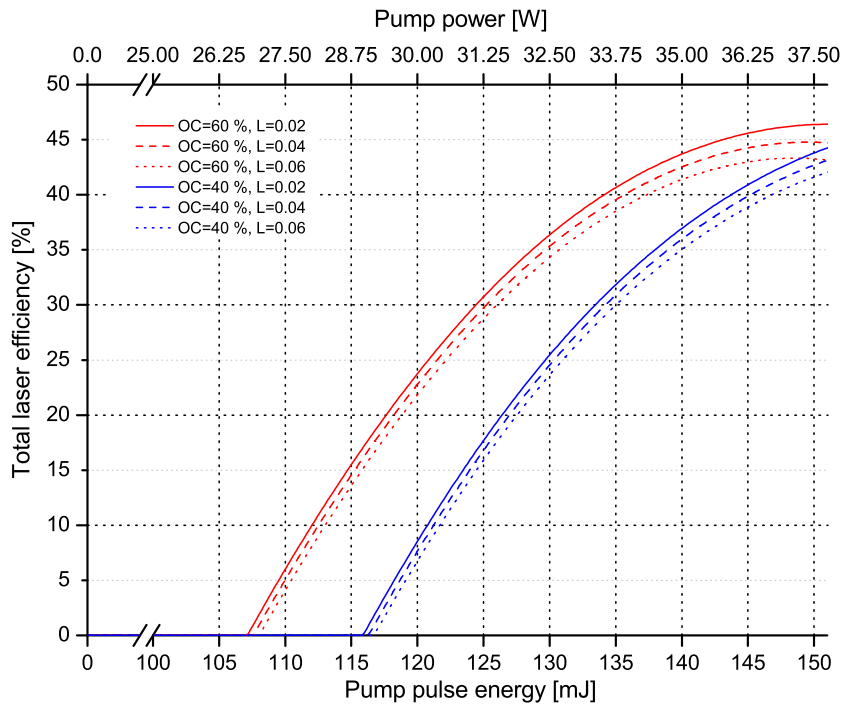
Figure 4.122: Unstable resonator TISA laser at 820 nm: calculated total laser efficiency.

820nm
UR
η_{total}
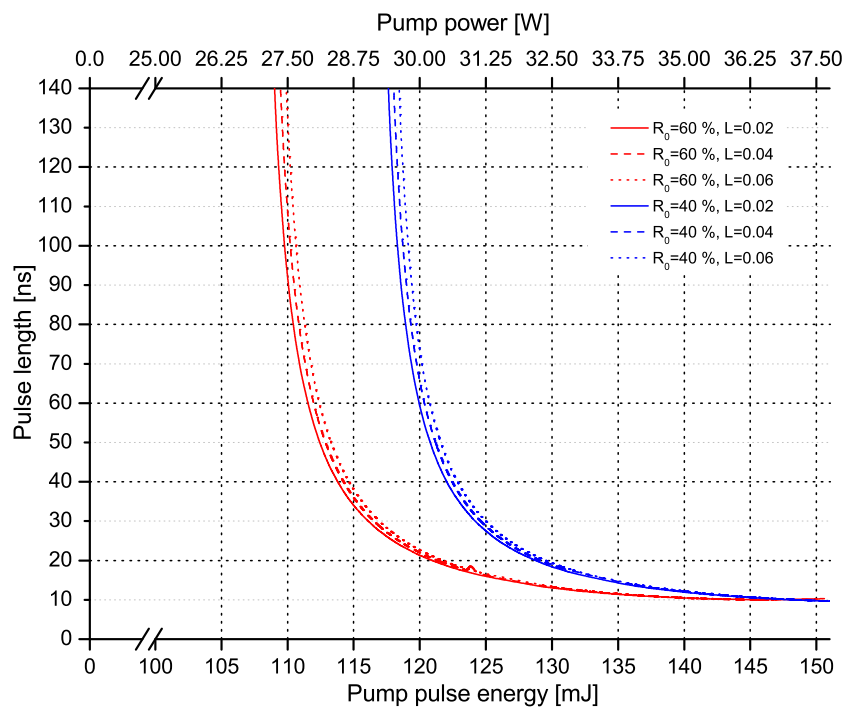
Figure 4.123: Unstable resonator TISA laser at 820 nm: pulse length.

820nm
UR
τ_p
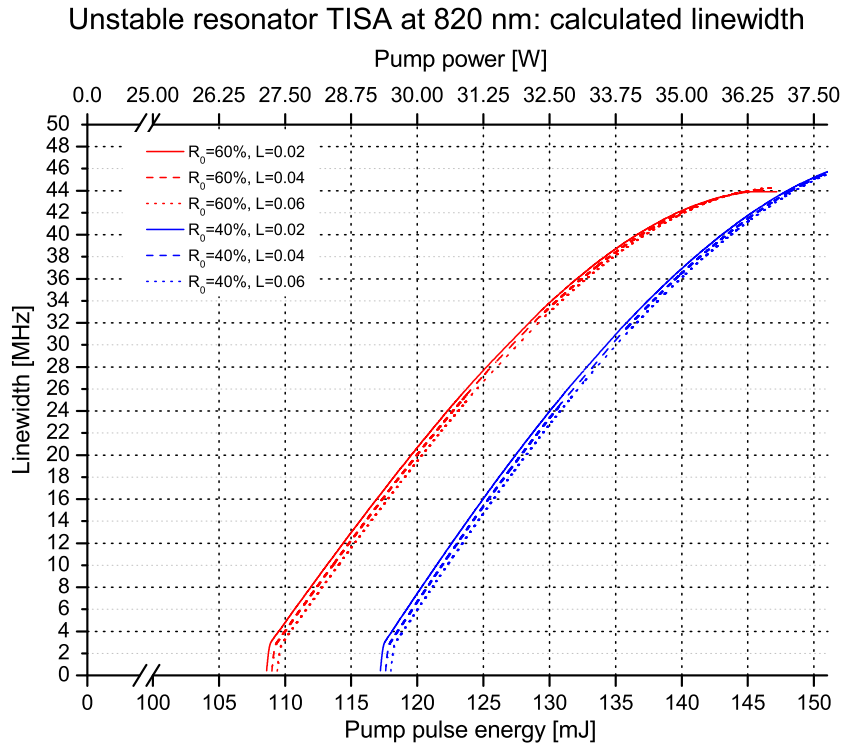
Figure 4.124: Unstable resonator TISA laser at 820 nm: linewidth.

820nm
UR
LW
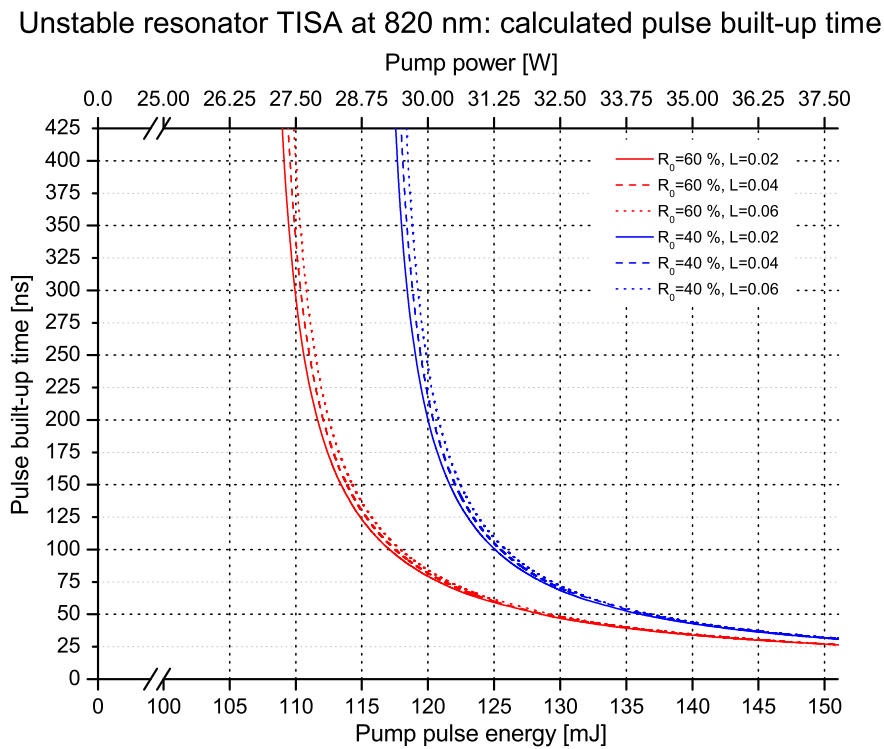
Figure 4.125: Unstable resonator TISA laser at 820 nm: pulse built-up time.

820nm
UR
PBUT

4.5.7 Output energy for stable resonator TISA laser at 600-1100 nm

Figures 4.126a-4.126c show the calculated output pulse energy of a stable resonator TISA laser for the complete gain region with output coupler reflectivities of 50,60, and 85%. It is assumed, that the resonator mirrors have the same reflectivity for each wavelength[40]. The influence of the output coupler on the overall TISA performance is clearly visible. A high reflectivity output coupler favours TISA operation at gain limits. In the high-gain region, lower reflectivity output couplers can be used to increase TISA laser output. Higher output coupler reflectivities are necessary for operation close to the gain borders.

(a) 50% OC.

(b) 60% OC.

(c) 85% OC.
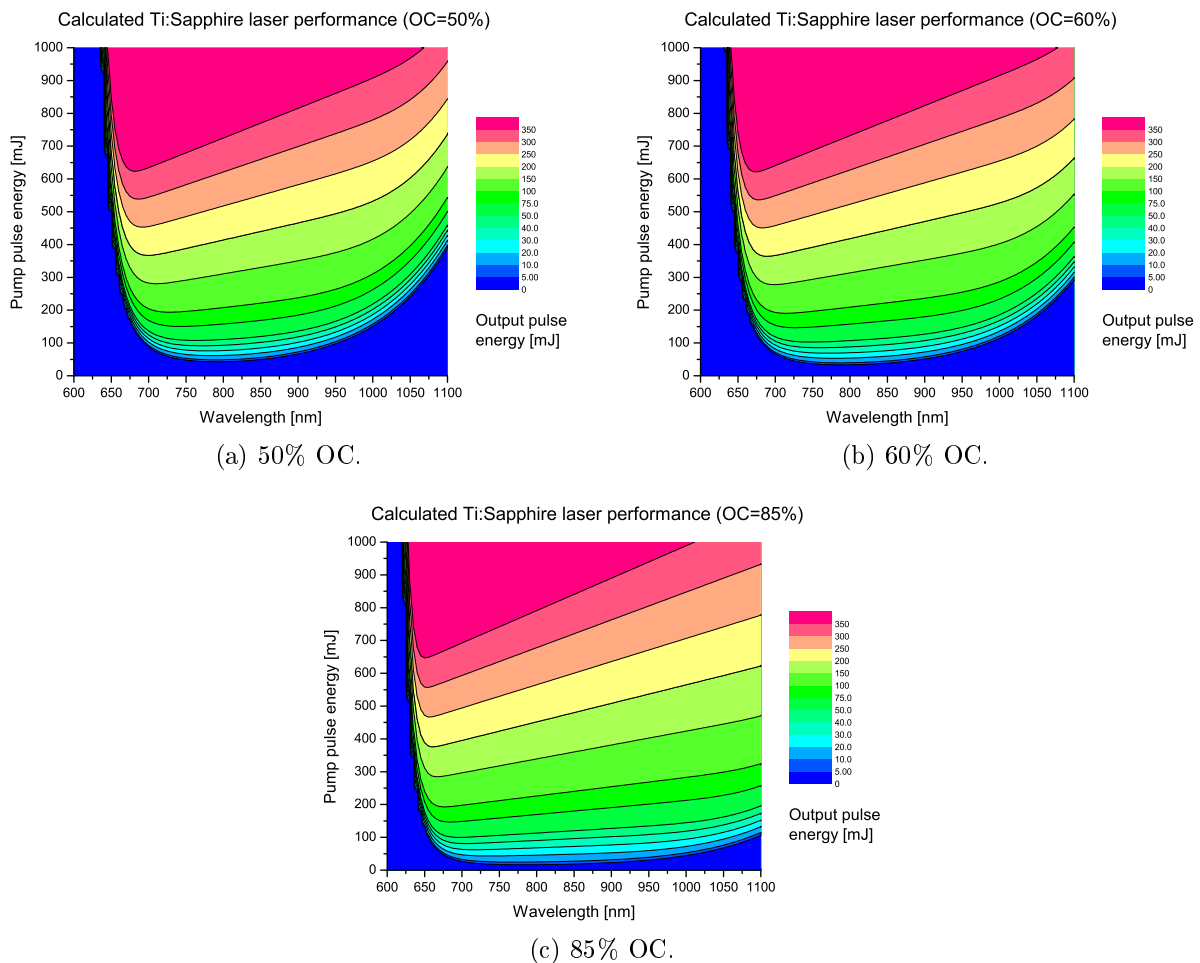
Figure 4.126: SR TISA laser at $600-1100$ nm: output pulse energy with $50, 60$, and 85% OC.

TISA
SR
FULL

---

[40]Usually, several mirror sets have to be used to cover the complete output wavelength range of TISA lasers.

4.5.8 Comparison of theory and experiment

The performance model calculations are compared with the experimental performance of a TISA laser, which is the transmitter of the water-vapor DIAL system at IPM. The transmitter consists of a stable resonator TISA laser. It is described in [Schiller09].

Table 4.5.8 lists the specifications of the resonator, the calculated theoretical performance using the models of this work, and the experimental results. The comparison is done for 935 nm, 820 nm, and 825 nm (2 measurements). Slightly different resonator setups were used for the 935 nm and 820 nm stable resonator experiment [Schiller09]. The measurements at 935 nm and 820 nm were performed with a pump laser having a maximum pump-pulse energy of $\approx$92 mJ at 532 nm, and the measurements at 825 nm were performed with a modified pump laser and a maximum pump-pulse energy of $\approx$140 mJ (532 nm).

The overlap of pump and cavity mode η_{a_2} (see Appendix A) has a decisive influence on the laser performance. η_{a_2} was used to adjust the model to the experiment. Additionally, the dissipative losses of the resonator are adjusted. η_{a_2} influences the initial conditions (Eq. 105, 139, 140) of the differential equation system. The loss L influences the differential equation system itself (Eqs. 102, 103). Figures 4.127-4.130 show the calculated output pulse energy versus the pump pulse energy together with the experimental data.

For the 935 nm stable resonator TISA, the comparison is as follows. In Fig. 4.127a, the overlap η_{a_2} was varied from 100...50% for a constant, experimentally estimated dissipative loss of L=0.08. Figure 4.127b shows the experimental data in comparison with a varying dissipative loss of L=0...0.2 and a constant, experimentally estimated overlap of η_{a_2}=77%. As a result, the overlap is decreasing from 80...85% to $\approx$65%, and the losses are increasing from $\approx$0.06...0.1% to $\approx$0.16.

For the 820 nm comparison (Fig.4.128), the results are as follows. At a constant, experimentally determined loss of L=0.05, an overlap of $\approx$70% results in good agreement of model calculations and experiment. The experimentally determined overlap of 74% showed good agreement for a loss of L=0.08...0.10.

Figures 4.129-4.130 show the comparison using the modified pump laser. An overlap of $\approx$50% is achieved. This result can be explained, as the pump-beam radius is significantly larger than the eigenmode radius at the crystal. As the pump power is increased, the resonator overlap is also increasing. The experimentally determined overlap of 73% (Fig. 4.130) seems to be much too high. A further reduction of the pump-beam radius to increase the overlap was not possible due to the shape of the pump-beam profile and the danger of optical damage at the crystal surface. The reduced overlap mostly explains the low efficiency of the TISA laser.

It is expected that the incorporation of a power dependent overlap to the model by use of the calculated stability zone of the stable TISA resonator and beam profiles at each pump-power

level results in even better agreement of model and experiment. This was not yet performed, as beam profiles at different pump power levels were not available. Nevertheless, the plots at various degree of overlap can help to identify problems concerning the overlap of pump and resonator mode. For a dynamically stable resonator, it can be expected that the overlap is almost constant for the width of the stability zone. This assumes that the pump-beam radius is not changing when increasing the pump-power. This seems to be the case for the measurement at 820 nm (see Fig. 4.128).

The comparison for all other laser parameters is listed in Tab. 4.5.8.

In summary, the comparison of model and experiment indicates that the overlap of pump and resonator mode seems to be a critical factor for the present experimental configuration. Consequently, further experimental optimization should be done to increase the overlap.

Table 4.18: Comparison of theory performance model calculations and experimental results. Experimental data courtesy of [Schiller09]. Note: experimentally estimated overlap of pump and resonator mode and dissipative losses used for calculations. Calculated slope efficiency at maximum pump pulse energy.

Parameter, Unit	935 nm		820 nm		825 nm, Meas. 1		825 nm, Meas. 2	
	Calc.	Exp.	Calc.	Exp.	Calc.	Exp.	Calc.	Exp.
Ring resonator length, m	1.35		1.45					
TISA mode radius at crystal, mm	0.65		0.78		0.8			
Output coupler reflectivity, %	72		55					
Pump pulse energy, mJ	92.23		91.2		140		135.36	
Output pulse energy, mJ	23.24	18	26.35	23.66	30.09	27.53	43.32	26.2
Threshold energy, mJ	≈40	≈44	≈46	-	≈68	≈95	≈51	-
Slope efficiency, %	36.9	40	49.9	60	35.3	-	42.2	-
Extraction efficiency, %	69.3	-	72.5	-	73.0	-	81.9	-
Excitation efficiency, %	36.4	-	39.9	-	29.5	-	39.1	-
Total laser efficiency, %	25.2	19.5	28.9	25.9	21.5	19.7	32.0	19.4
Pulse length, ns	41	40	35	40	32	40	23	35
Linewidth, MHz	11	≈170	13	-	14	157	19	-
Pulse built-up time, ns	138	100	122	90	110	-	74	100
Spectral purity, %	99.999	>99.99	99.997	-	99.998	>99.6	99.998	-
Overlap pump-resonator mode, %	77		74		55		73	
Dissipative resonator loss, %	8		5		6.5			

Stable resonator TISA at 935 nm: model calculation vs. experiment
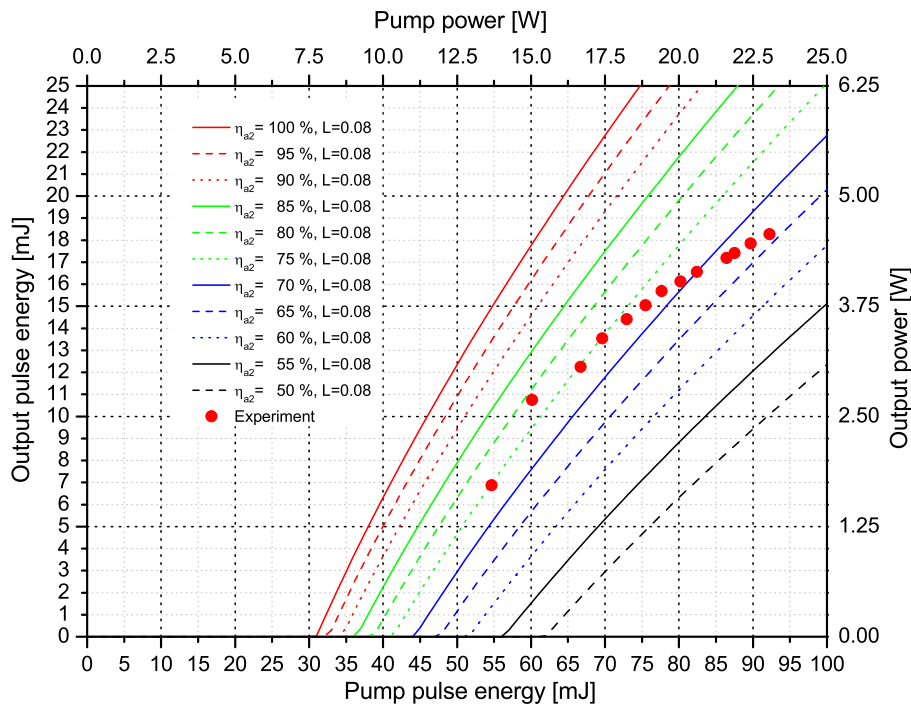
(a) Optical coupling efficiency η_{a_2}=100...50%, dissipative loss L=0.08.

Stable resonator TISA at 935 nm: model calculation vs. experiment
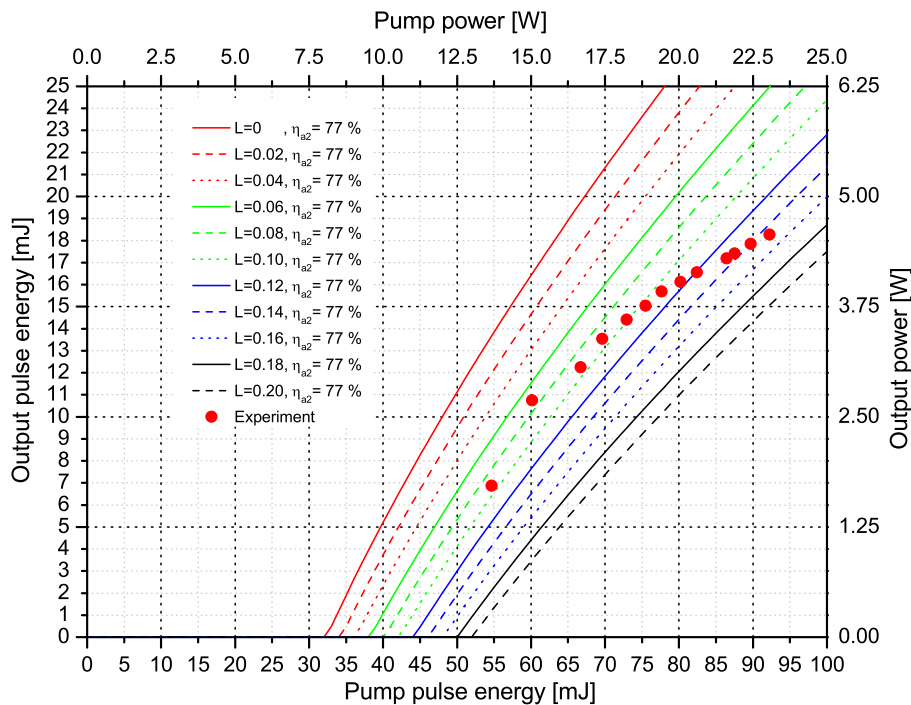
(b) Dissipative loss L=0...0.2, optical coupling efficiency η_{a_2}=77%

Figure 4.127: SR TISA 935 nm: model calculation vs. experimental results. Output pulse energy. Experimental data courtesy of [Schiller09].

935nm
Model
vs.
Exp.

Stable resonator TISA at 820 nm: model calculation vs. experiment
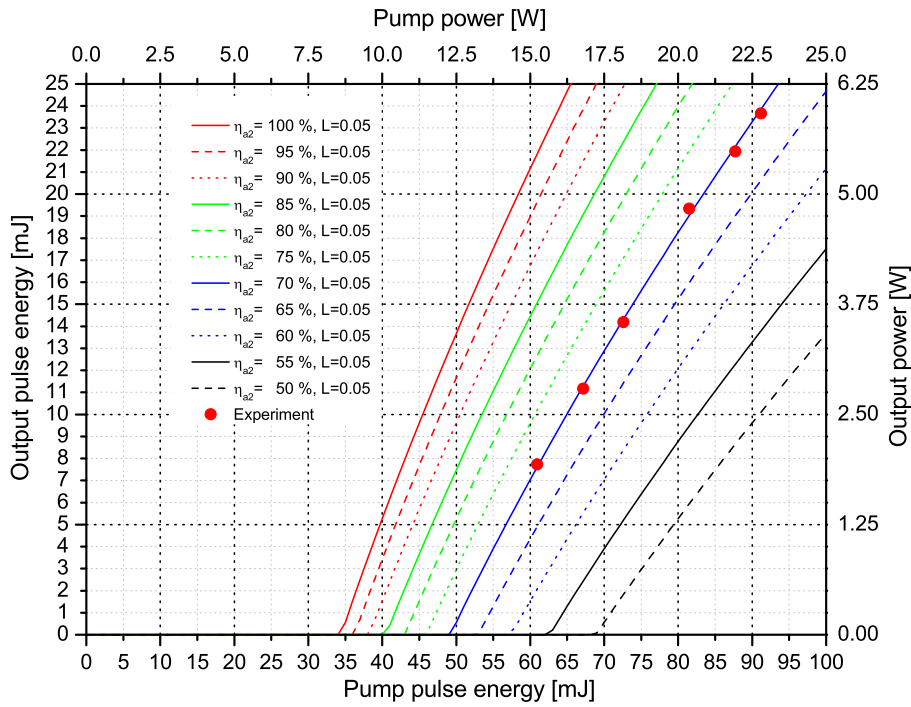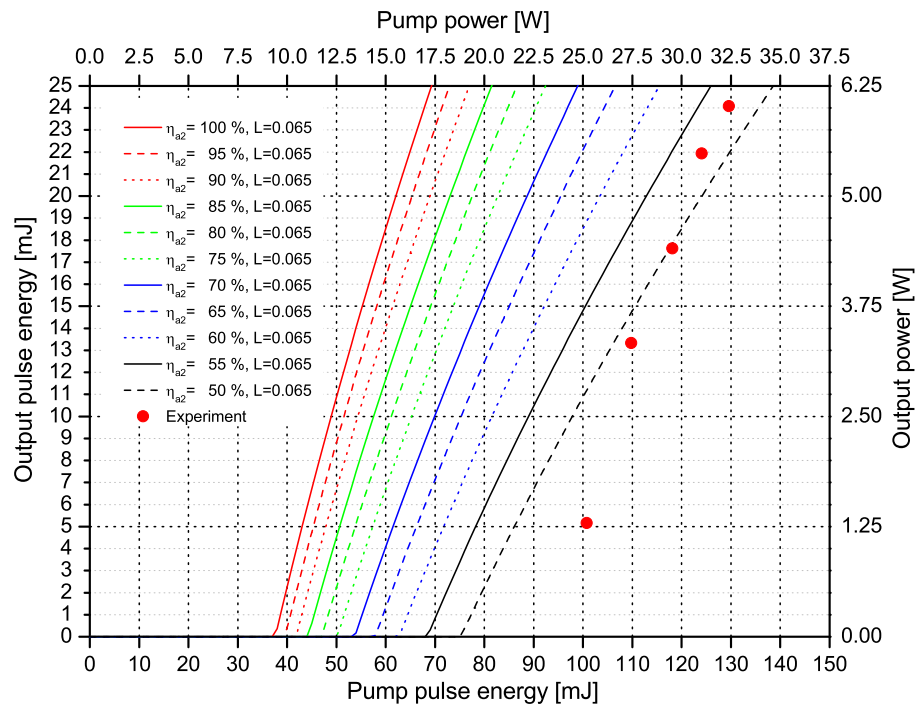
(a) Optical coupling efficiency η_{a_2}=100...50%, dissipative loss L=0.08.

Stable resonator TISA at 820 nm: model calculation vs. experiment

(b) Dissipative loss L=0...0.2, optical coupling efficiency η_{a_2}=77%

820nm
Model
vs.
Exp.

Figure 4.128: SR TISA 820 nm: model calculation vs. experimental results. Output pulse energy. Experimental data courtesy of [Schiller09].

(a) Optical coupling efficiency η_{a_2}=100...50%, dissipative loss L=0.08.
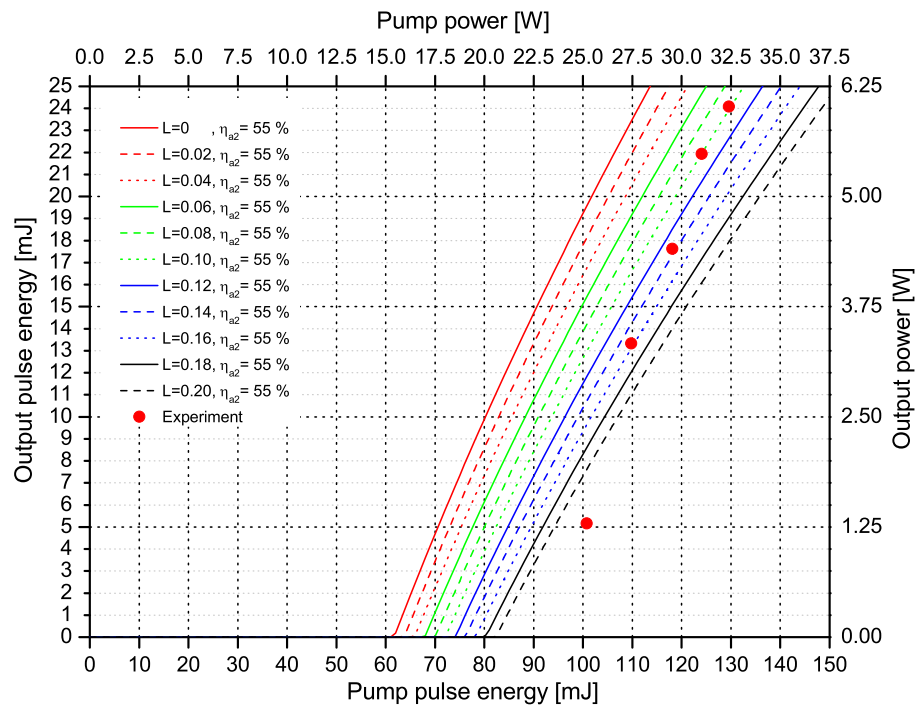
(b) Dissipative loss L=0...0.2, optical coupling efficiency η_{a_2}=77%

Figure 4.129: SR TISA 825 nm: model calculation vs. experimental results (measurement 1). Output pulse energy. Experimental data courtesy of [Schiller09].

Stable resonator TISA at 825 nm (2): model calculation vs. experiment

(a) Optical coupling efficiency η_{a_2}=100...50%, dissipative loss L=0.08.

Stable resonator TISA at 825 nm (2): model calculation vs. experiment

(b) Dissipative loss L=0...0.2, optical coupling efficiency η_{a_2}=77%

Figure 4.130: SR TISA 825 nm: model calculation vs. experimental results (measurement 2). Output pulse energy. Experimental data courtesy of [Schiller09].

825nm
Model
vs.
Exp.
Meas2

4.6 Spectral modeling

4.6.1 Introduction

The spectral characteristics of the output of the frequency converter are of main interest and concern for a DIAL transmitter, as they have major influence on the measurement quality. The spectral quality of a DIAL frequency converter transmitter output can be summarized in a single parameter called spectral purity (SP, see Ch. 4.6.4). Previously, the SP value could hardly be simulated. A measurement of it is indispensable to characterize the frequency converter. The factors that influence the spectral characteristics and therefore the spectral purity of the DIAL frequency converter can be divided into four main categories, which are addressed in detail on the following subsections together with their corresponding model approaches.

Inside the seeding model (Ch. 4.6.2), it is shown that injection of a low power signal[41] into a high-power (slave) oscillator can narrow the output up to single frequency operation (single mode, single frequency). In Ch. 4.6.3, the passive stability of frequency converters is discussed, and active frequency stabilization techniques with emphasis on pulsed lasers are presented. A corresponding modeling is not given here, as each method has its advantages and drawbacks, and is also dependent on the available quality of experimental parts.

A model for the spectral purity based on a new approach is presented in Ch. 4.6.4. The passive stability is also addressed in Ch. 4.6.5, where factors that contribute to laser noise and are discussed.

Although the modeling and especially experimental techniques (e.g. active frequency stabilization) are so far much more developed for lasers and OPO frequency converters, they can be adapted to other lasers, OPO or Raman laser, too.

4.6.2 Injection-seeding model

Spectral narrowing of a solid-state laser is generally achieved by injection-seeding of the resonator with an external cw laser. In principle, this can also be accomplished, e.g., by an intracavity frequency selection, but etalons and other filters are extremely sensitive to ambient changes (temperature, pressure). Additional elements inside the resonator contribute to losses and are a source of optical damage. Therefore, stabilized external cw lasers, such as single-frequency diode and ring lasers [Bruneau94, Wulfmeyer98a, Fix98] are used to inject a low power signal at the lasing wavelength into the resonator.

This favors a single resonator mode that can built-up and deplete the gain media, preferably before other modes can even reach lasing threshold. The corresponding injection-seeding

---

[41] The principle of injecting a low power signal (master) to drive a high-power signal (slave) is a standard technique to control a high-power signal (also for microwaves).

modeling is widely discussed in textbooks [Siegman86b] and therefore only briefly summarized here [Bowers94].

The scalar (real valued) cavity wave equation for the electric field E as function of resonator coordinate z (resonator length: L) and time t is given by

$$\left(\frac{\partial^2}{\partial z^2} - \mu_0 \, \sigma \, \frac{\partial}{\partial t} - \mu_0 \, \epsilon \, \frac{\partial^2}{\partial t^2} \right) E(z,t) \;\; = \;\; \mu_0 \, \frac{\partial^2 p(z,t)}{\partial t^2} \,, \tag{113}$$

where p is the polarization (due to laser gain), σ represents the resonator losses, μ_0 the magnetic permeability of free space, and ϵ the dielectric permeability of the laser gain media. Eq. 113 can be written in terms of a complex phasor amplitude $\tilde{E}(z,t)$ by

$$\tilde{E}(z,t) \;\; = \;\; \tilde{E}_L(z,t) + \tilde{E}_{inj}(z,t) \,, \tag{114}$$

with subscript L, inj for laser and injection seeder, respectively. If an injected signal is applied, this results in

$$\left(\frac{\partial}{\partial z} + \frac{\alpha_0}{c} + \frac{1}{c} \frac{\partial}{\partial t} \right) \tilde{E}_L(z,t) \;\; = \;\; -i \, \frac{k_0}{2\epsilon} \, \tilde{p}(z,t) \,, \tag{115}$$

with

$$c \;\; = \;\; 1/(\mu_0 \epsilon)^{1/2} \tag{116}$$

$$\alpha_0 \;\; = \;\; \sigma/2\epsilon \tag{117}$$

$$k_0 \;\; = \;\; \omega_0(\mu_0 \epsilon)^{1/2} \,, \tag{118}$$

where c is the speed of light, and ω_0: is the resonator carrier frequency. It can be seen that $\tilde{E}_L$ is a result of the injected signal.

Equation 115 can be further expressed in a rate equation approach written as

$$\left(\frac{\partial}{\partial z} + \frac{\alpha_0}{c} - \frac{1}{2} \, g(z,t) + \frac{1}{c} \frac{\partial}{\partial t} \right) \tilde{E}_L(z,t) \;\; = \;\; \frac{1}{2} \, g(z,t) \, \tilde{E}_{inj}(z,t) \,, \tag{119}$$

with a suitable expression for the gain, e.g. gain-switched (TISA) laser, given by

$$\frac{\partial g(z,t)}{\partial t} \;\; = \;\; -g(z,t) \, \frac{[I(z,t) + I(L-z,t)]}{E_{sat}} + R_p(t) \,, \tag{120}$$

with the intensity I, the saturation fluence E_{sat}, and the pumping term R_p. Solution of Eqs. 119, 120 yields the solution of single frequency operation or detuned behavior. Before that, switching to a phasor amplitude $\tilde{A}(z,t)$ followed by expansion in a Fourier series of longitudinal modes with subsequent solution of the equation system for each component provides

the result in frequency space. To conclude, seeding a solid-state laser is nowadays a straight-forward standard procedure which is well understood [Barnes93b, Barnes93a, Wulfmeyer95].

4.6.3 Active frequency stabilization techniques

The frequency stability of the frequency converter is determined by its passive stability and the quality of the active frequency stabilization. The passive frequency stability of a frequency converter (laser) is influenced by the mechanically stability of the laser set up and the environmental changes due temperature, pressure, and mechanical vibrations. These environmental effects lead to resonator length changes and misalignment of the beam propagation, resulting in a frequency instability or drift, e.g., in an extreme case to laser mode hops. Therefore a stringent requirement for the passive stability of the frequency converter system is that the frequency converter and any other optical parts should be mounted on a breadboard with low thermal expansion coefficient together with appropriate optical mounts. The temperature of the surrounding must be necessarily controlled and monitored at any time. For the measurement of water vapor, the frequency converter is installed in a temperature controlled box, which is purged with dry air or N_2 (Nitrogen).

Even when the passive stability seems to be as high as possible, and seeding is working, the resulting frequency stability does usually not fulfill the requirements (<60 MHz, see Tab. 2.1) for a DIAL measurement. Therefore it is necessary to adjust the resonator length using active frequency stabilization techniques. In the following, different approaches for the frequency stabilization of pulsed laser systems are given, but the methods can and have partly already been adapted to OPO and Raman laser frequency converters.

The techniques of stabilizing continuous-wave lasers have been mostly adapted to the application in a pulsed laser. [Rahn85, Schmitt86] and more recently [Schröder07] use the measurement of the pulse built-up time in a Q-switched Nd:YAG laser to detect if the slave laser is in resonance with the master (seed) laser. A minimization of the pulse built-up time indicates the locking status, and if a minimum is not detected, a PZT (PZT: piezoelectric mirror translator) adjusts the resonator length accordingly. This method is also found in commercially available Nd:YAG systems.

Another method is to detect an intensity dependent resonator interference signal, while the PZT is being ramped. The interference signal is given by the seeder together with multiple round-trips of the seeder inside the resonator. At signal intensity maximum, master and slave cavity are in phase, and the laser (Q-switch) is opened. This technique is called ramp-and-fire [Henderson86], and in a modification ramp-hold-fire [Walther01], where the ramp is stopped by a latch signal at resonance. In another variant by [Ertel05], the time between each laser pulse is kept constant, but the voltage of the ramp is adjusted (modulated) according to the resonance signal.

The phase shift between master and slave resonator can be detected by mixing of the modulated reference signal (master or seed laser) using an EOM (EOM: electro-optical modulator) with the same signal after a round-trip in the slave resonator. By this, a sign dependent error signal with zero-crossing at resonance is obtained, and the resonator length can be adjusted accordingly with a PZT. This technique bases on [Drever83] (PDH: Pound-Drever-Hall scheme) and was applied in e.g. [Wulfmeyer00, Ostermeyer05a, Ostermeyer05b, Sträßer07, Schiller09]. [Wulfmeyer00] stabilized a pulsed Tm:LuYAG laser to 0.2 MHz (rms). [Sträßer07] achieved a resulting frequency stability of 1.0 MHz (rms) for the master oscillator of a Nd:YAG laser, and [Schiller09] achieved a frequency stability of 10 MHz (rms) for a TISA laser.

Another method is to use a signed polarization dependent error signal to detect the frequency shift of the slave cavity [Esherick87], based on the technique presented by [Hänsch80].

The previous described methods are more or less suitable for the frequency stabilization of a DIAL transmitter. The PDH-stabilization technique is advantageous, as a phase measurement is used as reference and not the intensity of a resonance. Using PDH, the resonator is almost always at resonance compared to ramp-and-fire methods. The speed of the PDH-stabilization loop is also considerably faster, e.g., compared to the method of minimizing the pulse built-up time. Fast moving optical elements, e.g., by using a ramp to find a resonance, are also avoided. At present, the PDH method is therefore considered to be the best method for the frequency stabilization of a laser under a rough environment.

4.6.4 Spectral purity modeling

As pointed out in the introduction of this chapter, the spectral purity (SP) is a key parameter to judge the spectral characteristics of the emitted radiation of the frequency converter. The spectral purity[42] P is defined as [Barnes93b]

$$P \;=\; \frac{E_{LOS}}{E_{LOS} + E_{LON}}\,, \tag{121}$$

where E_{LOS} is the energy of the seeded mode, and E_{LON} is the total energy of natural unseeded (multimode) contribution. Even small amounts of E_{LON} can lead to high systematic errors in a DIAL measurement [Ismail89], and the requirement for the spectral purity for a DIAL frequency converter is given in Tab. 2.1 with a value of >99.7%. The origin of the spectral impurity energy (E_{LON}) is due to amplified spontaneous emission (ASE) in lasers and amplifiers or not true single-mode operation of the laser due to inefficient seeding.

The corresponding measurement of P is very challenging [Wulfmeyer95] and performed by means of a multipass absorption cell containing the trace gas under specified conditions (pres-

---

[42]P: spectral purity in formulas; SP: abbreviation in text.

sure, number density)[43] or, e.g., by a suitable metal vapor filter. An atomic or molecular transition of the species is selected and the frequency converter is tuned to this absorption line. The E_{LON} part is directly measureable through the ratios of transmission measurements through the cell T and without cell T_0. The spectral purity within the spectral limits under the specified conditions of the selected absorption line is then given by

$$P \;=\; 1 - \frac{T}{T_0} = 1 - \frac{E_{LON}}{E_{LOS} + E_{LON}} \,. \qquad (122)$$

Additionally, a spectral analysis (Fourier-transformation) of the output radiation indicates if other frequency components (e.g. higher-order frequency components) are apparent in the output spectrum.

The formalism found in [Barnes93b] is based on a heuristic principle. A new approach, which is based on modified rate equation modeling is presented in the following.

The spectral properties and performance of a laser can be calculated by coupled rate and atomic equations. However, the estimation of the loss term of each individual mode is problematic. A single-mode operation approach with an additional quantum noise term (see non-Q-switch rate equation approach in Ch 4.5.1, Eqs. 98,99) which represents the spontaneous emission could represent a way to simulate the spectral purity. However, the calculation of P overestimates the noise to the mode, and the resulting spectral purity is too low. It is the noise contribution out of which laser emission starts. The number of initial noise photons are given by the fraction of photons emitted in direction of the optical axis of the resonator, which are emitted into a solid angle of 1 mrad (sr). Also a factor of $1{\cdot}10^{-5}$ of the expected peak photon density [Kay05] is used for the initial photon density. Another approach, assuming that the fraction of spontaneous emission for a single mode is $1/p$ of the total spontaneous emission (p: total number of resonator modes) is also clearly misleading in a single-mode approach, as it would formally also attribute the total spontaneous emission to this mode.

A modification of the rate equations according to this fact is therefore not satisfactory, as it would formally be not correct according to quantum mechanics. The ultimate limit of the noise of the laser is represented by this extra single noise photon per Hz of bandwidth, and as a consequence lower noise lasers can not be built. The challenge is to transform or scale down a multimode approach to a single mode approach with an appropriate description of spontaneous emission noise or loss to other resonator modes. Concerning the solution, the following method for the modeling of the spectral purity is proposed.

In Ch. 4.5, a model for the Q-switch, gain-switch, cavity-dumped laser in single mode operation is used to calculate the TISA laser performance. The idea is to extend this model with a virtual noise mode equation that summarizes all contributions that decrease the spectral

---

[43]Different line broadening mechanisms are responsible for the shape of the absorption line.

purity due to spontaneous emission or modes that do not reach threshold, but have impact on the spectral purity due to the loss of energy transferred to these modes. Additionally, the equation describing the photon density of the single-mode output is extended with a term to account for the increased photon density by injection-seeding. The resulting modified system of coupled differential equations for the inversion density $n(t)$ and the corresponding photon densities for the laser mode ϕ_{λ_1} and the virtual noise mode $\phi_{\lambda_{av}}$ reads as follows:

$$\frac{dn(t)}{dt} = -\gamma\,c\,n(t)\left[\sigma_{e,\lambda_1}\,\phi_{\lambda_1}(t)+\sigma_{e,\lambda_{av}}\,\phi_{\lambda_{av}}(t)\right] \tag{123}$$

$$\frac{d\phi_{\lambda_1}(t)}{dt} = \left(\phi_{\lambda_1}(t)+\phi_{\lambda_{1,s}}\right)\left[c\,\sigma_{e,\lambda_1}\left(\frac{l}{l'}\right)n(t)-\frac{\epsilon}{t_r}\right] \tag{124}$$

$$\frac{d\phi_{\lambda_{av}}(t)}{dt} = \phi_{\lambda_{av}}(t)\left[c\,\sigma_{e,\lambda_{av}}\left(\frac{l}{l'}\right)n(t)-\frac{\epsilon}{t_r}\right]. \tag{125}$$

In Eqs. 123-125, γ is the inversion reduction factor (see Ch. 4.5), c is the speed of light, and σ_{e,λ_1}, $\sigma_{e,\lambda_{av}}$ are the stimulated emission cross sections of the lasing wavelength and the virtual noise wavelength, respectively. l,l' are the laser crystal and resonator lengths, respectively. ϵ/t_r is the term describing the total loss rate per round-trip, with t_r being the resonator round-trip time. Concerning the loss term ϵ/t_r, see corresponding equations for stable resonator (Eq. 104) and unstable resonator (Eq. 112). It is assumed, that the photon density of laser mode and virtual noise mode exhibit the same cavity loss. The value of $\sigma_{e,\lambda_{av}}$ is taken as the same as for the lasing wavelength, as it truncated, e.g., by the birefringent filter. The term $\phi_{\lambda_{1,s}}$ representing the additional photon density inside the resonator provided by the injection seeder in Eq. 124 is given by

$$\phi_{\lambda_{1,s}} = \frac{P_s\,\lambda_L}{h\,c}/V\,, \tag{126}$$

where P_s is the power of the injection seeder, λ_L is the seeder (=laser) wavelength, h is Planck's constant, and V is the resonator volume. As can be seen in Eq. 124, the injected photon density of the injection seeder is added to the photon density of the mode, and is consequently amplified and exhibits the same cavity loss. Table 4.19 shows the parameters and initial conditions for the simulation of the spectral purity for a laser operating at 935 nm or 820 nm. The simulations are performed at a constant pump pulse energy of 200 mJ, to be well above threshold for stable and unstable resonators[44]. The resulting calculated spectral purity P_{calc} is given by integration of the resulting solutions for $\phi_{\lambda_1}(t)$ and $\phi_{\lambda_{av}}(t)$ and taking

---

[44]The simulation for the unstable resonator is carried out with the assumption that a corresponding beam propagation still ensures unstable operation at the corresponding pump level.

Table 4.19: Spectral purity simulation parameter table of stable resonator (SR) and unstable resonator (UR) TISA laser simulation at 820 nm and 935 nm. For further details of single parameters, see Ch. 4.5.

Parameter, Unit	Value	Comment
TISA crystal length, cm	2	
SR resonator length, cm	150	stable ring resonator
UR resonator length, cm	98.5	unstable ring resonator
Pump beam radius, mm	0.75	top-hat beam profile
Pump wavelength, nm	532	
Pump pulse length, ns	25	
Pump pulse energy, mJ	200	
Repetition rate, Hz	250	according to pump laser
Stored pump pulse energy, %	42.5/48.5	Appendix A, [Coyle95]
Lasing wavelengths, nm	$935, 820$	
Virtual noise mode wavelength, nm	$935, 820$	
Stim. em. cross section at 935 nm, cm^2	$1.39 \cdot 10^{-19}$	π-polarization
Stim. em. cross section at 820 nm, cm^2	$2.85 \cdot 10^{-19}$	π-polarization
Fluorescence lifetime, μs	3.15	at 300 K
SR: Output coupler reflectivity, %	68.9/50.7	R_{opt} at 935/820 nm
UR: VRM reflectivity, %	60	variable, see Ch. 4.4.2
UR: Magnification, dim.-less	1.6	
Dissipative loss, %	2	
Inversion reduction factor γ, dim.-less	1	
Initial inversion density $n(0)$, 1/m^3	$\left(\frac{E_{ST}}{E_L}\right)/V$	see Eq. 105
Initial photon density $\phi_{\lambda_1}(0)$, 1/m^3	$\frac{n(0)\,A\,l\,\frac{l'}{c\,\tau_f}\,\frac{d\Omega}{4\,\pi}}{A\,l'} + \phi_{\lambda_1,s}\,t_r$	
Initial photon density $\phi_{\lambda_{av}}(0)$, 1/m^3	$\frac{n(0)\,A\,l\,\frac{l'}{c\,\tau_f}\,\frac{d\Omega}{4\,\pi}}{A\,l'}$	

the corresponding ratio:

$$P_{calc} \;=\; \frac{\int_0^\infty \phi_{\lambda_1}(t)\,dt}{\int_0^\infty \phi_{\lambda_1}(t)\,dt \,+\, \int_0^\infty \phi_{\lambda_{av}}(t)\,dt}. \tag{127}$$

The simulation for the spectral purity is carried out for a stable and unstable TISA laser resonator operating at 935 nm and 820 nm. Concerning the unstable resonator, a constant value for the magnification of M=1.6 is selected.

In Figs. 4.131-4.134, the spectral purity is depicted as function of seed power for a stable and an unstable TISA laser at 935 nm and 820 nm, respectively. For the unstable TISA laser, the spectral purity is also depicted as a function of the magnification (Fig. 4.135).

The results for the spectral modeling are summarized in Tab. 4.20. A seed-power level of $\approx$1 mW is necessary to achieve the required spectral purity for stable and unstable resonators. The seed-power level was not increased over a first maximum of the spectral purity, as at a
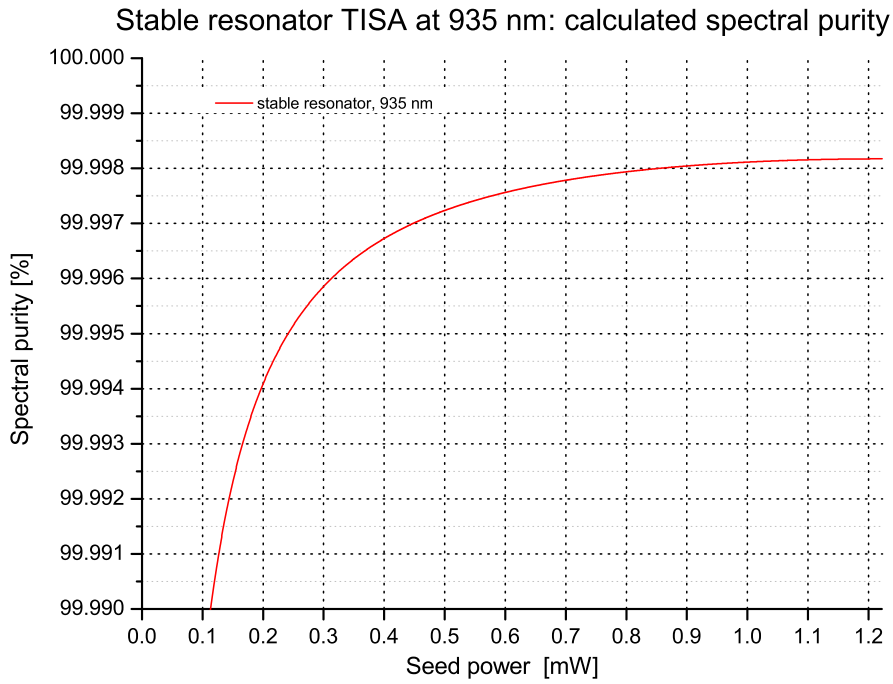
(a) SR TISA 935 nm.
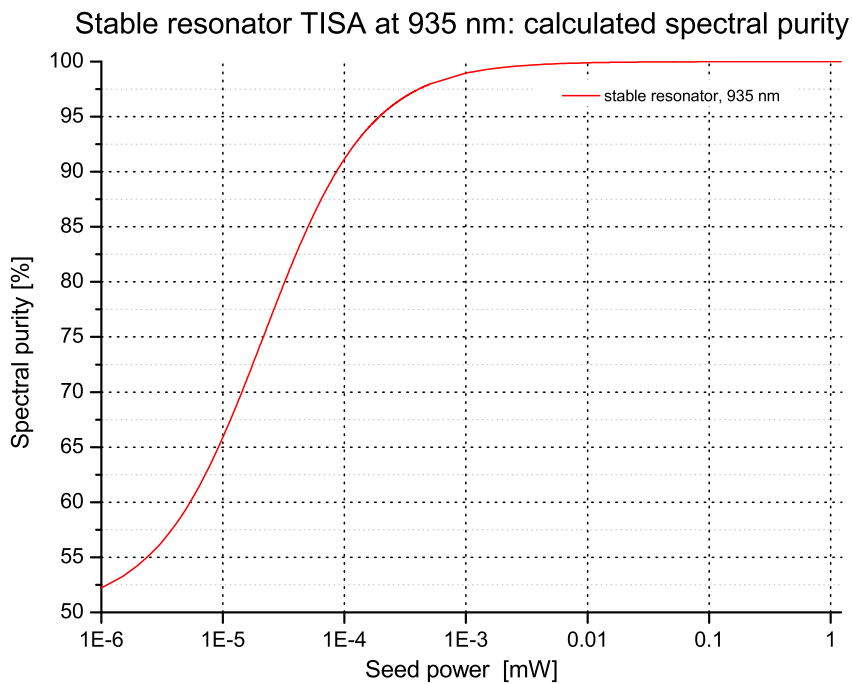
(b) SR TISA 935 nm. Logarithmic scale for seed power.

Figure 4.131: Spectral purity for stable TISA laser at 935 nm as function of seed power.

certain seed-power level the spectral purity was decreasing and then overall increasing again. This behavior repeated with increasing seed-power. Whether this can be attributed to the better mode discrimination of an unstable resonator, an optimum seed-power level for both resonators or numerical instabilities is currently under investigation.
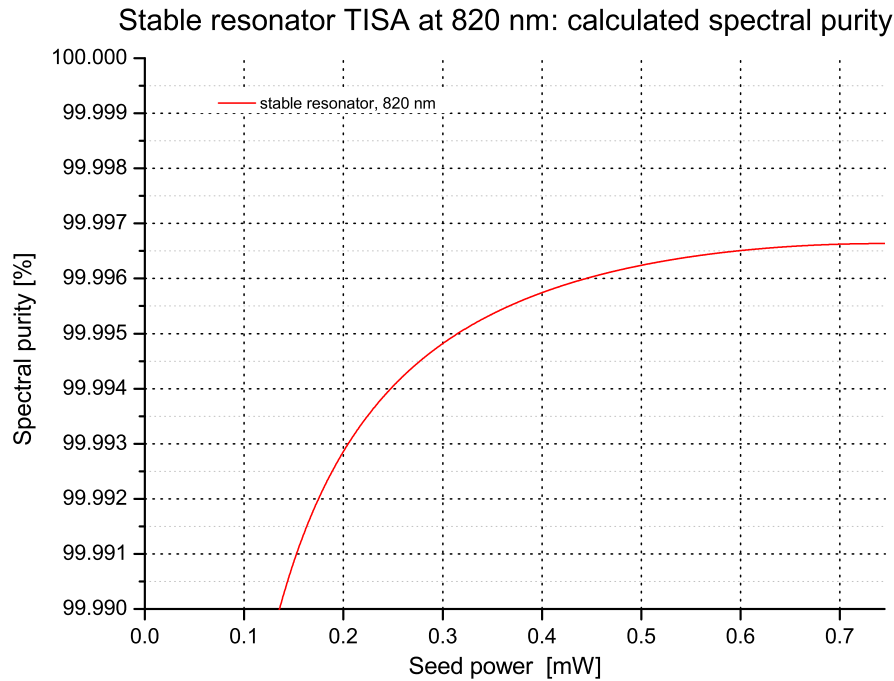
(a) SR TISA 820 nm.
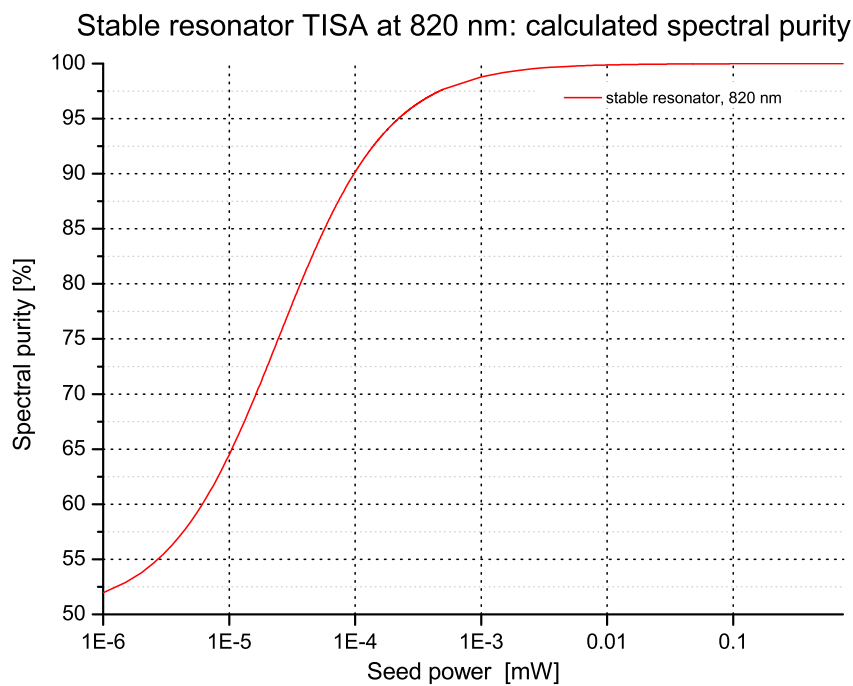
(b) SR TISA 820 nm. Logarithmic scale for seed power

Figure 4.132: Spectral purity for stable TISA laser at 820 nm as function of seed power.

The influence of magnification of the unstable resonator shows, that at a certain level of magnification the spectral purity drops significantly: at 935 nm for $M \approx 1.65$, at 820 nm for $M \approx 2$. This effect is also under investigation. In an experiment, it would be interesting to investigate the spectral purity as a function of the magnification. Concerning the unstable

Unstable resonator TISA at 935 nm: calculated spectral purity

(a) UR TISA 935 nm.

Unstable resonator TISA at 935 nm: calculated spectral purity
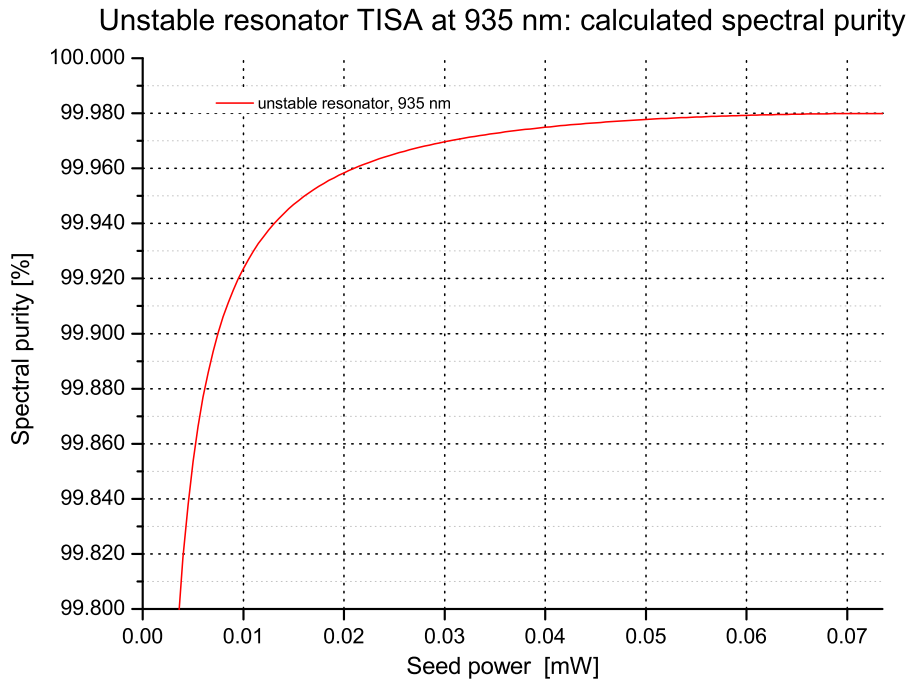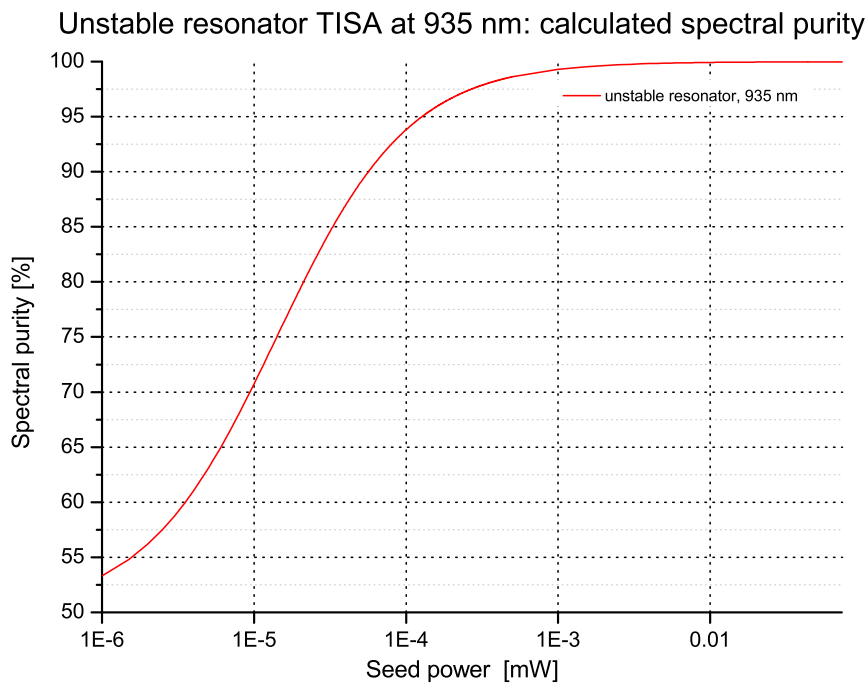
(b) UR TISA 935 nm. Logarithmic scale for seed power.

Figure 4.133: Spectral purity for unstable TISA laser at 935 nm as function of seed power.

resonator, [Lee03, Lee02] have measured a spectral purity of ≈99.99% at 780.24 nm with an unstable TISA laser using an Rubidium absorption cell. An increase in spectral purity by a factor of >10 to a value of at least 99.999% is demonstrated by the same authors by incorporation of an external-cavity stimulated Brillouin-scattering (SBS) phase-conjugate

Unstable resonator TISA at 820 nm: calculated spectral purity

(a) UR TISA 820 nm.

Unstable resonator TISA at 820 nm: calculated spectral purity
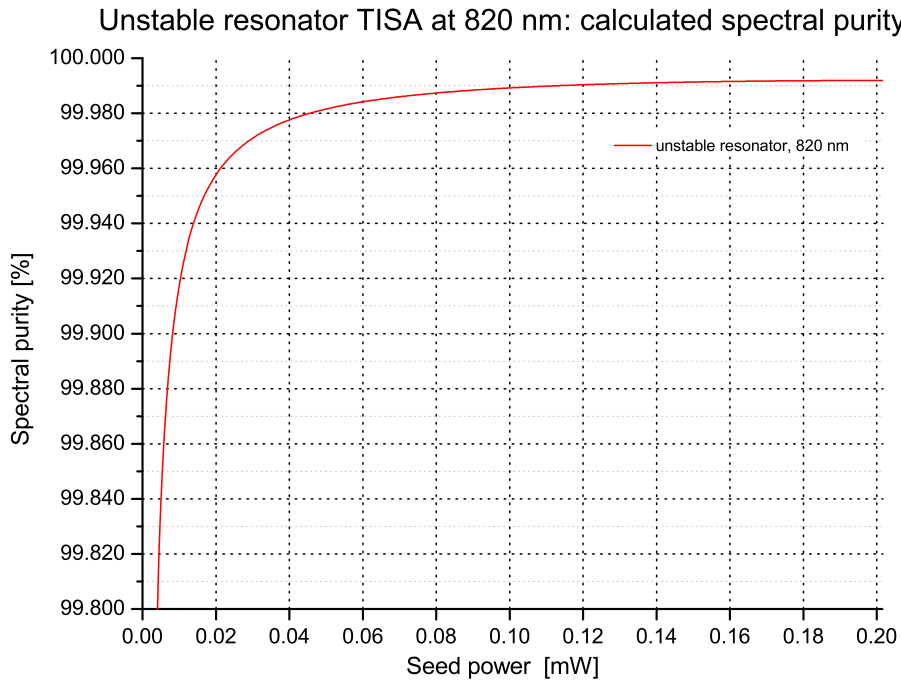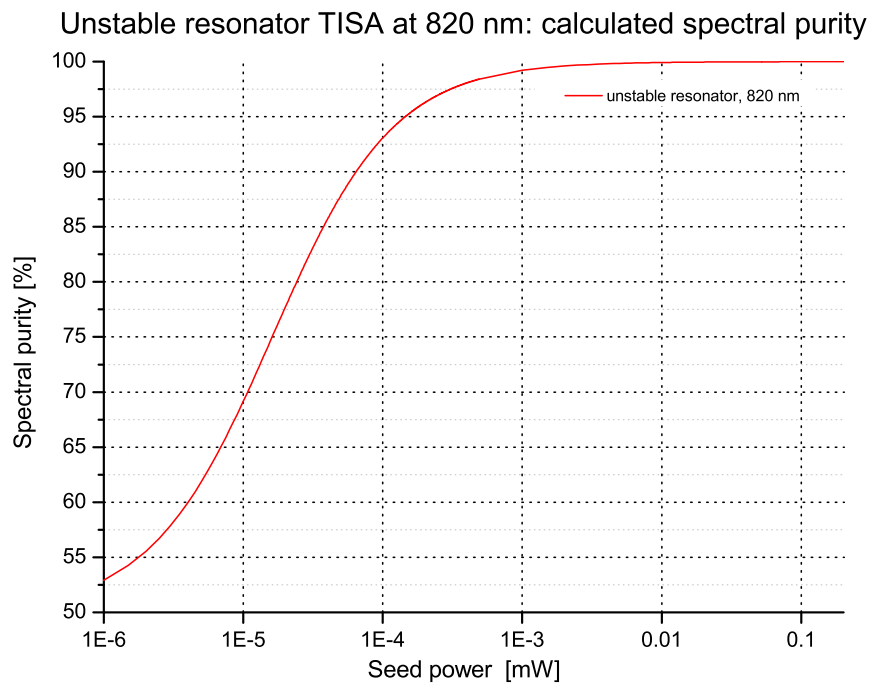
(b) UR TISA 820 nm. Logarithmic scale for seed power

Figure 4.134: Spectral purity for unstable TISA laser at 820 nm as function of seed power.

mirror (PCM) at the expense of a $\approx$65% reduced lower laser output power.

To conclude, stable and unstable resonator TISA lasers are able to fulfill the requirements of the spectral purity ($>$99.7%, Tab. 2.1) for a water-vapor DIAL measurement. The fact of better mode discrimination of unstable resonators at higher magnifications should be
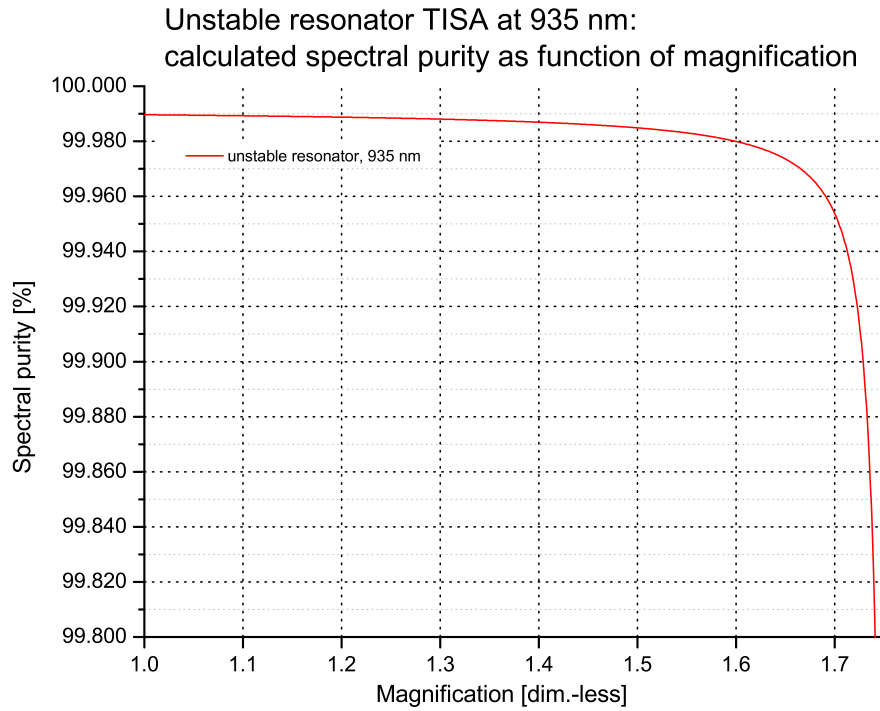
(a) UR TISA 935 nm. Seed power: 0.0735 mW.
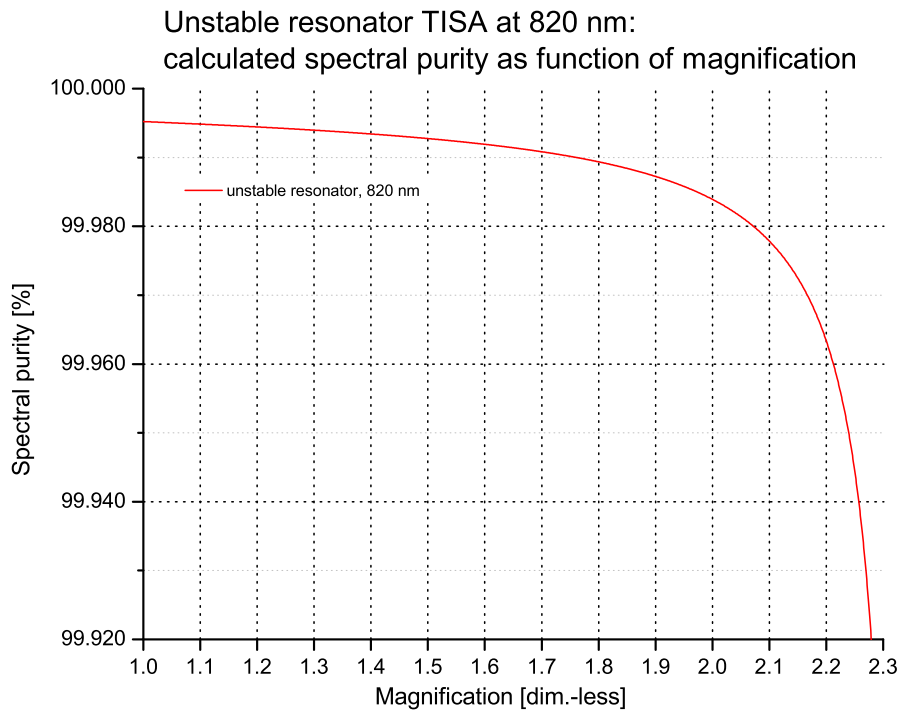
(b) UR TISA 820 nm. Seed power: 0.2015 mW.

Figure 4.135: Spectral purity for unstable TISA laser at 935 nm and 820 nm as function of magnification.

experimentally investigated regarding the influence on the spectral purity.

Table 4.20: Modeling results for spectral purity simulation (P_{calc}) at 820 nm and 935 nm for stable and unstable TISA laser. P_{calc} is given for the seed-power P_s.

Wavelength, resonator type	P_{calc}, %	P_s, mW
935 nm, stable resonator	99.982	1.222
935 nm, unstable resonator	99.800	0.0735
820 nm, stable resonator	99.997	0.745
820 nm, unstable resonator	99.919	0.2015

4.6.5 Laser noise

For the modeling of the spectral purity (see previous Ch. 4.6.4), a virtual noise mode approach was used to simulate the spectral impurity. Within this section, the basic processes contributing to laser noise are discussed. So far, this has never been addressed in a DIAL laser frequency converter analysis.

The noise of a laser is not a single effect phenomena, and one has generally to distinguish between intensity noise and phase noise. While the intensity noise[45] is limited and bound by the gain saturation effect in a laser, the phase noise is totally random. The intensity noise can be directly measured with a photodiode. For the measurement of the phase noise, an interference (heterodyne) measurement or a high-resolution frequency measurement is necessary.

The finite linewidth (frequency width) $\Delta\nu_{osc}$ of a laser is given by the Schawlow-Townes formula [Schawlow58]

$$\Delta\nu_{osc} \;=\; \frac{4\,\pi\,h\,\nu}{P_{out}}\,(\Delta\nu)^2\,, \tag{128}$$

where h is Planck's constant, ν the laser (photon) frequency, P_{out} the laser output power, and $\Delta\nu$ is the half-width of the resonance at half-maximum intensity, which can be expressed by:

$$\Delta\nu \;=\; \frac{1}{4\,\pi}\,\frac{l_{tot}}{T_R}\,, \tag{129}$$

with l_{tot} being the total cavity loss, and T_R the resonator round-trip time. The origin of this finite frequency width is due to spontaneous emission into the resonator mode. A full equivalent equation, and assuming parasitic cavity losses l_{par} ($l_{tot}=l_{par}+T_{OC}$) is given by [Paschotta07]

$$\Delta\nu_{osc} \;=\; \frac{h\,\nu\,l_{tot}}{4\,\pi\,T_R^2\,P_{int}} = \frac{h\,\nu\,l_{tot}\,T_{OC}}{4\,\pi\,T_R^2\,P_{out}}\,, \tag{130}$$

---

[45]The intensity noise is usually also called shot noise.

with T_{OC} as the output coupler transmission, and P_{int} the power in the resonator. Therefore, a longer resonator with a lower output-coupler transmission is advantageous concerning the linewidth.

Besides the spontaneous emission, the following factors contribute to intensity and phase noise [Paschotta07]:

– thermal drift in the gain medium (intensity and phase)

– cavity length changes due to mirror vibrations by e.g. acoustic noise (mostly phase)

– cavity length changes due to thermal expansion (phase)

– mirror tilt (intensity and phase)

– coupling effects: e.g. the Kerr-effect (phase shift by intensity fluctuation)

Additionally, noise induced by the pump (laser), and dipole fluctuation noise have to be considered. A laser noise model including pump, and seeder noise using a quantum mechanical treatment is given in [Ralph96].

Concerning the noise in the special case of an unstable resonator (UR) geometry, there has been executed significant theoretical and experimental research due to the so-called Petermann excess noise factor K [Petermann79]. As a result of the predicted increased spontaneous emission, the Schawlow-Townes linewidth (Eq. 128) is increased by a factor of K, and reads

$$\Delta \nu_{osc,UR} \quad = \quad K \, \Delta \nu_{osc} \, . \tag{131}$$

The spontaneous emission is being increased and amplified in unstable resonator geometries compared to a stable resonator due to the nonorthogonal eigenmodes within an unstable resonator. This has soon been realized, and intensive theoretical [Siegman89a, Siegman89b] and experimental research was performed[46]. The increased linewidth is experimentally verified [Cheng94, Cheng96], and depends on the magnification and beam propagation of the unstable resonator. For a positive-branch unstable resonator (PBUR), K_{00} can be approximated for the lowest order mode [Doumont89]

$$K_{00} \quad \approx \quad \left[\frac{\pi}{2} \left(\frac{M^2 - 1}{M} \right)^2 N_{GA} \right]^2 \, , \tag{132}$$

---

[46]See e.g. [Siegman95] for a review.

where M is the resonator magnification, and N_{GA} is the Fresnel number for the Gaussian aperture

$$N_{GA} \;\; = \;\; \pi^{-1} \left(\omega_{ga}/\omega_{cf} \right)^2 \tag{133}$$

where ω_{ga} is the $1/e$-amplitude reflectivity radius of variable reflectivity mirror (VRM), and ω_{cf} is the minimum mode radius. With M=1.6, ω_{ga}=1.5 mm, ω_{cf}=0.3 mm, one can expect an increased linewidth of a factor 141. With M=1.6, ω_{ga}=1.5 mm, ω_{cf}=0.75 mm, this reduced to a factor of about 4. Therefore it is strongly dependent on the beam propagation, e.g. magnification and mirror parameters of the resonator.

In summary, the excess noise factor is a criteria, which should can be taken into account in an unstable resonator design, although these quantum mechanic effects should play a minor role for a pulsed laser system, and have yet been only measured in cw-systems. A larger magnification creates a higher excess noise. However, a higher magnification is better for effective mode discrimination (Ch. 4.4.2) and this fact has a higher priority in an unstable resonator design in terms of single-mode, single-frequency operation (seeding).

For pulsed (e.g. Q-switched) laser systems, all the above considerations are valid, but have to be adapted according to a discrete time interval [Paschotta07] and by use of a single laser shot statistic analysis. On an appropriate time scale, the intensity noise is given by fluctuations in the average output power, according to deviations in pulse energy and repetition rate. The timing difference of each pulse (jitter), pulse duration, and also frequency chirp are factors that contribute to noise and are linked to each other.

5 Summary and outlook

Frequency converters based on parametric and non-parametric frequency conversion (optical parametric oscillator (OPO), Raman laser, laser) were investigated within this thesis regarding the capabilities to serve as high-average power water-vapor DIAL transmitters (DIAL: Differential Absorption LIDAR; LIDAR: Light Detection and Ranging) operating in the 935 nm and 820 nm wavelength regime for spaceborne, airborne, and ground-based measurements. A Ti:Sapphire (TISA) laser was selected as the most promising approach to fulfill simultaneously all the requirements (see Tab. 2.1, page 6). End-pumped TISA laser operation was modeled with a set of theory modules:

- **Thermal module**: Inside the thermal module, the thermal load of differently shaped TISA crystals including plane-parallel crystals, Brewster-cut crystals, and crystals with undoped end-caps was modeled using finite element analysis (FEA) to solve the heat equation. Different factors influencing the thermal modeling were investigated, e.g., various boundary conditions, influence of temperature dependence of material properties, absorption coefficient of TISA, variable pump-beam profile, and pump-beam radius. Moreover, the following thermal simulations were carried out: time-dependent thermal analysis, single-end and unevenly pumped TISA crystal, TISA crystal including aluminum cooler and simulated Peltier element failure, incorporation of an experimentally determined real pump-beam profile, and crystal cooling with liquid nitrogen. The obtained 3d-temperature field was used to calculate the optical path difference (OPD) and in result the focal length of the thermal lens. For instance, a $1/e^2$-pump-beam radius of 0.75 mm at an average pump-power level of 40 W (sum of both sides) resulted in focal lengths of the thermal lens of about 68 cm in sagittal, and about 30 cm in tangential plane for a Brewster-cut TISA crystal of 2 cm length (820 nm, see Tab. D.1). The heat-transfer coefficients between air-crystal and crystal-cooler were set to 10 W/m^2·K and 15000 W/m^2·K, respectively. The temperature of the surrounding air and the cooler were set to 298.15 K and 288.15 K, respectively. A different method which uses slices of the calculated temperature field followed by matrix formalism shows that an optimized parabolic approximation radius can be found for each slice. The FEA calculated values were compared with experimental measurements of a probe laser and the model of [Innocenzi90]. The calculated OPD can easily be compared with measurements of a wavefront sensor. The obtained thermal lens values can be used as input parameters for the modeling of the beam propagation of stable and unstable resonators.

- **Resonator design and optimization module:** Stable and unstable ring resonators were modeled (Ch. 4.3, Ch. 4.4), with emphasis on the design procedure for an unsta-

ble resonator because unstable resonator designs were promising higher mode volumes. The stability zone of the stable resonator and the beam propagation with the expected intracavity power density at crystal and beam waist were simulated using a GLAD model (GLAD: General Laser Analysis and Design program). For an average intracavity circulating power of 20 W, power densities above 1 GW/cm^2 at a TISA laser pulse length of 40 ns can be expected. Concerning the unstable resonator, it was shown that the design factors, which have been used so far almost exclusively in Nd:YAG unstable resonator modeling, can be used also for end-pumped TISA lasers, and that the design procedure is straightforward, if modifications for considering the end-pumped TISA configuration are taken into account. 4×4 matrices in a single astigmatic treatment were used to analyze the beam propagation of the unstable resonator. A treatment based on diffraction theory is not necessary in the design phase, e.g., with the GLAD Software package, but can optionally be used for simulation purposes of various variable reflectivity mirror (VRM) output couplers and the overall beam propagation.

– **Performance module:** The expected TISA laser performance based on stable and unstable resonators at both 935 nm and 820 nm (Ch. 4.5.3 - Ch. 4.5.6) was calculated using a coupled nonlinear differential equation system of first order describing inversion density and photon density for the case of a Q-/gain-switched situation. Solution of the equation system yielded for both stable and unstable resonators the optimum output coupler reflectivity (stable resonator), output pulse energy, slope efficiency, extraction efficiency, total laser efficiency, pulse length, linewidth, and pulse built-up time. Due to the high sensitivity of end-pumped unstable resonators concerning the thermal lensing effect and therefore the (effective) magnification of the beam propagation, the unstable resonator shows a limited operation range concerning the pump-pulse energy, which is about 10−45 mJ in width. Inside this range, all relevant resonator parameters show a high sensitivity concerning the pump-pulse energy. An energy-stable pump laser is therefore required. At this stage, the developed thermal module can help to find suitable pump configurations before testing in the laboratory. Nevertheless, the properties of the unstable resonator, especially concerning the mode volume, show higher potential for even higher-power operation compared to stable resonator designs. It it also expected, that more compact, high-mode-volume resonators can be built with unstable resonator geometries. The proposed unstable ring resonator design is an example. It is expected that the resonator can be further optimized so that it fits on a 20×20 cm^2 square with a resonator length of 80 cm. The output beam profile and propagation can be optimized with a VRM. The performance model calculations were compared with the experimental results of a stable TISA resonator at 935 nm and 820, 825 nm. The overlap of pump and resonator mode η_{a_2} and dissipative resonator

losses L were used to adjust the model to the experiment.

- **Spectral module:** Finally, the factors influencing the spectral properties of the TISA laser were investigated (Ch. 4.6). Required is a high passive frequency stability together with injection seeding and an appropriate active frequency stabilization technique. It is recommended to use a Pound-Drever-Hall technique.

  The spectral purity was modeled using a novel virtual noise mode approach. The spectral purity was modeled for both stable and unstable resonators, showing that seed power of around 1 mW is sufficient to fulfill the requirements of a water-vapor DIAL transmitter concerning spectral purity. Factors contributing to laser noise (Ch. 4.6.5) were treated together with, for the first time, the Petermann excess noise factor for unstable resonators. It is found that it can be expected that the Petermann factor has only a minor role in pulsed unstable resonator geometries for DIAL applications.

Concerning the goal for a high-average power water-vapor DIAL system, the results using a stable resonator TISA laser at 935 nm and 820 nm are as follows. A pump-pulse energy of ≈200 mJ is required to achieve ≈75 mJ pulse energy of the TISA laser at 935 nm. Thus a 20-W average-power TISA laser at 820 nm requires a pump laser with ≈170 mJ pump-pulse energy at 250 Hz resulting in a TISA laser pulse energy of ≈80 mJ. It is not recommended to increase the repetition frequency of the present pump laser (250 Hz) and therefore decrease the pump-pulse energy, because high pump-pulse energies are beneficial in terms of better energy extraction. For this, operation of several times above laser threshold is advantageous. At the same time, a high pulse energy is also beneficial for achieving low water-vapor measurement errors under daylight conditions. Concerning the spectral properties, no power limitation for TISA lasers concerning the spectral purity is expected. This is in contrast to OPO or Raman frequency converters, for which the spectral properties are expected to decrease with increasing pump-pulse energy.

The development of an unstable TISA resonator as proposed within this work should be further continued. This assessment is also supported by the experimental results achieved by other groups. Given a stable pump laser, the performance is expected to be the same as for stable resonators. However, operation and scaling to even higher energies is more promising compared to stable resonator designs.

The overall modeling strategy developed within this work can be applied, adapted, and extended in future applications to other present and future laser materials, resonators, and also other frequency converters in order to optimize the high-power lasers concerning their thermal properties, their resonator design, their frequency-conversion performance, and their spectral properties.

A Efficiency factors

The extraction efficiency η_{extr} of a laser is defined by

$$\eta_{extr} \quad = \quad \frac{E_{out}}{E_{st}}, \tag{134}$$

where E_{out} is the output (pulse) energy and E_{st} is the stored (pump-laser) energy in the upper laser level [Hodgson05b].
The excitation efficiency η_{excit} is defined by

$$\eta_{excit} \quad = \quad \frac{E_{st}}{E_{pump}}, \tag{135}$$

where E_{pump} is the pump (pulse) energy.
The total laser efficiency η_{total} is defined by

$$\eta_{total} \quad = \quad \eta_{extr}\,\eta_{excit} \tag{136}$$

$$= \quad \frac{E_{out}}{E_{pump}}. \tag{137}$$

The slope of the curve describing the output energy with respect to the pump energy is defined as the slope efficiency η_{slope}:

$$\eta_{slope} \quad = \quad \frac{dE_{out}}{dE_{pump}}. \tag{138}$$

The stored energy E_{st} in the upper laser level is a product of efficiency factors $\eta_{o,a,c,f}$ [Coyle95, Siegman86c] with the input pulse energy E_{pump}:

$$E_{st} \quad = \quad \eta_o\,\eta_a\,\eta_c\,\eta_f\,E_{pump}. \tag{139}$$

η_o is the optical coupling efficiency which accounts for the losses at optics.
η_a is the absorption efficiency which is a product of the efficiency of radiation coupled into the laser cavity mode η_{a_1}, the overlap between pump and cavity modes η_{a_2}, and the radiation absorbed by the laser crystal η_{a_3}:

$$\eta_a \quad = \quad \eta_{a_1}\,\eta_{a_2}\,\eta_{a_3}. \tag{140}$$

η_c is the color efficiency with

$$\eta_c \;=\; \frac{\nu_l}{\nu_p}\,, \tag{141}$$

where ν_l, ν_p are the frequencies of laser and pump, respectively.

η_f is the fluorescence storage efficiency or pumping efficiency with

$$\eta_f \;=\; \frac{1 - \exp(-T_p/\tau_f)}{T_p/\tau_f}\,, \tag{142}$$

where T_p is the pump pulse length and τ_f is the fluorescence lifetime.

The corresponding values used inside the performance modeling (Ch. 4.5) are given in Tab. A.1.

Table A.1: Efficiency factors for TISA performance modeling (935 nm, 820 nm).

Parameter, Unit	TISA wavelength		Comment
	935 nm	820 nm	
Optical coupling efficiency η_o, %	90.0		
Absorption efficiency η_a, %	83.4		$\eta_a = \eta_{a_1} \cdot \eta_{a_2} \cdot \eta_{a_3}$ [Coyle95]
			$= 0.95 \cdot 0.9 \cdot 0.975$
Color efficiency η_c, %	56.9	64.9	
Fluorescence storage efficiency η_f, %	99.6		pump efficiency

B Error estimation and accuracy

The accuracy of the performed FEA calculation itself is determined by the mesh resolution of the model. Several runs at different mesh refinement levels can determine if the obtained solution shows convergence towards a stable value. Inside the FEA modeling, the mesh resolution or number of elements was manually adjusted at first to a maximum value according to the available computer memory. Also a multiphysics model consisting of a thermal part and a structural mechanics part was not consequently used, and therefore the expansion part to the total OPD is calculated using the calculated temperature profile. This method is necessary inside this study, as the additional degrees of freedom in a multiphysics model dramatically reduced the available memory. Therefore, a higher mesh resolution for the thermal analysis is given a higher priority, instead of obtaining directly additional structural mechanics information. Manual adjustment of the mesh is done where appropriate. For instance, the mesh inside the model $\boxed{\textbf{T12}}$ on page 65 with the aluminum cooler was at first locally adjusted to be coarser for the cooler compared to the mesh of the TISA crystal itself, as the influence of the pump created strong gradients inside the TISA domain, and the domains are also of quite different sizes (volumes).

The refinement of the mesh at critical areas with strong gradients inside the modeling domain can also be performed by an adaptive mesh refinement (AMR) algorithm. Inside this algorithm, the model is solved starting with a low resolution mesh, and an error estimate is calculated for each element (local error indicator). Subsequently, a further refinement is done on the mesh elements according to the error estimate, and a new solution run starts. This procedure is done as long as a predefined number of elements or refinement runs is reached. For further information about adaptive mesh refinement see [Knabner03, Verfürth96, COMSOL06b].

An example for an adaptive mesh refinement is shown in Fig. B.1. Shown is the meshed crystal domain at the crystal end-face without adaptive mesh refinement in Fig. B.1a, and with adaptive refinement in Fig. B.1b of the TISA crystal for the thermal model simulation $\boxed{\textbf{T6}}$ on page 50. The final refined mesh is higher resolved at the crystal center with adaptive mesh refinement at a comparable total number of mesh elements. The logfile of the solution process without and with AMR is shown in Fig. B.2 and Fig. B.3, respectively. For the case of modeling using AMR, a smaller number of total mesh elements is often sufficient to achieve the same model accuracy. As can be seen in Figs. B.4-B.5, the temperature profiles of the model with AMR result in smooth, centered profiles at a comparable total number of mesh elements.
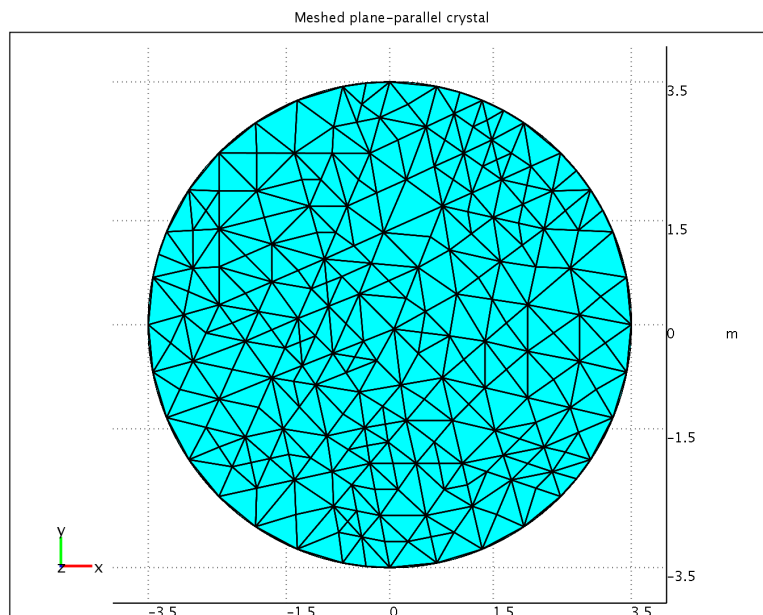
(a) Without AMR. 107621 mesh elements (complete crystal domain).
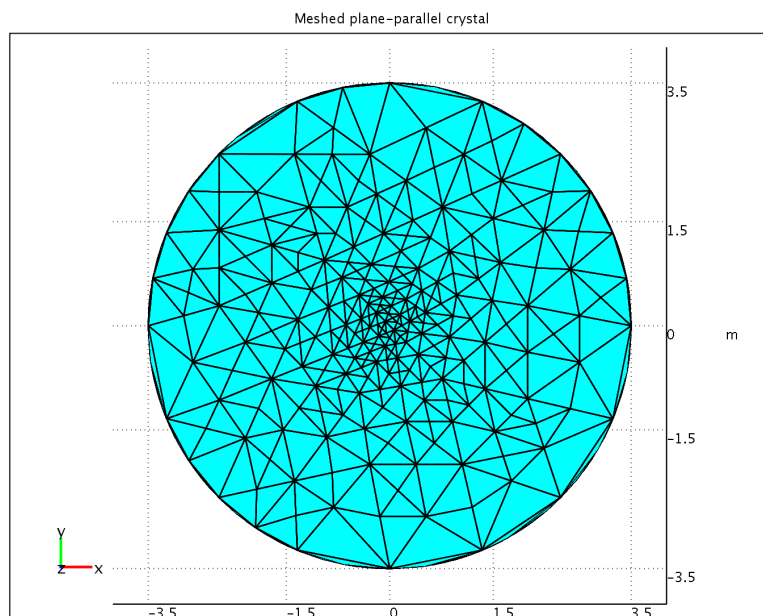
(b) With AMR. 107711 mesh elements (complete crystal domain).

Figure B.1: Meshed plane-parallel crystal: meshed crystal without and with adaptive mesh refinement (AMR). Shown is crystal end-face.

```
════════════════════════════════════════════════════════════
Progress − Open Model :  Sat Nov 22  19 :20 :31  CET  2008
════════════════════════════════════════════════════════════

════════════════════════════════════════════════════════════
Progress −  Initialize  Mesh :  Sat Nov 22  19 :21 :18  CET  2008
────────────────────────────────────────────────────────────

Number  of  vertex  elements :  8
Number  of  edge  elements :  84
Number  of  boundary  elements :  704
Number  of  elements :  3183
Minimum element  quality :  0.3873
────────────────────────────────────────────────────────────
Progress −  Refine  Mesh :  Sat Nov 22  19 :21 :20  CET  2008
════════════════════════════════════════════════════════════

════════════════════════════════════════════════════════════
Progress −  Refine  Mesh :  Sat Nov 22  19 :21 :21  CET  2008
════════════════════════════════════════════════════════════

════════════════════════════════════════════════════════════
Progress −  Refine  Mesh :  Sat Nov 22  19 :21 :22  CET  2008
════════════════════════════════════════════════════════════

════════════════════════════════════════════════════════════
Progress −  Solve  Problem :  Sat Nov 22  19 :21 :31  CET  2008
────────────────────────────────────────────────────────────
fem . sol=femnlin ( fem ,   . . .
               ' nullfun ' , ' flspnull ' ,   . . .
               ' conjugate ' , ' on ' ,   . . .
               ' solcomp ' , { 'T' } ,   . . .
               ' outcomp ' , { 'T' } ,   . . .
               ' ntol ' ,1E−6 ,   . . .
               ' linsolver ' , ' spooles ' ) ;
────────────────────────────────────────────────────────────
Number  of  degrees  of  freedom  solved  for :  152002
Iter        ErrEst        Damping       Stepsize  #Res  #Jac  #Sol
    1      0.00018     1.0000000          0.015     2     1     2
    2      1.3e−07     1.0000000        0.00019     3     2     4
```

Figure B.2: Logfile of solution process without using AMR (107621 mesh elements).

```
========================================================================
Progress − Open Model:  Fri Nov 21  21:54:45 CET 2008
========================================================================

========================================================================
Progress − Initialize Mesh:  Fri Nov 21  21:54:54 CET 2008
========================================================================
Number of vertex elements: 8
Number of edge elements: 84
Number of boundary elements: 704
Number of elements: 3183
Minimum element quality: 0.3873

========================================================================
Progress − Solve Problem:  Fri Nov 21  21:55:10 CET 2008
========================================================================
fem=adaption(fem, ...
            'nullfun','flspnull', ...
            'conjugate','on', ...
            'solcomp',{'T'}, ...
            'outcomp',{'T'}, ...
            'ntol',1E−6, ...
            'nonlin','on', ...
            'solver','stationary', ...
            'l2scale',[1], ...
            'l2staborder',[2], ...
            'eigselect',[1], ...
            'maxt',107621, ...
            'ngen',20, ...
            'resorder',[0], ...
            'rmethod','longest', ...
            'tppar',1.025, ...
            'linsolver','spooles', ...
            'geomnum',1);
------------------------------------------------------------------------
Mesh refinement level: 0
  Number of degrees of freedom solved for: 4994
  Iter        ErrEst      Damping      Stepsize #Res #Jac #Sol
    1       0.00021    1.0000000         0.016     2    1    2
    2       2.1e−07    1.0000000       0.00022     3    2    4
Global error indicator using 3183 elements and the L2−norm error estimator: 0.943153

Mesh refinement level: 1
  Number of degrees of freedom solved for: 17194
  Iter        ErrEst      Damping      Stepsize #Res #Jac #Sol
    1       8.9e−06    1.0000000        0.0023     2    1    2
    2       2.8e−10    1.0000000       8.8e−06     3    2    4
Global error indicator using 11986 elements and the L2−norm error estimator: 0.175358

Mesh refinement level: 2
  Number of degrees of freedom solved for: 41256
  Iter        ErrEst      Damping      Stepsize #Res #Jac #Sol
    1         4e−07    1.0000000       0.00034     2    1    2
    2       1.4e−12    1.0000000         4e−07     3    2    4
Global error indicator using 29544 elements and the L2−norm error estimator: 0.0442861

Mesh refinement level: 3
  Number of degrees of freedom solved for: 69551
  Iter        ErrEst      Damping      Stepsize #Res #Jac #Sol
    1       8.5e−09    1.0000000       5.4e−05     2    1    2
Global error indicator using 50032 elements and the L2−norm error estimator: 0.0231855

Mesh refinement level: 4
  Number of degrees of freedom solved for: 103342
  Iter        ErrEst      Damping      Stepsize #Res #Jac #Sol
    1       1.5e−09    1.0000000       2.4e−05     2    1    2
Global error indicator using 74402 elements and the L2−norm error estimator: 0.0146502

Mesh refinement level: 5
  Number of degrees of freedom solved for: 149353
  Iter        ErrEst      Damping      Stepsize #Res #Jac #Sol
    1         6e−10    1.0000000       1.5e−05     2    1    2
Global error indicator using 107711 elements and the L2−norm error estimator: 0.00993925

Maximum number of elements reached.
```

Figure B.3: Logfile of solution process using AMR with mesh refinement up until 107621 elements. Final mesh refinement level results in 107711 elements.
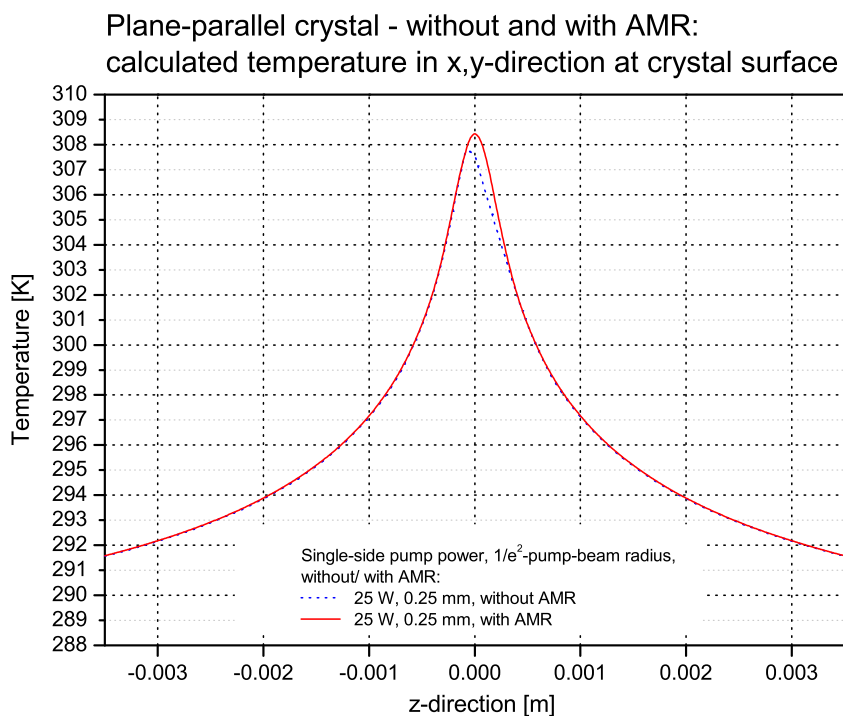
(a) Calc. temperature along x-, y-axis (surface).
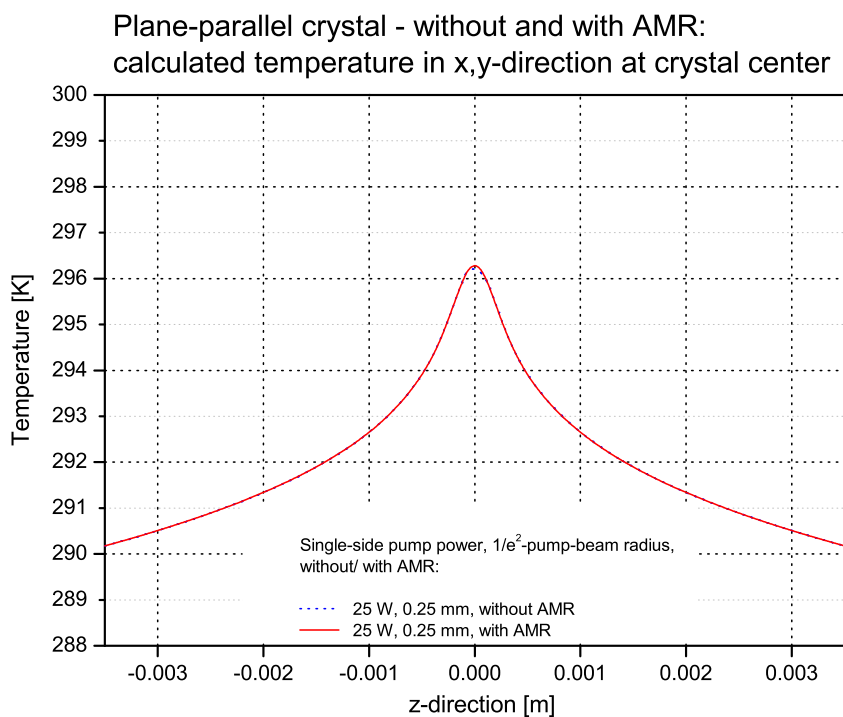
(b) Calc. temperature along x-, y-axis (center).

Figure B.4: Calc. temperature profile along z-axis, x-, y-axis (surface,center) without and with AMR for thermal simulation $\boxed{\textbf{T6}}$ on page 50. Shown is simulation with $1/e^2$-pump-beam radius of 0.25 mm.
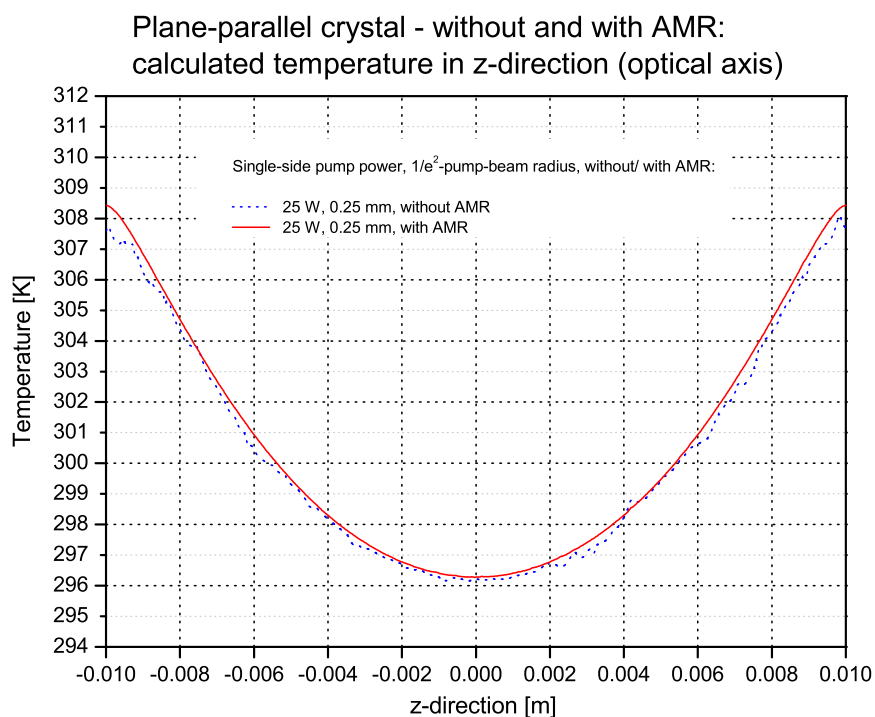
Figure B.5: Calc. temperature profile along z-axis without and with AMR for thermal simulation $\boxed{\text{T6}}$ on page 50. Shown is simulation with $1/e^2$-pump-beam radius of 0.25 mm.

C Multiphysics FEA model

A Brewster-cut TISA crystal pumped with 25 W single-side pump power ($1/e^2$-pump-beam radius: 1.5 mm) inside an aluminum cooler is modeled with a thermal model, and a structural mechanics model with corresponding parameters and boundary conditions is added. A simplified cooler model is used inside this simulation to save computer memory. The structural mechanics parameters for the model are given in Tab. C.1. The other parameters are the same as in $\boxed{\textbf{T12}}$. Figure C.1 shows the meshed crystal, and Figs. C.2a, C.2b show the resulting temperature in isosurfaces, and the overall resulting displacement (isosurfaces) of the cooler and the crystal, respectively.

Table C.1: Structural mechanics parameters for FEA multiphysics model.

Parameter, Unit	Sapphire	Aluminum
Density, kg/m^3	3990	2707
Thermal expansion coefficient, 10^{-6} K^{-1}	6.0	23.1
Young's modulus, 10^9 Pa	350	68.5
Poisson's ratio, [dim.-less]	0.25	0.359
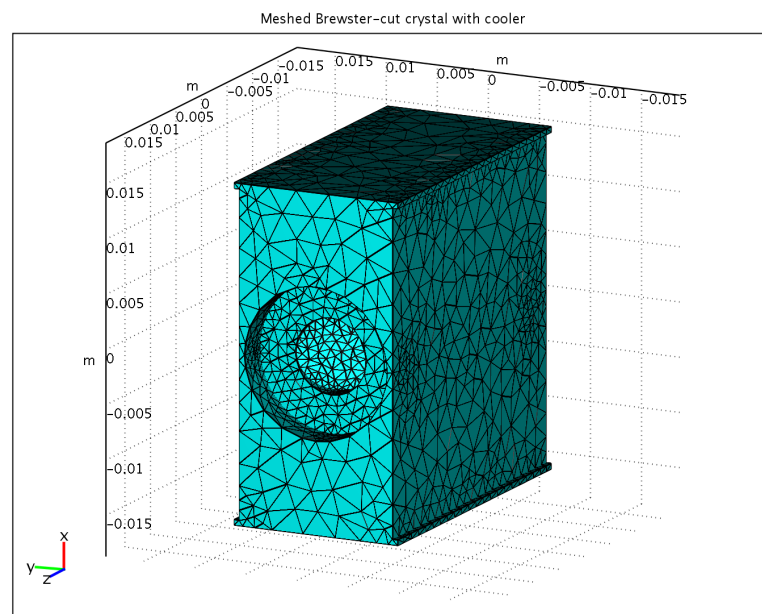
Figure C.1: Meshed Brewster-cut crystal with cooler (31393 elements).
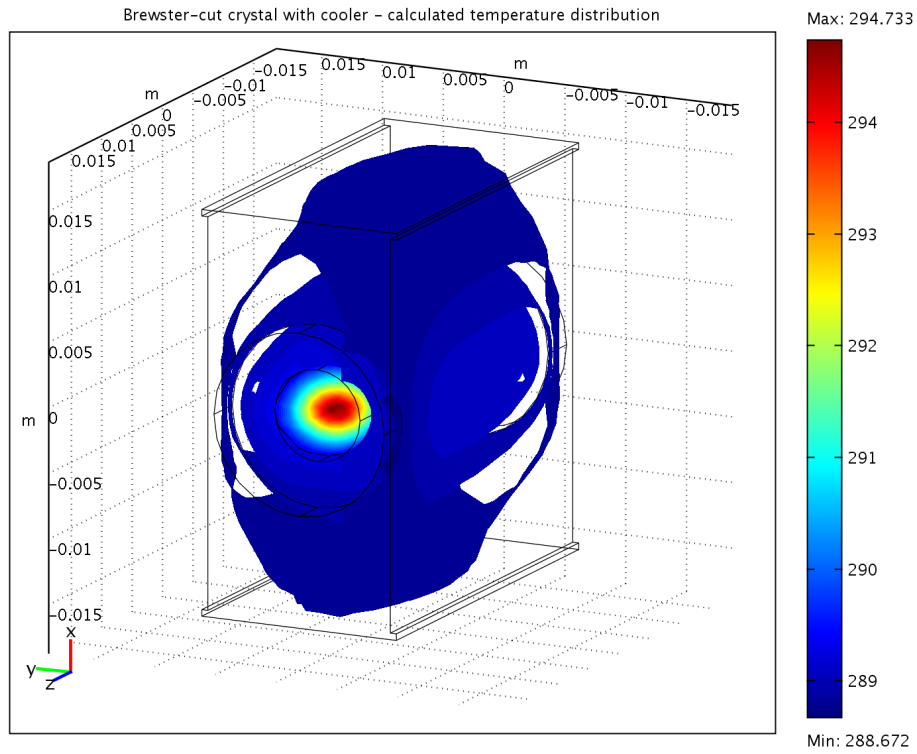
(a) Calc. temperature distribution in K (isosurfaces).
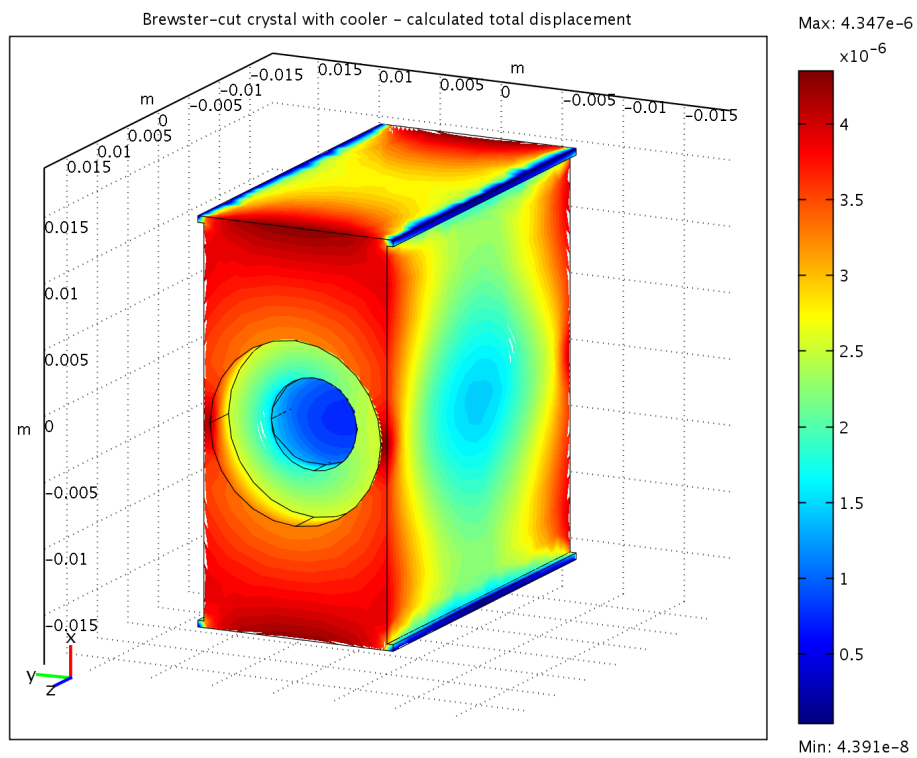
(b) Calc. total displacement in m (isosurfaces).

Figure C.2: Multiphysics FEA model. Shown is the calculated temperature profile in K, and the total displacement in m.

D Thermal lens data

Table D.1: Calc. thermal lens for BR TISA crystal. $1/e^2$-pump-beam radius: 0.75 mm.

Parameter, Unit	935 nm Thermal lens, m			820 nm Thermal lens, m		
Pump power, W	Sagittal	Tangential	Innocenzi	Sagittal	Tangential	Innocenzi
0	-	-	-	-	-	-
0.2	110.67972	49.55668	74.41737	135.90587	60.85166	91.37860
0.4	55.33986	24.77834	37.20869	67.95293	30.42583	45.68930
0.6	36.89324	16.51889	24.80579	45.30196	20.28388	30.45953
0.8	27.66993	12.38917	18.60434	33.97647	15.21291	22.84465
1	22.13594	9.91134	14.88347	27.18117	12.17033	18.27572
2	11.06797	4.95567	7.44174	13.59059	6.08516	9.13786
3	7.37865	3.30378	4.96116	9.06039	4.05678	6.09191
4	5.53399	2.47783	3.72087	6.79529	3.04258	4.56893
5	4.42719	1.98227	2.97669	5.43623	2.43407	3.65514
6	3.68932	1.65189	2.48058	4.53020	2.02839	3.04595
7	3.16228	1.41591	2.12621	3.88302	1.73862	2.61082
8	2.76699	1.23892	1.86043	3.39765	1.52129	2.28446
9	2.45955	1.10126	1.65372	3.02013	1.35226	2.03064
10	2.21359	0.99113	1.48835	2.71812	1.21703	1.82757
11	2.01236	0.90103	1.35304	2.47102	1.10639	1.66143
12	1.84466	0.82594	1.24029	2.26510	1.01419	1.52298
13	1.70276	0.76241	1.14488	2.09086	0.93618	1.40582
14	1.58114	0.70795	1.06311	1.94151	0.86931	1.30541
15	1.47573	0.66076	0.99223	1.81208	0.81136	1.21838
16	1.38350	0.61946	0.93022	1.69882	0.76065	1.14223
17	1.30211	0.58302	0.87550	1.59889	0.71590	1.07504
18	1.22977	0.55063	0.82686	1.51007	0.67613	1.01532
19	1.16505	0.52165	0.78334	1.43059	0.64054	0.96188
20	1.10680	0.49557	0.74417	1.35906	0.60852	0.91379
21	1.05409	0.47197	0.70874	1.29434	0.57954	0.87027
22	1.00618	0.45052	0.67652	1.23551	0.55320	0.83071
23	0.96243	0.43093	0.64711	1.18179	0.52914	0.79460
23.2	0.95414	0.42721	0.64153	1.17160	0.52458	0.78775
24	0.92233	0.41297	0.62014	1.13255	0.50710	0.76149
25	0.88544	0.39645	0.59534	1.08725	0.48681	0.73103
30	0.73786	0.33038	0.49612	0.90604	0.40568	0.60919
35	0.63246	0.28318	0.42524	0.77660	0.34772	0.52216
40	0.55340	0.24778	0.37209	0.67953	0.30426	0.45689
45	0.49191	0.22025	0.33074	0.60403	0.27045	0.40613
50	0.44272	0.19823	0.29767	0.54362	0.24341	0.36551
60	0.36893	0.16519	0.24806	0.45302	0.20284	0.30460
70	0.31623	0.14159	0.21262	0.38830	0.17386	0.26108
80	0.27670	0.12389	0.18604	0.33976	0.15213	0.22845

Table D.2: Same as Tab. D.1, but with $1/e^2$-pump-beam radius of 0.9 mm.

Parameter, Unit	935 nm Thermal lens, m			820 nm Thermal lens, m		
Pump power, W	Sagittal	Tangential	Innocenzi	Sagittal	Tangential	Innocenzi
0	-	-	-	-	-	-
1	31.66438	14.22420	21.43220	38.88134	17.46618	26.31704
2	15.83219	7.11210	10.71610	19.44067	8.73309	13.15852
3	10.55479	4.74140	7.14407	12.96045	5.82206	8.77235
4	7.91610	3.55605	5.35805	9.72033	4.36654	6.57926
5	6.33288	2.84484	4.28644	7.77627	3.49324	5.26341
6	5.27740	2.37070	3.57203	6.48022	2.91103	4.38617
7	4.52348	2.03203	3.06174	5.55448	2.49517	3.75958
8	3.95805	1.77802	2.67903	4.86017	2.18327	3.28963
9	3.51826	1.58047	2.38136	4.32015	1.94069	2.92412
10	3.16644	1.42242	2.14322	3.88813	1.74662	2.63170
11	2.87858	1.29311	1.94838	3.53467	1.58783	2.39246
12	2.63870	1.18535	1.78602	3.24011	1.45551	2.19309
13	2.43572	1.09417	1.64863	2.99087	1.34355	2.02439
14	2.26174	1.01601	1.53087	2.77724	1.24758	1.87979
15	2.11096	0.94828	1.42881	2.59209	1.16441	1.75447
16	1.97902	0.88901	1.33951	2.43008	1.09164	1.64481
17	1.86261	0.83672	1.26072	2.28714	1.02742	1.54806
18	1.75913	0.79023	1.19068	2.16007	0.97034	1.46206
19	1.66655	0.74864	1.12801	2.04639	0.91927	1.38511
20	1.58322	0.71121	1.07161	1.94407	0.87331	1.31585
21	1.50783	0.67734	1.02058	1.85149	0.83172	1.25319
22	1.43929	0.64655	0.97419	1.76733	0.79392	1.19623
23	1.37671	0.61844	0.93183	1.69049	0.75940	1.14422
24	1.31935	0.59267	0.89301	1.62006	0.72776	1.09654
25	1.26658	0.56897	0.85729	1.55525	0.69865	1.05268
26	1.21786	0.54708	0.82432	1.49544	0.67178	1.01219
27	1.17275	0.52682	0.79379	1.44005	0.64690	0.97471
28	1.13087	0.50801	0.76544	1.38862	0.62379	0.93989
29	1.09188	0.49049	0.73904	1.34074	0.60228	0.90748
30	1.05548	0.47414	0.71441	1.29604	0.58221	0.87723
35	0.90470	0.40641	0.61235	1.11090	0.49903	0.75192
40	0.79161	0.35560	0.53581	0.97203	0.43665	0.65793
45	0.70365	0.31609	0.47627	0.86403	0.38814	0.58482
50	0.63329	0.28448	0.42864	0.77763	0.34932	0.52634
60	0.52774	0.23707	0.35720	0.64802	0.29110	0.43862
70	0.45235	0.20320	0.30617	0.55545	0.24952	0.37596
80	0.39580	0.17780	0.26790	0.48602	0.21833	0.32896

Table D.3: Same as Tab. D.1, but with $1/e^2$-pump-beam radius of 1.05 mm.

Parameter, Unit	935 nm Thermal lens, m			820 nm Thermal lens, m		
Pump power, W	Sagittal	Tangential	Innocenzi	Sagittal	Tangential	Innocenzi
0	-	-	-	-	-	-
1	42.90095	19.41705	29.17161	52.67895	23.84259	35.82041
2	21.45048	9.70853	14.58580	26.33947	11.92130	17.91020
3	14.30032	6.47235	9.72387	17.55965	7.94753	11.94014
4	10.72524	4.85426	7.29290	13.16974	5.96065	8.95510
5	8.58019	3.88341	5.83432	10.53579	4.76852	7.16408
6	7.15016	3.23618	4.86193	8.77982	3.97377	5.97007
7	6.12871	2.77386	4.16737	7.52556	3.40608	5.11720
8	5.36262	2.42713	3.64645	6.58487	2.98032	4.47755
9	4.76677	2.15745	3.24129	5.85322	2.64918	3.98005
10	4.29009	1.94171	2.91716	5.26789	2.38426	3.58204
11	3.90009	1.76519	2.65196	4.78899	2.16751	3.25640
12	3.57508	1.61809	2.43097	4.38991	1.98688	2.98503
13	3.30007	1.49362	2.24397	4.05223	1.83405	2.75542
14	3.06435	1.38693	2.08369	3.76278	1.70304	2.55860
15	2.86006	1.29447	1.94477	3.51193	1.58951	2.38803
16	2.68131	1.21357	1.82323	3.29243	1.49016	2.23878
17	2.52359	1.14218	1.71598	3.09876	1.40251	2.10708
18	2.38339	1.07873	1.62064	2.92661	1.32459	1.99002
19	2.25794	1.02195	1.53535	2.77258	1.25487	1.88528
20	2.14505	0.97085	1.45858	2.63395	1.19213	1.79102
21	2.04290	0.92462	1.38912	2.50852	1.13536	1.70573
22	1.95004	0.88259	1.32598	2.39450	1.08375	1.62820
23	1.86526	0.84422	1.26833	2.29039	1.03663	1.55741
24	1.78754	0.80904	1.21548	2.19496	0.99344	1.49252
25	1.71604	0.77668	1.16686	2.10716	0.95370	1.43282
26	1.65004	0.74681	1.12198	2.02611	0.91702	1.37771
27	1.58892	0.71915	1.08043	1.95107	0.88306	1.32668
28	1.53218	0.69347	1.04184	1.88139	0.85152	1.27930
29	1.47934	0.66955	1.00592	1.81652	0.82216	1.23519
30	1.43003	0.64724	0.97239	1.75596	0.79475	1.19401
35	1.22574	0.55477	0.83347	1.50511	0.68122	1.02344
40	1.07252	0.48543	0.72929	1.31697	0.59606	0.89551
45	0.95335	0.43149	0.64826	1.17064	0.52984	0.79601
50	0.85802	0.38834	0.58343	1.05358	0.47685	0.71641
60	0.71502	0.32362	0.48619	0.87798	0.39738	0.59701
70	0.61287	0.27739	0.41674	0.75256	0.34061	0.51172
80	0.53626	0.24271	0.36465	0.65849	0.29803	0.44776

References

[ADM]   ADM. European Space Agency (ESA): ADM-Aeolus. URL `http://www.esa.int/esaLP/LPadmaeolus.html`.

[Afzal94]   Afzal, R. S., 1994: Mars Observer Laser Altimeter: laser transmitter. Appl. Optics, 33(15), 3184–3188.

[Albers86]   Albers, P., E. Stark, and G. Huber, 1986: Continous-wave laser operation and quantum efficiency of titanium-doped sapphire. J. Opt. Soc. Am. B, 3(1), 134–139.

[Anan'ev69]   Anan'ev, Y. A., N. A. Sventsitskaya, and V. E. Sherstobitov, 1969: Properties of a laser with an unstable resonator. Sov. Phys. JETP-USSR, 28(1), 69–74.

[Barnes93a]   Barnes, J. C., N. P. Barnes, L. G. Wang, and W. Edwards, 1993: Injection seeding II: Ti:Al$_2$O$_3$ experiments. IEEE J. Quant. Elect., 29(10), 2684–2692.

[Barnes93b]   Barnes, N. P. and J. C. Barnes, 1993: Injection seeding I: theory. IEEE J. Quant. Elect., 29(10), 2670–2683.

[Behrendt05]   Behrendt, A., 2005: Temperature Measurements with Lidar, volume 102 of Springer Series in Optical Sciences: LIDAR: Range-Resolved Optical Remote Sensing of the Atmosphere, chapter 10. Springer Science+Business Media Inc.

[Bierlein89]   Bierlein, J. D. and H. Vanherzeele, 1989: Potassium titanyl phosphate: properties and new applications. J. Opt. Soc. Am. B, 6(4), 622–633.

[Bjorkholm69]   Bjorkholm, J. E. and H. G. Danielmeyer, 1969: Frequency control of a pulsed optical parametric oscillator by radiation injection. Appl. Phys. Lett., 15(6), 171–173.

[Bloembergen67] Bloembergen, N., 1967: The stimulated Raman effect. Am. J. Phys, 35(11), 989–1023.

[Bloembergen96] Bloembergen, N., 1996: Experimental results, chapter 5. Nonlinear Optics. World Scientific Publishing, 4th edition, 121–165.

[Bösenberg98]   Bösenberg, J., 1998: Ground-based differential absorption lidar for water-vapor and temperature profiling. Appl. Optics, 37(18), 3845–3860.

[Bösenberg05]   Bösenberg, J., 2005: Differential-Absorption Lidar for Water Vapor and Temperature Profiling, volume 102 of Springer Series in Optical Sciences: LIDAR: Range-Resolved Optical Remote Sensing of the Atmosphere, chapter 8. Springer Science+Business Media Inc.

[Bowers94]   Bowers, M. S. and S. E. Moody, 1994: Cavity equations for a laser with an externally injected signal. J. Opt. Soc. Am. B, 11(11), 2266–2275.

[Breteau93]   Breteau, J. M., C. Jourdain, T. Lepine, and F. Simon, 1993: Numerical simulation and realization of a KTP optical parametric oscillator. In Advanced Solid-State Lasers, volume 15 of OSA Proceedings.

[Brosnan79]   Brosnan, S. J. and R. L. Byer, 1979: Optical parametric oscillator threshold and linewidth studies. IEEE J. Quant. Elect., 15(6), 415–431.

[Browell98]   Browell, E. V., S. Ismail, and W. B. Grant, 1998: Differential absorption lidar (DIAL) measurements from air and space. Appl. Phys. B - Lasers O., 67, 399–410.

[Bruneau91]   Bruneau, D., H. Cazeneuve, C. Loth, and J. Pelon, 1991: Double-pulse dual-wavelength alexandrite laser for atmospheric water vapor measurement. Appl. Optics, 30(27), 3930–3937.

[Bruneau94]   Bruneau, D., T. A. des Lions, P. Quaglia, and J. Pelon, 1994: Injection-seeded pulsed alexandrite laser for differential absorption lidar application. Appl. Optics, 33(18), 3941–3950.

[Bruneau01a]   Bruneau, D., P. Quaglia, C. Flamant, M. Meissonnier, and J. Pelon, 2001: Airborne lidar LEANDRE II for water-vapor profiling in the troposphere. I. System description. Appl. Optics, 40(21), 3450–3461.

[Bruneau01b]   Bruneau, D., P. Quaglia, C. Flamant, and J. Pelon, 2001: Airborne lidar LEANDRE II for water-vapor profiling in the troposphere. II. First results. Appl. Optics, 40(21), 3462–3475.

[Canova05]   Canova, F., J.-P. Chambaret, G. Mourou, M. Sentis, O. Uteza, P. Delaporte, T. Itina, J.-Y. Natoli, M. Commandre, and C. Amra, 2005: Complete characterization of damage threshold in titanium doped sapphire crystals with nanosecond, picosecond and femtosecond laser pulses. In Proceedings of SPIE, volume 5991 of Laser-induced damage in optical materials. 599123–7.

References

[Chénais04a]   Chénais, S., F. Balembois, F. Druon, G. Lucas-Leclin, and P. Georges, 2004: Thermal lensing in diode-pumped Ytterbium lasers - part I: theoretical analysis and wavefront measurements. IEEE J. Quant. Elect., 40(9), 1217–1234.

[Chénais04b]   Chénais, S., F. Balembois, F. Druon, G. Lucas-Leclin, and P. Georges, 2004: Thermal lensing in diode-pumped Ytterbium lasers - part II: evaluation of quantum efficiencies and thermo-optic coefficients. IEEE J. Quant. Elect., 40(9), 1235–1243.

[Chénais04c]   Chénais, S., S. Forget, F. Druon, F. Balembois, and P. Georges, 2004: Direct and absolute temperature mapping and heat transfer measurements in diode-end-pumped Yb:YAG. Appl. Phys. B - Lasers O., 79, 221–224.

[Cheng94]   Cheng, Y.-J., P. L. Mussche, and A. E. Siegman, 1994: Measurement of laser quantum frequency fluctuations using a Pound-Drever stabilization system. IEEE J. Quant. Elect., 30(6), 1498–1504.

[Cheng96]   Cheng, Y.-J., C. G. Fanning, and A. E. Siegman, 1996: Experimental observation of a large excess quantum noise factor in the linewidth of a laser oscillator having nonorthogonal modes. Phys. Rev. Lett., 77(4), 627–630.

[COMSOL06a]   COMSOL, 2006: COMSOL Multiphysics Modeling Guide - Version 3.3. COMSOL AB.

[COMSOL06b]   COMSOL, 2006: COMSOL Multiphysics User's Guide - Version 3.3. COMSOL AB.

[Cousins92]   Cousins, A. K., 1992: Temperature and thermal stress scaling in finite-length end-pumped laser rods. IEEE J. Quant. Elect., 28(4), 1057–1069.

[Coyle95]   Coyle, D. B., D. V. Guerra, and R. Kay, 1995: An interactive numerical model of diode-pumped, Q-switched/cavity-dumped lasers. J. Phys. D: Appl. Phys., 28, 452–462.

[Danger93]   Danger, T., K. Petermann, and G. Huber, 1993: Polarized and Time-Resolved Measurements of Excited-State Absorption and Stimulated Emission in Ti:YAlO$_3$ and Ti:Al$_2$O$_3$. Appl. Phys. A - Solids and Surfaces, 57, 309–313.

[Degnan89]   Degnan, J. J., 1989: Theory of the optimally coupled Q-switched laser. IEEE J. Quant. Elect., 25(2), 214–220.

[Degnan98]   Degnan, J. J., D. B. Coyle, and R. B. Kay, 1998: Effects of thermalization on Q-switched laser properties. IEEE J. Quant. Elect., 34(5), 887–899.

[DeShazer88]   DeShazer, L. G., J. M. Eggleston, and K. W. Kangas, 1988: Saturation of green absorption in titanium-doped sapphire laser crystals. Opt. Lett., 13(5), 363–365.

[DeSilvestri88a]   DeSilvestri, S., P. Laporta, V. Magni, and O. Svelto, 1988: Solid-state laser unstable resonators with tapered reflectivity mirrors: the super-Gaussian approach. IEEE J. Quant. Elect., 24(6), 1172–1177.

[DeSilvestri88b]   DeSilvestri, S., P. Laporta, V. Magni, O. Svelto, and B. Majocchi, 1988: Unstable laser resonators with super-Gaussian mirrors. Opt. Lett., 13(3), 201–203.

[Dmitriev99]   Dmitriev, V. G., G. G. Gurzadyan, and D. N. Nikogosyan, 1999: Handbook of nonlinear optical crystals. Springer-Verlag Berlin Heidelberg New York, 3rd revised edition.

[Doumont89]   Doumont, J.-L., P. L. Mussche, and A. E. Siegman, 1989: Excess spontaneous emission in variable-reflectivity-mirror lasers. IEEE J. Quant. Elect., 25(8), 1960–1967.

[Drever83]   Drever, R. W. P., J. L. Hall, F. V. Kowalski, J. Hough, G. M. Ford, A. J. Munley, and H. Ward, 1983: Laser phase and frequency stabilization using an optical resonator. Appl. Phys. B - Photo., 31, 97–105.

[Duan93]   Duan, Q. Y., V. K. Gupta, and S. Sorooshian, 1993: Shuffled complex evolution approach for effective and efficient global minimization. J. Optimiz. Theory App., 76(3).

[Dupré07]   Dupré, P. and T. A. Miller, 2007: Quasi-Fourier-transform limited, scannable, high energy titanium-sapphire laser source for high resolution spectroscopy. Rev. Sci. Instrum., 78, 033102–12.

[Ebrahimzadeh07] Ebrahimzadeh, M. and M. H. Dunn, 2007: Optical parametric oscillators, volume 4 of Handbook of Optics - Fiber optics and nonlinear optics, chapter 22. McGraw-Hill, 2nd edition, 22.1–22.72.

[Eggleston88]   Eggleston, J. M., L. G. DeShazer, and K. W. Kangas, 1988: Characteristics and Kinetics of Laser-Pumped Ti:Sapphire Oscillators. IEEE J. Quant. Elect., 24(6), 1009–1015.

References

[Ehret98]   Ehret, G., A. Fix, V. Weiß, G. Poberaj, and T. Baumert, 1998: Diode-laser-seeded optical parametric oscillator for airborne water vapor DIAL application in the upper troposphere and lower stratosphere. Appl. Phys. B - Lasers O., 67, 427–431.

[Eichler93]   Eichler, H. J., A. Haase, R. Menzel, and A. Siemoneit, 1993: Thermal lensing and depolarization in a highly pumped Nd:YAG laser amplifier. J. Appl. Phys. D, 26, 1884–1891.

[Eichler02]   Eichler, J. and H. J. Eichler, 2002: Laser: Bauformen, Strahlführung, Anwendung. Springer-Verlag Berlin Heidelberg.

[Eilers92]   Eilers, H., E. Strauss, and W. M. Yen, 1992: Photoelastic effect in Ti^{3+}-doped sapphire. Phys. Rev. B, 45(17), 9604–9610.

[Elsayed03]   Elsayed, K. A., R. J. DeYoung, L. B. Petway, W. C. Edwards, J. C. Barnes, and H. E. Elsayed-Ali, 2003: Compact high-pulse-energy ultra-violet laser source for ozone lidar measurements. Appl. Optics, 42(33), 6650–6660.

[Emanueli03]   Emanueli, S. and A. Arie, 2003: Temperature-dependent dispersion equations for $KTiOPO_4$ and $KTiOAsO_4$. Appl. Optics, 42(33), 6661–6665.

[Ertel05]   Ertel, K., H. Linné, and J. Bösenberg, 2005: Injection-seeded pulsed Ti:sapphire laser with novel stabilization scheme and capability of dual-wavelength operation. Appl. Optics, 44(24), 5120–5126.

[ESA]   ESA. European Space Agency (ESA): Observing the Earth. URL `http://www.esa.int/esaEO/`.

[Esherick87]   Esherick, P. and A. Owyoung, 1987: Polarization feedback stabilization of an injection-seeded Nd:YAG laser for spectroscopic applications. J. Opt. Soc. Am. B, 4(1), 41–47.

[Fix98]   Fix, A., V. Weiss, and G. Ehret, 1998: Injection-seeded optical parametric oscillator for airborne water vapour DIAL. Pure Appl. Opt., 7, 837–852.

[Frantz63]   Frantz, L. M. and J. S. Nodvik, 1963: Theory of pulse propagation in a laser amplifier. J. Appl. Phys., 34(8), 2346–2349.

[Frauchiger92] Frauchiger, J., P. Albers, and H. P. Weber, 1992: Modeling of thermal lensing and higher order ring mode oscillation in end-pumped cw Nd:YAG lasers. IEEE J. Quant. Elect., 28(4), 1046–1056.

[Freiberg74]   Freiberg, R. J., P. P. Chenausky, and C. J. Buczek, 1974: Asymmetric unstable traveling-wave resonators. IEEE J. Quant. Elect., 10(2), 279–289.

[Georgiev92]   Georgiev, D., J. Herrmann, and U. Stamm, 1992: Cavity design for optimum nonlinear absorption in Kerr-lens mode-locked solid-state lasers. Opt. Commun., 92, 368–375.

[Gerrard94a]   Gerrard, A. and J. M. Burch, 1994: Introduction to matrix methods in optics. Dover Publications Inc. Mineola, dover edition. Republication of John Wiley & Sons London and New York 1975.

[Gerrard94b]   Gerrard, A. and J. M. Burch, 1994: Locating the cardinal points of a system, chapter II.9. Introduction to matrix methods in optics. Dover Publications Inc. Mineola, dover edition, 54–99. Republication of John Wiley & Sons London and New York 1975.

[GLAD]   GLAD. GLAD: General Laser Analysis and Design program. Version 5.0.5. URL http://www.aor.com.

[Granot00]   Granot, E., S. Pearl, and M. M. Tilleman, 2000: Analytical solution for a lossy singly resonant optical parametric oscillator. J. Opt. Soc. Am. B, 17(3), 381–386.

[Grinberg93a]   Grinberg, M., A. Mandelis, and K. Fjeldsted, 1993: Theory of interconfigurational nonradiative transistions in transistion-metal ions in solids and application to the Ti^{3+} :Al_2O_3. Phys. Rev. B, 48(9), 5935–5944.

[Grinberg93b]   Grinberg, M., A. Mandelis, K. Fjeldsted, and A. Othonos, 1993: Spectroscopy and analysis of radiative and nonradiative processes in Ti^{3+}:Al_2O_3. Phys. Rev. B, 48(9), 5922–5934.

[Grinberg94]   Grinberg, M. and A. Mandelis, 1994: Photopyroelectric-quantum-yield spectroscopy and quantum-mechanical photoexcitation-decay kinetics of the Ti^{3+} ion in Al_2O_3. Phys. Rev. B, 49(18), 12496–12506.

[Grzeschik08]   Grzeschik, M., H.-S. Bauer, V. Wulfmeyer, D. Engelbart, U. Wandinger, I. Mattis, D. Althausen, R. Engelmann, M. Tesche, and A. Riede, 2008: Four-dimensional variational data analysis of water vapor Raman lidar data and their impact on mesoscale forecasts. J. Atmos. Ocean Tech., 25(8), 1437–1453.

References

[Guerra94]   Guerra, D. V., D. B. Coyle, and D. J. Krebs, 1994: A completely solid state Ti:sapphire laser system for lidar and atmospheric spectroscopy. Meas. Sci. Technol., 5, 1306–1308.

[Guerra99]   Guerra, D. V., M. A. M. II, and D. B. Coyle, 1999: An introduction to laser modeling studies with a nitrogen-pumped dye laser. Am. J. Phys, 67(9), 803–809.

[Hanna69]   Hanna, D. C., 1969: Astigmatic Gaussian beams produced by axially asymmetric laser cavities. IEEE J. Quant. Elect., 5(10), 483–488.

[Hannemann07] Hannemann, S., E.-J. van Duijn, and W. Ubachs, 2007: A narrowband injection-seeded pulsed titanium-sapphire oscillator-amplifier system with on-line chirp analysis for high-resolution spectroscopy. Rev. Sci. Instrum., 78, 103102–9.

[Hänsch80]   Hänsch, T. W. and B. Couillaud, 1980: Laser frequency stabilization by polarization spectroscopy of a reflecting reference cavity. Opt. Commun., 35(3), 441–444.

[Harris69]   Harris, S. E., 1969: Tunable optical parametric oscillator. P. IEEE, 57(12), 2096–2113.

[He97]   He, C. and T. H. Chyba, 1997: Solid-state barium nitrate Raman laser in the visible region. Opt. Commun., 135, 273–278.

[Henderson86] Henderson, S. W., E. H. Yuen, and E. S. Fry, 1986: Fast resonance-detection technique for single-frequency operation of injection-seeded Nd:YAG lasers. Opt. Lett., 11(11), 715–717.

[Henderson00a] Henderson, B. and R. H. Bartram, 2000: Crystal-field engineering of solid-state laser materials. Cambridge studies in modern optics. Cambridge University Press, paperback version 2005 edition.

[Henderson00b] Henderson, B. and R. H. Bartram, 2000: Octahedrally-coordinated Ti^{3+}, chapter 5.4.3. Crystal-field engineering of solid-state laser materials, Cambridge studies in modern optics. Cambridge University Press, paperback version 2005 edition, 166–168.

[Hodgson05a]   Hodgson, N. and H. Weber, 2005: The Laser Equations, volume 108 of Optical Sciences: Laser resonators and beam propagation, chapter 9.4. Springer Science+Business Media Inc., 2nd edition, 374–382.

[Hodgson05b]   Hodgson, N. and H. Weber, 2005: Laser resonators and beam propaga-tion, volume 108 of Springer Series in Optical Sciences. Springer Sci-ence+Business Media Inc., 2nd edition.

[Hodgson05c]   Hodgson, N. and H. Weber, 2005: Resonators with variable internal lenses, volume 108 of Optical Sciences: Laser resonators and beam prop-agation, chapter 13. Springer Science+Business Media Inc., 2nd edition, 451–503.

[Huang96]   Huang, X. G., W. K. Lee, S. P. Wong, J. Y. Zhou, and Z. X. Yu, 1996: Effects of thermal lensing on stability and astigmatic compensation of a Z-fold laser cavity. J. Opt. Soc. Am. B, 13(12), 2863–2868.

[Huber09]   Huber, G. and G. Wagner, 2009. Private communication concerning Ti:Sapphire (Fluorescence lifetime, energy level-system, ESA).

[Incropera02]   Incropera, F. P. and D. P. DeWitt, 2002: Fundamentals of heat and mass transfer. John Wiley & Sons, Inc., 5th edition.

[Innocenzi90]   Innocenzi, M. E., H. T. Yura, C. L. Fincher, and R. A. Fields, 1990: Ther-mal modeling of continuous-wave end-pumped solid-state lasers. Appl. Phys. Lett., 56(19), 1831–1833.

[Ismail89]   Ismail, S. and E. V. Browell, 1989: Airborne and spaceborne lidar mea-surements of water vapor profiles: a sensitivity analysis. Appl. Optics, 28(17), 3603–3616.

[Ito02]   Ito, S., H. Nagaoka, T. Miura, K. Kobayashi, A. Endo, and K. Torizuka, 2002: Measurement of thermal lensing in a power amplifier of a terrawatt Ti:sapphire laser. Appl. Phys. B - Lasers O., 74, 343–347.

[Kallmeyer07]   Kallmeyer, F., M. Dziedzina, X. Wang, H. Eichler, C. Czeranowsky, B. Ileri, K. Petermann, and G. Huber, 2007: Nd:GSAG-pulsed laser op-eration at 943 nm and crystal growth. Appl. Phys. B - Lasers O., 89, 305–310.

[Karman98]   Karman, G. P. and J. P. Woerdman, 1998: Fractal structure of eigen-modes of unstable-cavity lasers. Opt. Lett., 23(24), 1909–1911.

[Kay05]   Kay, R. B. and D. Poulios, 2005: Q-switched rate equations for diode side-pumped slab and zigzag slab lasers including Gaussian beam shapes. IEEE J. Quant. Elect., 41(10), 1278–1284.

References

[Knabner03]   Knabner, P. and L. Angermann, 2003: Grid generation and a posteriori error estimation, volume 44 of Texts in applied mathematics: Numerical methods for elliptic and parabolic partial differential equations, chapter 4. Springer-Verlag New York, 176–197.

[Koechner99a]   Koechner, W., 1999: Properties of solid-state laser materials, chapter 2. Solid-state laser engineering. Springer-Verlag Berlin Heidelberg New York, 28–87.

[Koechner99b]   Koechner, W., 1999: Q-switching, chapter 8. Solid-state laser engineering. Springer-Verlag Berlin Heidelberg New York, 469–519.

[Koechner99c]   Koechner, W., 1999: Thermo-optic effects and heat removal, chapter 7. Solid-state laser engineering. Springer-Verlag Berlin Heidelberg New York, 406–468.

[Koechner03]   Koechner, W. and M. Bass, 2003: Solid-state lasers. Springer Verlag New York Berlin Heidelberg.

[Kogelnik65]   Kogelnik, H., 1965: Imaging of optical modes - resonators with internal lenses. AT&T Tech. J., 44, 455–494.

[Kogelnik66]   Kogelnik, H. and T. Li, 1966: Laser beams and resonators. Appl. Optics, 5(10), 1550–1567.

[Kogelnik72]   Kogelnik, H. W., E. P. Ippen, A. Dienes, and C. V. Shank, 1972: Astigmatically compensated cavities for CW dye lasers. IEEE J. Quant. Elect., 8(3), 373–379.

[Kortz81]   Kortz, H. P., R. Iffländer, and H. Weber, 1981: Stability and beam divergence of multimode lasers with internal variable lenses. Appl. Optics, 20(23), 4124–4134.

[Kudryashov99] Kudryashov, A. V. and H. W. et al., 1999: Laser resonators: novel design and development. SPIE Bellingham, Washington.

[Lawrence92]   Lawrence, G. N., 1992: Optical modeling, volume XI of Applied Optics and Optical Engineering, chapter 3. Academic Press, Inc., 125–200.

[Lee02]   Lee, W. and W. R. Lempert, 2002: Spectrally filtered Raman/Thomson scattering using a Rubidium vapor filter. AIAA J., 40(12), 2504–2510.

[Lee03]   Lee, W. and W. R. Lempert, 2003: Enhancement of spectral purity of injection-seeded titanium:sapphire laser by cavity locking and stimulated Brillouin scattering. Appl. Optics, 42(21), 4320–4326.

[Lörtscher75]   Lörtscher, J. P. and J. Steffen, 1975: Dynamic stable resonators: a design procedure. Opt. Quant. Electron., 7, 505–514.

[Magni86]   Magni, V., 1986: Resonators for solid-state lasers with large-volume fundamental mode and high alignment sensitivity. Appl. Optics, 25(1), 107–117.

[Marenco02]   Marenco, F. and P. T. Brunozzi, 2002: Different possibilities for water vapour measurements by lidar in daytime at ENEA's observatory in Lampedusa, Italy: a simulation. J. Opt. A - Pure Appl. Op., 4, 408–418.

[McCormick05]   McCormick, M. P., 2005: Airborne and Spaceborne Lidar, volume 102 of Springer Series in Optical Sciences: LIDAR: Range-Resolved Optical Remote Sensing of the Atmosphere, chapter 13. Springer Science+Business Media Inc.

[Metcalf87]   Metcalf, D., P. de Giovanni, J. Zachorowski, and M. Leduc, 1987: Laser resonators containing self-focusing elements. Appl. Optics, 26(21), 4508–4517.

[Morin97]   Morin, M., 1997: Graded reflectivity mirror unstable laser resonators. Opt. Quant. Electron., 29, 819–866.

[Moulton82]   Moulton, P., 1982: Ti-doped sapphire: tunable solid-state laser. Optics News, 9.

[Moulton86]   Moulton, P. F., 1986: Spectroscopic and laser characteristics of $Ti:Al_2O_3$. J. Opt. Soc. Am. B, 3(1), 125–133.

[NASA]   NASA. National Aeronautics and Space Administration (NASA): Earth Observatory. URL http://earthobservatory.nasa.gov/.

[New01]   New, G. H. C., M. A. Yates, J. P. Woerdman, and G. S. McDonald, 2001: Diffractive origin of fractal resonator modes. Opt. Commun., 193, 261–266.

[Nye57]   Nye, J. F., 1957: Natural and artificial double refraction. Second-order effects, chapter 13. Physical properties of crystals. Oxford science publications, 1985 edition, 235–259.

[Ostermeyer05a]   Ostermeyer, M., P. Kappe, R. Menzel, and V. Wulfmeyer, 2005: Diode-pumped Nd:YAG master oscillator power amplifier with high pulse energy, excellent beam quality, and frequency-stabilized master oscillator as a basis for a next-generation lidar system. Appl. Optics, 44(4), 582–590.

[Ostermeyer05b]   Ostermeyer, M., P. Kappe, R. Menzel, and V. Wulfmeyer, 2005: Diode-pumped Nd:YAG master oscillator power amplifier with high pulse energy, excellent beam quality, and frequency-stabilized master oscillator as a basis for a next-generation lidar system - erratum. Appl. Optics, 44(34), 7451.

[Ostermeyer06]   Ostermeyer, M., D. Mudge, P. J. Veitch, and J. Munch, 2006: Thermally induced birefringence in Nd:YAG slab lasers. Appl. Optics, 45(21), 5368–5376.

[Ottusch91]   Ottusch, J. J., M. S. Mangir, and D. A. Rockwell, 1991: Efficient anti-Stokes Raman conversion by four-wave mixing in gases. J. Opt. Soc. Am. B, 8(1), 68–77.

[Pace94]   Pace, C., E. Nava, and C. Cali, 1994: A simple GRM design for tunable Ti:sapphire lasers. Pure Appl. Opt., 3, 441–447.

[Pal08]   Pal, S., A. Behrendt, H. Bauer, M. Radlach, A. Riede, M. Schiller, G. Wagner, and V. Wulfmeyer, 2008: 2-dimensional observations of atmospheric variables during the field campaign COPS. In Earth Environm. Sci., IOP Conference Series. 012031.

[Parent92]   Parent, A., M. Morin, and P. Lavigne, 1992: Propagation of super-Gaussian field distributions. Opt. Quant. Electron., 24, S1071–S1079.

[Paschotta07]   Paschotta, R., H. R. Telle, and U. Keller, 2007: Noise of solid-state lasers, chapter 12. Solid-state lasers and applications. CRC Press (Taylor & Francis Group).

[Pask03a]   Pask, H. M., 2003: The design and operation of solid-state Raman lasers (review). Prog. Quant. Electron., 27, 3–56.

[Pask03b]   Pask, H. M., S. Myers, J. A. Piper, J. Richards, and T. McKay, 2003: High average power, all-solid-state external resonator Raman laser. Opt. Lett., 28(6), 435–437.

[Penzkofer79]   Penzkofer, A., A. Laubereau, and W. Kaiser, 1979: High intensity Raman interactions. Prog. Quant. Electron., 6(2), 55–140.

[Petermann79]   Petermann, K., 1979: Calculated spontaneous emission factor for double-heterostructure injection lasers with gain-induced waveguiding. IEEE J. Quant. Elect., 15(7), 566–570.

[Pfistner94]   Pfistner, C., R. Weber, H. P. Weber, S. Merazzi, and R. Gruber, 1994: Thermal beam distortions in end-pumped Nd:YAG, Nd:GSGG, and Nd:YLF rods. IEEE J. Quant. Elect., 30(7), 1605–1615.

[Poberaj02]   Poberaj, G., A. Fix, A. Assion, M. Wirth, C. Kiemle, and G. Ehret, 2002: Airborne all-solid-state DIAL for water vapour measurements in the tropopause region: system description and assessment of accuracy. Appl. Phys. B - Lasers O., 75, 165–172.

[Powell86]   Powell, R. C., G. E. Venikouas, L. Xi, J. L. Tyminski, and M. R. Kokta, 1986: Thermal effects on the optical spectra of Al_2O_3:Ti^{3+}. J. Chem. Phys., 84(2), 662–665.

[Powell98]   Powell, R. C., 1998: Physics of solid-state laser materials. Atomic, molecular, and optical physics. Springer-Verlag New York, Berlin, Heidelberg.

[Rahn85]   Rahn, L. A., 1985: Feedback stabilization of an injection-seeded Nd:YAG laser. Appl. Optics, 24(7), 940–942.

[Ralph96]   Ralph, T. C., C. C. Harb, and H.-A. Bachor, 1996: Intensity noise of injection-locked lasers: Quantum theory using a linearized input-output method. Phys. Rev. A, 54(5), 4359–4369.

[Ramanathan06]   Ramanathan, V., J. Lee, S. Xu, X. Wang, L. Williams, W. Malphurs, and D. H. Reitze, 2006: Analysis of thermal aberrations in a high average power single-stage Ti:sapphire regenerative chirped pulse amplifier: Simulation and experiment. Rev. Sci. Instrum., 77, 103103–7.

[Rapoport88]   Rapoport, W. R. and C. P. Khattak, 1988: Titanium sapphire laser characteristics. Appl. Optics, 27(13), 2677–2684.

[Rines90]   Rines, G. A. and P. F. Moulton, 1990: Performance of gain-switched Ti:Al_2O_3 unstable resonator lasers. Opt. Lett., 15(7), 434–436.

[Rines91]   Rines, G. A., H. H. Zenzie, and P. F. Moulton, 1991: Recent advantages in Ti:Al_2O_3 unstable resonator lasers. In OSA Proc. on Advanced Solid State Lasers (ASSP), volume 6.

[Saito01]	Saito, N., S. Wada, and H. Tashiro, 2001: Dual-wavelength oscillation in an electronically tuned Ti:sapphire laser. J. Opt. Soc. Am. B, 18(9), 1288–1296.
[Saleh07]	Saleh, B. E. A. and M. C. Teich, 2007: Lasers, chapter 15. Fundamentals of photonics. Wiley, 567–626.
[Sanchez88]	Sanchez, A., A. J. Strauss, R. L. Aggarwal, and R. E. Fahey, 1988: Crystal growth, spectroscopy, and laser characteristics of $Ti:Al_2O_3$. IEEE J. Quant. Elect., 24(6), 995–1002.
[Schawlow58]	Schawlow, A. L. and C. H. Townes, 1958: Infrared and optical masers. Phys. Rev., 112(6), 1940–1949.
[Schiller09]	Schiller, M., 2009: A high-power laser transmitter for ground-based and airborne water-vapor measurements in troposphere. Ph.D. thesis, IPM, University of Hohenheim.
[Schmitt86]	Schmitt, R. L. and L. A. Rahn, 1986: Diode-laser-pumped Nd:YAG laser injection seeding system. Appl. Optics, 25(5), 629–633.
[Schröder07]	Schröder, T., C. Lemmerz, O. Reitebuch, M. Wirth, C. Wührer, and R. Treichel, 2007: Frequency jitter and spectral width of an injection-seeded Q-switched Nd:YAG laser for a Doppler wind lidar. Appl. Phys. B - Lasers O., 87, 437–444.
[Schulz91]	Schulz, P. A. and S. R. Henion, 1991: Liquid-nitrogen-cooled $Ti:Al_2O_3$ laser. IEEE J. Quant. Elect., 27(4), 1039–1047.
[Siegman]	Siegman, A. E. Corrections for LASERS. URL http://www.stanford.edu/~siegman/lasers_book_errata.pdf.
[Siegman65]	Siegman, A. E., 1965: Unstable optical resonators for laser applications. P. IEEE, 53(3), 277–287.
[Siegman76]	Siegman, A. E., 1976: A canonical formulation for analyzing multielement unstable resonators. IEEE J. Quant. Elect., 12(1), 35–40.
[Siegman86a]	Siegman, A. E., 1986: Coupled cavity and atomic rate equations, chapter 13.3. Lasers. University Science Books, 505–510.
[Siegman86b]	Siegman, A. E., 1986: Laser injection locking, chapter 29. Lasers. University Science Books, 1129–1170.

[Siegman86c]   Siegman, A. E., 1986: Lasers. University Science Books.

[Siegman89a]   Siegman, A. E., 1989: Excess spontaneous emission in non-Hermitian optical systems. I. Laser amplifiers. Phys. Rev. A, 39(3), 1253–1263.

[Siegman89b]   Siegman, A. E., 1989: Excess spontaneous emission in non-Hermitian optical systems. II. Laser oscillators. Phys. Rev. A, 39(3), 1264–1268.

[Siegman95]   Siegman, A. E., 1995: Lasers without photons - or should it be lasers with too many photons? Appl. Phys. B - Lasers O., 60, 247–257.

[Smith95]   Smith, A. V., W. J. Alford, T. D. Raymond, and M. S. Bowers, 1995: Comparison of a numerical model with measured performance of a seeded, nanosecond KTP optical parametric oscillator. J. Opt. Soc. Am. B, 12(11), 2253–2267.

[Sträßer07]   Sträßer, A., T. Waltinger, and M. Ostermeyer, 2007: Injection seeded frequency stabilized Nd:YAG ring oscillator following a Pound-Drever-Hall scheme. Appl. Optics, 46(34), 8358–8363.

[Touloukian70]   Touloukian, Y. and C. Ho (editors), 1970: Thermal conductivity - metallic elements and alloys, volume 1 of Thermophysical properties of matter. IFI/Plenum New York Washington.

[Touloukian72a]   Touloukian, Y. and C. Ho (editors), 1972: Specific heat - metalic elements and alloys, volume 4 of Thermophysical properties of matter. IFI/Plenum New York Washington.

[Touloukian72b]   Touloukian, Y. and C. Ho (editors), 1972: Specific heat - nonmetalic solids, volume 5 of Thermophysical properties of matter. IFI/Plenum New York Washington.

[Touloukian72c]   Touloukian, Y. and C. Ho (editors), 1972: Thermal conductivity - nonmetalic solids, volume 2 of Thermophysical properties of matter. IFI/-Plenum New York Washington.

[Treichel04]   Treichel, R., C. Czeranowsky, B. Ileri, K. Petermann, and G. Huber, 2004: Mixed Garnet laser crystals for water vapour DIAL transmitter. In B. Warmbein (editor), Proceedings of the 5th International Conference on Space Optics (ICSO), 30 March - 20 April 2004, Toulouse, France, SP-554. ESA Publications Division, 639–642.

References

[Verfürth96]   Verfürth, R., 1996: A review of a posteriori error estimation and adaptive mesh refinement techniques. Wiley-Teubner.

[Vogelmann08]   Vogelmann, H. and T. Trickl, 2008: Wide-range sounding of free-tropospheric water vapor with a differential absorption lidar (DIAL) at a high-altitude station. Appl. Optics, 47(12), 2116–2132.

[Wagner05]   Wagner, G., M. Shiler, and V. Wulfmeyer, 2005: Simulations of thermal lensing of a Ti:Sapphire crystal end-pumped with high average power. Opt. Express, 13(20), 8045–8055.

[WALES04]   WALES, 2004: European Space Agency (ESA): WALES (Water vapour lidar experiment in space). Reports for mission selection SP-1279(3). ESA Publications Division, ESTEC, Noordwijk, The Netherlands.

[Walther01]   Walther, T., M. P. Larsen, and E. S. Fry, 2001: Generation of Fourier-transform-limited 35-ns pulses with a ramp-hold-fire seeding technique in a Ti:sapphire laser. Appl. Optics, 40(18), 3046–3050.

[Wang94]   Wang, X., G. Hu, Y. Li, and J. Yao, 1994: Numerical analysis of beam parameters and stability regions in a folded or ring cavity. J. Opt. Soc. Am. A, 11(8), 2265–2270.

[Webb98]   Webb, M. S., P. F. Moulton, J. J. Kasinski, R. L. Burnham, G. Loiacono, and R. Stolzenberger, 1998: High-average-power $KTiOAsO_4$ optical parametric oscillator. Opt. Lett., 23(15), 1161–1163.

[Weber93]   Weber, H., 1993: Nichtlineare Optik, volume 3 of Bergmann - Schaefer - Lehrbuch der Experimentalphysik, chapter 8. Walter de Gruyter, 9th edition, 911–981.

[Weber98]   Weber, R., B. Neuenschwander, M. MacDonald, M. B. Roos, and H. P. Weber, 1998: Cooling schemes for longitudinally diode laser-pumped Nd:YAG rods. IEEE J. Quant. Elect., 34(6), 1046–1053.

[Wirth08]   Wirth, M., A. Fix, P. Mahnke, H. Schwarzer, F. Schrandt, and G. Ehret, 2008: The airborne multiwavelength NIR-H2O-DIAL WALES: system layout and performance. In Reviewed and revised papers presented at the 24th International Laser and Radar Conference (ILRC), 23-28 June 2008, Boulder, CO, USA. 27–30.

[Wulfmeyer95]   Wulfmeyer, V., J. Bösenberg, S. Lehmann, C. Senff, and S. Schmitz, 1995: Injection-seeded Alexandrite ring laser: performance and application in a water-vapor differential absorption lidar. Opt. Lett., 20(6), 638–640.

[Wulfmeyer98a]   Wulfmeyer, V., 1998: Ground-based differential absorption lidar for water-vapor and temperature profiling: development and specifications of a high-performance laser transmitter. Appl. Optics, 37(18), 3804–3824.

[Wulfmeyer98b]   Wulfmeyer, V. and J. Bösenberg, 1998: Ground-based differential absorption lidar for water-vapor profiling: assessment of accuracy, resolution, and meteorological applications. Appl. Optics, 37(18), 3825–3844.

[Wulfmeyer00]   Wulfmeyer, V., M. Randall, A. Brewer, and R. M. Hardesty, 2000: 2-μm Doppler lidar transmitter with high frequency stability and low chirp. Opt. Lett., 25(17), 1228–1230.

[Wulfmeyer01a]   Wulfmeyer, V. and C. Walther, 2001: Future performance of ground-based and airborne water-vapor differential absorption lidar. I. Overview and theory. Appl. Optics, 40(30), 5304–5320.

[Wulfmeyer01b]   Wulfmeyer, V. and C. Walther, 2001: Future performance of ground-based and airborne water-vapor differential absorption lidar. II. Simulations of the precision of a near-infrared, high-power system. Appl. Optics, 40(30), 5321–5336.

[Wulfmeyer03]   Wulfmeyer, V., H.-S. Bauer, S. Crewell, G. Ehret, O. Reitebuch, C. Werner, M. Wirth, D. Engelbart, A. Rhodin, W. Wergen, A. Giesen, H. Grassl, G. Huber, H. Klingenberg, P. Mahnke, U. Kummer, C. Wührer, P. Ritter, R. Wallenstein, and U. Wandinger, 2003: Lidar Research Network Water Vapor and Wind. Meteorol. Z., 12(1), 5–24.

[Wulfmeyer05]   Wulfmeyer, V., H. Bauer, P. di Girolamo, and C. Serio, 2005: Comparison of active and passive water vapor remote sensing from space: an analysis based on the simulated performance of IASI and space borne differential absorption lidar. Remote Sens. Environ., 95, 211–230.

[Wulfmeyer06]   Wulfmeyer, V., H.-S. Bauer, M. Grzeschik, A. Behrendt, F. Vandenberghe, E. V. Browell, S. Ismail, and R. A. Ferrare, 2006: Four-dimensional variational assimilation of water vapor differential absorption lidar data: the first case study within IHOP_2002. Mon. Weather Rev., 1, 209–230.

[WWRP]   WWRP. World Weather Research Programme (WWRP): Mesoscale
                   Forecasting. URL `http://www.wmo.int/pages/prog/arep/wwrp/new/`
                   `wwrp_new_en.html`.

[Zavelani-Rossi00] Zavelani-Rossi, M., F. Lindner, C. LeBlanc, G. Chériaux, and J. P. Cham-
                   baret, 2000: Control of thermal effects for high-intensity Ti:sapphire laser
                   chains. Appl. Phys. B - Lasers O., 70(Suppl.), S193–S196.

[Zverev99]   Zverev, P. G., T. T. Basiev, V. V. Osiko, A. M. Kulkov, V. N. Voit-
                   sekhovskii, and V. E. Yakobson, 1999: Physical, chemical and optical
                   properties of barium nitrate Raman crystal. Opt. Mater., 11, 315–334.

List of publications

Papers and conferences

Behrendt, A., G. Wagner, A. Petrova, M. Shiler, S. Pal, T. Schaberl, and V. Wulfmeyer, 2005: Modular lidar systems for high-resolution 4-dimensional measurements of water vapor, temperature, and aerosols. In: U. N. Singh and Kohei Mizutani (Eds.), Lidar Remote Sensing for Industry and Environment Monitoring V (Proceedings of SPIE 5653), November 8-12, 2004, Honolulu, Hawaii, USA, p. 220-227.

Wagner, G., M. Shiler, and V. Wulfmeyer, 2005: Simulation of thermal lensing of a Ti:Sapphire crystal end-pumped with high average power. Opt. Express, 13, 8045-8055.

Petrova, A., G. Wagner, and V. Wulfmeyer, 2004: Eye-safe lidar transmitter at 1.45 μm based on a Cr4+:YAG laser. In: G. Pappalardo, A. Amadeo (Eds.), Reviewed and Revised Papers of the 22nd International Laser Radar Conference (ILRC 2004), July 12-16, 2004, Matera, Italy (ESA SP-561, June 2004), p. 199-202.

Wagner, G., M. Shiler, and V. Wulfmeyer, 2004: Design and development of a high-power Ti:Sapphire laser transmitter. In: G. Pappalardo, A. Amadeo (Eds.), Reviewed and Revised Papers of the 22nd International Laser Radar Conference (ILRC 2004), July 12-16, 2004, Matera, Italy (ESA SP-561, June 2004), p. 203-206.

Wagner, G., V. Wulfmeyer et al., 2009: Frequency conversion methods for space-borne water vapor DIAL, in preparation.

Wagner, G., V. Wulfmeyer et al., 2009: High-power Ti:Sapphire laser based on an unstable resonator - design and measurements, in preparation.

Conferences

Wulfmeyer, V., A. Behrendt, M. Shiler, S. Pal, A. Riede, H. Bauer, G. Wagner, A. Fix, M. Wirth, G. Ehret, U. Wandinger and D. Althausen, 2008 (invited): High-resolution water-vapor measurement using a ground-based, mobile differential absorption lidar system, 88th Annual Meeting of the American Meteorological Society, New Orleans, January 2008.

Schiller, M., G. Wagner, and V. Wulfmeyer, 2007: A high-power, single-frequency Ti:Sapphire laser for water-vapor DIAL. Conference on Lasers and Electro-Optics, Baltimore, USA, May 8th-10th, 2007.

Behrendt, A., V. Wulfmeyer, M. Schiller, A. Riede, H. Bauer, G. Wagner, and S. Pal, 2007: Water vapour differential absorption lidar measurements at Hornisgrinde during COPS. DACH Meteorologentagung, Hamburg, September 2007.

Behrendt, A., A. Petrova, T. Schaberl, M. Shiler, G. Wagner, and V. Wulfmeyer, 2004: Lidar systems for 4-dimensional observations of atmospheric key parameters in development at University of Hohenheim. Verhandlungen der Deutschen Physikalischen Gesellschaft zur 68. Physikertagung (Proceeding of the 68th Meeting of the German Physical Society), Fachvortrag UP 3.7, 176.

Selected Presentations

Wagner, G., 2004: Theoretical modeling of high power lasers, Lidar Expert Network: Lidar Research Water Vapor and Wind, Hohenheim, September 15th, 2004.

V. Wulfmeyer, G. Wagner, A. Behrendt, 2005: DIAL Instrument analysis - Proposed transmitters for CO_2 IPDA, Requirements Definition for Future DIAL Instrument - ESA Final Presentation Meeting, ESTEC, Noordwijk, April 22nd, 2005.

Wulfmeyer, V., G. Wagner, A. Behrendt, M. Shiler, 2005: DFG Research Project: Lidar Reference System Based on a High-power Laser, ESA-DLR Technology Activities for Space borne DIAL Instruments - Meeting, ESTEC, Noordwijk, November 18th, 2005.

Wagner, G., 2005: TISA: Thermal modeling update, DFG Lidar Reference System, Project Status Meeting, DLR Oberpfaffenhofen, October 5th-6th, 2005.

Wagner, G., 2006: TISA: Unstable resonator concepts, DFG Lidar Reference System, Project Status Meeting, Ift Leipzig, March 21st-23rd, 2006.

Acknowledgment